PhD Thesis

Single Donors in Silicon for Atomic Scale Devices

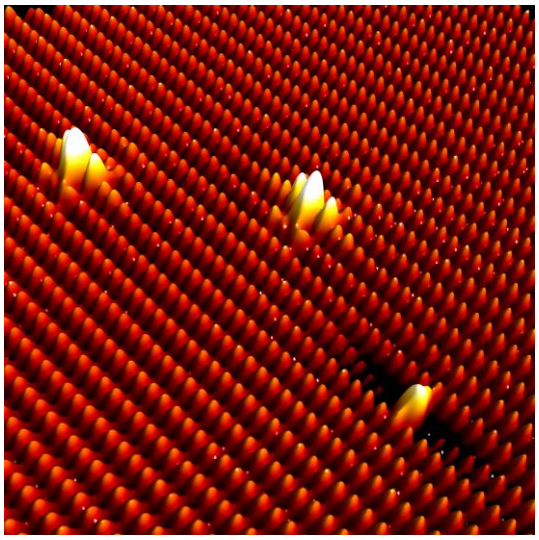

PhD in Electronic and Electrical Engineering

Philipp René Studer

Supervisors:
Dr. Neil Curson
Prof. Arokia Nathan

Declaration

I, Philipp Studer confirm that the work presented in this thesis is my own. Where information has been derived from other sources, I confirm that this has been indicated in the thesis.

Philipp Studer

Abstract

This thesis describes a detailed characterization of the atomic scale properties of individual donor atoms in silicon. A cross sectional sample preparation technique was developed, allowing us to study cleaved silicon surfaces using scanning tunnelling microscopy (STM). The Si(111)-2x1 surface is characterized and in particular the properties of anti phase boundaries are investigated. We identify a strain induced band shift associated with the boundaries and furthermore show that they can be controllably manipulated, making them an ideal model system to study and control strain in silicon at the atomic scale.

To enable the characterization of individual deep dopants such as bismuth (Bi), which are not used in semiconductor industry, a novel STM sample preparation method was developed. We demonstrate that ion implantation can be used to produce almost defect free samples with high Bi concentrations, suitable for STM measurements. Using cross sectional STM we are furthermore able to laterally resolve the implanted dopant profile and visualize its influence on the band structure of the silicon host crystal.

The new sample preparation method is used to investigate the fundamental properties of different group V dopants at the atomic scale. We identify individual bismuth and antimony donors in the Si(111)-2x1 surface and show that their large dopant cores not only induce new atomic reconstructions but also influence the measured charge states. Using scanning tunnelling spectroscopy we furthermore resolve the Coulomb potential well of individual dopants and characterize the influence of surface states on charge screening at the atomic scale.

In addition to the described STM work, a state of the art cleanroom fabrication process was developed[1] to allow the placement of individual dopants in silicon[2] with atomic scale precision. This will enable the use of the insights gained about individual donors in this thesis for the fabrication of future single dopant devices.

Acknowledgements

I would like to thank all the people supporting me during the last three years, with scientific advice or simply encouraging words, completing this thesis would not have been possible without you.

My deepest gratitude goes to Neil Curson for the opportunity to be part of his group and for his unfailing support and encouragement over the whole time of my PhD, making my stay here not only interesting but also enjoyable. I am also greatly indebted to Cyrus Hirjibehedin for his continuous guidance and advice during my thesis, always pointing me in the right direction and helping me to focus on the relevant points. I am truly grateful to both of you.

I would like to thank Steven Schofield, for supporting me in the lab, showing me everything there is to know about STM and introducing me to the confusing world of cricket. Further I would like to thank the whole STM lab, Ben, Fadi, Adam, Reyes, Jenny, Benjamin, Chris, Kevin and Kitiphat for their warm welcome, the coffee breaks and the wonderful time I could spend here. I couldn't have asked for a better bunch of friends.

I would also like to thank my collaborators, Veronika Brazdova, Greg Lever and David Bowler for valuable discussions and for providing all DFT calculations. Andy Smith from Surrey University for his invaluable help with ion implantation, Hall and RBS measurements.

I am also grateful to my parents for always supporting me throughout my whole life, giving me the possibility and the confidence to achieve my goals. Heartfelt thanks to Rachel, for being a wonderful person, supporting me, reminding me of what really counts and for sharing my life.

Table of contents

1 Introduction

The properties of individual dopant atoms are of fundamental importance not only for highly scaled electronic devices but also for future computation concepts such as quantum information processing (QIP) or spintronics. It is known that the atomic scale environment of dopants, for example their proximity to surfaces or contact areas of different materials, can severely influence the dopant characteristics such as the shape of their wave function[3] or their ionization energy.[4] For conventional semiconductor devices, variations in the ionization energy of individual dopants used to be negligible because the device functionality was based on statistically averaged properties of thousands of donors. However, as scaling continues and devices are becoming smaller, an increasing proportion of dopants are situated in close proximity to an interface and the way in which their properties are influenced becomes crucial for the device characteristics. In highly scaled metal–oxide–semiconductor field-effect transistors (MOSFETs), the random distribution of dopants in the channel already leads to variations in the threshold voltage, preventing the scaling of the supply voltage. As outlined in the International Technology Roadmap for Semiconductors,[5] this is considered one of the main challenges that has to be addressed in order to continue the trend in scaling for future MOSFETs.

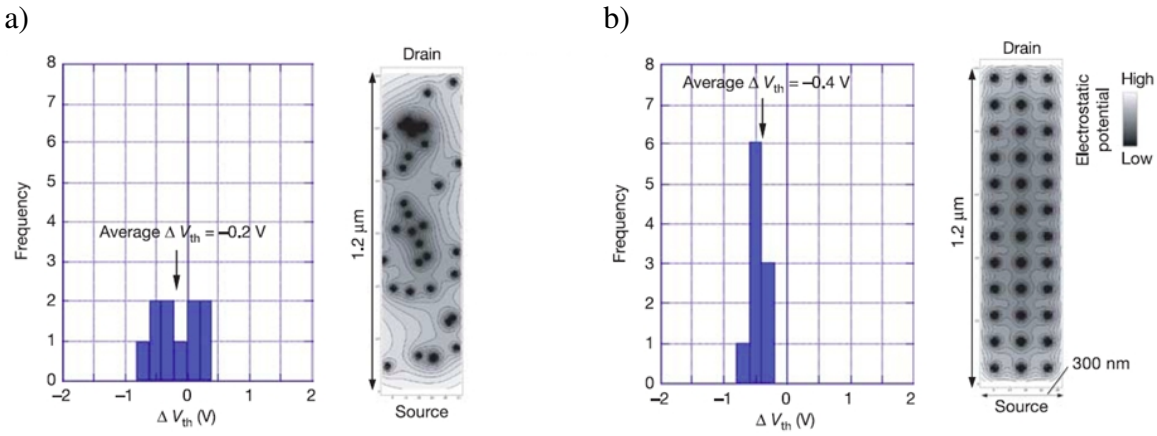

Figure 1.1: a) Measured threshold voltages of ten devices and the calculated electrostatic potential of randomly distributed dopants. b) Measured threshold voltages of ten devices and the calculated electrostatic potential of an ordered dopant array. Image from [6].

A possible solution to this problem was presented by Shinada et al.[6] as shown in Fig.

1.1. Using single ion implantation they demonstrated that it is possible to create devices with a controlled number of well ordered dopants. This enabled them to engineer the interactions of dopants with each other and their surrounding environment, avoiding the variation in the threshold voltage of MOSFETs caused by random dopant distribution. It can be seen that the random placement of dopants, shown in Fig. 1.1 a), produces a wide spread of threshold voltages whereas the ordered dopant array, shown in Fig. 1.1 b), results in much more controlled device characteristics. These results demonstrate the importance of finding techniques that enable the precise control of the location of individual dopants. However, manufacturing highly scaled devices with deterministic dopant structures requires almost atomic scale control over the dopant location. This represents a formidable challenge for fabrication processes as conventional techniques like optical or electron-beam lithography (EBL) reach their inherent resolution limits.

Besides controlling the characteristics of highly scaled semiconductor devices, being able to place and characterize individual dopants at the atomic scale is also of crucial importance to realize fascinating new computational concepts such as spintronics or quantum information processing (QIP). Possible implementation schemes for these next generation electrical devices have been proposed,[7, 8] relying on the quantum states of single donor atoms in silicon. To enable the implementation of such novel device architectures, typical separations between dopant pairs or dopants and gates are envisaged on the order of a few nanometers, as described in the following section. Understanding how dopants interact with their atomic scale environment is therefore of fundamental importance and much effort is currently devoted towards developing new ways to characterize and control individual dopants at the atomic scale.

1.1 Quantum Computing Concepts

A theoretical concept for the realization of solid state quantum information processing in silicon was proposed by B. E. Kane[7] as shown in Fig. 1.2. In this scheme, information is encoded onto the nuclear spin of phosphorus dopants and metallic gates are used to control the electron mediated spin coupling between them.

The exact dimensions of such a quantum computer are crucial, as for example the separation between the P dopants determines their interaction and therefore the required time for elementary operations. In the proposal of Kane, gate widths and their separation are assumed on the order of 10 nm, resulting in a dopant separation of 25 nm. Dopants furthermore should be located no more than 20 nm below the gate to make sure the electric field applied to the donor is sufficiently strong to shift the electron wavefunction away from the nucleus and reduce the hyperfine interaction. These formidable fabrication requirements have proven challenging, as dopants not only have to be placed with atomic

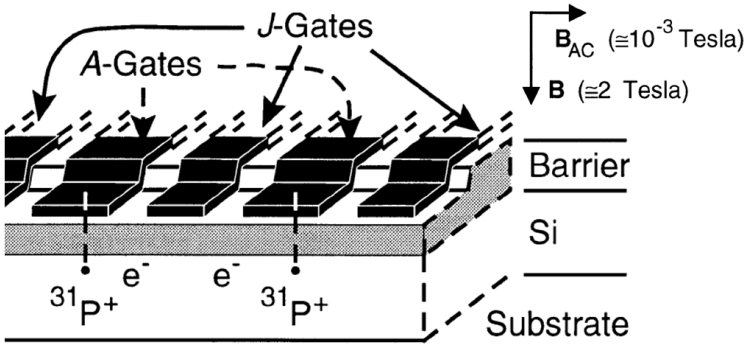

Figure 1.2: A silicon-based nuclear spin quantum computer proposed by B. E. Kane. Image from [7].

scale precision but also with perfect alignment to the respective gates. The proximity of the P dopants to the metallic gates and to the oxide layer furthermore highlights the importance of investigating how these interfaces influence the dopant characteristics.

For the Kane proposal to work, P atoms have to be in their non ionized state to make sure their valence electrons remain bound, requiring operation temperatures below 100 mK. The use of metallic gates and insulating layers furthermore increases the risk of introducing atomic scale defects at the interfaces, possibly disturbing the operation of the device. An alternative approach has therefore been suggested by Stoneham et al.,[8] based on deep donors in silicon and avoiding the use of electrodes. This not only facilitates the fabrication process as fewer alignment steps are required but possibly also enables operation at liquid nitrogen temperature. The proposed scheme is shown in Fig. 1.3, based on three impurities in silicon. Dopant A and B form the quantum bits (qubits) similar to the P atoms in the Kane proposal, except that information is encoded in the spin of the donor valence electrons as opposed to the donor nuclear spins. However, instead of using metallic gates to control the interaction of these dopants, a control impurity C is placed in between them that has a different optical excitation frequency compared to the donors forming the qubits. In their ground states, the three impurities are not interacting. However, upon excitation of the control impurity, its wavefunction extends across the two neighboring dopants and therefore creates an exchange interaction between the qubit spins. Optical excitation and stimulated de-excitation can therefore be used to controllably switch interactions between qubits on and off respectively. The use of deep donors such as bismuth (Bi) is suggested to enable QIP operations at higher temperatures. For the Si:Bi system, separations between the two Bi atoms on the order of 5 nm -10 nm are required to enable sufficient interaction between them.

The fact that this scheme is based on optical excitation and therefore does not require metallic gates potentially makes the fabrication simpler but also creates new challenges regarding the scalability. As the spatial resolution of optical techniques will not be high

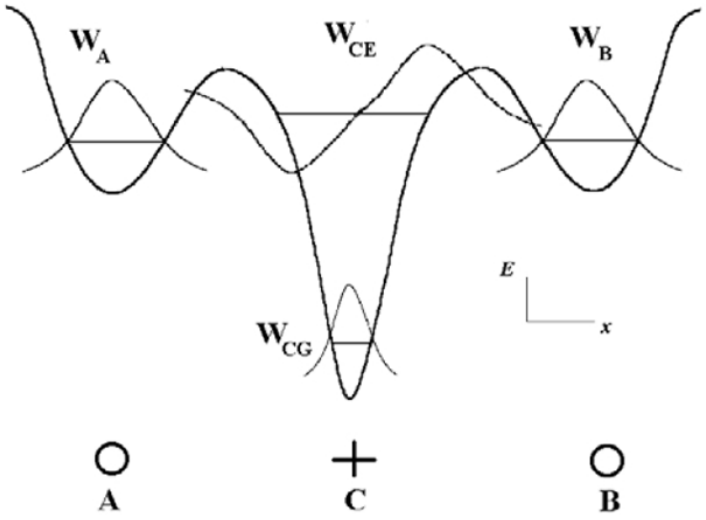

Figure 1.3: Optically driven silicon-based quantum gates with potential for high-temperature operation. Image from [8].

enough to single out an individual qubit, it is necessary to make them spectroscopically distinguishable by slight variations of their energy states. Besides natural fluctuations occurring from their random positions, it might therefore be necessary to develop techniques that allow one to engineer the inhomogeneous broadening of dopants in silicon. In this work we suggest a possible approach for modifying energy levels of individual dopants using strain. As discussed in Chap. 5, we present a model system to study and control strain in silicon at the atomic scale, providing the possibility to engineer the energy states of dopants close to cleaved silicon surfaces.

Both QIP architectures are relying on the unique quantum states of donors in silicon, requiring the placement of dopants with high spatial accuracy in respect to gates or each other. Among many challenges, two of the most important aspects that have to be investigated are therefore the controlled placement of dopants and the characterization of their properties at the atomic scale. Different approaches are pursued to reach each of these goals and the most recent achievements are presented in the following sections.

1.2 Atomically Precise Device Fabrication

Fabrication techniques that allow the incorporation of a controlled number of dopants with atomic scale precision are required to build future single dopant devices. Single ion implantation is a promising approach that enables the deposition of a controlled number of impurities into various substrates. One possible approach to realize single ion implantation with high spatial accuracy was implemented by Schenkel et al.[9], using the setup shown in Fig. 1.4.

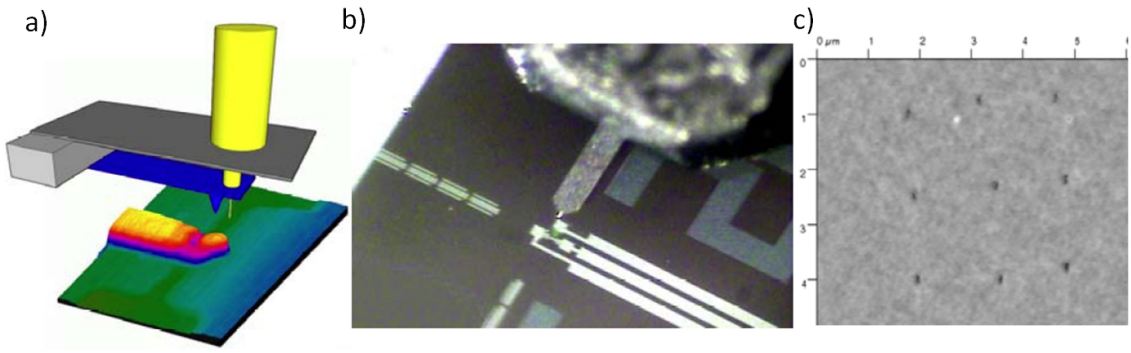

Figure 1.4: Single dopant implantation. a) Schematic and b) image of the SPM setup for single ion implantation. c) Ordered dopant array. Images from [9–11].

To control the lateral position of the implanted dopant ions, they are collimated in a dynamically positionable shadow mask that is integrated into a scanning probe tip as shown in Fig. 1.4 a) and b). The impact of individual ions is then detected electrically, allowing one to controllably implant a precise number of dopants. Using this technique, the placement accuracy is dependent on the implantation depth and the mass of the donors used. For the example of individual P dopants and a nominal implantation depth of 20 nm, an accuracy of around 10 nm can be achieved. The lateral resolution is dependent on the shadow mask used and holes as small as 5 nm diameter were demonstrated. This allows the creation of ordered dopant arrays as shown in Fig. 1.4 c).

The advantage of this technique is that it enables the implantation of almost every element into different substrates, and with arbitrary device designs. The integration with scanning probe techniques further allows one to align the dopants to existing surface features and the depth of the implanted donors can be controlled over a wide range by varying the beam energy. However, the spatial control over the dopant positions is on the order of the dimensions required to implement the presented QIP schemes and would have to be further improved to allow the controlled fabrication of qubits in silicon.

An alternative technique to allow the placement of dopants in silicon with atomic precision has recently been demonstrated for the case of phosphorus, using a scanning tunnelling microscope.[1, 2] The single atom manipulation capabilities of STM are used to selectively remove individual hydrogen (H) atoms from a monolayer H resist, as shown in the left panel of Fig. 1.5 a). Phosphene gas is then used to selectively deposit P onto the desorbed area, taking advantage of the increased reactivity of depassivated Si bonds compared to the hydrogen terminated surface. This process, described in more detail in Chap. 4, not only allows the atomically precise placement of P but can also be used to create larger structures, as shown in Fig. 1.5 b), enabling the fabrication of whole devices with atomic scale precision.

The experiments shown in Fig. 1.5 impressively demonstrate that it is possible to con-

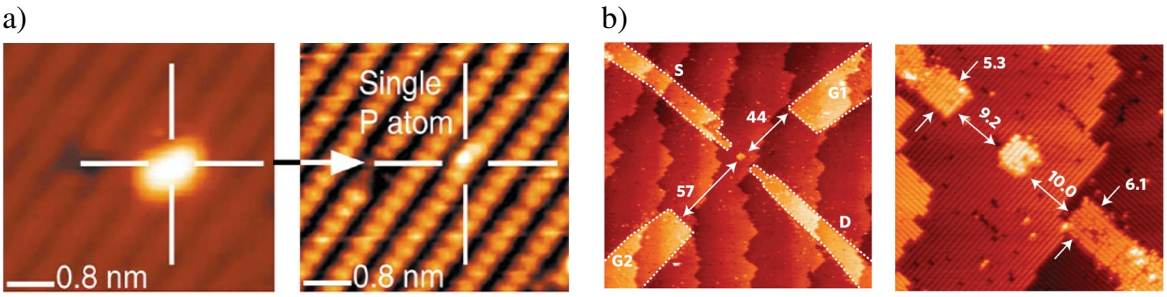

Figure 1.5: a) Placing an individual P dopant in silicon with atomic scale precision, image from [2]. b) Device structure of a few dopant quantum dot fabricated using STM lithography, image from [12].

trol dopants with sufficient accuracy to enable the fabrication of the discussed QIP structures. The capability of STM to image surfaces with atomic resolution furthermore allows one to characterize the fabricated device at the atomic scale and scanning tunnelling spectroscopy (STS) can be used to measure its electronic properties. This makes STM a very powerful technique for both fabricating and characterizing single dopant devices. In the scope of this thesis, a fabrication process similar to the one described was developed with the aim of also enabling the incorporation of different dopant elements. The necessary cleanroom processes were implemented and characterized, allowing the combined use of highly aligned STM and EBL fabrication. Additionally, gas dosing systems and tip preparation facilities for the STM were designed, installed and tested, providing all the necessary components for future work focussing on placing different group V donors with atomic scale precision.

As it has been successfully demonstrated that few dopant structures can be built with high precision, one of the next important steps is to study individual dopants to understand how they are influenced by their atomic scale environment. This is necessary in order to engineer how dopants interact with each other or with metallic gates and material interfaces in close proximity. Again, much progress has already been demonstrated regarding the characterization of individual dopant atoms and some milestones are presented in the following sections.

1.3 Studying Single Donor Effects in Randomly Doped Semiconductor Devices

We have seen that the random distribution of dopants in highly scaled semiconductor devices can adversely influence device characteristics. However, these influences can also be exploited to study the characteristics of individual dopants and how they modify the functionality of nanoscale devices. Sellier et al.[13] studied fin field effect transistors

(FinFETs), as shown in the left panel of Fig. 1.6, and were able to demonstrate that the influence of single dopants can be extracted from the measured subthreshold conductance. The FinFET devices have a gate that is wrapped around the channel, as shown in the middle panel of Fig. 1.6. If a gate voltage is applied, the field is strongest in the corners, as indicated in the image. If a dopant, by chance, is located within this area, its influence can be measured in the subthreshold conductance due to resonant tunnelling through the dopant. The right panel of Fig. 1.6 shows the band structure along the y direction with the gate stack, the Coulomb well of a dopant in black and a possible electron wavefunction in red. By studying a large number of samples Sellier et al. were able to identify devices with dopants in the necessary location, allowing them to characterize individual dopants in close proximity to the metal gate. From the measured subthreshold current it was possible to determine many fundamental dopant characteristics as for example their binding energy, charge states and capacitive coupling to nearby electrodes.[13, 14]

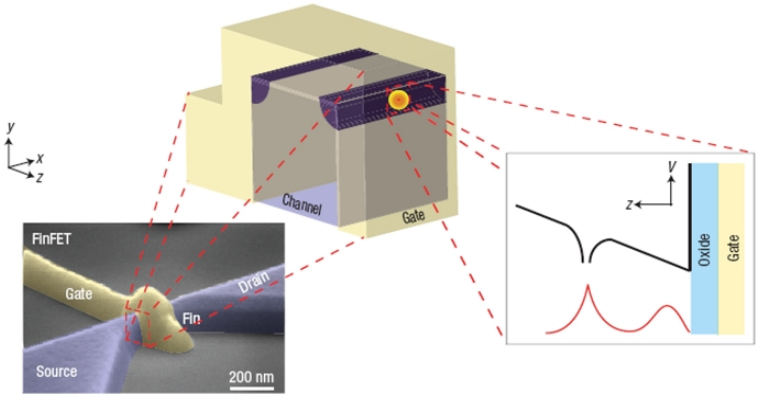

Figure 1.6: Single dopant effects measured in a FinFET, image from [14].

Another device taking advantage of randomly distributed dopants was developed by Morello et al.,[15] as shown in Fig. 1.7. They fabricated a single electron transistor (SET) on a silicon sample and implanted phosphorus dopants in close proximity to the island, within an area of 90 nm by 90 nm, as indicated in the image. A gate was deposited over the P implanted area which can be used to control the alignment of the P dopant energy levels with respect to the states in the island of the SET. They demonstrated that it is possible to use the coupling of the SET island to the P dopants in order to implement high-fidelity, single-shot electron spin readout. Furthermore they were able to measure the spin relaxation time of the electron bound to the P donor, providing an important step towards the realization of solid state quantum computing in silicon.

Using randomly doped devices to study the characteristics of individual dopants has provided valuable insights towards the fabrication of few dopant devices. However, one of the main problems with this approach is the fact that the exact location of the dopants with respect to the device geometry is not known. Morello et al.[15] for example report

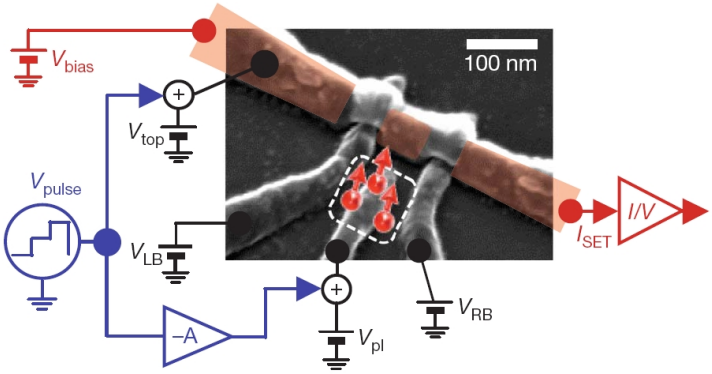

Figure 1.7: SET for single shot electron spin readout in silicon, image from [15].

a variability in the measured spin relaxation times which they attribute to the uncontrolled and therefore varying distance between the dopants and the electrostatic gates or the Si/SiO_2 interface. In order to study these interactions and understand how fundamental dopant characteristics are influenced by their atomic scale environment it is therefore necessary to use techniques that allow the characterization of dopants at the atomic scale.

1.4 Studying Dopants at the Atomic Scale using STM

STM is ideally suited to study the properties of individual dopants in semiconductors. Its ability to image surfaces with atomic resolution enables the identification of individual donor atoms within their atomic scale environment and can distinguish between dopants, contaminations or atomic scale defects. Scanning tunnelling spectroscopy further allows the measurement of the local density of states around the dopants and can therefore visualize their local influence on the semiconductor band structure.

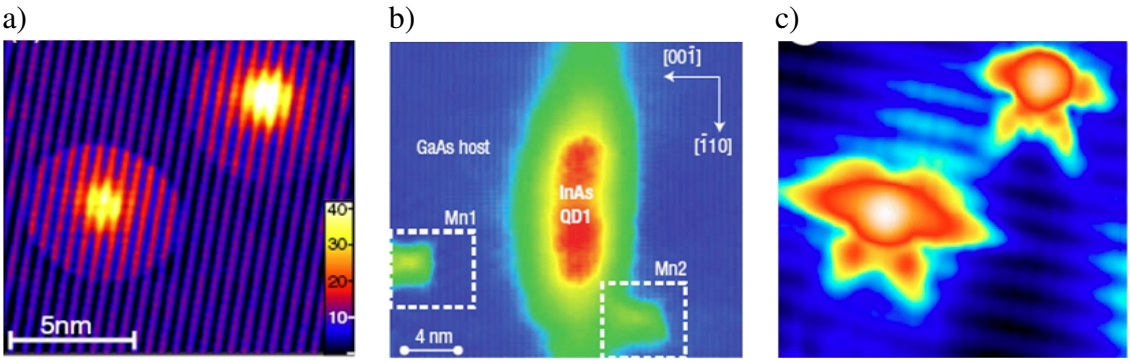

Figure 1.8: STM study of individual dopants in GaAs. a) Controlled charge switching of Si donors, image from [3]. b) Influence of strain on the Mn wafefunction, image from [16]. Mn pair in GaAs, image from [17].

Individual dopants were successfully studied in different semiconductors such as for example Si and GaAs.[18–22] Whereas it is possible to identify individual donors in many

different systems and surface orientations, the cleaved GaAs(110) surface has so far proven most convenient to study single dopant characteristics due to the absence of surface states and the consequently resulting unpinned Fermi level. This enables the visualization of dopants deep below the surface and furthermore allows one to controllably switch their charge state, as shown in Fig. 1.8 a). In this image the charge state of Si donors in GaAs is controlled by tip induced band bending, as visible by the characteristic circle around the donor, indicating its ionization. Other measurements include the characterization of the manganese (Mn) wavefunction under the influence of strain, as shown in Fig. 1.8 b), and the spin-spin interaction of Mn pairs in GaAs, shown in Fig. 1.8 c).

Performing similar measurements in silicon is highly desirable as they can provide valuable insights regarding the use of individual dopants in future quantum computing devices. However, the presence of surface states and the need to heat silicon surfaces to clean them make comparable measurements challenging. Furthermore, deep dopants such as Bi are not commonly used in semiconductor industry due to their low equilibrium solid solubility and sample preparation methods to incorporate them into substrates suitable for STM characterization therefore have to be developed first. In this work we implement and characterize a cross sectional surface preparation method, allowing us to study silicon without an in situ annealing step and therefore avoiding temperature induced dopant diffusion. This has the advantage that dopants can then be characterized in their original crystal sites and do not all diffuse into the same, lowest energy ground state. To enable the study of Bi donors we further develop a new STM sample preparation method based on ion implantation and demonstrate that it is possible to create almost defect free samples for STM measurements with doping concentrations far higher than the equilibrium solid solubility of Bi.

Employing this novel sample preparation technique enables us to study and compare different group V donor elements, namely bismuth (Bi) and antimony (Sb), in the same crystal sites and therefore in identical atomic scale environments. Individual Bi and Sb dopants have not been studied to date and since Bi is the largest of all group V donors,[23] with the highest binding energy, its atomic scale electronic and structural properties are expected to be substantially different from shallow donors such as P or Sb. Based on high resolution STM topography images and DFT calculations we are able to resolve how the fundamental characteristics of these different group V dopant elements interact with their atomic scale environment. The reconstructions formed by the different donor elements are identified and, using laterally resolved STS measurements, we are able to demonstrate how these reconstructions modify important properties of the dopant atoms such as their charge state and the screening of their Coulomb potential, providing valuable insights for the design of future atomic scale devices.

2 Background and Literature

2.1 Scanning Tunnelling Microscope

The scanning tunnelling microscope (STM) was invented in 1982 by Gerd Binning and Heinrich Rohrer.[24, 25] Using a sharp metal tip to probe the surface they were able to circumvent the diffraction limit of optical techniques and resolve individual atoms in real space for the first time.[26] The ability of this new technique to not only image but also manipulate individual atoms[27] quickly made it an invaluable surface analysis tool used in many different scientific fields. Nowadays a variety of different scanning probe techniques have emerged from this idea like for example atomic force microscopy (AFM)[28] or scanning near field optical microscopy (SNOM).[29] They all allow the probing of specific surface properties with a high lateral resolution and have further expanded the range of examinable surfaces to non conductive substrates.

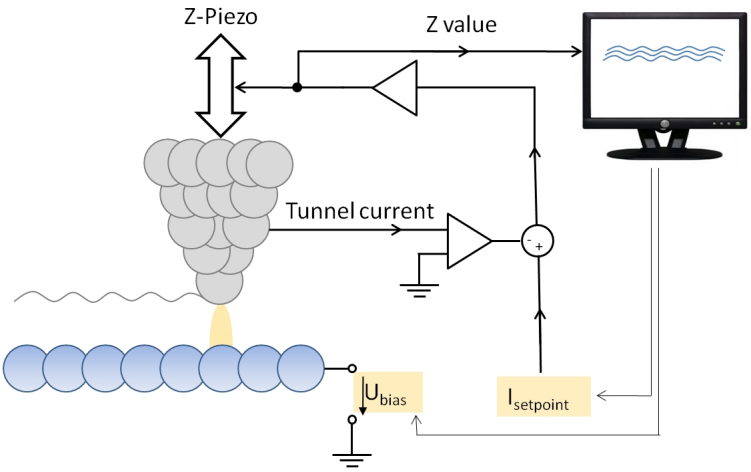

Figure 2.1: Operating principle of an STM applying the bias voltage to the sample.

The operating principle and the essential elements of an STM are shown in Fig. 2.1. An atomically sharp metal tip is used to probe a conducting or semiconducting surface. The bias voltage is applied to the sample and the tip is brought in close proximity to the surface, usually around 5 $\AA$, to allow a tunnel current to flow between tip and sample. While scanning the tip over the surface, a control system regulates the height of the tip in order to keep the tunnelling current constant. The tip therefore follows the contour of the

surface and from the regulation signal a two dimensional image of the surface topography can be recorded.

2.1.1 Tunnelling Concept

To reach its high resolution, an STM takes advantage of the quantum mechanical tunnel effect. In contrast to the classical point of view, an electron can overcome a barrier higher than its energy by tunnelling through it. This effect allows a current to flow between tip and sample even though they are not in direct contact.

For the simple case of a one dimensional tunnelling barrier, the problem can be solved analytically[30] and the probability that an electron can be found at a position z in the barrier is given by Eq. 2.1. In this equation, m is the electron mass, ψ the electron wavefunction, κ the decay constant, E the energy and U the potential barrier.

$$P = |\psi(0)|^2 e^{-2\kappa z} \qquad \kappa = \frac{\sqrt{2m(U-E)}}{\hbar} \tag{2.1}$$

In the context of STM, the barrier is represented by the vacuum gap between tip and sample and therefore the tunnelling current is exponentially sensitive to the tip sample distance, leading to the exceptionally high resolution of STM.

In order to understand the formation of the STM tunnel current, not only the tunnelling barrier has to be considered but also the local density of states (LDOS), the available states at a certain energy that can be occupied by electrons. The band structure for a semiconducting sample and a metal tip is shown in Fig. 2.2.

When a positive voltage is applied to the sample, as shown in Fig. 2.2 a), the Fermi level of the sample will be lowered respectively to the Fermi level of the tip. For small bias voltages no current will flow as there are no states in the bandgap of the semiconductor. Once the Fermi energy of the tip reaches the conduction band of the sample, electrons can tunnel from the tip into the empty states of the semiconductor. By further increasing the bias voltage the current will increase proportionally with the available LDOS of the sample and scanning with a positive bias voltage is therefore also called empty states imaging.

In Fig. 2.2 b), the band structure for imaging with a negative sample bias is shown. Again for small bias voltages no current flows, as there are no occupied states in the bandgap of the semiconductor. Once the bias voltage pushes the valence band of the sample above the Fermi energy of the tip, electrons from occupied states of the semiconductor can tunnel into the tip. By further decreasing the bias voltage the current increases proportionally with the occupied LDOS in the valence band and scanning with a negative bias voltage is therefore also called filled states imaging.

To analytically calculate the tunnel current we therefore have to sum up the all the

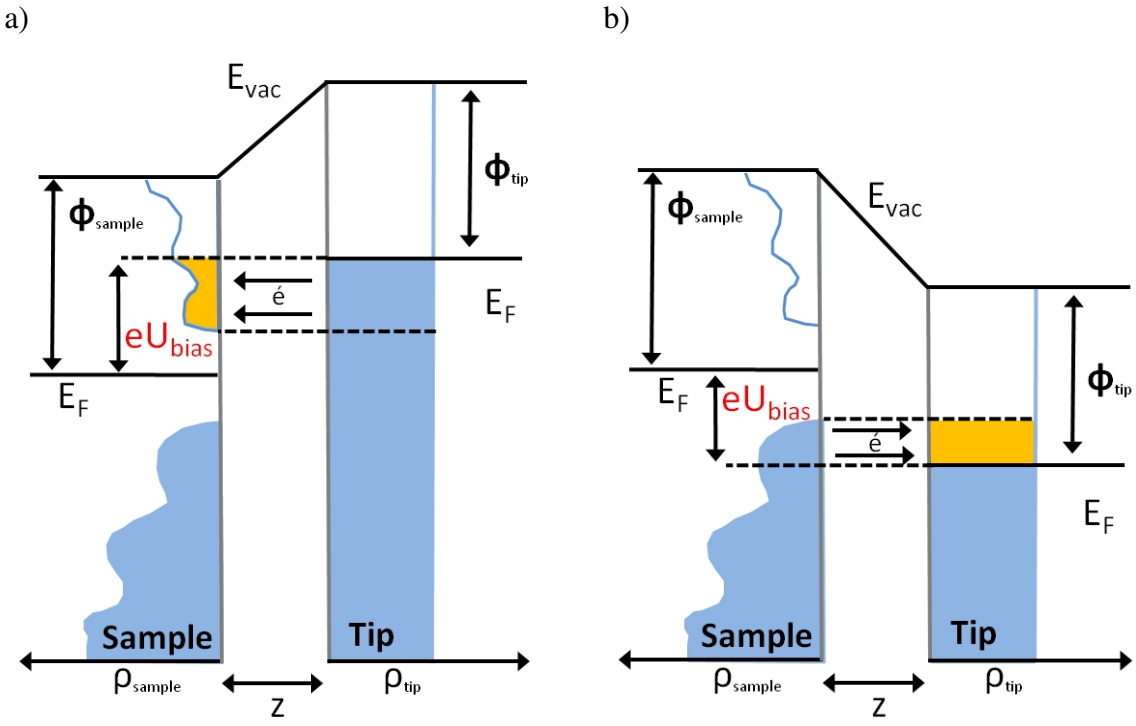

Figure 2.2: Band structure of a metal tip and a semiconducting sample. a) Positive sample bias, imaging empty states. b) Negative sample bias, imaging filled states.

electrons tunnelling through the vacuum barrier from or into available states in the semiconductor between the Fermi energy and the applied bias, as shown in Eq. 2.2.

$$I_t \sim \int_{E_F}^{E_F+eU} \rho_s(E) e^{-\alpha z} dE \tag{2.2}$$

In this equation, ρ_s describes the LDOS in the sample, α is a constant and z is the tip sample distance. To reach such an elegant equation for the tunnel current several simplifications have to be made. First of all the tunnelling matrix element is assumed to be constant over all voltages. Furthermore, it is assumed that the LDOS of the tip are constant and do therefore not influence the change of the current with the bias voltage. This is a good approximation for clean metal tips but can be very different for tips that have an oxide on the surface or are contaminated with other materials like a semiconductor. On top of that, temperature effects that change the distribution of occupied states around the Fermi energy are not taken into account.

2.1.2 Constant Current and Constant Height Imaging

The most commonly used imaging mode of STM is constant current imaging, presented in Fig. 2.3 a). The user defines a bias voltage and a regulation setpoint current. The control system then regulates the tip sample distance to maintain the setpoint current at this

bias voltage at all times. By scanning the surface and recording the z adjustments necessary to maintain the setpoint current an image is obtained that contains the convoluted information of the electronic and topographic structure of the sample.

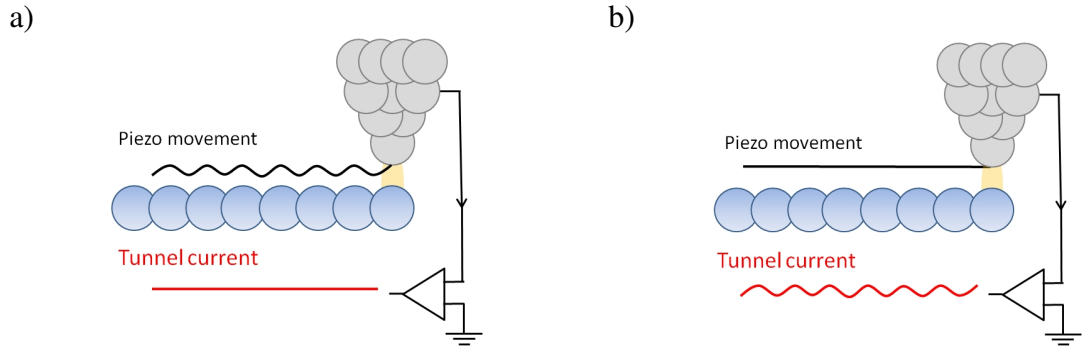

Figure 2.3: STM measuring modes. a) Constant current measurement. b) Constant height measurement.

Constant height imaging, shown in Fig. 2.3 b), does not regulate the z-position of the tip during scanning but keeps it at a constant height while recording the current. This imaging mode does not require a feedback loop and can therefore acquire images at much higher speed. Again an image that contains the convoluted information of electronic and topographic sample structure is recorded. The difficulty with this imaging mode is that, due to the lacking feedback control, the tip might crash into the surface if the sample is not perfectly flat.

2.1.3 Scanning Tunnelling Spectroscopy

From Eq. 2.2 we have seen that the tunnel current is directly related to the integrated LDOS between E_F and U_{Bias} as shown in Fig. 2.2. The LDOS can therefore be probed by recording the current at different bias voltages, called scanning tunnelling spectroscopy (STS). Similar to the imaging mode a bias voltage and tunnel current setpoint have to be selected by the user, defining the tip sample distance during the spectroscopy. The tip is placed over the point of interest where the LDOS shall be measured, the feedback loop regulating the z height of the tip to maintain the setpoint. The feedback loop is then disabled, keeping the tip fixed at the preset height over the sample, while sweeping the bias voltage over the desired range and recording the current.

In order to extract the LDOS from the recorded STS curve some numerical processing is required. As seen in Eq. 2.2, the current is proportional to the integrated LDOS between E_F and U_{Bias}. The LDOS of the sample can therefore be visualized by numerically differentiating the STS curve. This said, one has to keep in mind all the approximations made to reach Eq. 2.2. The tip has to be made out of clean metal with a flat DOS to avoid measurement artifacts and, depending on the measurement temperature, energy features

will be broadened due to the Fermi Dirac distribution of carriers around the Fermi energy. The third approximation, that the tunnelling matrix element will remain constant over the whole voltage range, is usually very good for metals with typical voltage measurement ranges of several hundred millivolts. When measuring semiconductors however, the voltage range has to be larger than the bandgap and therefore usually goes up to several volts. In this regime the approximation of a constant tunnelling matrix element is breaking down and the current actually scales, in a first approximation, with an additional $(1+V^2)$ term as calculated by Simmons.[31] To compensate this additional current increase with high voltages and display the actual LDOS, Feenstra et al.[32] proposed to normalize the differential conductance to the absolute conductance as they are both similarly dependent on the measurement voltage and therefore the error cancels itself out. They calculate that the result of this normalization is proportional to the LDOS of the sample with an added constant background A and normalized by another constant B as shown in Eq. 2.3.

$$\frac{\frac{dI}{dV}}{\frac{I}{V}} = \frac{LDOS(sample)+A}{B} \tag{2.3}$$

Applying this method to semiconductors can however create problems as there is very low or no conductance within the bandgap. Dividing through the absolute conductance therefore creates band edge and zero bias artifacts as shown by Nagaoka et al.[33] They in turn proposed an alternative approach, plotting spectra on a logarithmic scale. The influence of these different normalization techniques is shown in Fig. 2.4 by comparing measured and simulated LDOS of Si(100).

In the top row, simulated tunnelling spectra of a one dimensional well are shown. In Fig. 2.4 a), it can be seen that the simulated LDOS measurement does not perfectly match the one dimensional well as it shows the artificial increase at higher voltages due to the $(1+V^2)$ term as previously discussed. By plotting the spectra in a logarithmic scale, shown in b), this effect is reduced but not completely removed. Feenstra‘s normalization, shown in Fig. 2.4 c), removes this effect but introduces band edge artifacts by displaying the shoulders where the bands start as peaks. The scaling and offset discussed earlier are also clearly visible. In the lower images, experimental data from Si(100) is shown. The surface bands around the silicon bandgap form a situation similar to a one dimensional well and the same effects as in the simulated spectra can be seen when looking at the different normalizations.

In this report we will display tunnel spectra in a Log(dI/dV) scale. This means that they will show slightly enhanced LDOS at high voltages but avoids the introduction of any artificial peaks around areas of low conductance.

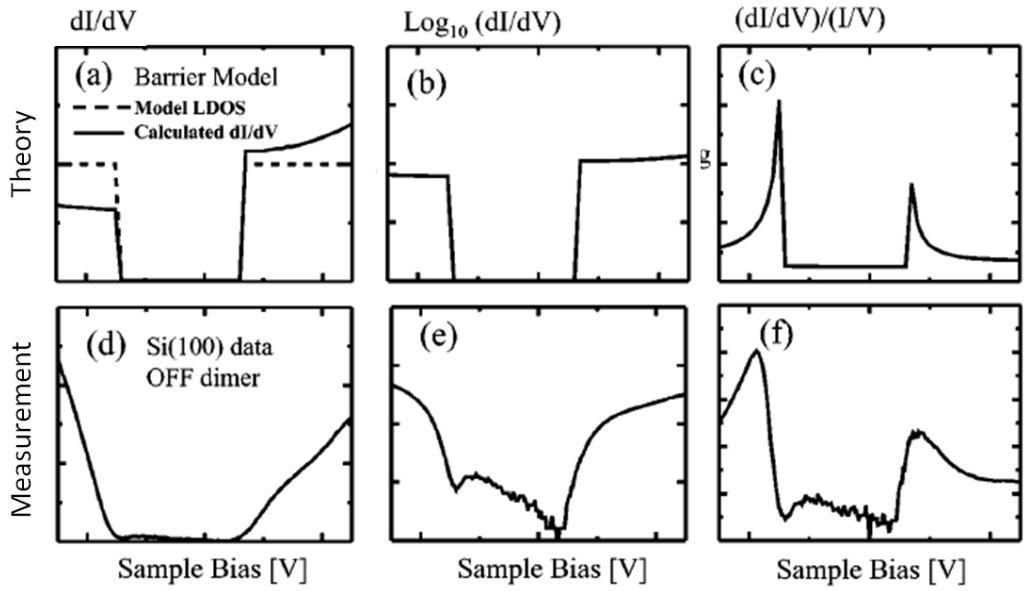

Figure 2.4: a)-c) Simulated tunnelling spectra of a one dimensional well depicted in a). d)-f) Measured tunnelling spectra of Si(100) on an off dimer position. Image reproduced from [33].

2.1.4 Tip Induced Band Bending

In Sec. 2.1.1, the band structure for a semiconducting sample and a metal tip were introduced and subsequently used to interpret the energy scales of the tunnelling process during imaging and spectroscopy. This idealized band structure treats the tip as a non invasive probe and therefore assumes that the bands in the semiconductor are not influenced by the measurement process. This assumption may be wrong, especially for low doped semiconductors with surface band gaps, as the sample band structure can be altered significantly due to the presence of the electric field around the metal tip, an effect investigated by Feenstra et al.[34] that is called tip induced band bending (TIBB).

In Fig. 2.5 a), the tip is depicted over the sample surface, forming an electrical capacitance C_{ts}. In order to establish a bias voltage for the measurement, this capacity is charged and carriers accumulate at the end of the tip and at the surface directly underneath it, forming a space charge region (SCR). Depending on the availability of charged carriers in the region underneath the tip, this space charge region will vary in size. For metallic samples, where a large carrier density is present in the sample, the SCR is strongly confined, whereas it can extend several nanometers into the sample for semiconductors.[35]

A space charge region that extends far into the sample can have significant influence on the tunnelling process. A large SCR means that a part of the tip sample bias is actually being dropped across a region of the semiconductor and not between tip and sample surface. Since electrons very close to the surface dominate the tunnelling process, usually to a depth of 5 $\AA$ into the sample,[36] this means that the effective tip sample voltage

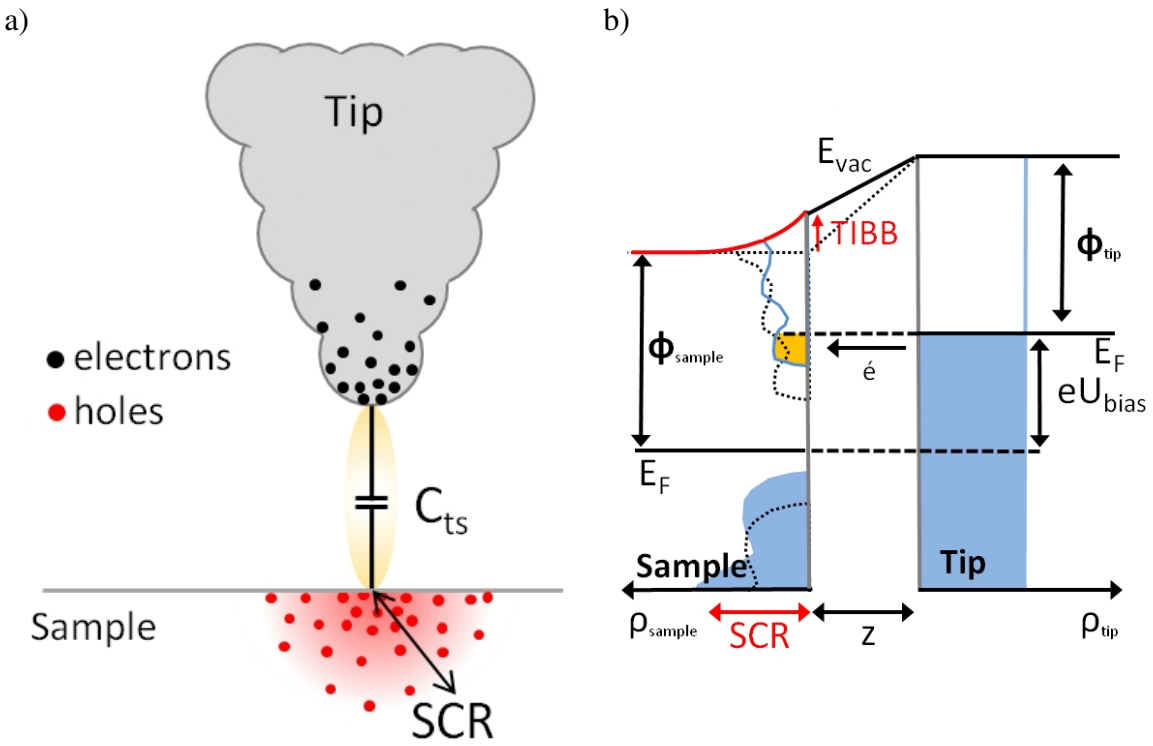

Figure 2.5: Tip induced band bending. a) Formation of a space charge region underneath the tip. b) Influence of the space charge region onto the sample band structure.

will be diminished by the voltage dropping in the SCR. It has to be mentioned at this point that electrons from within or behind the space charge region can dominate the current if there are no other carriers available for tunnelling as for semiconductors biased into depletion.[34] Using this very simple model one can immediately see that the SCR and therefore TIBB depend on many different factors such as the LDOS of the sample, the tip sample capacitance and consequently the shape of the tip apex and the tip sample distance.

To visualize the influence of TIBB on STM measurements, a band diagram including the band bending is shown in Fig. 2.5 b). The tip induces a SCR in the sample due to the applied bias voltage or simply due to different material work functions. Depending on the LDOS in the sample these excess carriers will change the position of the Fermi energy underneath the tip and therefore shift the LDOS addressed for tunnelling during topography and spectroscopy measurements. Putting it simply one could say that tip induced band bending decreases the actual bias voltage involved in the tunnelling process. Due to this effect energies measured in STM spectroscopy may be shifted significantly.

As mentioned before, TIBB strongly depends on the tip work function and the tip sample capacitance which can both change with the shape of the tip apex. The exact conformation of a tip is very difficult to determine and can easily change during a measurement. It is therefore very difficult to measure and interpret the band structure of an unknown

semiconductor surface relying solely on STS.

McEllistrem et al.[36] modified an STM in order to directly and qualitatively measure the TIBB on various silicon surfaces. To do this they used a HeNe laser, modulated at 4kHz, which they pointed at the tip sample junction in order to locally modify the charge carrier density underneath the tip. With this method they were able to create a surface photovoltage (SPV) that can compensate the TIBB. In order to measure the SPV they added an unipolar modulated component to the bias voltage of the tip that was synchronized with the laser modulation and regulated in order to cancel out the influence of the laser illumination. The modulation voltage then quantitatively determines the sign and magnitude of the tip induced band bending.

Using this technique they investigated different doping densities, surface orientations and hydrogen terminated surfaces. Their results are shown in Fig. 2.6.

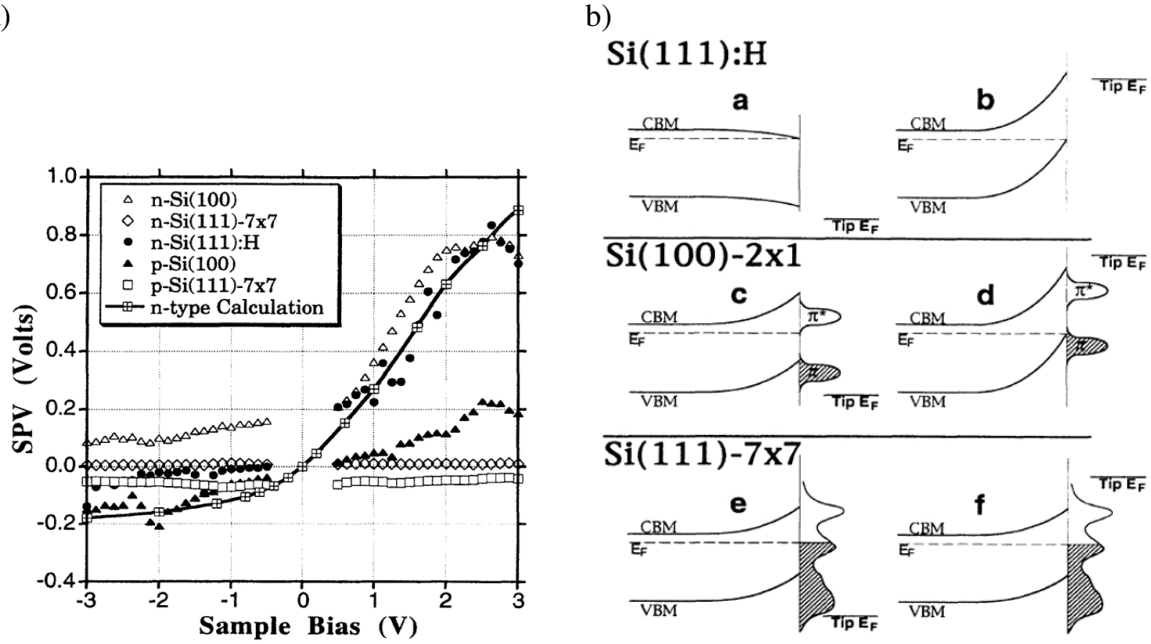

Figure 2.6: Direct measurement of tip induced band bending by McEllistrem et al.[36] a) Measured surface photovoltage for different samples. b) Schematic illustration of the band structure in positively and negatively saturated TIBB.

In Fig. 2.6 a) the results of the different measurements can be seen whereas in Fig. 2.6 b), the maximum positively and negatively bent band structures are shown. For hydrogen terminated n-Si(111):H, which does not have any surface states, the measured TIBB saturates at +0.8 V and -0.1 V, in good agreement with the calculated conduction band at +0.97 V and the valence band at -0.15 V. This shows that, in the absence of surface states, the tip bends the bands all the way through the band gap until the Fermi energy reaches the conduction or the valence band. Once this happens, the available LDOS for tunnelling increase dramatically and the SCR does not further expand.

The results for n-Si(100) and p-Si(100) show that there is significantly less tip induced band bending due to the surface states in the band gap. The measured TIBB for n-Si(100) saturates at +0.81 V, again in good agreement with the expected values of +0.97 V. For negative bias TIBB saturates at +0.09 V, reaching the bottom of the surface valence band. The measured TIBB for p-Si(100) shows a similar trend but the curve is shifted because of the different starting position of the Fermi level due to the doping.

The last two traces display clean n-Si(111) and p-Si(111) surfaces which have a high LDOS through the whole band gap. The measured TIBB voltage is again shifted due to the different doping levels but constant over the whole bias range. This shows that there is no significant TIBB because the high LDOS around the Fermi energy prevent the SCR underneath the tip from extending far into the semiconductor.

This experiment impressively demonstrates the effect of tip induced band bending and the need to be very careful when interpreting energy scales measured with an STM.

2.1.5 Z-Spectroscopy

While tunnelling spectroscopy can measure the LDOS in the sample, it does not provide any information about the apparent barrier height or the decay constant of the tip sample junction. This information can be important when comparing tunnelling spectra recorded with different setpoints or at different locations, as it allows linking the tip sample distance to the magnitude of the tunnelling current. This relationship can be expressed according to Eq. 2.4.[30] κ is called the decay constant, z is the tip sample distance and ϕ is the barrier height.

$$I(z) = I(0)e^{-2\kappa z} \qquad \kappa = \frac{\sqrt{2m\phi}}{\hbar} \tag{2.4}$$

The barrier height directly corresponds to the work function of tip/sample, assuming they are the same and small bias voltages are used for the measurement. This would theoretically allow the calculation of the decay constant for a given tip sample combination. In an experiment however, the apex of the tip will be slightly different every time and as the work function is dependent on the crystal orientation of the material, the decay constant will vary from tip to tip.

To record a z spectrum a bias voltage is chosen together with a tunnelling current setpoint, defining the initial tip sample distance. The current is then recorded while retracting or approaching the tip, keeping the voltage constant. Eq. 2.4 can then be fitted to the recorded trace to determine the decay constant κ and the measured, apparent barrier height ϕ as in Eq. 2.5

$$\Phi = \frac{\hbar^2}{8m}\left(\frac{dlnI}{dz}\right)^2 \tag{2.5}$$

2.1.6 Current Imaging Tunnelling Spectroscopy

Current imaging tunnelling spectroscopy (CITS) is a combination of constant current topography and scanning tunnelling spectroscopy measurements. The tip images the surface with a user defined bias. At each point the z displacement of the piezo, necessary to maintain the current setpoint, is recorded and a tunnel spectrum is acquired over the desired voltage range. In this manner, a three dimensional data set I(x,y,E) is acquired simultaneously with the constant current topography image. By differentiating all spectra, the lateral distribution of the local density of states LDOS(x,y,E) can be calculated.

The interpretation of this data set is not straightforward due to the way it was acquired. The tip positioning in constant current mode leads to the fact that the tip sample distance in the measured area will actually follow a plane of constant integrated density of states. The problem is most obvious when looking at the measured LDOS at the setpoint bias voltage. $I(x,y,eV_{bias})$ will, due to the feedback circuit adjusting the tip height, always be a plane of constant current I_{set}, even though the LDOS(x,y) at eV_{bias} are not flat as indicated in Fig. 2.7. To obtain a correct measurement of LDOS(x,y,E) we would ideally like to keep the tip at a constant height over the sample while performing the CITS measurement. As a data set consists of up to two thousand I/V curves and can take several hours to acquire this is not possible as thermal drift would significantly change the distance between tip and sample during this time and might lead to the tip crashing into the surface.

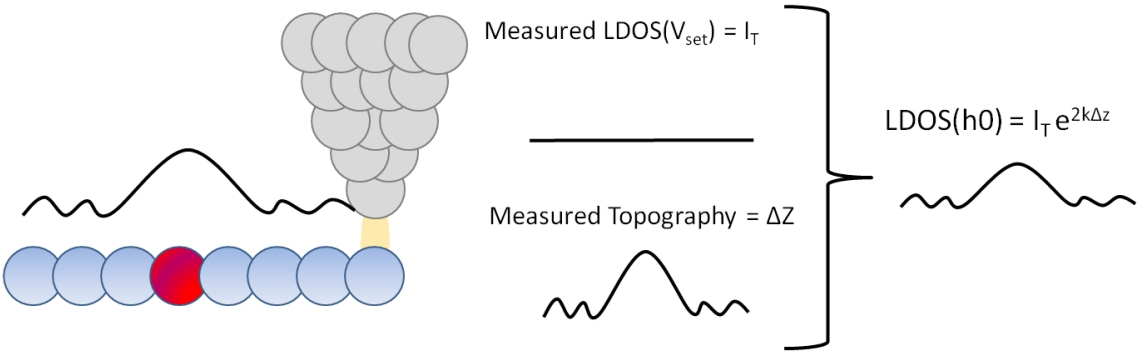

Figure 2.7: CITS measurement. Due to the tip positioning in constant current mode the tip follows a line of constant integrated density of states. The measured LDOS at the setpoint bias will therefore always be flat. It is however possible to topography correct the data set using the simultaeously acquired tip height.

It is possible to correct the CITS data acquired in constant current mode using the simultaneously acquired topography image. This image contains the change of the tip sample separation for all I/V spectroscopy curves relative to each other. The offset and eventual tilt of the sample can be removed and Δz can be calculated as the relative height difference of all the spectra to the surface. From Eq. 2.4 we know the relation between tunnelling current and tip sample distance. If z-spectroscopy is used to measure the decay

constant κ it is therefore possible to topography correct the data set by rescaling all I/V using Eq. 2.6.

$$I(h_0) = I_T e^{2\kappa\Delta z} \tag{2.6}$$

To do this we neglect the change of the barrier height with the scan voltage and assume that κ is constant over the full spectroscopy voltage range and within the whole measurement area. Like this we map all I/V spectra onto a flat imaging plane and acquire a topography corrected set of LDOS(x,y,E), allowing us to visualize the actual spatial variation of LDOS at different energy levels.

2.2 Silicon (111)-2x1

Historically the Si(111)-2x1 surface reconstruction was, due to its easy and reproducible formation upon cleaving in ultra high vacuum (UHV), used as a prototype system to study many fundamental concepts in surface science. The 2x1 unit cell of the Si(111) surface is small enough to calculate numerically and therefore allows comparison of theoretical concepts with experimental results, leading to fundamental insights about the physics of semiconductor surfaces. The surface has been extensively studied using various techniques including LEED,[37, 38] ion scattering,[39] optical absorption[40] and STM.[26]

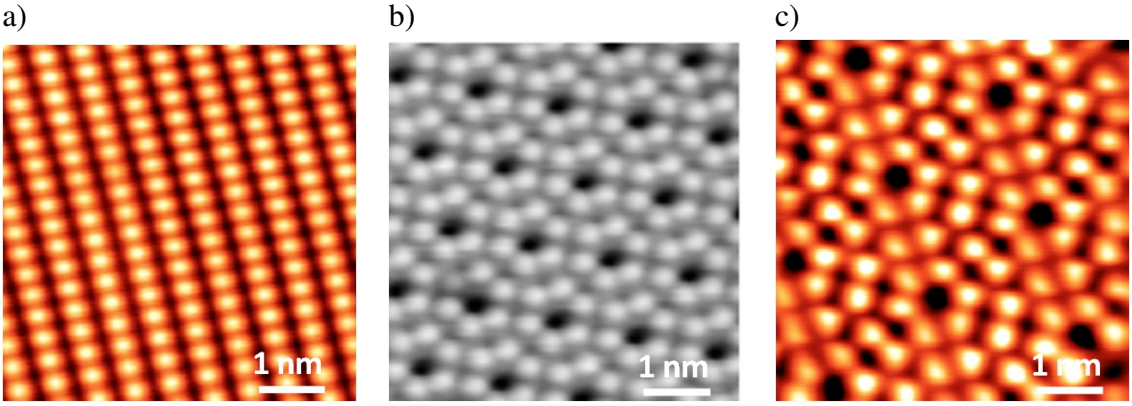

Figure 2.8: Si(111) surface reconstructions. a) Si(111)-2x1. b) Si(111)5x5; reproduced from [41]. c) Si(111)7x7.

Lander et al.[37] showed that cleaved samples initially exhibit a 2x1 reconstruction as shown in Fig. 2.8 a). When annealed to 500 °C-600 °C he found that this surface transforms into a 5x5 reconstruction as shown in Fig. 2.8 b) and if further annealed to temperatures above 600 °C-700 °C it reconstructs to form the 7x7 surface shown in Fig. 2.8 c). By changing the annealing temperature he was able to switch between the 5x5 and the 7x7 reconstruction, but the 2x1 reconstruction only showed after the cleaving process and

could not be recreated once the surface was annealed. Theoretical calculations by Qian et al.[42] later explained the order in which these surface reconstructions appear with temperature in terms of surface energy. They calculated that compared to an unrelaxed surface, the energy gain per 1x1 unit cell for 2x1, 5x5 and 7x7 is 0.36 eV, 0.395 eV and 0.403 eV respectively, making the 7x7 reconstruction the lowest energy surface of Si(111).

For STM experiments, silicon surfaces are usually prepared and cleaned inside UHV using a thermal annealing process. This allows one to prepare the sample several times if it is not sufficiently flat or gets contaminated over time, whereas cleaving usually only allows one preparation. On the other hand, flash annealing of the Si(111) surface does not allow studying the 2x1 reconstruction which only forms upon cleaving.

To study dopants in silicon, the flash annealing surface preparation can create various problems as the dopants might react to the increased temperatures in an undesired manner. Dopants can segregate to the surface and form pairs,[43] interact with defects[44] or evaporate from the crystal and form a depletion layer near the surface.[45] In order to study the dopants in their intrinsic bulk lattice positions it is therefore preferable to use sample preparation techniques such as cleaving that do not allow thermally activated dopant diffusion.

2.2.1 Cleaving Silicon

To achieve an atomically flat surface suitable for STM experiments, silicon has to be cleaved along a $\{111\}$ plane. Even though silicon also cleaves readily along $\{011\}$ planes, no atomically ordered reconstruction has been found.[46–48] This behavior could be attributed to the surface energies involved[49] as the $\{111\}$ surface is the lowest energy cleaving plane with 1.44 J/m^2 and therefore the preferred cleaving direction. The cleaving energy of the $\{011\}$ plane is less favorable with 1.733 J/m^2 but nevertheless very small and therefore it is not immediately obvious why the resulting surface should be rough. To explain this behavior atomistic models of the cleavage process were necessary. Monocrystalline silicon is a model material for brittle fractures and was therefore studied extensively.[47, 49–51] In Fig. 2.9 a), a sample is sketched which is cleaved through a $\{110\}$ plane, making the crack propagate in $[\bar{1}10]$ and $[001]$ directions.

A large anisotropy has been measured between these two directions which was modeled by Pérez et al.[52] They found that the crack nicely propagates in the $[\bar{1}10]$ direction and produces perfectly flat fractures, whereas it does not propagate along the $[001]$ direction but deflects onto $\{111\}$ and $\{112\}$ planes.

Atomic scale models revealed that the crack expanding along the $[\bar{1}10]$ direction, as shown in Fig. 2.9 b), expands continuously and easily through the crystal. If stress is applied the atomic bonds get expanded continuously until they reach a certain critical length

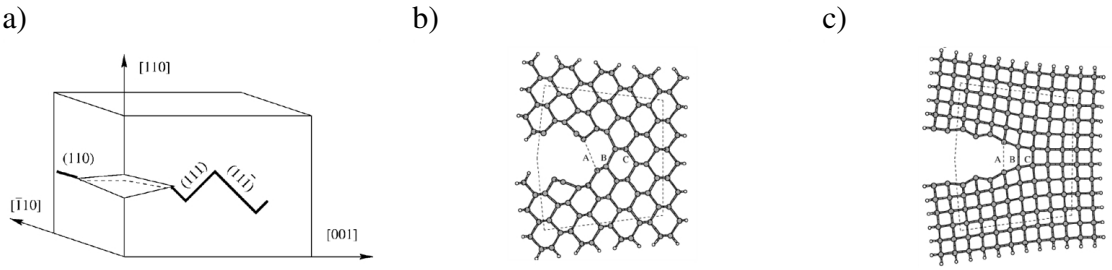

Figure 2.9: Cleaving silicon samples, images from [52]. a) Crack propagation when cleaving in a $\{011\}$ plane. b) Crack along $[\bar{1}10]$. c) Crack along $[001]$.

where they break. For a crack propagating along the $[001]$ direction on the other hand, the propagation was very discontinuous. This behavior is called lattice trapping, an effect arising from the discreetness of the lattice. It leads to a crack that does not significantly stretch the involved atomic bond but distributes the energy onto surrounding atoms until the load exceeds a critical value upon which the atomic bond suddenly ruptures and the adjacent atoms relax again. According to Pérez et al.[52] lattice trapping may be responsible for the deflection of the cleave to other breaking planes because the stress on the surrounding atoms is maximized just before the bond breaks. If a sample is cleaved in the $\{111\}$ plane on the other hand, lattice trapping in all directions is low enough to allow the formation of an atomically flat surface.

2.2.2 Silicon (111)-2x1 Surface Reconstruction

The silicon (111)-2x1 reconstruction, according to the π-bonded chain model suggested by Pandey,[53] is shown in Fig. 2.10. In this model the surface reconstructs into alternating rings of five and seven atoms. From inspection of the three dimensional crystal structure it can be seen that the atoms in the top layer are buckled and each up buckled atom has two neighboring down buckled atoms. Therefore no dimerisation occurs as in silicon (001) but the atoms create a zig-zag line following the $[01\bar{1}]$ direction.

The unit cell size of the reconstructed surface is 6.65 Å in $[\bar{2}11]$ and 3.84 Å in the $[01\bar{1}]$ direction. The height difference between up and down buckled atoms was found to be 0.5 Å with 1 Å between atoms in the π-bonded chain and in the trough.[54–56] The atoms in the π-bonded chains of the Pandey reconstruction are only threefold coordinated and would therefore end up with an unsaturated dangling bond. As the name suggest, these orbitals form a π-bond to minimize the surface energy similar to the case of Si(100). Rohlfing et al.[57] found that the buckling is associated with a charge transfer from the down to the up buckled atom leading to a filled p_z-like dangling bond on the up atom and an empty dangling bond at the down atom. The up atom of the chain has therefore predominantly occupied states and will show up in filled states imaging whereas the down atom will

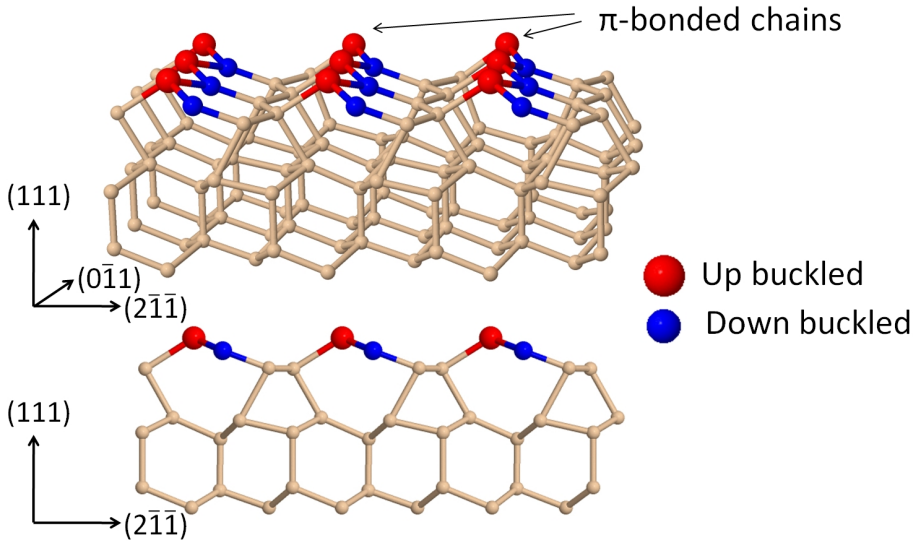

Figure 2.10: Si(111)-2x1 reconstruction according to the Pandey chain model.

show up mostly in empty states imaging. The charge distribution of the filled states on the up atom and the empty states on the down atom as calculated by Rohlfing et al.[54] is shown in Fig. 2.11.

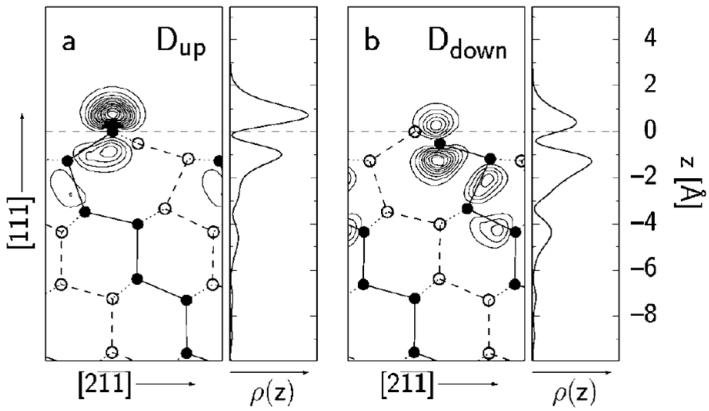

Figure 2.11: Charge distribution of surface states in Si(111)-2x1 by Rohlfing et al.[54] Filled circles show atoms in the drawing plane. a) Occupied states at the up atom. b) Empty states at the down atom.

Even though the Pandey π-bonded chain model is today widely recognized to be correct, the literature has for decades discussed various other models like the buckling model[58] and the three bond scission (TBS) model.[59] In 1986 the first STM real space observation of the Si(111)-2x1 surface by Feenstra[55] was able to discard the buckling model since the corrugation amplitude did not match. Due to similar surface corrugations of the TBS and the Pandey model, as shown in Fig. 2.12, STM data was however not able to conclusively rule out either of them.[32, 60] Total energy calculations were also unable to determine the correct reconstruction with certainty as the Pandey model was found to

be only 0.25 eV more stable than the TBS model.[61] Another unresolved issue was the orientation of the buckling in both of the surface reconstructions.

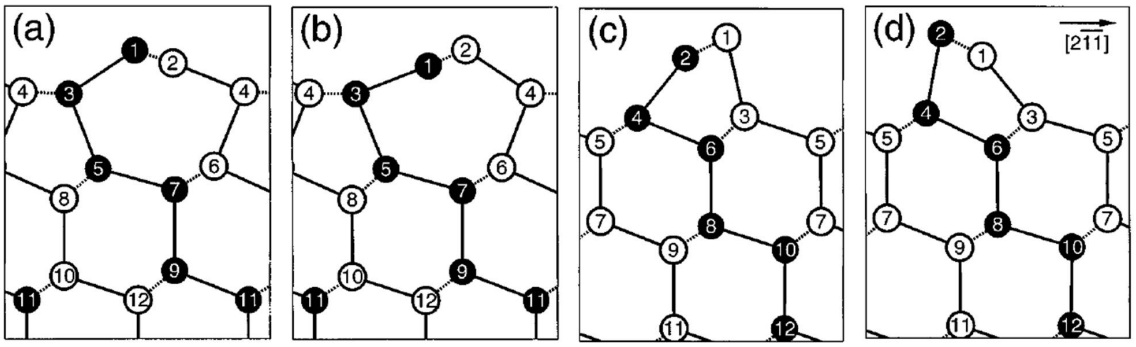

Figure 2.12: Si(111)-2x1 reconstructions by Lee et al.[61] a) Forward buckled Pandey. b) Backward buckled Pandey. c) Forward buckled TBS. d) Backward buckled TBS.

One of the main arguments against the π-bonded chain model was the fact that the formation of the alternating five atom and seven atom rings would require too much energy since one has to break one bond per atom on the surface. The energy barrier to reach this new reconstruction was believed to be too high to be overcome by the energy introduced into the surface by the cleaving process. Northrup et al.[62] was able to show that this assumption, based on bulk values, is incorrect as they calculated the energy barrier to switch between unrelaxed and reconstructed surface to be less than 0.03 eV per atom.

Much experimental evidence has since been brought forward supporting the Pandey model including LEED,[63] ion scattering[64] and photoemission.[65, 66] Also, additional theoretical calculations support the Pandey model. Lee et al. have calculated the band structure for both the TBS and the Pandey model and compared it to photoemission[65] and inverse photoemission[66] data as shown in Fig. 2.13. It can be seen that the data nicely match the predicted band structure for the Pandey but not the TBS model. It was nevertheless not possible to distinguish between positive and negative buckling.

Craig et al.[67] calculated that forward and backward buckling are energetically very similar, with backward buckling being only 0.006 eV per surface atom more stable. In 2004, Nie et al.[68] were able to use voltage dependent STM imaging in order to determine the buckling direction. By varying the bias, either the up atom of the chains in filled states or the down atom in empty states were imaged. The contrast change from filled to empty states was always found in the $2\bar{1}\bar{1}$ direction and they therefore suggested that the π-bonded chain model is positively buckled. In 2011, Bussetti et al.[69] confirmed this result for low doped substrates but also found that negative and positive buckling can coexist in highly n-doped substrates.

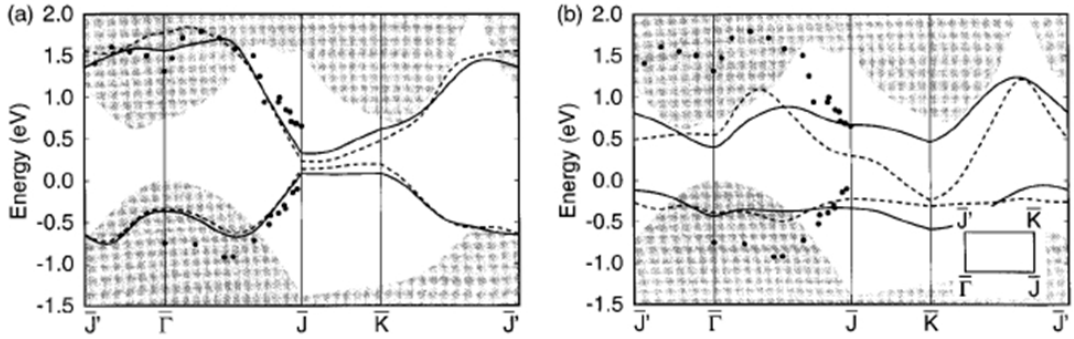

Figure 2.13: Calculated Si(111)-2x1 band structure by Lee et al.[61] for forward (solid line) and backward buckling (dashed line). Circles indicate measurement data.[65, 66] a) Pandey model. b) TBS model.

2.2.3 Band Structure of Si(111)-2x1

The Si(111)-2x1 surface reconstruction leads to a charge transfer in the π-bonded chains from the down atom to the up atom as described in Sec. 2.2.2. This leads to two new surface bands, an occupied state at the up atom and an unoccupied state at the down atom, as shown in Fig. 2.11. These two new surface states are energetically within the bandgap of the silicon bulk and therefore dominate the tunnelling behavior for low voltages.

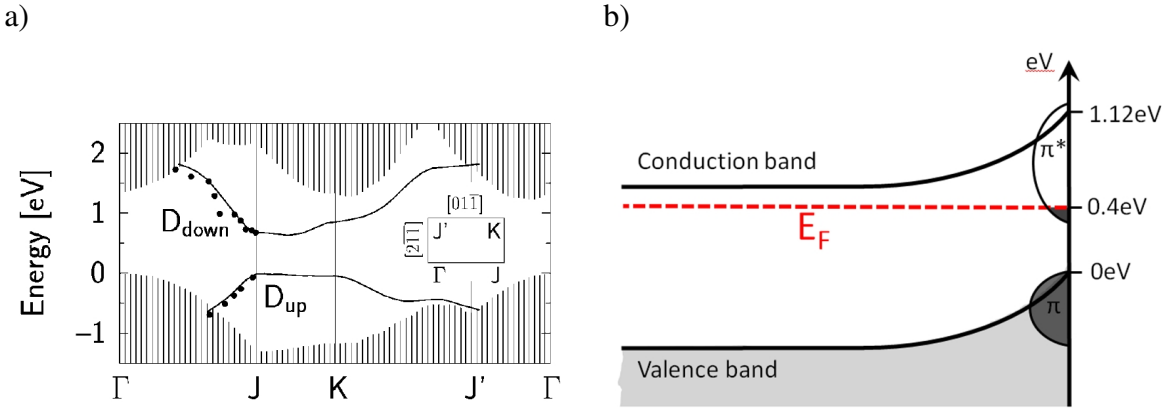

Figure 2.14: Band structure of Si(111)-2x1. a) Calculated band structure by Rohlfing et al.[54] Black lines indicate the surface bands, the shaded areas represent the bulk. b) Schematic illustration of the band structure perpendicular to the surface.

Rohlfing et al.[54] calculated the band structure for the Si(111)-2x1 surface as shown in Fig. 2.14 a). The two surface bands are shown as solid lines whereas the bulk is indicated by shaded areas. It can be seen that the surface valence band and the bulk valence band both lay at the same energy, chosen to be zero in this diagram. The surface conduction band is reaching far into the bulk band gap and is therefore reducing the surface band gap to 0.69 eV. The surface conduction band is highly dispersive in the ΓJ direction along the

π-bonded chains, indicating that electrons can move freely along the chain.

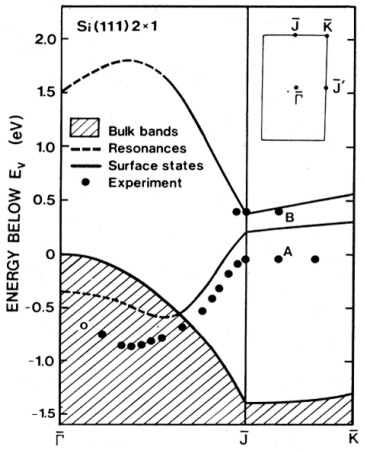

Figure 2.15: Angle-resolved photoemission of Si(111)-2x1, image from [70].

In Fig. 2.14 b), the influence of the surface states onto the overall sample band structure is shown at the surface of a highly n-type doped sample. The Fermi energy in the bulk has been shifted upwards close to the conduction band due to the doping. At the surface however, the additional states in the surface conduction band pin the Fermi energy at around 0.4 eV above the valence band, as experimentally determined by Himpsel et al.[71] for intrinsic silicon. Due to this pinning the bands are bent upwards, electrons accumulate in the bottom of the surface conduction band and a depletion region is created underneath the surface that can extend several nanometers into the semiconductor, depending on the doping level. This was confirmed by photoemission experiments, shown in Fig. 2.15, that were able to measure emission from electrons located in the bottom of the surface conduction band, as indicated on the calculated band structure.

2.2.3.1 STS of Si(111)-2x1

Stroscio et al.[72] have measured the band structure of Si(111)-2x1 using STS at room temperature. They investigated a range of p- and n-doped crystals and found that the measured surface LDOS was invariant apart from a slight shift in the Fermi energy.

By measuring the current as a function of tip sample separation they were able to calculate the decay constant κ as a function of voltage as described in Sec. 2.1.5. They found that the decay constant increases for energies below 1 eV, as shown in Fig. 2.16 a) i). This can be explained with the orientation of the wave vectors involved in the tunnelling process. As seen in Fig. 2.14 a), for very small voltages only the surface state bands at the J point contribute to the tunnelling current which have a wave vector parallel to the surface $k_{\|}$. At higher bias voltages bulk states also contribute to the tunnelling current, some of which have a wave vector perpendicular to the surface $k_{\perp}$. The fact that $k_{\|}$ decays

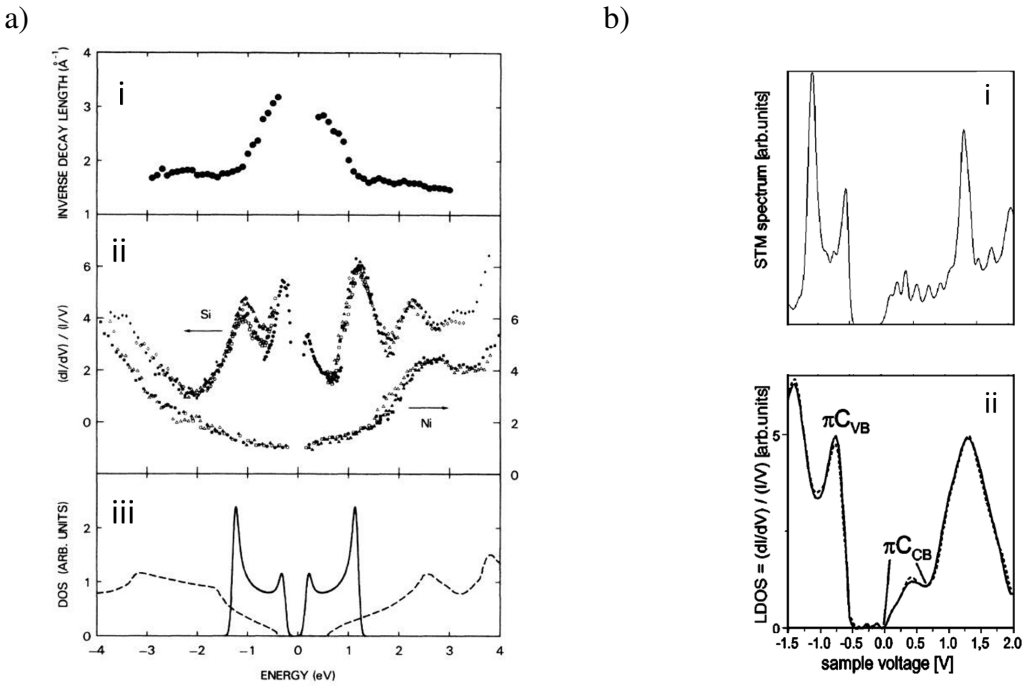

Figure 2.16: a) STS data of Si(111)-2x1 at room temperature by Stroscio et al.[72] i) Measurement of the tunnelling decay constant over different bias values. ii) Normalized STS data taken at room temperature. iii) Theoretically calculated LDOS for the Si(111)-2x1 surface. b) STS data of Si(111)-2x1 at 8 K by Garleff et al.[56] i) Theoretically calculated LDOS for the Si(111)-2x1 surface, ii) STS data of Si(111)-2x1 at 8 K.

much faster into the vacuum above the sample than $k_\perp$ explains the rise in the measured decay constant for low bias values.

In Fig. 2.16 a) ii) the normalized STS data is shown and in Fig. 2.16 a) iii) the theoretically calculated LDOS of the surface (solid line) and the bulk (dashed line) can be seen. To make sure tip DOS do not contribute to the measured spectra Ni was measured as shown in the lower part of Fig. 2.16 a) ii). They found it to be flat apart from an expected peak at 2.7 eV and could therefore assume a flat tip DOS. When comparing theory and experiment, peaks at -0.3 eV and 0.2 eV can be attributed to the onset of the occupied and unoccupied surface states. The peaks at -1.1 eV and 1.2 eV were then attributed to the end of the occupied and unoccupied surface bands. More recent calculations and STS measurements at 8 K by Garleff et al.[56] are shown in Fig. 2.16 b).

Comparing STS data acquired at at 8 K, shown in Fig. 2.16 b) ii) to the room temperature STS of Stroscio, Garleff et al. noted that the onset of the surface valence band is shifted to lower bias values, whereas the peaks at positive voltages stay at around the same energy values. A systematic temperature dependent study of STS on Si(111)-2x1 is however not available to date.

2.2.4 Anti Phase Boundaries

Little is known about defects in the Si(111)-2x1 reconstruction. Features that have attracted interest in the past are the different types of domain boundaries found on the surface. Due to the threefold symmetry of the hexagonal Si(111) surface, the π-bonded chains can be oriented in all three equivalent $\{01\bar{1}\}$ orientations. In Fig. 2.17 a) a large scale image of the Si(111)-2x1 surface with several domain boundaries can be seen. Two different types of domain boundaries can be identified in this image. If π-bonded chains with different orientations meet they form a boundary as shown in Fig. 2.17 b). It is also possible that the π-bonded chains are shifted by half a unit cell with regards to the underlying bulk crystal. When two domains with shifted π-bonded chains in the same orientation meet they form an anti phase boundary (APB), as shown in Fig. 2.17 c).

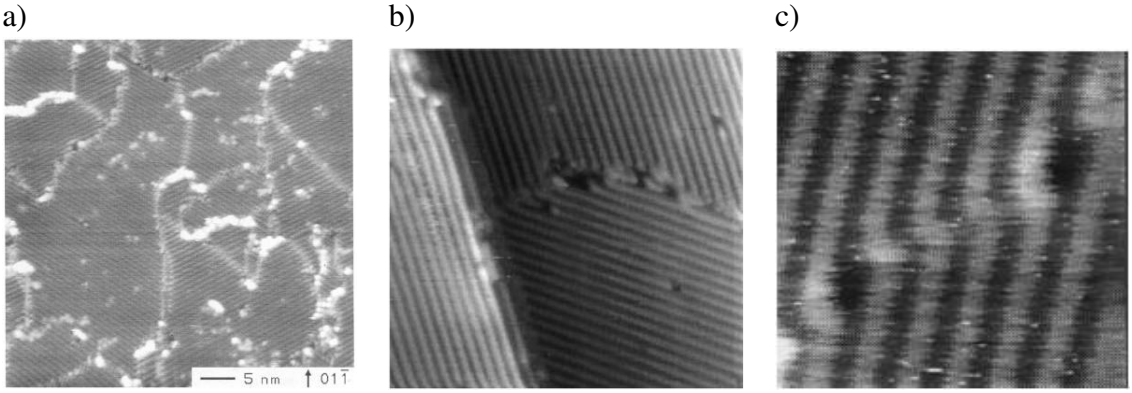

Figure 2.17: Silicon domain boundaries. a) Surface overview.[73] b) Domain boundary of different chain orientations.[74] c) Domain boundary of different chain phase.[47]

Feenstra et al.[73] reported that domain boundaries in the Si(111)-2x1 surface act as a starting point for the thermal conversion of the 2x1 into the 5x5 or 7x7 reconstruction. They observed domain boundaries acting as nucleation sites for silicon adatoms and saw 5x5 domains growing out of the domain boundaries at elevated temperatures. Due to this behavior they also suggested that domain boundaries play a significant role in epitaxial growth on silicon.[73] Similar behavior was found for domain boundaries on Ge(111)-2x1 which also shows the Pandey reconstruction.[75]

Other interesting features of anti phase boundaries were reported by Trappmann et al.[74] He used dual bias imaging whereby he acquired an image on the forward scan with 1.1 V and an image on the backward scan with -1.1 V bias voltage. The anti phase boundary he observed is shown in Fig. 2.18 and it can be seen that it follows a different path in the forward and the backward scan.

Due to the scan speed Trappmann was able to determine that the rearrangement of the phase boundary in between the two positions between the line traces happens within less

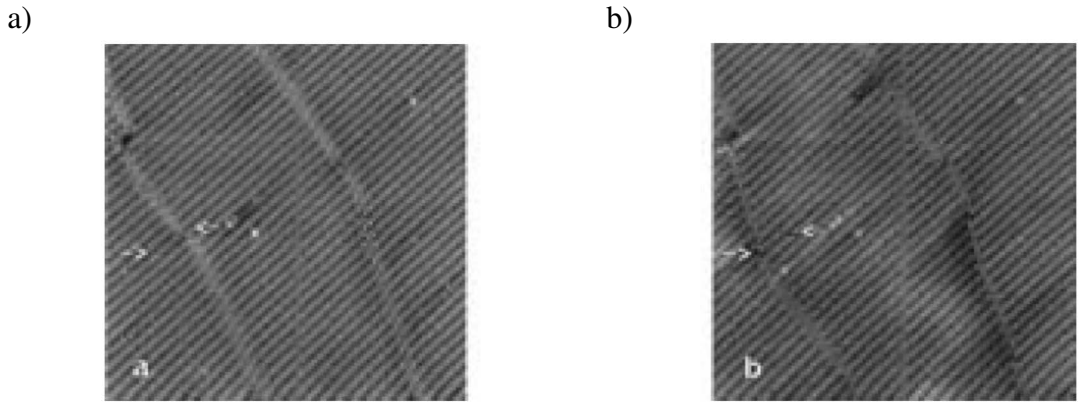

Figure 2.18: Moving anti phase boundary [74]. Arrows indicate the same position in both images. a) Forward scan at +1.1 V. b) Backward scan at -1.1 V.

than 0.1 s. He assumes that the movement is tip induced either due to the proximity of the tip or the applied electric field. The tip may push the boundary to the left or the right where it gets pinned by the defects marked with the white arrows. In the right APB he also points out a presumably electronic effect which leads to the darker areas around the APB on the backward scan. Neither of these effects were studied in more detail and the atomic structure of the APB, the mechanism of the movement as well as the exact nature of the electronic effect were not resolved.

For germanium, whose (111)-2x1 surface has a very similar crystal structure and surface reconstruction to that of silicon, more literature concerning domain boundaries can be found.[75–78] This can of course not be directly compared to silicon but may provide valuable insights. Hirayama et al.[76] proposed three different atomic models for the anti phase boundary as shown in Fig. 2.19 a). The top structure shows a boundary where the phase is not shifted but the buckling changes. The middle one is a boundary with shifted chains and no buckling change whereas the bottom one shows a chain shift and a buckling change.

By comparing his data with the atomic model, Hirayama was able to rule out the boundary that only consisted out of a buckling change as all the observed phase boundaries had staggered π-bonded chains. To determine whether the measured APB only has a pure phase shift in the $[11\bar{2}]$ direction or also a change of buckling, Hirayama checked whether the up atoms align across a boundary as indicated with the arrows in Fig. 2.19 a). It can be seen that the up atoms of an APB that does have a changed buckling are aligned over the boundary, whereas they are out of phase if there is no change in buckling. Hirayama reports that all ten boundaries show no shift in filled states, displayed in the top image in Fig 2.19 b). When imaging in empty states surprisingly six of the ten boundaries showed a shift, as shown in the the bottom image in Fig 2.19 b).

To resolve this controversy, Hirayama suggested that phase boundaries with a buckling

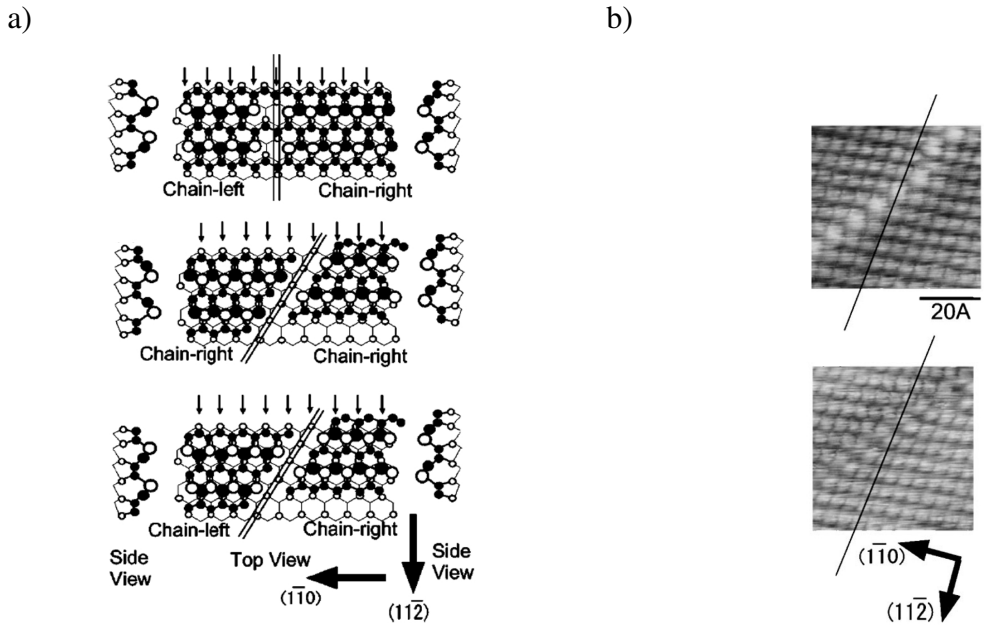

Figure 2.19: Model for germanium domain boundaries.[76] a) Top: No phase shift but the buckling changes. Middle: Phase shift buckling stays the same. Bottom: Phase and buckling changes. b) Top: Filled states image -0.56 V. Bottom: Empty state image +0.3 V.

change do exist, but that the chain right (positive buckling) reconstruction converts into the chain left (negative buckling) reconstruction due to the tip influence at high negative bias.

2.3 Dopants in Silicon(111)-2x1

Dopants play a vital role in modern semiconductor devices and have experienced renewed interest due to their potential application in spintronics and quantum computing.[7, 8] Cross sectional sample preparation is especially well suited to measure the properties of individual dopant atoms as the low temperature preparation method prevents dopant diffusion, leading to dopants equally distributed through all lattice positions. Before the work of this thesis only phosphorus and boron were measured in the Si(111)-2x1 surface.[20, 74, 79–81]

2.3.1 Phosphorus

Phosphorus is a group V atom and therefore acts as an electron donor in silicon. Due to its low ionization energy it is a very commonly used dopant in semiconductor industry. Individual phosphorus atoms at room temperature were identified in the Si(111)-2x1 surface as protrusions in empty states and depressions in filled states, shown in Fig. 2.20 a).

Trappmann et al.[79] used counting statistics to associate these features with phosphorus atoms in the top layer of the Si(111)-2x1 surface.

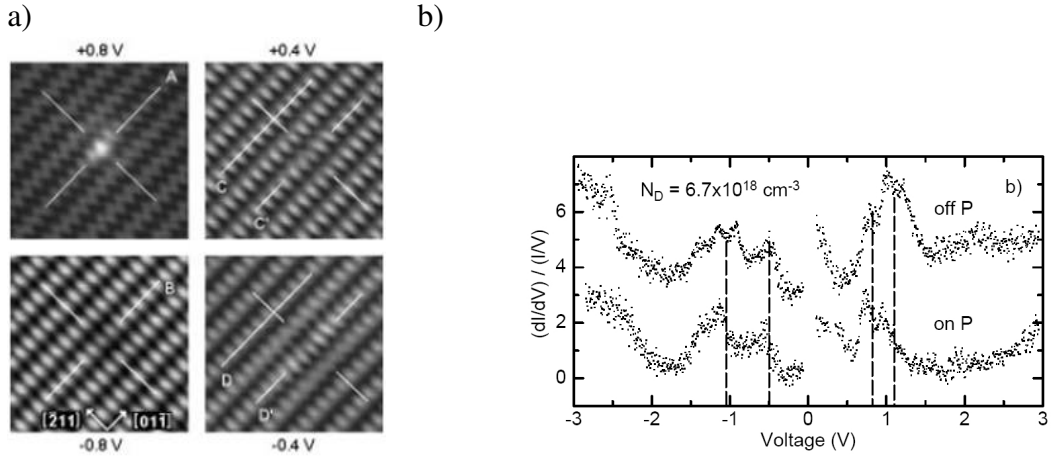

Figure 2.20: Phosphorus in Si(111)-2x1 at room temperature.[79] a) Voltage dependent images, 5 nm x 5 nm, 0.3 nA. b) STS on the dopant and on the clean surface.

In Fig. 2.20 b) STS data can be seen taken above a P atom and on the clean surface. Apart from the usual surface peaks they measured a shift of -0.1 V between the two spectra and concluded from this that the P donors are ionized, the Coulomb potential of the donor locally shifting the bands.

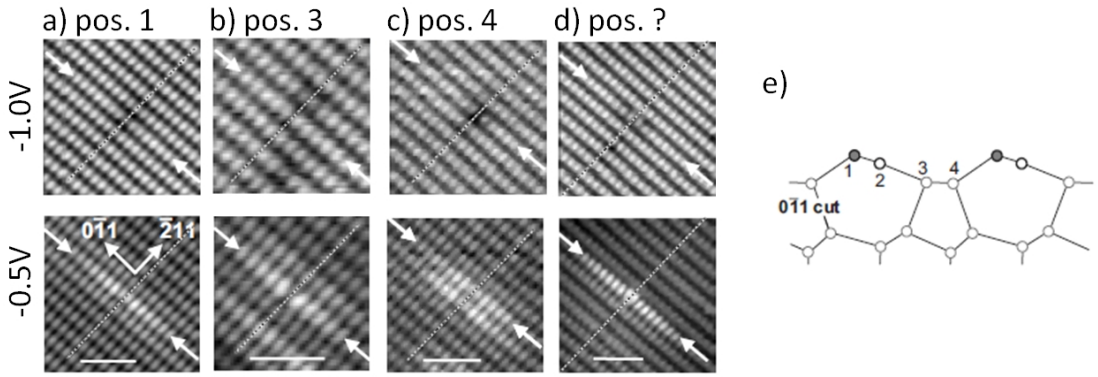

Figure 2.21: Voltage dependent images of phosphorus at 8 K by Garleff et al.[20] a)-c) Phosphorus dopant in position 1, 3, 4 respectively. d) Unidentified feature. e) Denomination of surface positions.

Garleff et al.[20] also measured phosphorus in Si(111)-2x1 but at 8 K. They were able to distinguish four different contrasts which they assumed to correspond to the four inequivalent surface positions of the Pandey reconstruction as shown in Fig. 2.21. They modeled the expected contrast of P dopants in all four positions and were able to correlate position one, three and four. Surprisingly the contrast shown in Fig. 2.21 d) did not match the simulated contrast of position two as it shows the wrong symmetry. For a dopant in this

position the contrast would have to be symmetric around the down atom in the π-bonded chain which was not the case. It is unclear if the feature shown in d) is a phosphorus atom in a surface relaxation that was not considered or something entirely different and if so, why no phosphorus atom in position two was found.

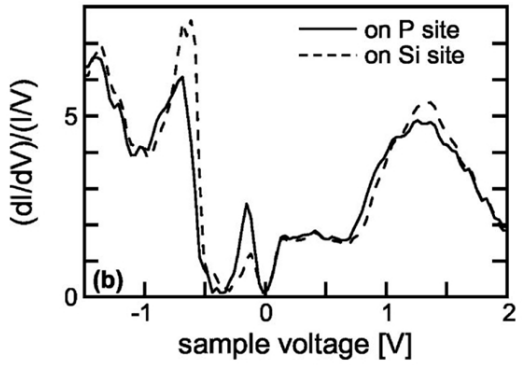

Figure 2.22: STS of phosphorus at 8 K by Garleff et al.[82] Data acquired over the clean silicon surface (dashed line) and over the phosphorus dopant (solid line).

They also acquired STS data at 8 K but did not measure the negative shift on the donor that Trappmann observed at room temperature as shown in Fig. 2.22. It was therefore concluded that phosphorus atoms were not ionized at this temperature. STS data of phosphorus dopants located at different interstitial positions were found to be identical, only showing a decreased LDOS at the surface valence band and increased LDOS in the surface band gap.

2.3.2 Boron

Boron is a group III element and therefore acts as an acceptor in the silicon crystal. Individual boron atoms in the Si(111)-2x1 reconstruction were measured by Schöck et al.[80] They found that boron is imaged as a protrusion in filled states and low empty states, whereas it appears as a depression in high empty states as shown in Fig. 2.23. This contrast is explained by a local upwards shift of the bands due to the negative charge of the boron acceptor. The shift gives rise to additional LDOS in filled states but decreases the available states to tunnel into in empty states. The fact that boron appears bright at low positive bias is assumed to be because of the additional empty states of the acceptor itself.

STS data aquired on the boron dopant (bottom) and on the bare surface (top) can be seen in Fig. 2.23 b). Again a small shift ($<$0.1 V) was found for the peak at 1.45 V due to the Coulomb potential of the negatively charged acceptor. The peak at -0.9 V is shifted towards -0.4 V over the B atom, giving rise to the bright appearance of the acceptor at negative voltages. Most prominently, the peak at 0.5 V, corresponding to the unoccupied states of the down buckled atom, is strongly reduced above a B acceptor. This

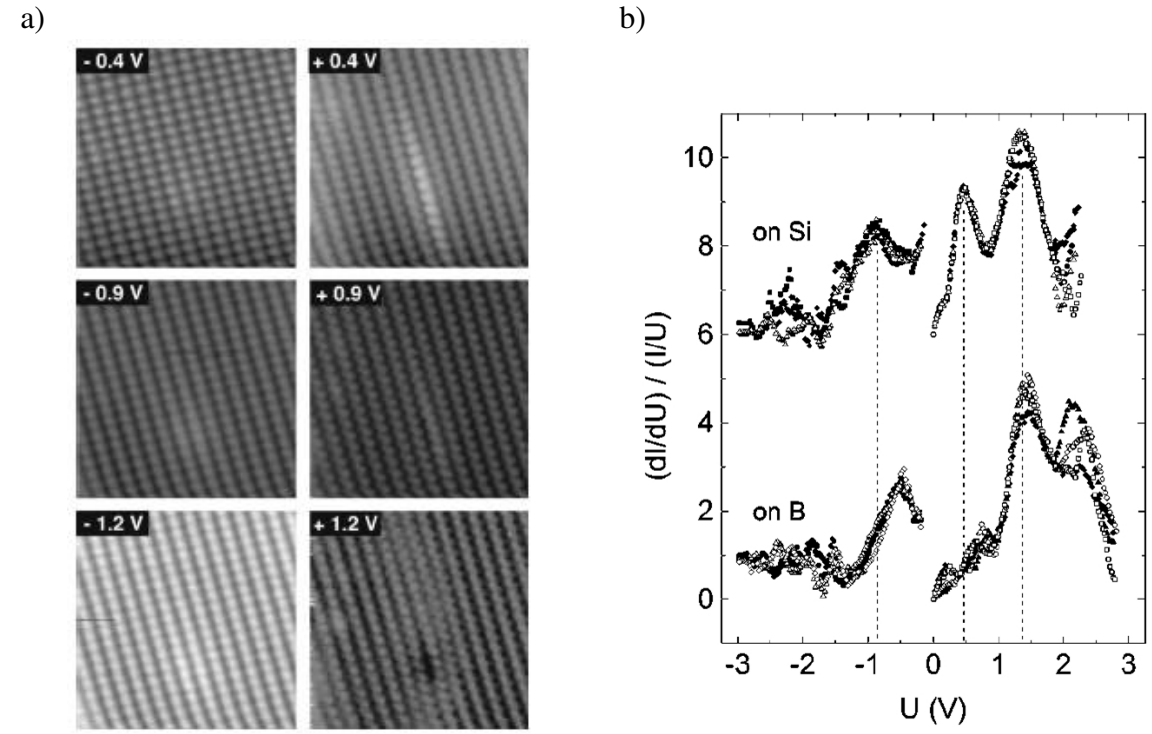

Figure 2.23: Boron in Si(111)-2x1 at room temperature from Schöck.[80] a) Voltage dependent imaging at 0.7 nA. b) STS data on the boron dopant (bottom) and over the bare surface (top).

is attributed to a missing dangling bond state at the boron atom due to the missing orbital of the acceptor compared to the silicon lattice.

3 Materials and Methods

3.1 Low Temperature and Variable Temperature STM

All work on cleaved samples has been performed on a commercially available low temperature scanning tunneling microscope (LT STM) from Omicron. The STM is housed in a ultra high vacuum (UHV) chamber together with a second variable temperature (VT) STM.

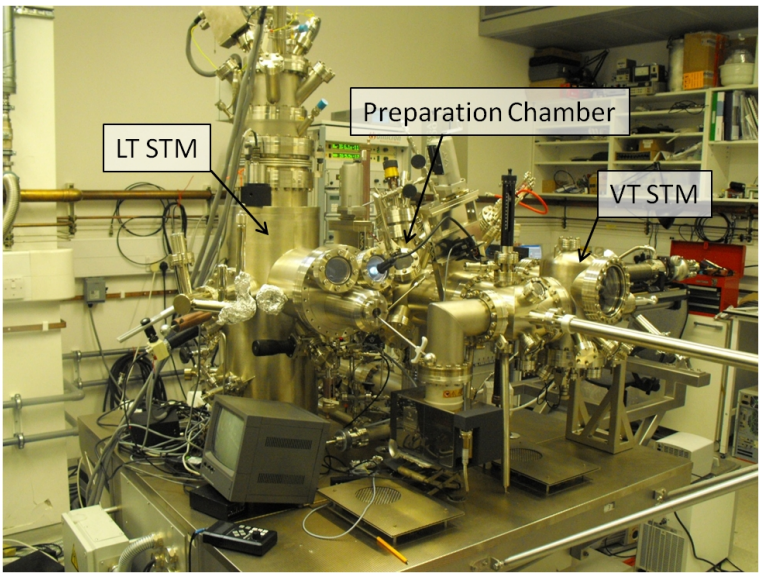

Figure 3.1: Combined low temperature and variable temperature STM system.

The complete system consists of three connected UHV chambers as indicated in Fig. 3.1. The preparation chamber is used to clean and prepare samples as required by the specific experiment. The samples are then transferred under UHV conditions into one of the STM chambers where they can be analyzed.

3.1.1 Ultra High Vacuum Chamber

To reach ultra high vacuum the stainless steel chamber is pumped with a turbomolecular pump and baked to 150 °C for 72 hours. This removes water condensation from the chamber walls which forms upon exposure to atmosphere and will lead to pressures in the 10^{-9}mbar range. To further decrease the pressure, ion getter pumps and titanium

sublimation pumps are used which will pump the chambers to below $5 \cdot 10^{-11}$mbar, the pressure reading limit of the gauges. This very high vacuum is necessary to prevent unwanted gas molecules from reacting with the sample and contaminating it. We found that cleaved silicon substrates remain clean in the STM for several weeks.

3.1.2 Vibration Isolation System

During a measurement the STM tip has to be held within 5 Å of the surface and therefore even the smallest vibrations of the tip sample junction would significantly influence the measured tunnel current. Both STM systems are mounted on springs within their respective UHV chamber and have an eddy current damping system to minimize mechanical vibrations. Additionally, the whole table has its own damping system to isolate it from vibrations from the floor.

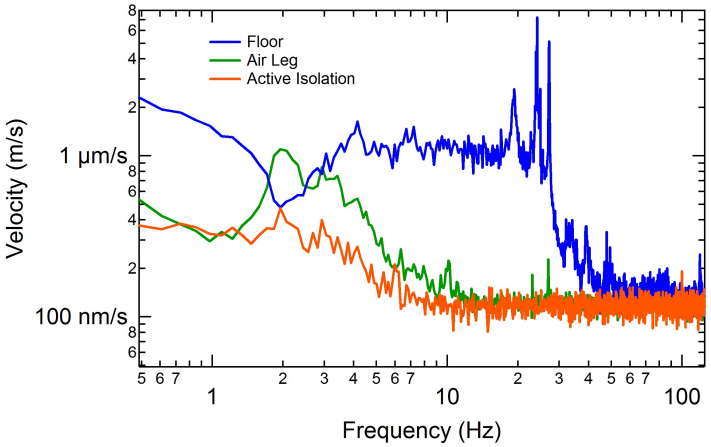

Figure 3.2: Measured vibration spectrum on the floor and the table using air legs or active vibration isolation.

We use an accelerometer to determine the vibrations of the table. Air legs, decoupling the table from the floor by floating it on an air cushion, turned out to be disadvantageous as they have a resonance frequency at around 2 Hz. They therefore amplify noise coming from the floor in this frequency range as shown in Fig. 3.2. Active vibration isolation was installed which measures vibrations on the table and actively compensates them using piezo elements. Even though active vibration isolation does not damp significantly at very low frequencies, it also does not show any amplifying behavior. As it can be seen in Fig. 3.2, the vibrations of the floor are consistently damped by an order of magnitude between 3 Hz and 50 Hz.

3.1.3 LT and VT Scan Heads

The Omicron low temperature STM can be seen in Fig. 3.3 a) inside its thermal shields. It is attached to a bath cryostat that can be filled with liquid helium or liquid nitrogen. An internal heater additionally allows one to counter heat the STM and therefore it can be operated in a temperature range between 5 K to 50 K using liquid helium or 78 K to room temperature when running with liquid nitrogen. Operating the STM at low temperatures not only allows one to minimize the thermal broadening of spectroscopic features but significantly increases the stability of the tip sample junction. Especially for current imaging tunnelling spectroscopy (CITS) measurements that can take several hours it is important to suppress the lateral drift which is often only possible at low temperatures. The STM is implemented as a tube scanner pointing upwards and holding the tip. The sample is clamped above it and facing downwards. The coarse approach is a slip stick drive with a range of 10 mm and there are two other slip stick drives for x and y coarse motion, both with a range of 2.5 mm. The maximum scan range of the tube is 10 μm at room temperature, 4.4 μm at 78 K and 1.8 μm at 5 K.

a) b)

Figure 3.3: Scan heads of the microscopes. a) LT STM inside its thermal shields. b) VT STM outside the chamber.

The Omicron variable temperature STM head is shown in Fig. 3.3 b). It is in principle very similar to the LT STM head but instead of cooling it is possible to heat the sample while scanning, by passing a current through it. This allows one to study samples between room temperature and 1500 K. The STM is also implemented as a tube scanner with a scan range of 12 μm that is slightly larger than in the LT. The coarse motion in X and Y is again realized with slip stick drives that have a travel of 5 mm each, facilitating the access to markers and specific areas on the sample.

3.2 Cryogenic STM

The Cryogenic STM consists of two Omicron UHV chambers connected to a cryostat from Oxford Instruments as shown in Fig. 3.4 a). Samples can be prepared in UHV and

then loaded into the STM, which itself can be lifted into the cryostat. The helium flow cryostat allows one to measure at temperatures down to 1.6 K and contains superconducting magnets that can apply fields of 6 T perpendicular to the sample or 1 T in any direction.

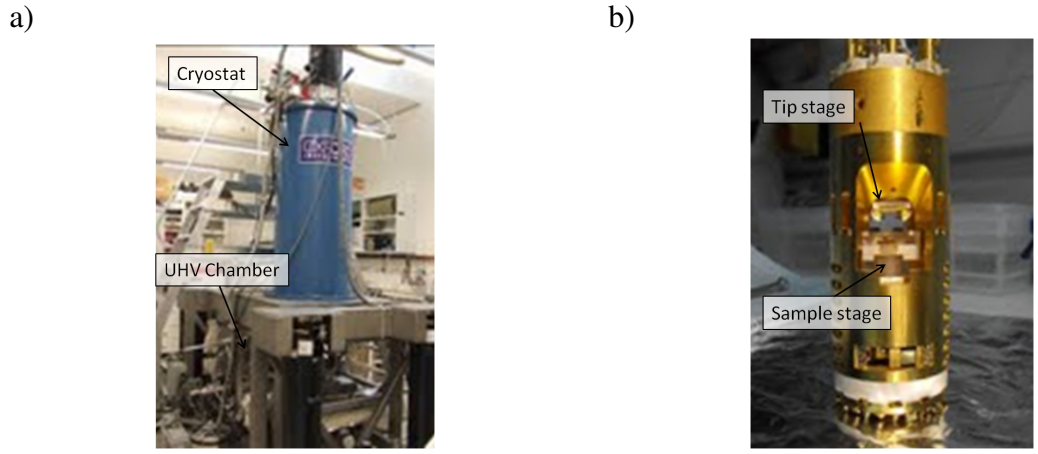

Figure 3.4: Cryogenic STM. a) Vacuum chamber and cryostat. b) Cryo STM head.

The STM head is shown in Fig. 3.4 b). The sample is facing upwards and is connected to two slip stick drives for the coarse approach and movement in one axis. The STM is implemented as a tube scanner visible in the top of the image. Tip preparation methods were implemented and tested on this machine but no experimental data has been acquired on it for the work of this thesis.

3.3 Sample Preparation

Silicon samples are highly reactive and therefore the surface is usually covered with water and carbon in an ambient atmosphere. To study a clean silicon surface it therefore has to be prepared in UHV. In this work we used two different approaches depending on the prepared surfaces. As described in the following paragraphs Si(100) wafers were cleaned using flash annealing whereas Si(211) wafers were cleaved in UHV, therefore exposing a fresh and uncontaminated surface that can be measured with STM.

3.3.1 Wafer

Three types of wafer were used in this study. Low phosphorus doped Czochralski (Cz) grown $\{100\}$ wafers were purchased from Compart Technology Ltd with a conductivity of 1-10 Ωcm, corresponding to a doping level around 1×10^{15} cm^{-3}. These wafers were cut with a tolerance of only ±0.1 degree in the $\{100\}$ plane, lower than the standard ±1 degree tolerance, in order to minimize the number of atomic steps on the surface and

facilitate the creation of large atomically flat terraces. They were used in all cleanroom fabrication processes described in Chap. 4, towards the development of an atomic scale device fabrication process.

Phosphorus doped Si(211) wafers were purchased from Virginia semiconductors. They were Cz grown and have a conductivity lower than 10 Ωcm, corresponding to a doping level higher than 1×10^{15} cm^{-3}. These wafers were used to study the bare Si(111)-2x1 surface and also for all experiments with implanted dopants. The very low phosphorus doping concentration ensures that measurements are not influenced by the phosphorus dopants as less than one dopant is expected in the surface per square micrometer.

The second wafer type is highly antimony doped with a $\{211\}$ surface orientation purchased from NOVA semiconductors. They are Czochralski grown with a conductivity smaller than 0.02 Ωcm, corresponding to a doping level higher than 1×10^{18} cm^{-3}. These wafers were used to study Sb dopants in the Si(111)-2x1 surface with an expected density of over 2 dopants per scan area of 100 nm square.

3.3.2 Flashing Silicon

The most commonly used technique to prepare clean silicon $\{100\}$ surfaces is flash annealing.[83] The sample is heated by passing a current through it and brought to a temperature of 1200 °C in order to evaporate all contaminants from its surface. At this temperature silicon atoms are also evaporated, making the surface atomically rough and the sample is therefore only kept at this stage for a short time, 10 s in our case. The sample temperature is then immediately dropped to 900 °C where silicon atoms have enough thermal energy to move across the surface and reorder but cannot detach from it. From there the sample is annealed towards room temperature within 200 s in order to allow the surface to find its minimum energy reconstruction. This cleaning method can be repeatedly applied and reliably produces atomically clean surfaces with large terraces.

3.3.3 Cleaving Silicon

To cleave samples in UHV we fabricated purpose built sample holders shown in Fig. 3.5 a). A 4 mm by 6 mm piece of silicon is cut from the wafer using a diamond dicing saw. It then gets scratched with a diamond scribe 3 mm above the bottom at a length of 1 mm. As indicated in the image, this notch is placed just above the clamps of the sample holder and will nucleate a fracture when struck, defining the position of the cleaving plane. After scratching the sample it is glued to a cover glass using crystal bond and then manually grinded down to a thickness of 100 μm. This makes the sample very fragile and ensures that it readily cleaves at the desired position in UHV.

The sample is then transferred into the sample holder standing upright as indicated in

Fig. 3.5 a). To minimize the clamping strain and to make sure there is a good electrical contact, a small amount of indium is placed between the sample and the clamps at both sides. The whole assembly is then heated to 160 °C, just above the melting point of indium, and the clamps are tightened, clamping the sample at only one side at a length of about 1 mm. The rest of the sample is therefore not subjected to any strain from the clamps and the cleave can propagate freely along the atomic crystal plane.

a) b)

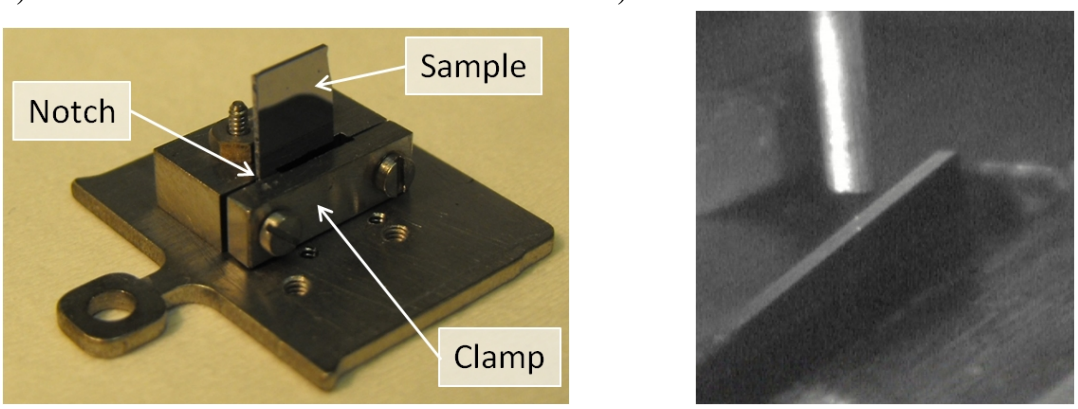

Figure 3.5: Cleaving silicon samples. a) Uncleaved sample mounded in a holder before loading into UHV. b) Cleaved sample in UHV with STM tip approaching.

The sample is then loaded into the UHV chamber and heated to 140 °C for one hour in order to remove adsorbed water from the sample holder. Just before loading the sample into the STM, the wobble stick is used to cleave it by gently pushing the corner above the clamped part. Once the sample is loaded into the STM, the tip is approached to the exposed cleaving surface as shown in Fig. 3.5 b). The surface is extremely flat even on a macroscopic scale and the reflection of the tip can be easily seen and is used to guide the tip close to the surface.

3.4 Ex Situ Tip Preparation

Reliably preparing atomically sharp and clean metal tips is crucial for a successful STM measurement. In this work we use etched tungsten tips for all experiments. Tips are cut from a 250 μm diameter polycrystalline tungsten wire. The wires are then inserted 1 mm deep into 3 mol KOH solution together with a platinum ring electrode around it. When applying a positive voltage of 4.5 V between wire (anode) and platinum electrode (cathode), etching of the tungsten occurs at the air-electrolyte interface and the tip apex starts forming. After a few minutes the wire is completely etched through and the part below the surface will fall off. This leads to a sudden drop in the etch current that is detected and the applied voltage is immediately turned off to avoid blunting the tip by

further etching. Tips are then removed from the electrolyte and cleaned in deionized water and isopropanol before loading them into the UHV chamber for further treatment.

3.5 In Situ Tip Preparation

Tungsten is oxidizing in the etch solution and in air and therefore tips are coated with an insulating WO_3 layer after fabrication. This layer may not necessarily have a negative impact on the quality of topography images but can shift the energy scales involved in both topography and spectroscopy. To get accurate and reproducible measurements it is therefore crucial to completely remove this oxide.

This is usually achieved by heating the tip in UHV to temperatures above 725 °C when reaction 3.1 takes place and WO_2 is released from the surface.

$$2WO_3 + W \rightarrow 3WO_2 \uparrow \tag{3.1}$$

Two tip preparation tools were designed by the author and built as part of this work, one for each STM chamber, adapted to the chamber geometry and tip holders of the specific system. They both have direct current heating sample preparation capabilities and allow heating of the tip by electron bombardment and characterizing it using field emission.

3.5.1 Cryo Tip Preparation Tool

The tip preparation tool of the cryogenic STM was built in the workshop according to my designs as shown in Fig. 3.6. It is mounted in the STM chamber to make sure tips and samples can directly be transferred into the STM after preparation.

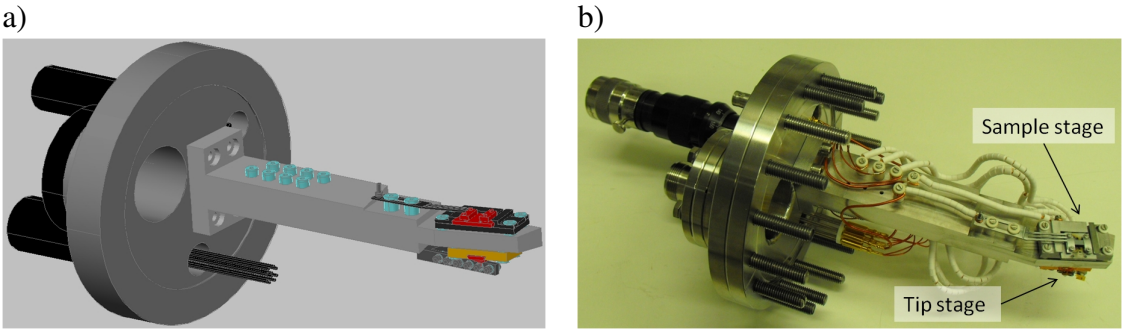

Figure 3.6: Tip preparation tool of the cryogenic STM. The tip stage allows electron bombardment heating, direct current heating and field emission characterization of the tip. Additionally samples can be direct current heated in the sample stage. a) CAD model. b) Finished tool.

The tip stage is made out of oxygen free copper and electrically isolated from the system using alumina ceramics as shown in Fig. 3.7 a). The tip can be inserted into the

stage pointing down and a rotary linear UHV feedthrough allows one to position a filament directly in front of the tip. Three filaments are available to create redundancy in case one of them should break. All filaments are held by molybdenum screws in order to avoid extensive outgassing when getting hot and are electrically and thermally isolated from the system by alumina ceramics. They are all made out of 0.1 mm diameter thoriated tungsten wire which has a reduced work function compared with pure tungsten and therefore emits more electrons when heated,[84] in this setup realized by passing a current through the filament.

The tip stage is connected to a high voltage (HV) feedthrough that allows one to apply up to 25 kV to the tip. This is used to accelerate electrons emitted from the filament towards the tip to heat it up or for field emission from the tip onto a metal plate as shown in Fig. 3.7 b). The metal plate is made out of gold and can be used as a grounded electrode for field emission or to make electrical contact to the tip by touching it from the side. This enables heating the tip by passing a current through it.

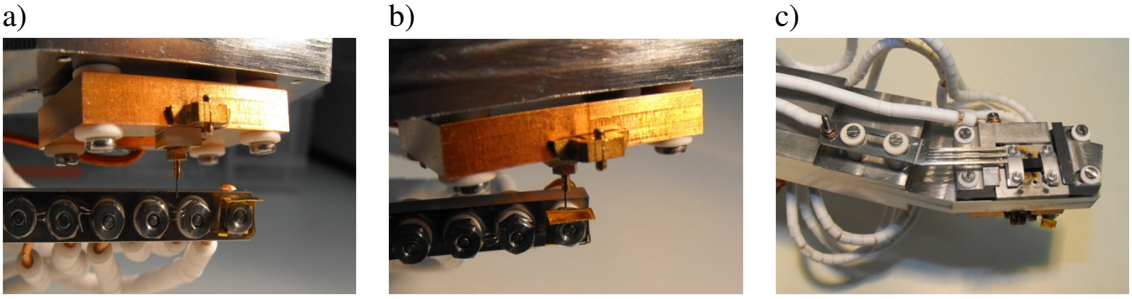

Figure 3.7: a) Tip Stage in configuration for electron bombardment. b) Tip Stage in configuration for field emission characterization. c) Sample stage with contact finger for direct current heating.

The sample stage is shown in Fig. 3.7 c) and can be used to prepare samples by direct current heating. The contact finger that comes in from the left and the sample reception are both made from molybdenum and again electrically and thermally isolated from the rest of the system by alumina ceramics. It can be seen that the molybdenum finger makes contact to the left side of the sample holder and allows one to pass a current through the sample to the grounded stage. The sample stage is additionally designed to be very rigid in order to provide a cleaving position in the cryogenic STM.

3.5.2 VT Tip Preparation Tool

The tip preparation tool of the VT STM consists of a commercially available omicron sample stage and a tip stage that was designed by the author and manufactured in the workshop. Tip and sample stage are mounted on linear translation feedthroughs on opposite flanges as shown in Fig. 3.8 a). The sample stage is attached underneath the transfer

carrousel as it can be seen in Fig. 3.8 b). It can be used to prepare samples by direct current heating but also acts as a filament holder for electron bombardment of the tip. The filament is mounted on a custom made sample plate which has an electrically isolated molybdenum contact on it that touches the contact fingers of the stage, similar to the direct current heating plates. Instead of heating a sample the current passes through the filament which is mounted between the contact block and ground. This has the advantage that filaments can be replaced through the load lock without venting the chamber in case they break.

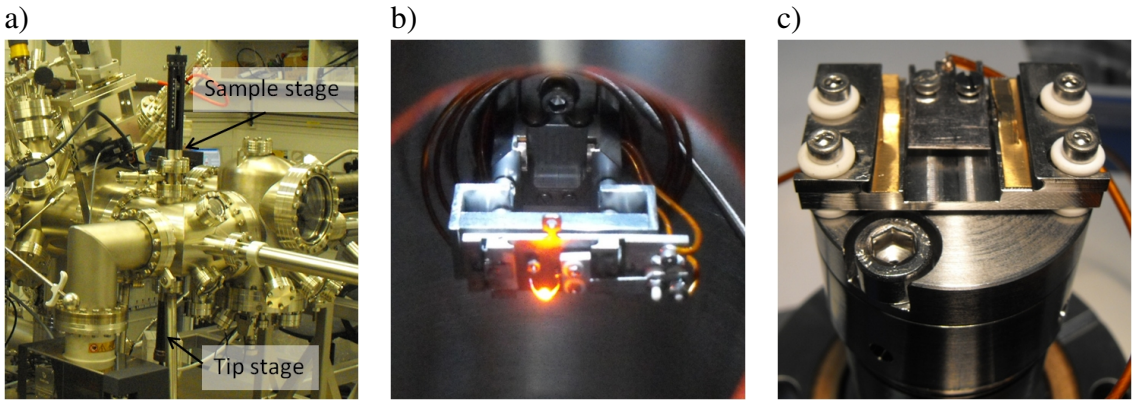

Figure 3.8: Tip preparation tool VT STM. a) Mounting configuration on the system. b) Filament and sample stage in the chamber. c) Tip stage with contact plate and springs.

The tip stage is mounted on the lower translational feedthrough pointing upwards and can therefore be shifted into close proximity of the filament. The design is complicated by the fact that VT tips are electrically isolated from their carrier plates and therefore a mechanism had to be implemented that directly contacts the tip. The stage is shown in Fig. 3.8 c) and in the center a thin plate made out of tantalum can be seen. This plate is located directly underneath the tip carrier and will touch the leg of the tip when it is inserted, making electrical contact. To ensure a firm connection between the tip and the tantalum plate, springs made out of phosphor bronze hold the tip carrier plate in place.

3.5.3 Electron Bombardment

Electron bombardment is used to heat the tips in UHV above 725°C to remove the WO_3 oxide layer. Electrons are emitted from a tungsten filament heated by passing a current through it. A positive voltage of 400 V is applied to the tip in order to accelerate the thermally emitted electrons towards it. The filament current is then increased until the emission current reaches 30 μA and the tip is heated at this current for five minutes. This procedure locally heats the tip apex and removes the oxide. The parameters were

determined experimentally and reproducibly created clean tungsten tips, confirmed by measuring the well known I-V spectra of the Si(100) surface.

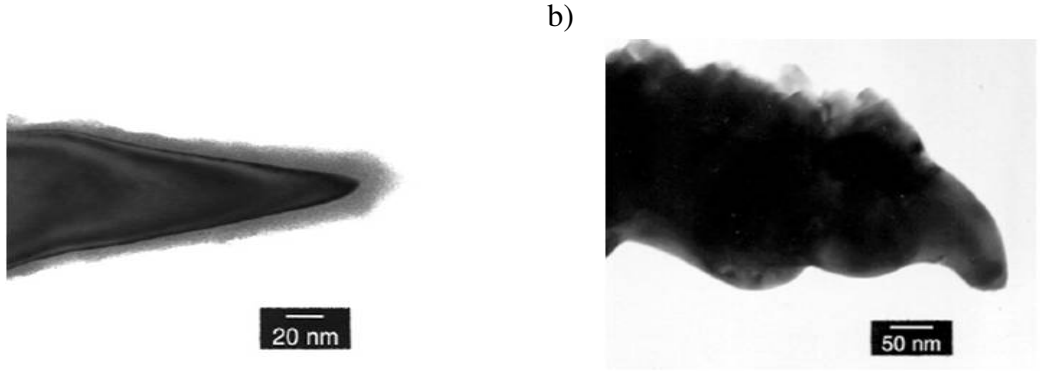

Figure 3.9: Influence of electron bombardment, imaged with TEM by Ekvall et al.[85] a) Tip before treatment. b) Tip after electron bombardment.

Ekvall et al.[85] used TEM to look at tips before and after electron bombardment heating. As shown in Fig. 3.9 a) the tip is coated with an oxide layer of about 5-10 nm thickness after etching. Their study did not show any difference between freshly etched tips and tips that were left in air for a full day, emphasizing the fact that in situ tip preparation is necessary even for freshly prepared tips. Care has to be taken to ensure that the tip is not heated above 3410 °C, the melting temperature of tungsten. Due to the very local effect of the heating, this can easily happen and leads to a blunt tip that will not field emit anymore. A tip that had its oxide layer removed by electron bombardment is shown in Fig. 3.9 b) and it can be seen that only the very end of the tip is cleaned.

3.5.4 Field Emission

Field emission (FE) is used to characterize the tip and condition its very end. The tip is brought close to a grounded electrode and then a large negative bias is applied. Electrons can leave the tip by tunnelling through the barrier represented by the tungsten work function. This process is called Fowler-Nordheim tunnelling[86] and described by Eq. 3.2. V is the applied voltage and ϕ the work function of the tip. η and ζ are constants depending on the tip radius, the exact geometry of the setup and the material constants involved.

$$I = \eta V^2 exp\left(\frac{-\zeta\phi^{3/2}}{V}\right) \tag{3.2}$$

We sweep the voltage to -1100 V and record the emission current, limiting it to 1 μA in order to prevent excessive heating of the tip. Five recorded traces for an untreated tip can be seen in Fig. 3.10 a), all are very different and characterized by a highly unstable current. It is assumed that the field emission current locally changes the tip apex due to

the high current density, leading to the noisy traces. After the electron bombardment, tips are tested again and the measured current is generally found to be very stable and reproducible as shown in Fig. 3.10 b). If tips show successive FE traces that perfectly overlap, they are loaded into the STM, usually resulting in very stable, clean tungsten tips that can be used for several weeks.

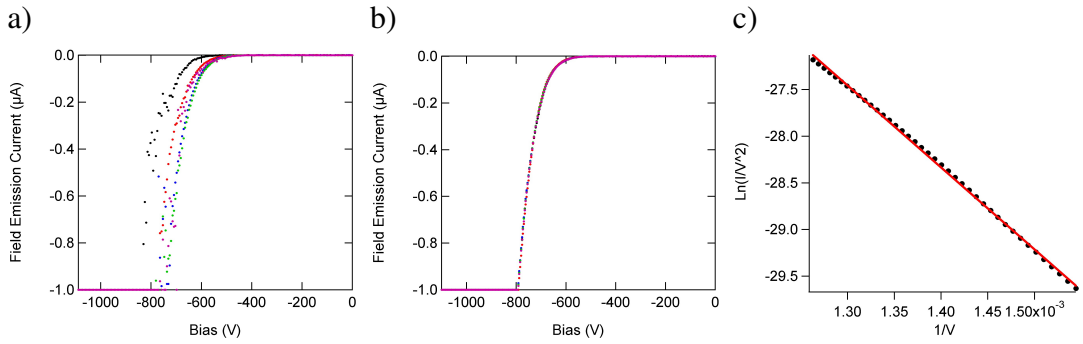

Figure 3.10: FE preparation of W tips. a) Initial FE traces before electron bombardment treatment. b) FE traces after treatment. c) Fowler-Nordheim tunnelling plot.

The recorded field emission current can be plotted as $ln(I/V^2)$ over $1/V$ which, in the case of Fowler-Nordheim tunnelling, should result in a straight line according to Eq. 3.3. This is nicely confirmed by our data as seen in Fig. 3.10 c).

$$ln(\frac{I}{V^2}) = m\frac{1}{V} + C; \qquad m = -\zeta\phi^{3/2}; \qquad C = ln(\eta) \tag{3.3}$$

According to the Fowler-Nordheim theory the field E at the cathode is proportional to the applied voltage V with the product of the field-voltage proportionality factor K and the tip radius R as shown in Eq. 3.4.

$$E = \frac{V}{KR} \tag{3.4}$$

This can be used to estimate the tip radius as described by Gomer.[87] The dependence of the constant ζ on the tip radius can be approximated according to Eq. 3.5

$$\zeta = 6.8 \times 10^7 [V \cdot eV^{-1} \cdot m^{-1}] \sqrt{1 - \frac{3.8x10^{-4}[eV \cdot V^{-0.5} \cdot m^{0.5}]\sqrt{E}}{\phi}(KR)} \tag{3.5}$$

If the experimentally determined tungsten work function ϕ=4.55 eV is used together with a field-voltage proportionality factor K=5, usually found for etched tungsten tips, the radius R of the tip can be approximately determined. To do so the slope of the fitted Fowler-Nordheim tunnelling is used to determine ζ which then allows to calculate R from Eq. 3.4 and Eq. 3.5 using the average of all tunnelling voltages. For the tip shown in Fig.

3.10 this leads to an estimated radius of 38 nm. We usually find tips with radii between 15 nm and 40 nm, comparing nicely with the expected range for etched tungsten.[85]

3.6 High Precision Tip Alignment

For the atomic scale device fabrication process it is necessary to approach the tip within an area of 100 μm x 100 μm. To reach such a high alignment accuracy the K2/S long distance microscope, as seen in Fig. 3.11, was purchased from Infinity with components selected to match our specific requirements. It has an eyepiece for coarse positioning with an overall 120x magnification and a camera port for fine alignment with up to 600x magnification. The mounted Watec WAT DM2S CCD camera was selected for its superior light sensitivity and the resolution of the microscope at the full working distance of 250 mm is 3 μm. The microscope is mounted on a boom stand with two micrometer stages allowing a precise manipulation of the image even at highest magnification. We found that approaching a 100 μm x 100 μm area was quickly and routinely possible using this setup.

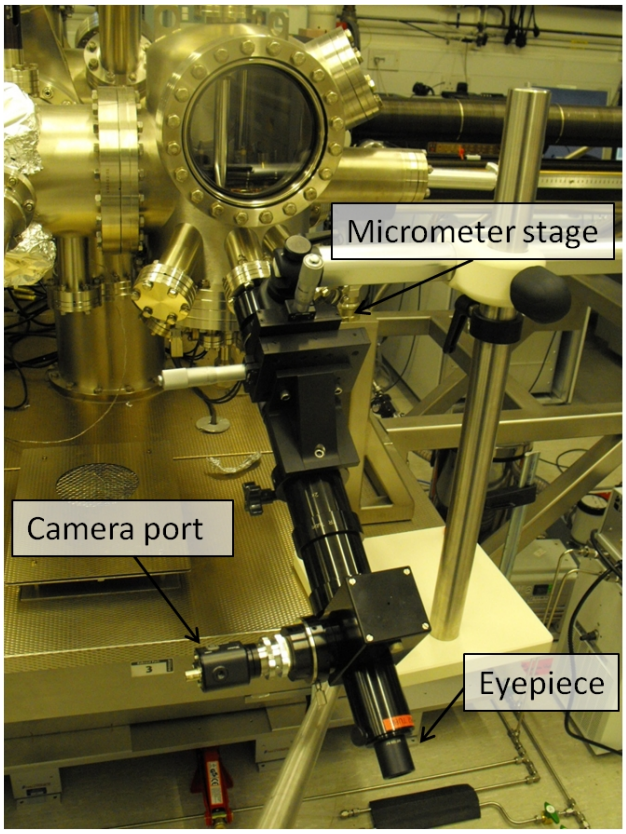

Figure 3.11: Long distance microscope with stand mounted on the VT STM.

3.7 Gas Dosing System

A gas dosing system allowing one to controllably insert two different gases into the UHV space of the VT STM was designed and installed by the author during this work. The assembly was manufactured by Swagelok and has only welded joints in order to maximize security for the use of highly toxic gases such as phosphine or diborane. As it can be seen in Fig. 3.12, the assembly allows the attachment of two gas vials and provides the ports to pump and purge all gas lines to clean them after exposure to atmosphere. Two high precision leak valves allow a controlled dosing of gases into the UHV space, a capillary mounted inside the UHV chamber transporting the gases directly in front of the sample surface to maximize exposure.

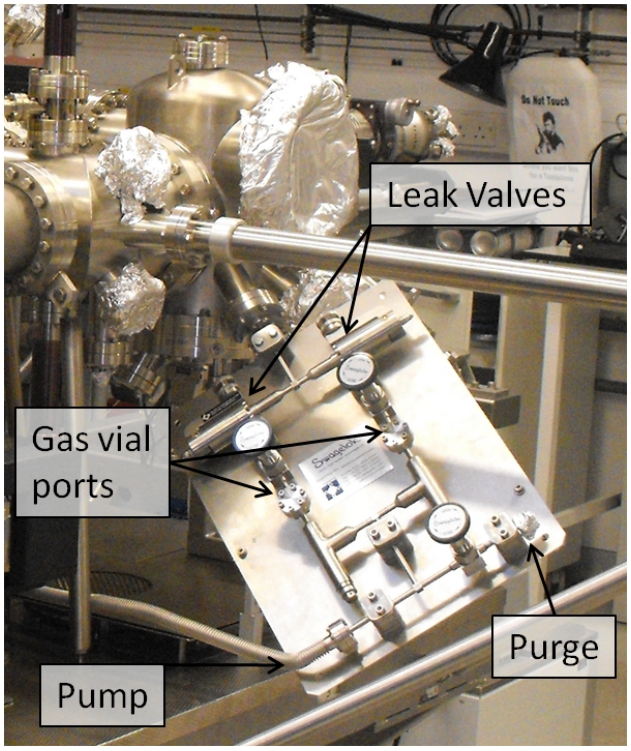

Figure 3.12: Dual gas dosing system mounted on the VT STM.

4 Development of an Atomic Scale Device Fabrication Process

The fabrication and characterization of single dopant devices in silicon requires precise control over the location of individual atoms. This ultimate control in fabrication was so far only realized in the form of single atom manipulation using scanning probe microscopy.[27, 88] Schofield et al.[2] demonstrated that it is possible to use an STM to place phosphorus dopants in silicon with atomic scale precision, enabling the integration of atomic scale STM fabrication into conventional semiconductor technology. The process is based on the use of a hydrogen (H) resist[89], terminating the silicon surface and making it chemically inert, as shown in Fig. 4.1 a). The STM tip can then be used to desorb single hydrogen atoms, indicated in Fig. 4.1 b), allowing the controlled positioning of the subsequently deposited phosphorus which only sticks to desorbed areas, as shown in Fig. 4.1 c). This process was demonstrated with phosphorus deposited from gaseous and solid sources,[90] enabling the fabrication of arbitrary dopant structures on silicon surfaces. To use these atomically precise structures for the fabrication of devices, there is however an additional complication in that samples have to be removed from the UHV chamber of the microscope and contacts and gates have to be fabricated ex situ with a very high alignment accuracy. A process to achieve this was developed at the University of New South Wales (UNSW) [1, 91–95] resulting in the first STM fabricated dopant structures, such as wires and few dopant quantum dots, which could be contacted and characterized ex situ. [12, 96–100]

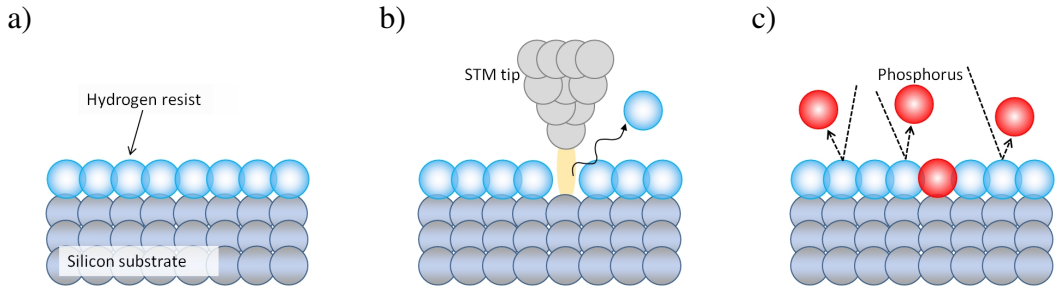

Figure 4.1: Atomically precise placement of dopants. a) Hydrogen terminated silicon. b) Controlled removal of a single H atom. c) Deposition of phosphorus, only sticking to silicon in desorbed areas.

In this chapter the development of a process based on previous work done at UNSW is described, which allows us to contact atomic scale structures fabricated with an STM. The main points include the fabrication of markers allowing for a high alignment accuracy between structures fabricated in the STM and the cleanroom, the creation of an atomically flat terrace as a suitable substrate for atomic scale devices and the effective contacting of buried dopant structures. During the course of this work, samples were created and tested for all of these criteria. Together with the designed and installed gas dosing system described in Sec. 3.7, the following work provides the basis for future projects focusing on the fabrication on single dopant devices.

4.1 Marker Fabrication

In order to align STM and cleanroom fabrication steps with high accuracy, markers have to be created on the silicon sample that satisfy a wide range of criteria. They have to be visible in optical microscopy for tip alignment and in EBL for contact alignment and subsequent fabrication. Furthermore, markers must be able to resist the flashing process described in Sec. 3.3.2 without significant distortion and they have to be scannable by the STM tip. Marker fabrication is of course a standard technique used in semiconductor technology where usually metallic structures are deposited on the surface as a reference, providing a high contrast in both optical and scanning electron microscopy. However, heating the sample to 1200 °C is not compatible with the use of standard gold or aluminum markers as they would get significantly distorted, preventing high alignment accuracy. Further it is known that even the smallest amount of metal on silicon samples induces the undesirable 2xn reconstruction, most commonly associated with nickel contamination,[101] making the surface unsuitable for STM nanofabrication.

Therefore an alternative marker technique has to be used, consisting of structures etched into the silicon surface. These markers were found to be compatible with STM fabrication[93] even though the flashing process does slightly distort their shape due to step migration in silicon at elevated temperatures. In order to use etched markers for monitoring with the long distance microscope and for EBL alignment they have to be etched deep into the sample, whereas scannable markers for the STM tip alignment are preferably very shallow to minimize the risk of crashing the tip into the surface. Two different sets of markers are therefore fabricated and etched to different depths.

4.1.1 Deep Etched Marker Fabrication Process

The fabrication process for the deep etched markers is shown in Fig. 4.2 a). In a first step a high quality SiO_2 layer is grown with a thickness of 60 nm using a high temperature

furnace. This layer not only serves as a mask for the silicon etching in a later step but also prevents a direct contact between the photoresist and the silicon sample and therefore helps to reduce contamination induced during cleanroom fabrication. A 100 nm thick layer of standard positive photoresist S1805 is then deposited on top of the SiO_2, using spin coating, before exposing the desired marker structure. Using a chrome on glass mask with the layout shown in the top image of Fig. 4.2 b), the marker pattern is transferred into the photoresist using UV light and subsequently developed using the standard solvent MF-319. The chrome mask allows one to expose over one hundred STM sample structures on one single four inch wafer, each with a unique identification number and a layout as shown in the second image of Fig. 4.2 b). Every STM sample has three marker structures on it, consisting of four large arrows for the optical long distance microscope and four small crosses in the center of the arrows for electron beam lithography alignment. Like this, three STM devices can be fabricated on each silicon sample loaded into UHV. The mask design further includes larger markers used for dicing and beam calibrations in EBL.

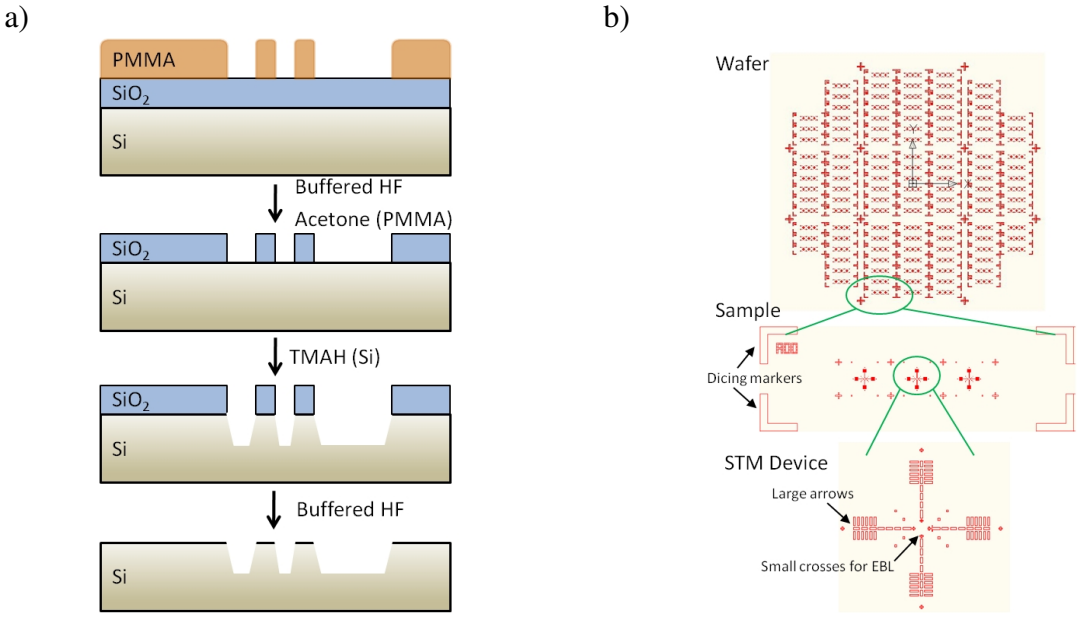

Figure 4.2: Deep marker fabrication and design. a) Cleanroom process for the fabrication of etched markers. b) Mask design for optical lithography to create the deep etched marker structure

After the marker structure is successfully transferred into the photoresist the pattern is etched into the SiO_2 layer using buffered hydrofluoric acid (HF, Riedl de Haen 40207). Because HF etching of SiO_2 is isotropic, a significant increase in the designed pattern dimensions due to undercutting of the resist has to be prevented by optimizing the etch time. It was found that 60 s are necessary to etch through the 60 nm SiO_2 layer, in good agreement with the expected etch rate of 1 nm/s. As the absolute size of the registration marker is not of crucial significance for the alignment process, relying on the center of

the structure, an etch time of 90 s was chosen to make sure the pattern is fully transferred but still keep the undercut below 100 nm. Once the pattern is etched into the SiO_2 layer the resist is removed in acetone as shown in the second step in Fig. 4.2 a).

In order to etch the marker structure into the silicon wafer, tetra methyl ammonium hydroxide (TMAH, Sigma Aldrich 331635) is used. Due to its selective etch rate between silicon and silicon oxide the patterned SiO_2 layer serves as an etch mask and the anisotropic etching of silicon in TMAH prevents significant undercutting. To increase the etch rate the TMAH is heated to 50 °C and the marker pattern is etched to a depth of 400 nm at a measured rate of 57 nm/min. In a subsequent HF etch the SiO_2 layer can be removed if the sample is to be used in the STM unless a second layer of shallow markers shall be etched into the central device region as will be described in Sec. 4.2.

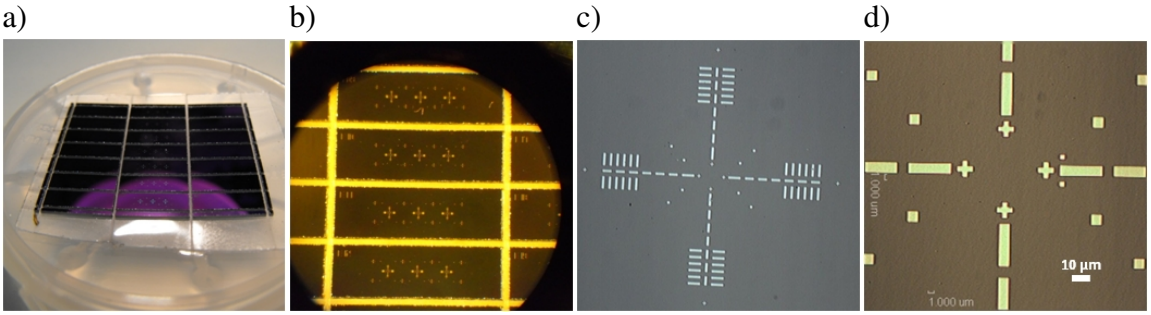

Figure 4.3: Results of the deep etched marker fabrication a) STM samples after dicing. b) Etched marker structure on STM samples. c) Optical microscope picture of etched marker structure. d) Device area in the center of the marker structure

The results of this process are shown in Fig. 4.3. The wafer is cut into individual samples using a diamond dicing saw as shown in Fig. 4.3 a) and the three marker structures on each sample can be clearly identified in Fig. 4.3 b). A single etched marker structure is shown in Fig. 4.3 c) with a magnification of the device area displayed in Fig. 4.3 d). The four crosses in the center of the image mark the boarder of a 100 μm write field for EBL fabrication and serve as the primary registration markers for subsequent fabrication steps.

4.1.2 Identification in the STM and EBL after Flashing

To test the marker structures, samples were loaded into the STM and the tip was approached to the central device fabrication area using the long distance microscope. It was found that an approach to the 100 μm square field was reliably possible without any difficulties as the large marker structures, etched to 400 nm depth, were well visible as shown in Fig. 4.4.

The second control for the deep marker structures is that they need to resist the flash annealing of the surface. The alignment process used in the EBL is shown in Fig. 4.5 a)

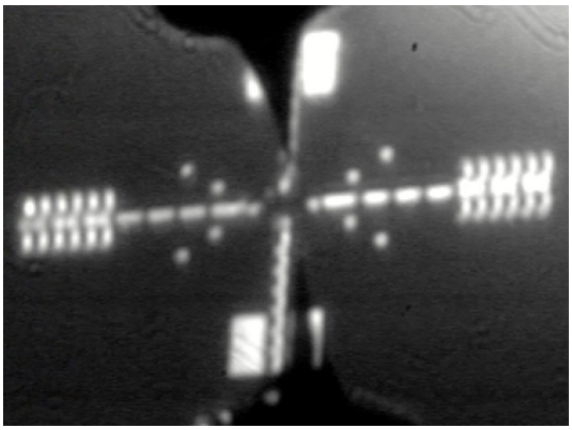

Figure 4.4: Optical tip alignment using the long distance microscope on the VT STM.

for a sample after etching, the SiO_2 not yet removed. The 400 nm deep cross structure is clearly resolved and two line scans, indicated by the red lines in the image, are acquired. One of them is displayed to the right and shows the measured intensity along the scanned line. An edge detection algorithm is used to determine the borders of the scanned structure and the center of the two detected edges is used to determine the location of one axis of the cross on the sample. Applying this technique in two different directions, as indicated in the image, it is possible to determine the center of the cross with very high accuracy. In Fig. 4.5 b) the same marker is shown after flash annealing the sample for 1 min at 1200 °C in the STM. The edges of the structure have blurred due to the high temperature anneal but the cross is nevertheless clearly visible. In the displayed line scan it can be seen that the edge detection is still working, allowing the determination of the marker position on the sample. Because the blurring of the marker structure is uniform it does not significantly affect the alignment accuracy, due to the fact that the center of the cross is used as a reference.

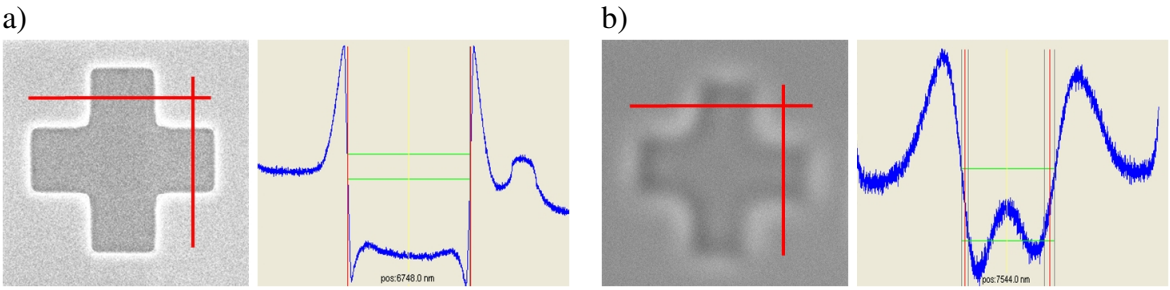

Figure 4.5: Alignment in the EBL system. a) Before flashing. b) After flashing.

It was found that structures etched deeper than 300 nm could be reliably used in the EBL alignment process after flash annealing them whereas shallower structures provided only very weak contrast. For the deep marker structure an etch depth of 400 nm was therefore used.

4.2 Creating Shallow Markers and a Large Atomically Flat Terrace for Device Fabrication

The second set of alignment markers is fabricated using electron beam lithography and only shallow etched into the silicon sample to make sure they are still scannable by STM. To make the device area suitable for STM nanofabrication, these markers are, in addition, designed to control the step flow in silicon in order to fabricate a large atomically flat terrace at a predefined device location. Controlling the terrace size of silicon surfaces by introducing step flow barriers in the form of ridges or trenches is a commonly used technique and is capable of creating micron size atomically flat terraces.[102–106] By annealing the sample at 900 °C, silicon atoms can detach from step edges, diffuse across the surface and will eventually reattach to the step edge or evaporate from the silicon surface. The ratio between reattachment and evaporation depends on the spacing between step edges whereby a larger spacing leads to more evaporation and therefore faster step migration.[107] By introducing etched structures on the surface with steep sidewalls, representing regions of large step density with very small spacing, a step flow barrier is created that leads to the formation of a large atomically flat terrace in its center. For our purpose the terrace is ideally several hundred nanometers in diameter in order to precisely mark a specific spot on the surface for alignment but still allow enough space to fabricate a device on it, as proposed by Füchsle et al.[108]

4.2.1 Shallow Etched Marker Fabrication Process

The process to etch the shallow marker structure into the silicon sample is identical to the one shown in Fig. 4.2 a), except that the photoresist is structured using electron beam lithography instead of optical lithography. The pattern is aligned to the four crosses in the central device region as shown in Fig. 4.6 a), taking advantage of the high EBL alignment accuracy which is below 10 nm. To reliably produce atomically flat terraces, a variety of different shapes were tested including circular or square pits and trenches as shown in Fig. 4.6 b). Diameters ranged from 3 μm to 7 μm with a 1 μm trench width and all markers were etched to a depth of 200 nm, following the recipe of Fuechsle et al.[108] The results of the TMAH etch to transfer the pattern into the silicon sample are shown in Fig. 4.6 c) and it can be seen that the anisotropic etch alters the exposed shapes especially for the circular features. Furthermore, the influence of the EBL alignment process on the registration markers is clearly visible as the scan line used to identify the marker edges resulted in the exposure of the resist, leading to additional etching. The markers are nevertheless still usable for the alignment of subsequent fabrication steps as the scan lines can be placed in a different orientation and there are also additional markers further away from the active

area, which serve as a backup.

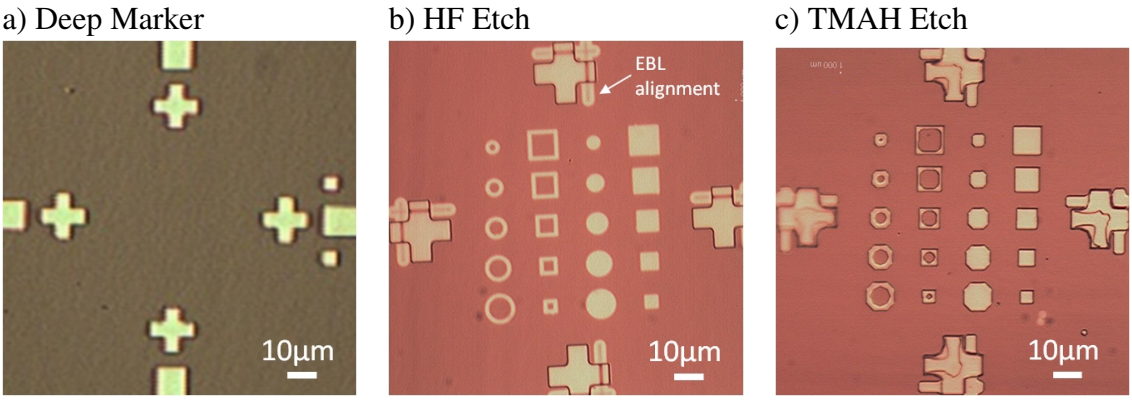

Figure 4.6: Shallow marker structure. a) Device area marked by deep markers. b) Shallow markers etched into the SiO_2 layer using HF. c) Shallow markers etched into the silicon sample using TMAH.

To test the surface quality and the depth of the different marker structures after the fabrication process, samples were characterized using atomic force microscopy (AFM) as shown in Fig. 4.7. The patterned features were found to be of high quality and uniformly etched to the desired depth. The surface roughness did not increase during the cleanroom fabrication, demonstrating the protective nature of the SiO_2 layer.

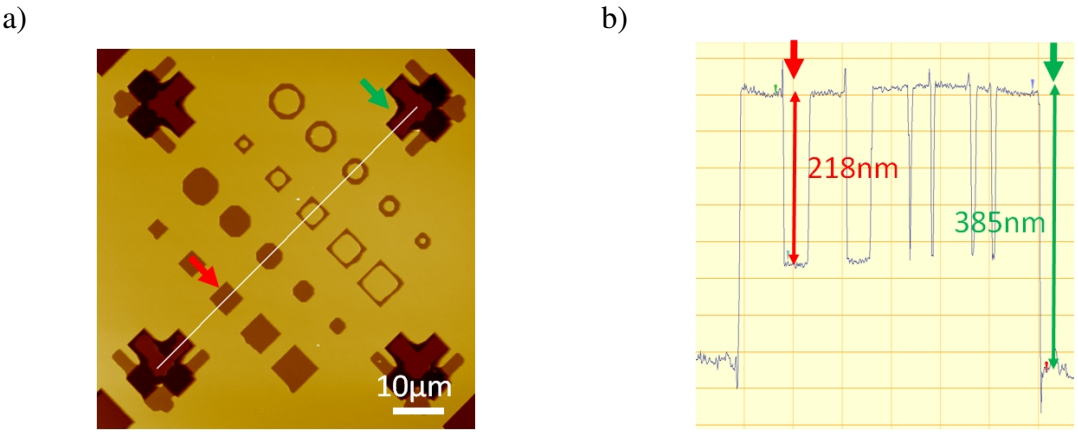

Figure 4.7: a) AFM image of shallow markers. The white line in the image indicates the cross section shown in b). Colored arrows mark the same location in the image and the depth profile. Note that the contrast in AFM images is inverted compared to optical microscopy, because etched Si areas are deeper but also more reflective than the surrounding SiO_2.

4.2.2 Characterization in STM

To test which shallow marker structure would reliably create an atomically flat surface in its center, samples were flash annealed using the standard procedure described in Sec.

3.3.2, but the temperature was kept at 900 °C for 1 min before ramping it down to room temperature. The 200 nm deep markers were found to be scannable without any danger for the STM tip and finding the atomically flat terrace was quickly and reliably possible. Results for four representative structures are shown in Fig. 4.8. It was found that all shallow markers produced atomically flat terraces with a diameter between 200 nm and 300 nm, independent of their shape and size. This demonstrates that the form of the step flow barrier has negligible influence compared to the used annealing time and allows to choose the marker shape to suit the specific contact geometry of the target device.

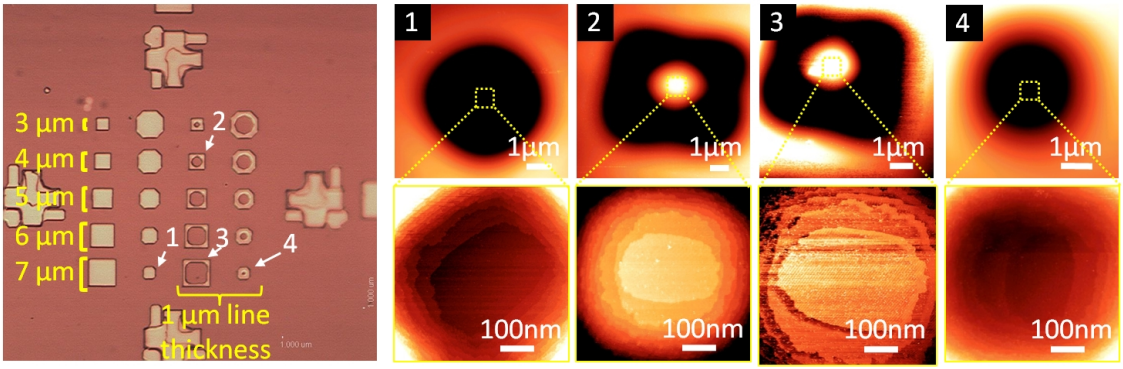

Figure 4.8: Atomically flat terrace creation. Four different step flow barrier structures are displayed, all tested shapes lead to the formation of an atomically flat terrace in their center.

One interesting observation to point out is that structure four in Fig. 4.8 is a pit rather than a hillock, demonstrating that a 1 μm island is too small and will completely disappear as a result of the anneal. In order to create an atomically flat terrace on top of a hillock its diameter therefore has to be larger than 2 μm.

4.2.3 Hydrogen Lithography

To create the hydrogen resist for atomic scale STM fabrication and characterize the controlled depassivation, the Si(100) surface was hydrogen terminated using a commercially available H-cracker and the standard recipe developed by Lyding et al.[89] The cracker consists of a heated tungsten capillary and allows one to thermally crack H_2 into atomic hydrogen. By heating the sample to 375 °C, etching is suppressed and the atomic hydrogen forms a stable monolayer on the silicon surface, as shown in Fig. 4.9 a).

To utilize this hydrogen resist for atomically precise device fabrication it is necessary to controllably desorb H atoms using the STM tip. Shen et al.[109] demonstrated that electrons tunnelling from the tip to the sample at bias voltages above 6.5 V have an energy sufficiently high to excite a Si-H bond, desorbing the H atom. To control the movement of the tip across the surface and pattern arbitrary device areas, MATE scripts were implemented. These scripts are run using a programming language which automates functions

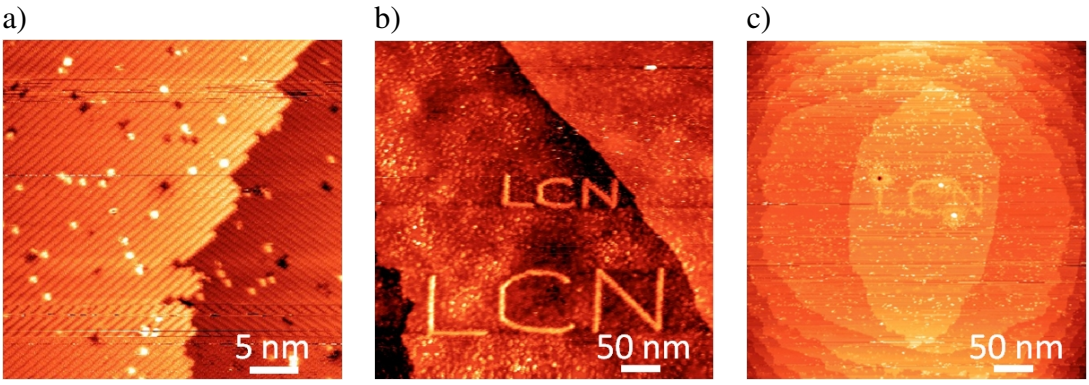

Figure 4.9: Hydrogen lithography. a) H terminated surface. b) H lithography on a normal surface. c) H lithography on an engineered, atomically flat terrace.

of the STM control system. The result of the implemented H-lithography is shown in Fig. 4.9 b) and c) on a normal surface and an artificially created atomically flat terrace respectively.

4.3 Contacting Buried Dopant Layers

We have demonstrated hydrogen lithography on an atomically flat terrace at a well controlled position on the surface, providing the sample necessary for atomically precise STM fabrication. The only process step that must be performed outside of the STM is the electrical contacting of the dopant device after it was created within the STM. Before removing the fabricated device from UHV a 20 nm thick silicon capping layer has to be deposited to prevent the oxidation of the dopant structure. This effectively protects the device but makes contacting it more challenging, as metallic contacts not only need a high alignment accuracy but also a way to penetrate the capping layer to reach the buried dopant structure.

The design of such contacts, as proposed by Fuhrer et al.,[99] is shown in Fig. 4.10. We have already demonstrated that the deep etched marker structure can located by the EBL system even after flashing and can be used for the alignment of metallic contacts. This is depicted in Fig. 4.10 a), where a sketch of the deep marker structure can be seen together with four metallic contacts in pink. In the magnified image of the central area the four contacts can be seen together with a possible layout of an atomic scale device. The STM is used to not only pattern the functional area but also two large contact pads, indicated yellow in Fig. 4.10 a), that overlap with the metallic contacts fabricated in a subsequent step by EBL. If the metallic contacts are simply deposited on the sample surface they will however be separated from the buried dopant structure by the 20 nm silicon capping layer. To avoid this problem, holes have to be etched that allow the metal to penetrate

a)

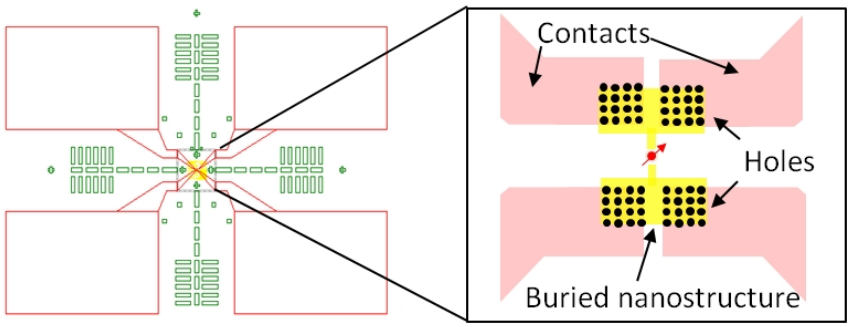

b)

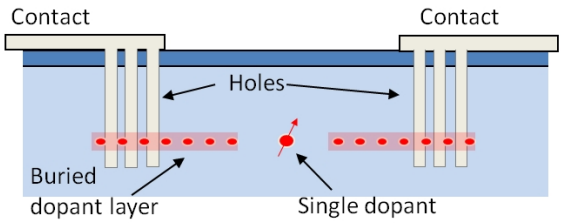

Figure 4.10: Contact design. a) Design of deep markers and contact patches in red, zoom in showing the overlapping regions with the STM fabricated device and the locations of the holes. b) Cross section of hole structure to contact a buried dopant layer.

the capping layer and make direct contact with large dopant patches as indicated in the image. A cross sectional schematic of a contacted device is shown in Fig. 4.10 b). Here the contacts and the etched holes used to contact the dopant layer can be seen.

In a first step the holes are etched, using the process shown in Fig. 4.11 a). EBL is used to pattern 100 nm diameter holes into 300 nm thick photoresist as shown in Fig. 4.11 b), again aligned with high accuracy to the buried dopant structure. Reactive ion etching (RIE) using a Cl_2/N_2 mixed gas plasma is then used to etch this pattern into the silicon to a depth of 50 nm and the resist is subsequently removed in acetone. AFM was used to characterize the results of this process as shown in Fig. 4.11 c). The cross sectional depth profile, acquired at the position indicated by the white dotted line, shows a uniform etch over all holes to the desired depth.

The second step, depositing highly aligned metallic contacts onto the buried nanostructure and into the holes, is shown in Fig. 4.12 a). It should be noted that dimensions are not drawn to scale. EBL is used to pattern the design of the metallic contacts into 300 nm thick resist. After development the sample is HF etched to remove any native oxide and ensure good electrical contacts. A 100 nm thick layer of aluminium is then deposited using thermal evaporation and a standard lift off process. The results of this process are shown in Fig. 4.12 b). The AFM image confirms the high alignment between etched holes and the deposited metallic contacts. The height profile, indicated by the white line in the

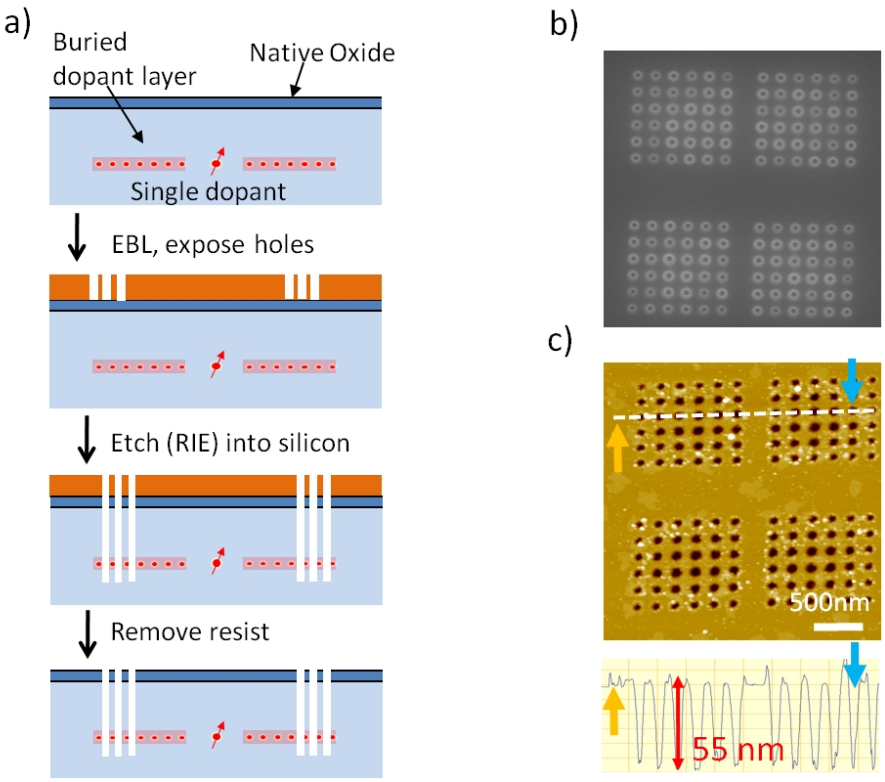

Figure 4.11: a) Fabrication process for the contact hole etching. b) SEM image of developed holes in photoresist. c) AFM image of the silicon surface with the etched holes. The position of the cross sectional depth profile is indicated by the white line, colored arrows indicate the same position in both images.

image, clearly shows the etched holes with a depth of 50 nm, demonstrating that the metal has sunk down into the silicon, penetrating the capping layer and contacting the buried structure. In Fig. 4.12 c) the shape of a possible buried dopant structure is indicated in red. A device fabricated in the STM would consist of an active area, here just sketched as single dopant in the center, with two leads and two large contact patches. It can be seen that each of these patches would be contacted by two sets of holes, allowing for a four terminal measurement.

The test sample used for this experiment had a layer of bismuth underneath the surface, ion implanted to a concentration of $1\text{x}10^{18}$ cm^{-3} and subsequently annealed to 600 °C for 30 min, followed by an anneal to 900 °C for 1 min. Even though this is not a delta doped layer, which would be created when using STM fabrication, it allowed us to measure the contact resistances at low temperatures and test the contacting of buried dopant structures. Electrical transport measurements were performed using an Oxford MagLab, equipped with a helium flow cryostat and allowing electrical transport measurements between temperatures of 2 K and 300 K. The contacts formed between the metallic leads and the implanted dopant layer were found to be ohmic with very low contact resistance between 100 Ω and 2 kΩ in the whole temperature range. This compares well to similar

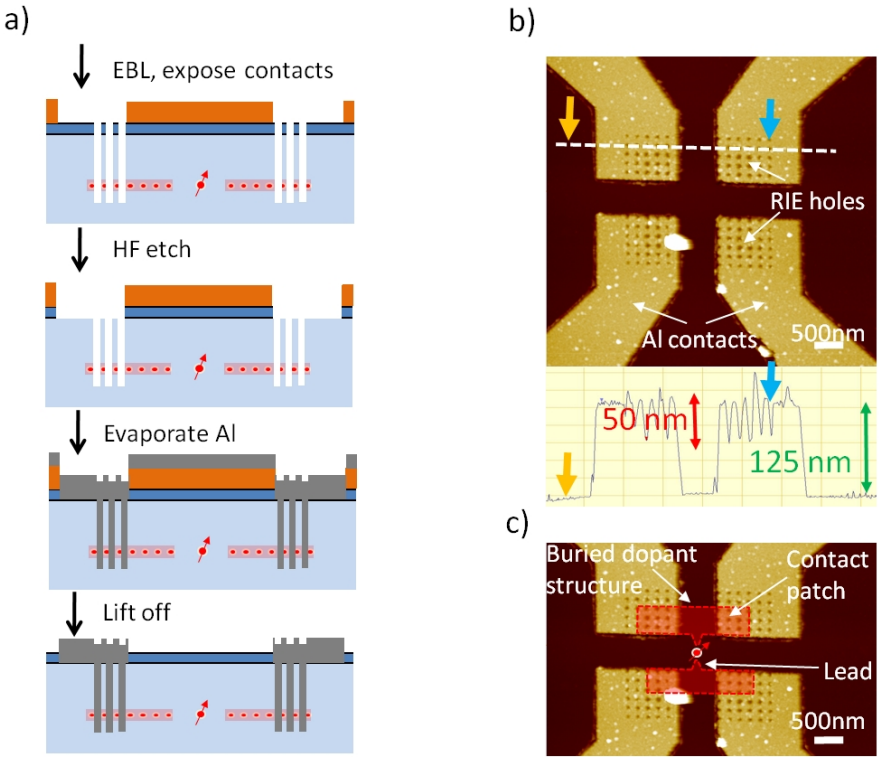

Figure 4.12: a) Fabrication process for the contact deposition. b) AFM image of the metal contacts. The position of the cross sectional height profile is indicated by the white line, colored arrows indicate the same position in both images. c) Sketch indicating the location of a possible buried dopant structure.

contacts described in literature with resistances around 10 kΩ.[99]

Using the four contact design it is furthermore possible to measure the Hall resistance in a van der Pauw geometry[110] to calculate the implanted carrier density. Simplifications have to be made as the van der Pauw method assumes a layer of homogenous carrier density with uniform thickness. In our case the implantation process has created a subsurface layer of Bi dopants with a nominal thickness of 200 nm across the whole sample. Due to the Gaussian distribution of ion implanted species around the nominal implantation depth it is however assumed that the layer is not perfectly confined to its nominal thickness and is further broadened by the subsequent anneal. Nevertheless, it should allow us to test if the measured Hall resistance is the correct order of magnitude, indicating the successful contacting of the implanted region. To calculate the Hall resistance Eq. 4.1 can be used, assuming the four contacts are perfectly symmetric.

$$R_H = \frac{V_{24}}{I_{13}} = -\frac{1}{d\eta e}B \tag{4.1}$$

In this equation η indicates the charge carrier density, d the sheet thickness and I_{xy}/V_{xy} the measured current/voltage between contacts x and y as indicated in Fig. 4.13 a). If contacts are slightly asymmetric, part of the measured Hall voltage might actually arise

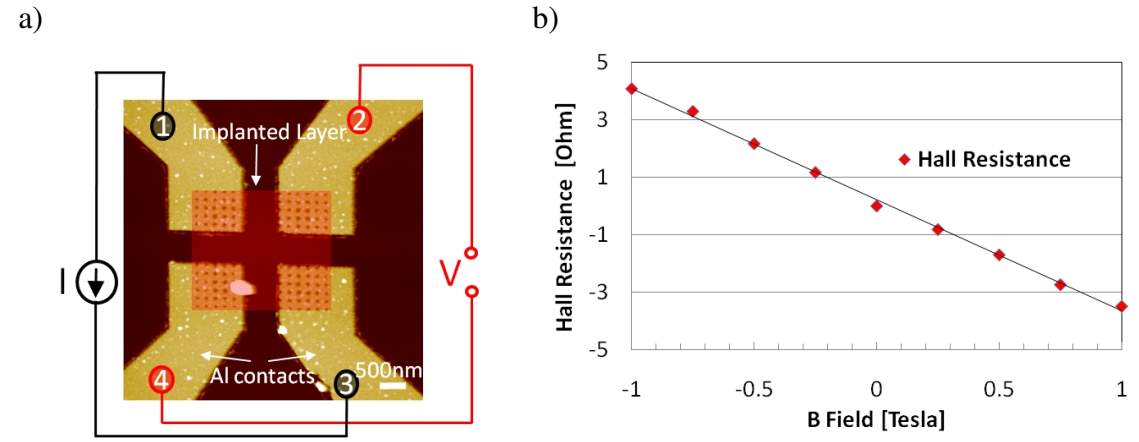

Figure 4.13: Hall resistance measurement. a) Measurement configuration. b) Hall resistance measured as a function of magnetic field.

due to the induced potential difference of the contacts used to generate the measurement current and not purely due to deflection of carriers in the magnetic field. This offset would however not change with the direction of the magnetic field and can therefore be eliminated by calculating the Hall resistance as the average of the values at equal positive and negative magnetic fields. The measured Hall resistance is shown in Fig. 4.13 b) and a carrier density of $8\text{x}10^{18}$ cm^{-3} was calculated assuming a layer thickness of 200 nm. This compares reasonably well with the implanted carrier density of $1\text{x}10^{18}$ cm^{-3} but also shows that the layer is most likely significantly thicker than the assumed 200 nm.

The results presented here confirm the fabrication of metallic leads with very high alignment accuracy and excellent contact resistances. Together with the Hall measurements this demonstrates that buried dopant structures can be successfully contacted and characterized, providing the complete cleanroom fabrication capability for the fabrication of atomic scale devices in the future.

5 Cross Sectional STM on Silicon

Cross sectional scanning tunnelling microscopy (XSTM) is ideally suited to identify and characterize individual dopant atoms in their intrinsic silicon crystal site as no thermal annealing step is required, inhibiting dopant diffusion during the surface preparation process. As described in Sec. 2.3, only phosphorus has been previously identified in the Si(111)-2x1 surface and it is therefore important to establish a good understanding of the clean surface without any dopants first, to make sure single donor atoms can be distinguished from randomly occurring surface defects. To do so, very low phosphorus doped wafers were studied as described in Sec. 3.3.1. The doping density of 1×10^{15} cm^{-3} leads to an expected concentration of less than 1 donor per square micrometer in the surface and it is therefore very unlikely to encounter P dopants in the STM measurement.

In the course of characterizing the cleaved Si(111)-2x1 surface and its intrinsic defects we have further gained a deep understanding of the surface dynamics and characteristics of domain boundaries. As described in Sec. 2.2.4, several interesting observations were reported regarding anti phase boundaries (APBs) in Si(111)-2x1, including fast movement and a characteristic local contrast in their vicinity, presumably electronic in nature. Based on acquired low temperature scanning tunnelling spectroscopy data we were able to identify strain as the driving mechanism behind all these observations and propose how this specific defect could be used as a model system to study and control the influence of strain on single dopants at the atomic scale, as it will be described in the second half of this chapter.

5.1 Macroscopic Cleaving Structure

Cross sectional samples were prepared as described in Sec. 3.3.3 and loaded into the LT STM at liquid nitrogen temperature (78 K). When approaching the tip to the cross section of the cleaved wafer, several characteristic regions can be identified as shown in Fig 5.1, similar to reported patterns in GaAs.[111] In area one, where the wafer is strained by the clamping of the sample holder, the fracture is very rough. The tip was kept well away from this area and approached further away in the free standing part of the sample.

The surface away from the clamps can be divided in two main areas. The sample was cleaved along the direction of the red arrow indicated in Fig 5.1 and it can be seen that

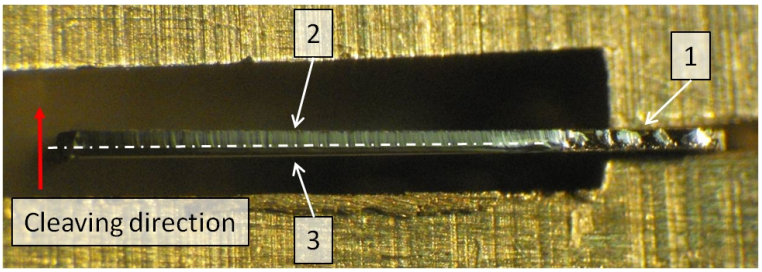

Figure 5.1: Macroscopic cleaving structure, three different regions can be distinguished. 1: Clamped part, very rough. 2: Structured surface at the back of the cleave. 3: Mirror flat surface at the beginning of the fracture.

the fracture at first produced a mirror flat area which becomes more structured at the back of the sample. STM measurements of area two and three are shown in Fig. 5.2. It was found that the surface is atomically flat in both areas but the step density is significantly increased in region two.

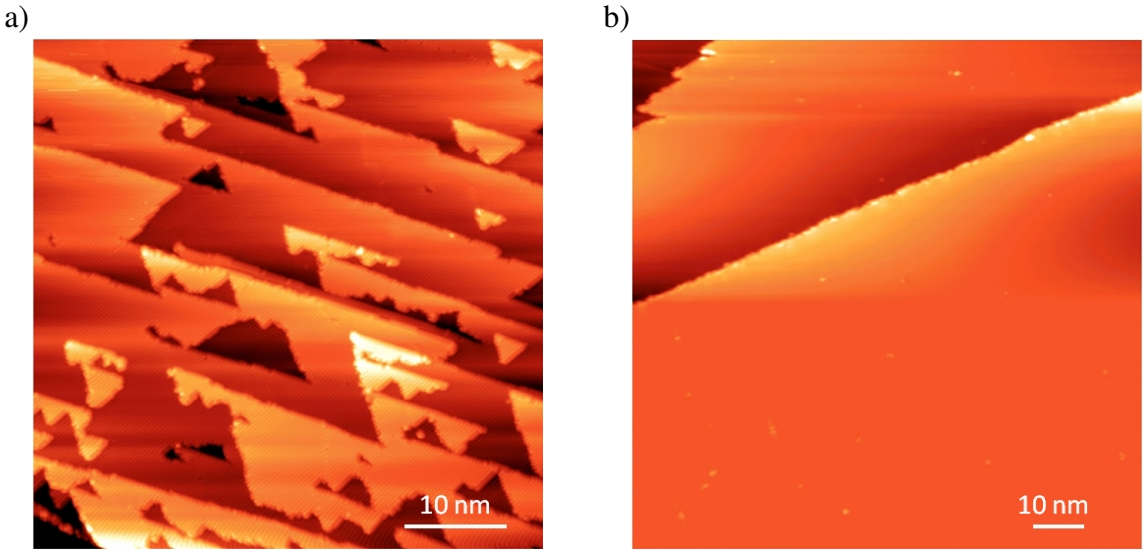

Figure 5.2: STM Cleaving Structure. a) STM image of the surface in area 2. b) STM image of the surface in area 3.

In region two the average terrace width was on the order of 10-20 nm as shown in Fig. 5.2 a). In the mirror flat part of the sample, area three, the terraces were found to be significantly larger on the order of 100 nm as shown in Fig. 5.2 b). This terrace width is comparable to reported values in the literature of 10 nm to 150 nm [74, 112] and sufficiently large to allow the study of features in the undisturbed surface far away from step edges.

5.2 STM on non Degenerate Semiconductors at Reduced Temperatures

To obtain high quality STS data, the measurements were performed in the LT STM operated at liquid nitrogen temperature. Because the sample is only lightly doped and non degenerate, the carrier density will strongly vary with temperature. For shallow dopants such as phosphorus, carrier freeze out has to be considered below 100 K and can be calculated according to Eq. 5.1 and Eq. 5.2.

$$N_C exp\left(-\frac{E_C - E_F}{kT}\right) = \frac{N_D}{1+2exp((E_F - E_D)/kT)} + N_V exp\left(\frac{E_V - E_F}{kT}\right) \tag{5.1}$$

$$N_D^+ = N_D\left[1 - \frac{1}{1+\frac{1}{2}exp((E_D - E_F)/kT)}\right] \tag{5.2}$$

The Fermi energy can be calculated by solving Eq. 5.1 where N_C and N_V are the effective number of states in the conduction and valence band respectively whereas N_D stands for the dopant concentration. E_C and E_D stand for the energy level of the conduction band and the donors respectively, whereas E_F denotes the Fermi level. If the Fermi energy is known, Eq. 5.2 gives the concentration of ionized donors and therefore also the electron density due to the doping.

The activation energy of 45 meV for phosphorus in silicon[113] leaves around 70% of the dopants ionized at 78 K, leading to an electron density of 7×10^{14} cm^{-3}. The intrinsic carrier concentration of silicon will add to the available free carriers and can be calculated according to Eq. 5.3. At 78 K there are effectively no intrinsic carriers and the only mobile charges are the electrons of the ionized dopants.

$$n_i = \sqrt{N_C N_V} exp\left(\frac{-E_g}{2kT}\right) \tag{5.3}$$

To establish a stable tunnelling junction for STM experiments a potential difference between the tip and the sample has to be induced and therefore mobile charge carriers are required as illustrated in Fig. 2.5 a). We have calculated that at 78 K electrons but no holes are available and a stable tunnelling contact can therefore only be created when the sample is negatively biased. With a positive bias, a hole accumulation in the sample would be required to establish a potential difference but the only positive charges in the sample are the ionized dopant atoms which cannot move and are therefore unable to effectively compensate the electric field between tip and sample.

The experiment confirmed this as topography images could only be acquired measuring at negative bias whereas in positive bias the tip crashed into the surface. Nevertheless it

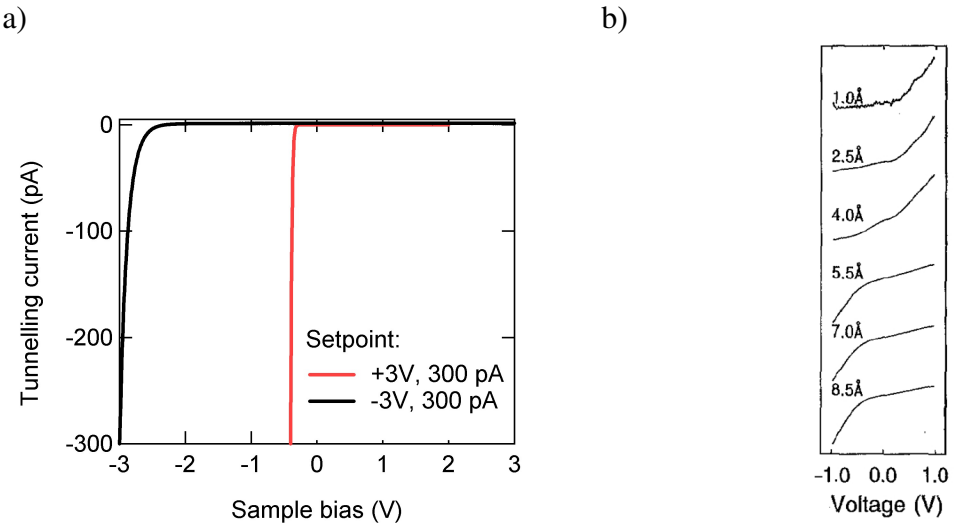

Figure 5.3: Spectroscopy at 78 K a) STS acquired with a positive and negative setpoint voltage. b) STS at different tip sample distances, contact assumed to be formed at 6 $\AA$, image from Hasegawa et al.[114]

was possible to reach the current setpoint even at positive voltages. As discussed above, this is not expected from the model we used so far to explain the formation of the tunnelling current and therefore more measurements were performed to clarify this behavior.

STS data acquired at different setpoint voltage polarities are shown in Fig. 5.3 a). It can be seen that both spectra exhibit strong rectifying behavior but have a very different onset voltage. This can be explained considering the transition from a tunnelling regime to a point contact regime, the latter resulting in a Schottky diode. The tip induced band bending increases with decreasing tip sample distance because more of the electric field of the tip will decay within the semiconductor. The maximum tip induced band bending is reached at the ideal Schottky barrier limit when the tip touches the sample and all of the electric field decays within the semiconductor. At this point the tunnelling description of the tip sample junction breaks down because electrons can flow between tip and sample and the Fermi levels will align, forming a Schottky diode. The operating principles of a Schottky diode are shown in Fig. 5.4 for the equilibrium, forward and reverse bias conditions.

It is assumed that under positive bias the tip touches the sample due to the lack of free positively charged carriers and forms a Schottky diode, the STM regulating off the leakage current. In this situation scanning is not possible because moving the tip dislocates atoms from its surrounding. To forward bias the Schottky diode into a conducting mode the applied voltage has to overcome the built in potential Ψ_{bi} that can be calculated as $\Psi_{bi} = \Phi_m - (\Phi_s + E_f)$ if surface and interface states are neglected. In this equation Φ_m and Φ_s stand for the metal and semiconductor electron affinities, assumed as 4.55 eV for tungsten and 4.05 eV for silicon. E_f is the Fermi level in the semiconductor, calculated according

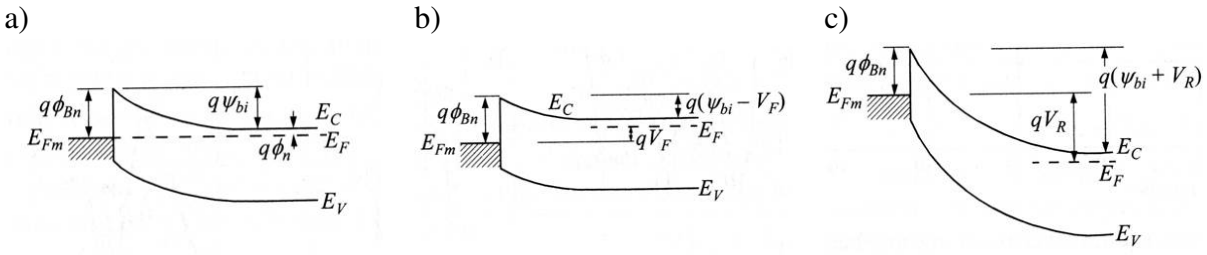

Figure 5.4: Schottky diode, image from Sze[113]. a) Equilibrium. b) Forward bias. c) Reverse bias.

to Eq. 5.1. This leads to a calculated turn on voltage of -0.45 V, in reasonable agreement with the observed value of -0.4 V. The difference in these values is most likely arising from the surface states of the Si(111)-2x1 reconstruction that will alter the position of the Fermi level.

The crossover between a tunnelling and Schottky contact has previously been investigated on metals[115, 116] and on hydrogen terminated n-Si(111) 7x7 by Avouris and Hasegawa[114, 117] as shown in Fig. 5.3 b). They acquired STS data at different tip sample separations by shifting the tip towards the surface after opening the feedback loop. It can be seen that the spectra show current flowing for both bias values up to a distance of 4 $\AA$ and then become more rectifying with current only flowing at negative bias. They assume that contact was established at 6 $\AA$ and attribute the rectifying behavior to the formation of an n-type Schottky diode.

When regulating the current at a negative bias we expect a tunnelling junction to form, which was confirmed by the fact that we could obtain topographic images. Nevertheless we still see a strong rectifying behavior and observe a turn on voltage that has strongly increased to below -1 V. It is assumed that we are operating in a regime of very strong band bending due to the small carrier density and the consequently short tip sample distance. When a negative bias is applied, the bands bend downwards but because there is no physical contact, electrons can not travel from the semiconductor to the metal once Ψ_{bi} is compensated, they have to tunnel through the vacuum gap. To do so they need empty density of states on the tip side. These become only available once the tip Fermi level drops below the semiconductor conduction band and therefore at a significantly higher negative voltage compared to the contact regime. A similar argument can be used to explain the fact that almost no current is measured in the positive bias side of the spectra. Because there are no free holes in the sample a bias can not be established and the electric field of the tip will extend far into the semiconductor, the bands closely following the tip Fermi level. Tunnelling into the empty states of silicon is therefore inhibited because it is not possible to sufficiently shift the tip Fermi energy with respect to the sample band structure.

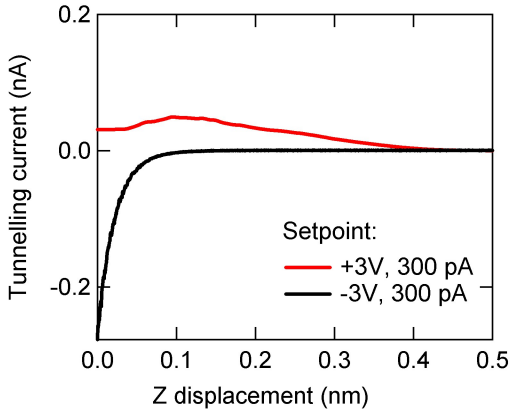

Figure 5.5: Z Spectroscopy of Si(111)-2x1 at 78 K. Spectra were recorded with 3 V and -3 V bias while retracting the tip 0.5 nm. For both curves the tip was stabilized above the surface at a current setpoint of 300 pA and a bias of -3 V.

To verify our interpretation about tunnelling and contact regimes at different bias values we have measured the z dependence of the current as described in Sec. 2.1.5. For a tunnel junction we expect an exponential decay with increasing tip sample separation as indeed observed for the negative bias trace shown in Fig. 5.5. To obtain reliable z spectroscopy for positive bias values without crashing the tip we slightly modified the standard procedure to acquire data. The tip was stabilized above the surface at negative bias before the feedback was opened and subsequently the bias switched to positive voltage. The z ramp was then executed recording the current, therefore not retracting the tip from a point contact but from the exact same distance above the surface as for the measurement in negative bias.

In Fig. 5.5 it can be seen that the positive voltage curve does not resemble an exponential decay as the current initially increases while retracting the tip. This is a strong indicator that no stable tunnel junction can be formed since further approaching the tip to reach the current setpoint would decrease the current and the tip would crash into the surface.

This behavior could be explained following the argument of Weimer et al.[118] They investigated the behavior of the tip sample interaction as a function of separation. When retracting the tip from the surface, two different processes take place at the same time. The tunnel current exponentially decreases when increasing the distance, whereas the surface potential in the semiconductor decreases due to decreased tip induced band bending, and therefore exponentially increases the amount of carriers available for tunnelling. Usually the number of carriers is not the limiting factor but rather the available density of states in which to tunnel. In this special case it may on the other hand be that the current is carrier limited and therefore it initially increases when more carriers become available and then decreases due to the inhibited tunnelling probability.

A different explanation may be the formation of a covalent bond between the tip and the surface dangling bonds which has shown to lead to a drop in conductance when approaching the surface[119] due to a local change in the electronic structure. To conclusively determine the exact mechanism of this behavior is however beyond the scope of this work.

5.3 Temperature Dependent STS

In order to perform STM measurements on the Si(111)-2x1 surface we need to be able to establish a tunnel contact in both bias polarities and therefore have to increase the hole carrier concentration. This was done by heating the sample to increase the intrinsic carrier concentration. Fig. 5.6 shows STS data acquired at various different temperatures, with the I/V traces displayed in Fig. 5.6 a). The current at positive bias is clearly seen to increase with temperature due to the decreased tip induced band bending. At temperatures above 160 K it was possible to establish a stable tunnel junction in both bias polarities and at 200 K the spectra look symmetric and comparable to spectra for Si(111)-2x1 reported in literature as discussed in Sec. 2.2.3.1. Measurements on this sample were therefore always conducted at 200 K in order to get high quality STS data without being limited by free carrier availability.

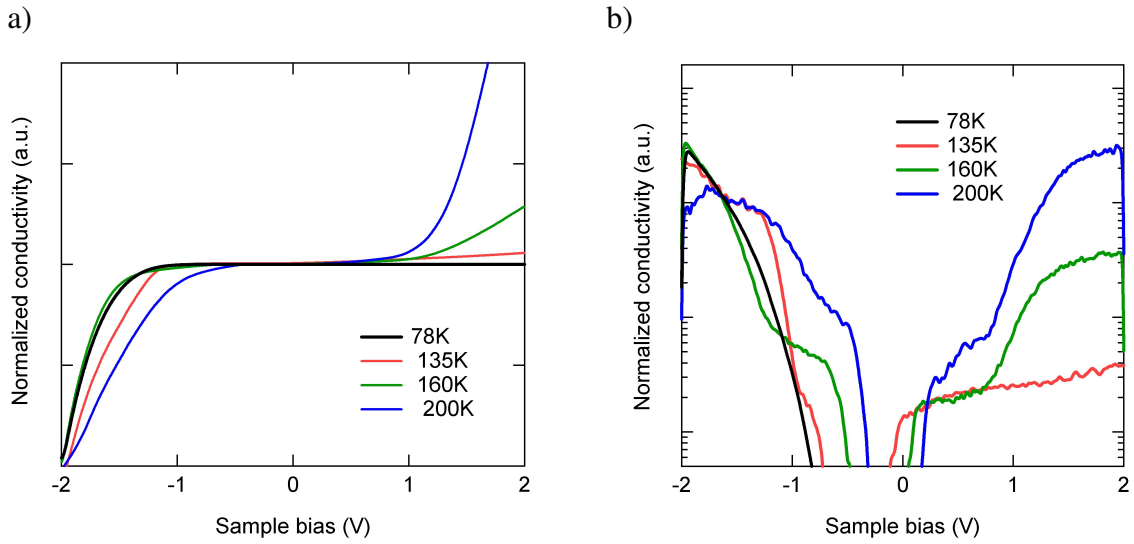

Figure 5.6: Temperature dependent STS recorded at 78 K, 130 K, 160 K and 200 K. a) I/V spectra. b) Normalized dI/dV conductance measurement.

In Fig. 5.6 b) dI/dV traces are shown of the spectroscopy at 78 K, 135 K, 160 K and 200 K. Again it can be seen that the empty states tunnelling is increased with increasing temperature, explained by the decrease in tip induced band bending with increasing carrier concentration. A second interesting feature to note is the shift of the bandgap to higher voltage, indicating a decrease of the Fermi energy. This is in qualitative agreement

with carrier freeze-out in n-type semiconductors. Using equation 5.1 we can calculate the shift in Fermi energy between 135 K and 200 K to be 60 mV. This is considerably smaller than the measured shift of 500 mV, suggesting that another effect must be dominating. A possible explanation may be the temperature dependence of the Fermi level pinning at the surface. The calculated Fermi position at 300 K in the bulk is 0.85 eV above the valence band but experiments have shown that it is actually pinned at 0.4 eV directly at the surface.[71] The temperature dependence of the Fermi level at the surface may therefore be considerably different from the bulk and explain the increased shift we observed experimentally. This will be discussed in more detail in Sec. 6.4.1

5.4 Voltage Dependent Topography

Constant current STM images contain convoluted information about the electronic and topographic structure of the sample surface as discussed in Sec. 2.3. Depending on the sample bias polarity either filled or empty states are imaged, located mainly at the up/down atom respectively for the Si(111)-2x1 surface. To correlate the measured constant current topography with the underlying crystal lattice, Garleff et al.[56] compared the acquired data with simulations of the LDOS. We find that our measurements show a very similar topography and therefore interpret the measured corrugation accordingly.

In Fig. 5.7 the voltage dependent topography can be seen for selected bias values. The position of the underlying lattice is indicated in the images according to the current interpretation found in literature.[56, 120] The images were all acquired in constant current mode at a current setpoint of 50 pA with the indicated bias value.

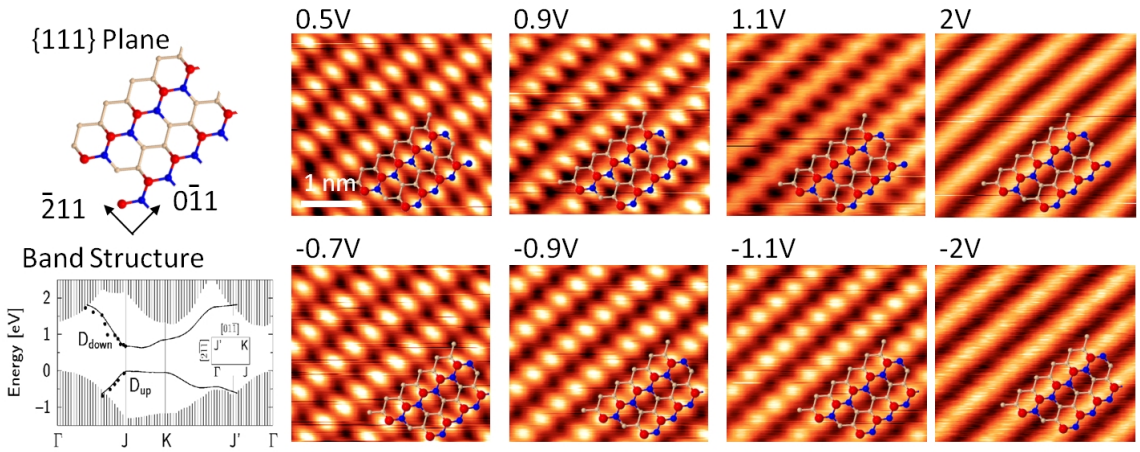

Figure 5.7: Voltage dependent imaging at 200 K, current setpoint of 50 pA. The position of the underlying crystal structure is indicated according to literature. Band structure by Rohlfing et al.[54]

At low positive bias the empty surface state is the only LDOS available to tunnel into

as seen in the band structure in Fig. 5.7. This state is localized at the down atom as discussed in Sec. 2.2.2. The observed corrugation therefore coincides with the down atom of the π-bonded chains. Upon increasing the bias, bulk states start to contribute to the measured tunnelling current and the topographic height of the atoms becomes more important, therefore shifting the contrast towards the up buckled atom. At 1.1 V a zigzag pattern is observable arising from equal contributions of the up and down atoms in the π-bonded chains. Above this value the corrugation along the $[0\bar{1}1]$ direction decreases and the topography of the π-bonded chains dominates the image, the contrast maximum being on the up atom.

At low negative voltages the filled surface state dominates the tunnelling current. As previously discussed, the electrons are mainly located at the up buckled atom and, because it is also sticking out furthest from the surface, the contrast is centered on the up atom at all negative bias voltages. Again it can be seen that the corrugation along the π-bonded chains decreases with increasing bias because the bulk states start to dominate the tunnel current.

It can be seen that constant current images recorded at low bias show rows along the $[\bar{2}11]$ direction whereas at higher bias this changes to the $[0\bar{1}1]$ direction along the pi bonded chains, regardless of the polarity. This can be explained taking the wave vectors of the states involved in the tunnelling into account. At low biases the density of states contributing to the tunnel current are the surface states at the *JK* point as shown in Fig. 2.14 a). These states are modulated along the π-bonded chains and slightly dispersive along the $[\bar{2}11]$ direction. This also applies for negative bias because the Fermi level is pinned within the empty surface state band and some of it is therefore extending below the Fermi energy. These states have a wave vector $k_{\parallel}$ parallel to the surface which decays quickly into the vacuum as measured by Stroscio et al.[72] and discussed in Sec. 2.2.3.1. Upon increasing the bias bulk states with wave vectors $k_{\perp}$ perpendicular to the surface become available for tunnelling and dominate the current, leading to the observation of the π-bonded chains.

The exact bias voltages at which the corrugations in Fig. 5.7 can be observed are depending on tip induced band bending and therefore on the doping level of the measured sample, the current setpoint and the measurement temperature. Because Si(111)-2x1 has a pinned Fermi energy at the surface these variations are nevertheless expected to be small and the correlation between the measured contrast and the underlying crystal structure, discussed above, should be applicable for all samples.

5.5 Scanning Tunnelling Spectroscopy

Scanning tunnelling spectroscopy data of the clean surface were acquired as described in Sec. 2.1.3. Usually one hundred spectra are recorded and averaged to reduce the influence of vibrational and electrical noise. Spectra are then smoothed over 20 points using a gliding median algorithm and differentiated numerically, resulting in an energy resolution of 80 mV.

A typical spectrum for the bare Si(111)-2x1 surface at 200 K is shown in Fig. 5.8 b). It agrees very well with other results published in literature [56, 72, 73, 120] and shows two shoulders at low bias values and two peaks at higher bias. In Fig. 5.8 c) the same spectrum is shown but normalized to (dI/dV)/(I/V). As discussed in Sec. 2.1.3 it can be seen that this normalization introduces band edge artifacts and we therefore usually do not use it for analyzing data.

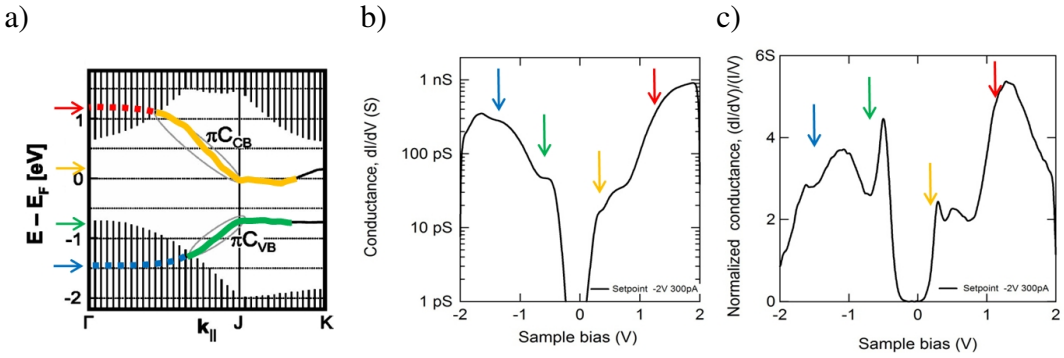

Figure 5.8: STS on Si(111)-2x1 at 200 K. Colored arrows indicate the same energy in all three images. a) Theoretically calculated band structure from Garleff et al.[56] b) STS acquired at a setpoint of 300 pA at -2 V. Plotted as dI/dV on a logarithmic scale. c) STS acquired at a setpoint of 300 pA at -2 V normalized as (dI/dV)/(I/V).

To visualize the origins of the the observed peaks the calculated band structure from Rohlfing et al.[56] is plotted again in Fig. 5.8 a). The Fermi level has been shifted to match the experimentally observed pinning at 0.4 V.[71] The two surface states are indicated and have been extended into the bulk states up to the Γ point according to Garleff et al.[120] As indicated by the different colors, the two shoulders at -0.6 V and +0.3 V can be linked to the two surface states whereas the peaks at -1.4 V and 1.6 V are attributed to tunnelling into the surface resonances. It can be seen that especially the peaks at high bias values seem to have a slightly different position depending on the chosen normalization of the data, illustrating the difficulty in comparing theoretically calculated and measured LDOS. Nevertheless, the experiment is in good qualitative agreement with theory and demonstrates the capability of the STM to resolve the LDOS on the Si(111)-2x1 surface.

5.6 Anti Phase Boundaries - A Model System for Controlling Strain in Silicon at the Atomic Scale

A frequently observed defect in the Si(111)-2x1 surface reconstruction is the anti phase boundary (APB). Upon cleaving, the formation of the Si(111)-2x1 reconstruction transforms the 6-fold rings of the silicon crystal to alternating rings of 5 and 7 atoms at the surface, as described in Sec. 2.2.2. The position of the seven fold ring with respect to the underlying crystal is arbitrary and most likely determined by the atomic scale cleavage process. APBs form when two domains meet that have their π-bonded chains shifted by half a unit cell in the $[\bar{2}11]$ direction. They are fundamental for many properties of the Si(111)-2x1 surface as they have been identified as the starting point of thermally excited changes in the surface reconstruction and as a nucleation site for epitaxial growth.[73] Furthermore, many interesting properties have been observed such as a very high mobility and a strong electronic contrast. However, despite the frequent observation of this defect, its central role in defining the properties of the Si(111)-2x1 surface and the various unexplained characteristics, very little is known about it. Here we present a systematic study of anti phase boundaries in the Si(111)-2x1 surface using scanning tunnelling microscopy measurements, laterally resolved scanning tunnelling spectroscopy and density functional theory (DFT). Experiments were performed in the LT-STM at 200 K on low n-type doped cleaved silicon.

5.6.1 Structure

In order to study APBs we have performed experiments in the area of the cross section with a high step density as described in Sec. 5.1. We found that the number of APBs is significantly higher in areas with a high step density whereas few APBs are found on large terraces. As the π-bonded chains can be oriented in any of the three equivalent $\langle 01\bar{1}\rangle$ directions, APBs are showing the same symmetry and we therefore characterize the different structures we observe with respect towards the π-bonded chain orientation.

We studied over sixty anti phase boundaries on different samples and all of them can be classified as one of the three different reconstructions shown in Fig. 5.9 which we denote as APB-I, APB-II and APB-III. Boundaries were sometimes found to change from one reconstruction to another during their course across the surface but always terminate in a step edge. APB-I shown in Fig. 5.9 a) was the most common, accounting for approximately 80% of the observed boundaries. It is oriented along the $[\bar{1}10]$ direction following the hexagonal symmetry of the underlying silicon crystal. APB-II in Fig. 5.9. b) is very similar to APB-I as it follows the $[\bar{1}01]$ direction which is equivalent to the $[\bar{1}10]$ in bulk silicon. On the surface it nevertheless has to be treated as a separate reconstruction since

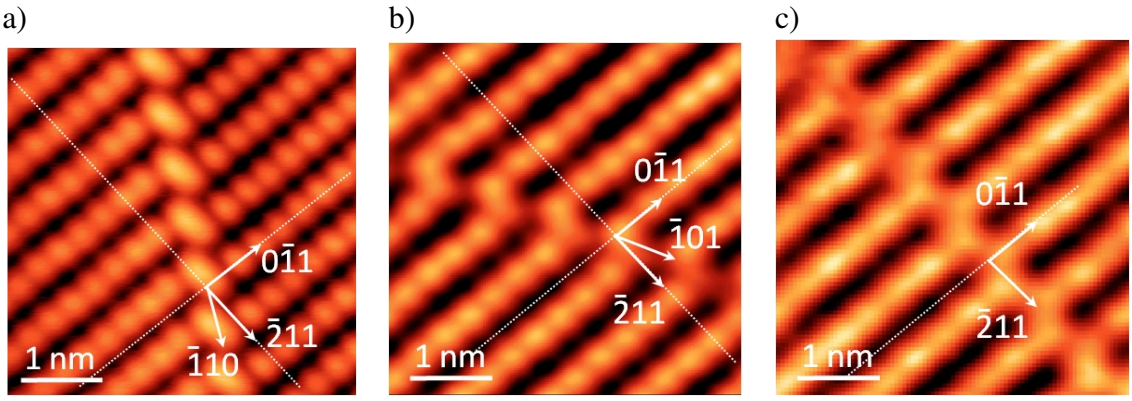

Figure 5.9: STM constant current topography of different APB orientations. a) APB-I. b) APB-II. c) APB-III.

the buckling of the π-bonded chains lifts the symmetry in the [$\bar{2}$11] direction and therefore the atomic scale structure of the two APBs is expected to differ slightly. Its occurence was less frequent as only little over 10% of all boundaries were found in this orientation. APB-III shown in Fig. 5.9. c) has an angle of 90° towards the π-bonded chains following the [$\bar{2}$11] direction and also accounts for only slightly over 10% of all boundaries.

As discussed in Sec. 2.2.2 the buckling of the Si(111)-2x1 surface is very difficult to determine experimentally and even though positive buckling is expected for this doping level,[68] the occurrence of negative buckling cannot be excluded[69] due to the very low energy difference between the two reconstructions.[67]

To determine the exact atomic structure of the APBs, a change of buckling over the boundary therefore has to be considered. The observed shift of the π-bonded chains in the [$\bar{2}$11] direction is too large to arise purely due to a change of buckling and we therefore only consider structures with staggered π-bonded chains. To check if the buckling changes across a boundary together with the phase of the π-bonded chains we test whether the up atoms are in phase on both sides as suggested by Hirayama et al.[76] and shown in Fig. 2.19. Due to the underlying crystal structure a boundary with a change in buckling across it has the up atoms aligned whereas a boundary between domains of the same buckling has the up atoms out of phase. In Fig. 5.9 we have indicated the [$\bar{2}$11] direction in APB-I and APB-II with a white line and it can be clearly seen that the measured up atoms are out of phase. The same test was done for all measured APBs using different voltage and current setpoints and we have never observed a change of buckling. For APB-III this test is not applicable but based on the fact that we have not measured a change in buckling for all other boundaries we assume that our surface is always positively buckled, in agreement with Nie et al.[68]

Based on the measured topography data we have developed a model for the atomic structure of the APBs in the Si(111)-2x1 reconstruction as shown in Fig. 5.10 for APB-I

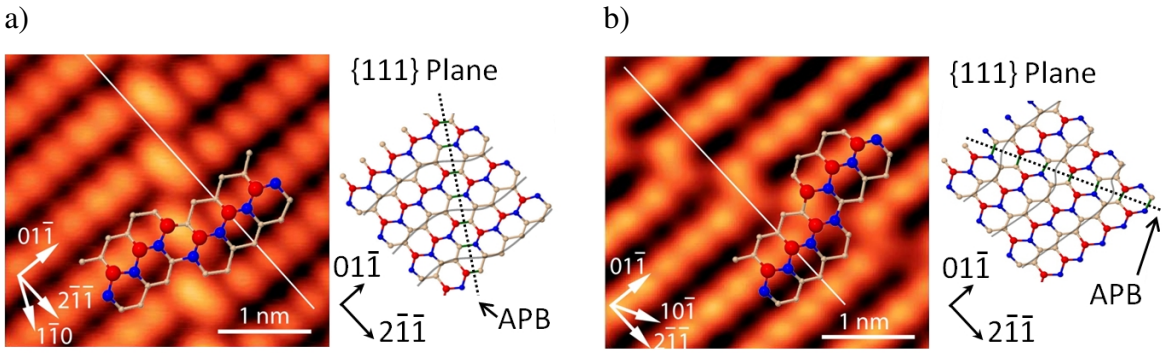

Figure 5.10: Atomic structure model. a) APB-I. b) APB-II.

and APB-II. The structure of APB-I is similar to the structure suggested by Hirayama et al.[76] for phase boundaries observed in germanium. It can be seen that the structure is asymmetric, as π-bonded chains from the bottom left end in an up buckled atom whereas π-bonded chains from the top right end in a down buckled atom. The boundary is indicated in the structure model by the black dotted line and the structural overlay of the model and the STM measurement shows excellent agreement. The structure of APB-II shown in Fig. 5.10 b) is the exact copy of APB-I but mirrored at the $\{2\bar{1}\bar{1}\}$ plane. π-bonded chains from the bottom left therefore now end in a down buckled atom whereas π-bonded chains from the top right domain end in an up buckled atom.

In the model it can be seen that due to the asymmetry in the structure the π-bonded chains kink to the right for APB-I and to the left for APB-II when moving along the $[0\bar{1}1]$ direction. This is indicated in the model by the grey lines, added as a guide to the eye, and in excellent agreement with the measurement.

For the structure of APB-III we found two different possible models as shown in Fig. 5.11. To achieve an APB along the $[\bar{1}10]$ or $[\bar{1}01]$ direction we have shown that the π-bonded chains alternatingly terminate in an up buckled or down buckled atom at the boundary. To form a boundary that propagates along the $[2\bar{1}\bar{1}]$ direction, all the π-bonded chains end in either an up buckled atom as shown in Fig. 5.11 a) or a down buckled atom as shown in Fig. 5.11 b). To distinguish between these two models we name them APB-IIIup and APB-IIIdown respectively. From the topography image it looks as if this specific boundary has π-bonded chains terminating in up buckled atoms but the image quality is not high enough to definitively discard one of the two models.

In order to check which model for APB-III is more likely and to validate the model for APB-I and APB-II we used density functional theory (DFT) calculations to determine the total energy of the different structures. DFT calculations, performed by Greg Lever,[121] of the APB structures were performed using VASP [122] with the PW91 GGA [123] functional. A ten layer Si slab (320 atoms), with the top eight layers free to move and the bottom terminated with H (32 atoms), was used. Cells had to contain several APBs to satisfy

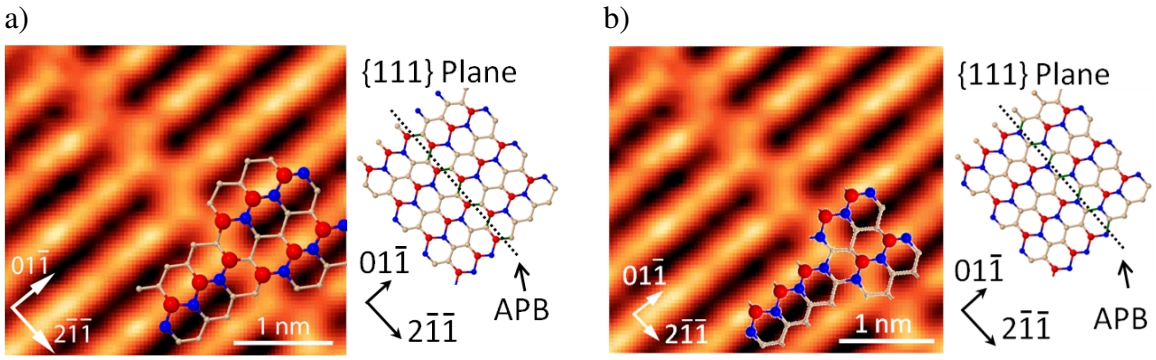

Figure 5.11: Atomic structure model. a) APB-IIIup . b) APB-IIIdown.

the periodic boundary conditions. All forces were converged to within 0.03 eV/Å and total energies are normalized as energy per boundary between two individual π-bonded chains. The results of the calculations are shown in table 5.1. In order to validate the calculations on a simple structure, the difference between positive and negative buckling was evaluated and found to be very small, in good agreement with literature.[67]

Table 5.1: Total energy calculations of anti phase boundaries.

Geometry	Total energy	Normalized
Bare surface, positive buckling	0.00 eV	0 eV/surface atom
Bare surface, negative buckling	0.05 eV	0.00208 eV/surface atom
APB-I	2.42 eV	0.30 eV/boundary
APB-II	2.72 eV	0.34 eV/boundary
APB-IIIup/down	1.36 eV	0.34 eV/boundary
APB-IIIdown/down	1.58 eV	0.39 eV/boundary

For APB-I and APB-II we find an energy of 0.30 eV and 0.34 eV respectively, which shows that the boundary is an unfavorable configuration compared to the clean surface. It nevertheless forms a stable energy minimum since all forces were able to converge to below 0.03 eV/Å. The energy of APB-IIIup could not be determined because while one of the two boundaries in the cell converged to the proposed APB-IIIup structure shown in Fig. 5.11 a), the other APB converged to APB-IIIdown. Because the energy of a unit cell consisting of an APB-IIIup and an APB-IIIdown boundary was lower than a unit cell with two APB-IIIdown boundaries it is nevertheless likely that APB -IIIup is energetically more stable. It is unclear why the cell with two APB-IIIup structures would not converge, a possible explanation may be an interaction between the two defects in the small unit cell. Future work using larger cells will clarify why the two boundaries converged differently and determine the energy of APB-IIIup.

To validate the different models against our measurement, simulated STM images were calculated using the Tersoff-Hamann method. The results are shown in Fig. 5.12 for a

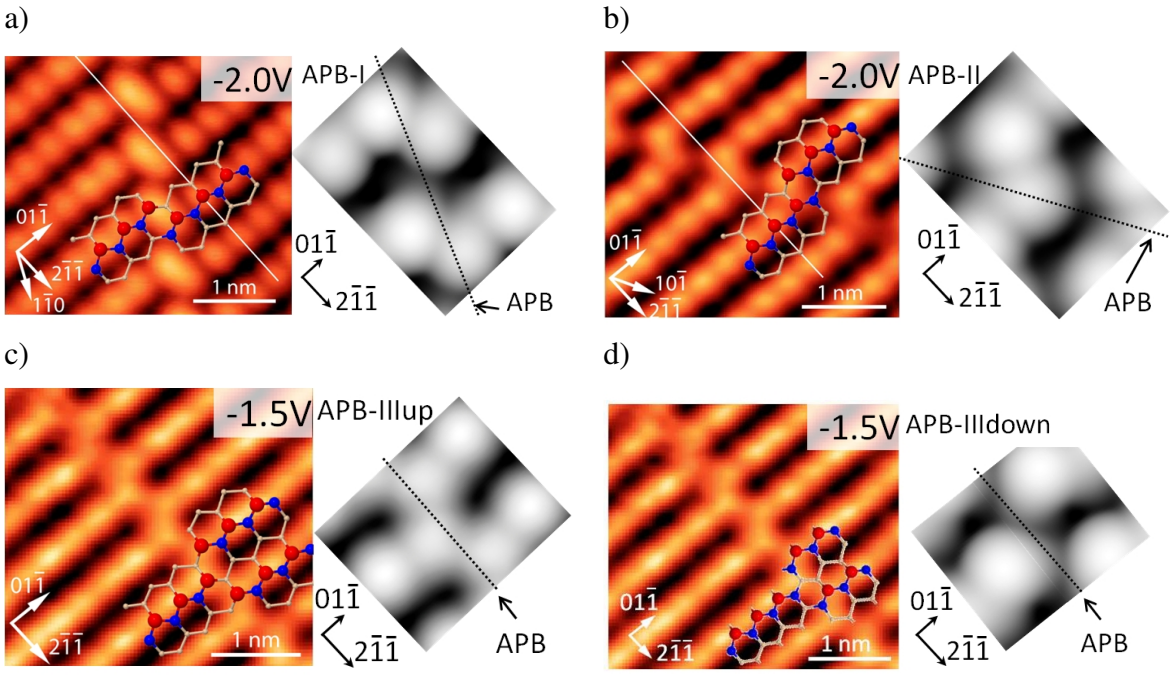

Figure 5.12: Simulated STM images at -1.1 V. a) APB-I. b) APB-II. c) APB-IIIup. d) APB-IIIdown.

simulated STM bias of -1.1 V. It can be seen that the simulated topography images compare well with the measurement for APB-I and APB-II, reproducing the central kink of the boundary in the correct orientation. APB-IIIup also matches the simulation, reproducing the measured protrusion between the π-bonded chains, whereas APB-IIIdown does not match the experiment because the boundary is simulated as a depression. This nicely confirms the result of the comparison between structure and topography shown in Fig. 5.11 and allows us to conclude that the three different observed boundary orientations are described by the structure models APB-I, APB-II and APB-IIIup.

5.6.2 Movement

We have shown that the atomic scale structure of APBs consists of a crossover from the seven atomic rings to five atomic rings over the boundary, therefore changing from a π-bonded chain into the trough region. As was previously reported in literature [74] we have found several APBs that show considerable movement during the measurement. However, in contrast to the previous measurements of other groups we also find boundaries that completely relocate to a different position and do not remain pinned at the same end points. In Fig. 5.13 a), a boundary is shown in its initial position. Image b) and c) are successively recorded as up and down scans respectively and it can be seen that the boundary moves on a large scale. The movement is very fast and happens in between two line scans, therefore is not resolved in our measurement. From the scan speed we can

calculate that the complete relocation happened within less than 0.5 s. In Fig. 5.13 d) it can be seen that the boundary has moved to a completely new position.

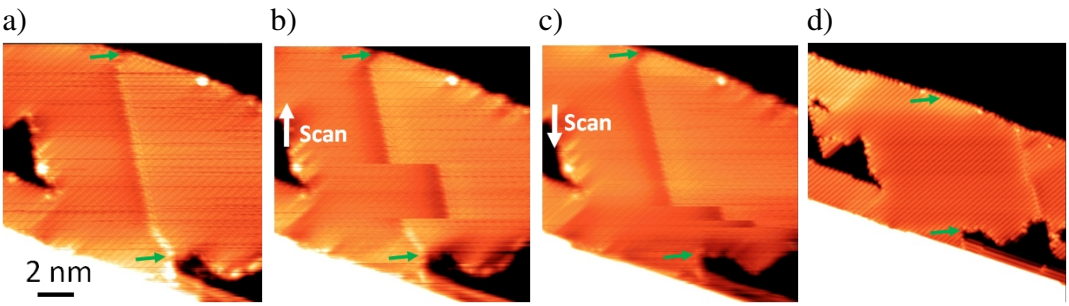

Figure 5.13: Anti phase boundary movement. a) The green arrows mark the original position of the APB. b)+c) Large scale movement of the APB. d) APB imaged in new position.

The movement is surprising because a shift of the APB means that the rings of seven and five atoms in the surface reconstruction have to change place, which requires breaking and reforming atomic bonds. This process is usually thought to cost about 1 eV per atomic bond in bulk silicon and because the movement happens on a nanometer scale, over 100 bonds have to be rearranged. This apparently huge barrier is unlikely to be overcome by energy induced by the tip and therefore a different explanation has to be found. As discussed in Sec. 2.2.2, Northrup et al.[62] calculated the barrier energy to form the Si(111)-2x1 reconstruction from the buckled surface and found that it is very small with only 0.03 eV per surface atom. This despite the fact that Si bonds have to be broken, similar to the case of APB movement. Based on their proposed mechanism shown in Fig. 5.14 we are able to suggest a low energy pathway for APB movement. In Fig. 5.15 a possible reconstruction to move the APB by one unit cell is shown in five steps.

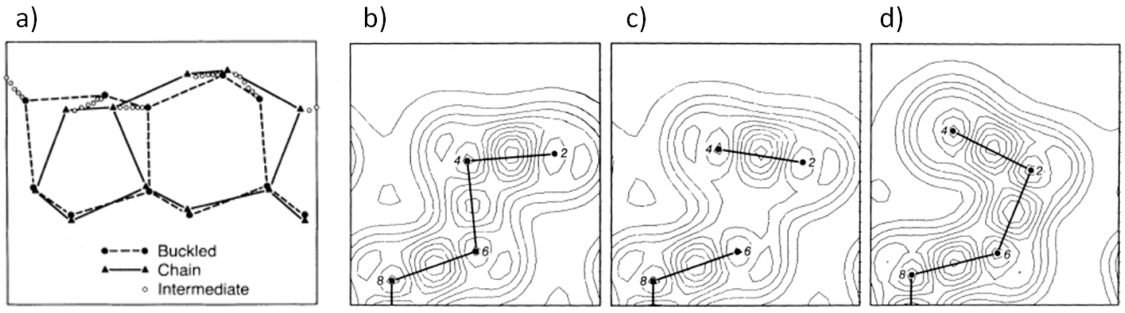

Figure 5.14: Si(111)-2x1 reconstruction mechansim by Northrup et al.[62] a) Buckled and chain geometry. b)-d) Change of the calculated atomic positions.

It can be clearly seen that the movement of the APB is very similar to the process shown in Fig. 5.14. In the initial structure we see the π-bonded chains with the alternating rings of five and seven atoms. In step III one bond is rearranged and the structure effectively

goes back to the buckled model of the unreconstructed surface with equal rings of 6 atoms. Now a similar process is repeated backwards but the bond at the other side of the six atomic ring is broken leading to π-bonded chains shifted by half a unit cell.

A different way to look at this process is to start from the unreconstructed surface in step III. Depending on whether one moves to the left or the right, a different bond of the six atomic ring is broken and the Pandey reconstruction is formed but with opposite phase. To estimate the energy barrier for this movement, it has to be considered that the pathway calculated by Northrup et al. is executed twice, once forward and once backward. We can therefore give an upper limit of the expected energy barrier consisting of the barrier calculated by Northrup et al., plus the total energy gain of the process, which in total amounts to approximately 0.1 eV. Based on this process and the work from Northrup et al. [62] we therefore assume that it is possible to move the boundary along the π-bonded chains with a very low energy barrier of only 0.1 eV per surface atom.

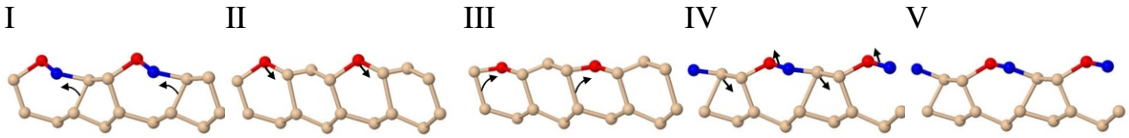

Figure 5.15: Mechanism of APB movement showing a single cut along the boundary.

The calculated formation energies of APBs together with the low energy barrier for their movement allows us to explain the driving forces involved in APB movements and the consequently resulting APB locations we observe on the surface. The fact that APBs have a higher energy than the clean surface makes it energetically favorable to eliminate them. Because a boundary has the possibility to change in length by relocating on the surface, its free energy acts as a driving force[124] to move it in a direction where it becomes shorter. The potential landscape in which an APB moves is therefore defined by the local environment of its end points, since they determine how its length is affected by any movement, as sketched in Fig. 5.16.

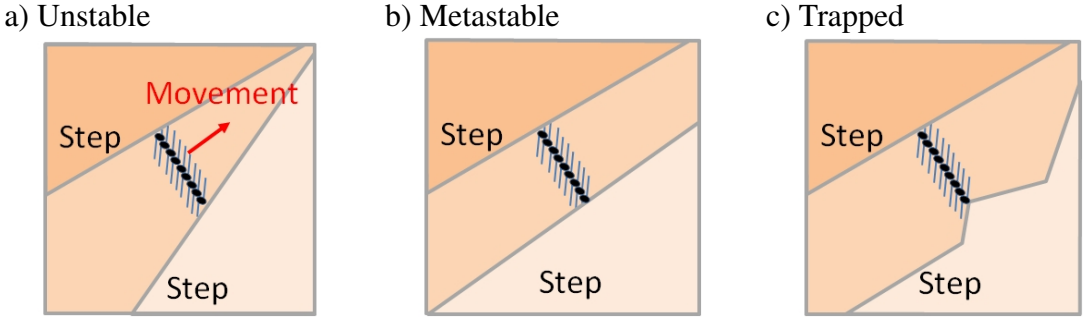

Figure 5.16: Schematic for different states of APBs pinned by their end points.

In unstable environments, as shown in Fig. 5.16 a), both ends can reduce the length of

the APB and therefore minimize its free energy by propagating in the same direction. The boundary shown in a trapped environment in Fig. 5.16 c) on the other hand cannot move in either direction without increasing its free energy and is therefore pinned. The APB shown in a metastable environment in Fig. 5.16 b) can move without changing in length and would likely diffuse across the surface until it reaches either a trapped state or an atomic scale defect that pins one of its ends. We propose that after the cleave all unstable APBs propagate through the surface until they vanish or are pinned, in good agreement with the fact that all boundaries were found in either a trapped or a metastable position. APBs in metastable environments were observed to readily relocate during imaging, confirming their weak local pinning. It is important to note that a boundary between two single π-bonded chains cannot move independently of the adjacent boundaries since this would create two π-bonded chains or two trough regions directly next to each other.

To verify this behavior we evaluate the positions in which we find the boundaries as shown in Fig. 5.17. It can be seen that some of the boundaries appear in a metastable state but it is striking how many originate from a kink in the step edge and are therefore in a trapped position. It is assumed that upon cleaving of the surface many regions of different phase are created forming APBs in between them. They will try to move into a local energy minimum and, depending on their initial location, move over the surface reducing their length until they either vanish or get pinned in a trapped state. This is in excellent agreement with the observed APB positions in our measurement.

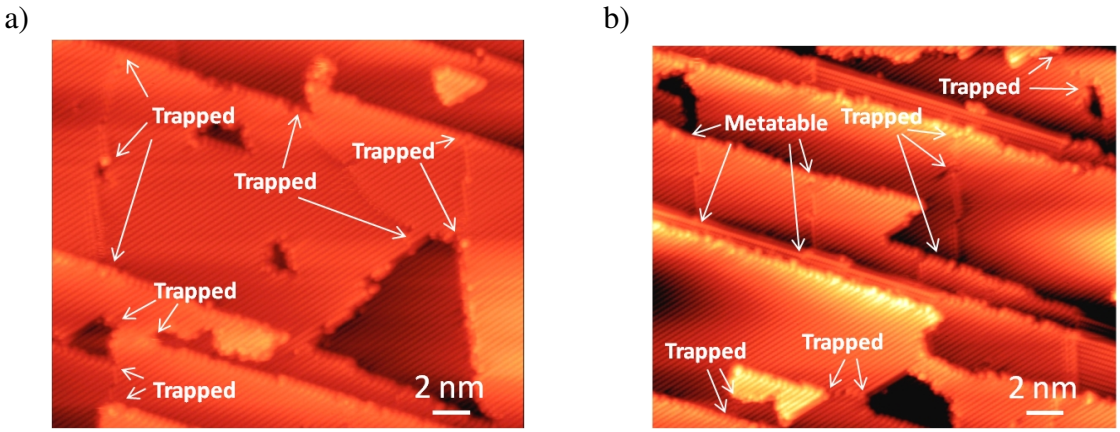

Figure 5.17: Identification of the pinning of APBs in large scale Si(111)-2x1 topography images. a) -1.1 V. b) -2.0 V.

We can use this model to finally explain the movement shown in Fig. 5.13. When looking at the initial and final position of the APB we can see that the observed movement happened between two trapped positions. The boundary was in a trapped state and therefore in a small local energy minimum. Due to an interaction with the STM tip, as will be explained in Sec. 5.6.4, it was then able to overcome this minimum and move, driven by its inherent instability, to end up in the next energy minimum with a reduced total length.

5.6.3 Band Structure and Electronic Effects

All anti phase boundaries show a characteristic local contrast, presumed to be electronic in nature and previously reported by Trappmann et al.[74] As shown in Fig. 5.18 the effect is characterized by an increased and decreased brightness to either side of the phase boundary respectively. As seen in the line profile in Fig. 5.18 b) the effect extends to about 3-5 nm to either side of the APB.

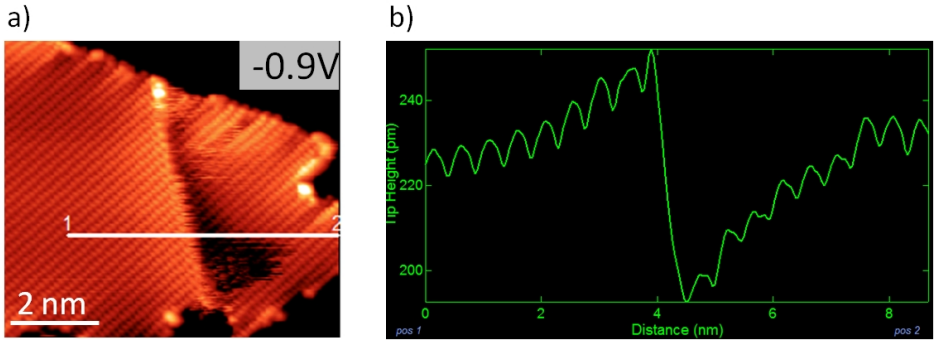

Figure 5.18: Electronic effect of APBs. a) Topography image of an APB. b) Line profile across the phase boundary between points 1 and 2 in a).

We found that the electronic contrast around APBs is bias dependent and strongly asymmetric. As seen in Fig. 5.19, both domains to either side of the APB appear identical when imaged at high bias voltages whereas they become bright and dark respectively when imaged at low bias. The fact that the contrast reverses with the voltage polarity clearly demonstrates the electronic nature of this effect. The electronic contrast was always found to increase the brightness to one side and decrease it to the other side of the APB, giving it a clear orientation. Surprisingly we observed APBs of identical reconstruction type with opposite sides of increased and decreased brightness respectively as shown in Fig. 5.19 a) and b).

Various effects could be responsible for the origin and the asymmetry of the observed contrast. The most obvious explanation for the asymmetry would be to link it to the structural asymmetry of APB-I as described in Sec. 5.6.1. This can however not be the case since both APBs shown in Fig. 5.19 have an APB-I reconstruction whereas the orientation of the electronic contrast is reversed. In fact we have found that all three APB reconstructions show the electronic effect in both orientations with about equal distribution. The simple structural asymmetry of the reconstruction can therefore be ruled out as the origin of the effect.

Another possible explanation is that the boundary separates two domains that have a slightly different reconstruction such as positive and negative buckling. Theoretical calculations have proposed that the negatively buckled Si(111)-2x1 reconstruction would show a significantly smaller surface band gap[125] compared to the positive buckling. Such a

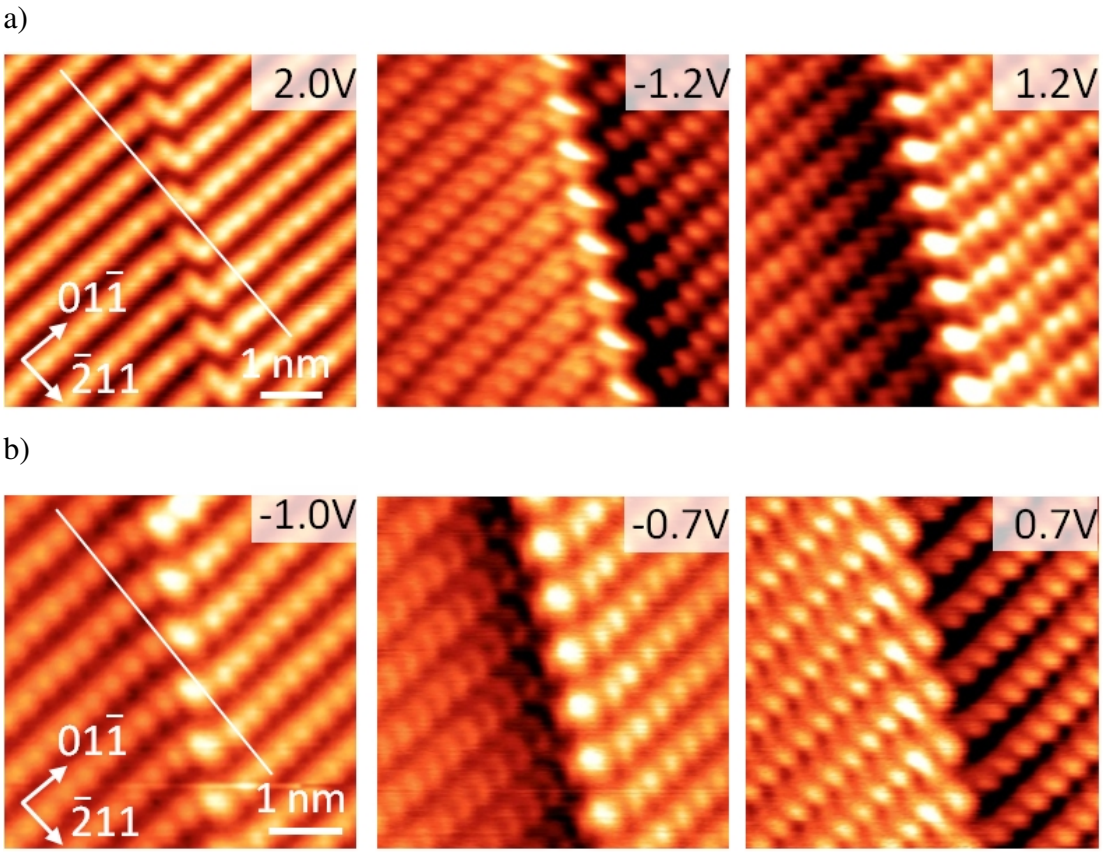

Figure 5.19: a)+b) Voltage dependent imaging of two identically reconstructed APBs with opposite polarity of the electronic effect.

band gap mismatch might well explain the measured electronic contrast at the boundary. To test this theory we again checked whether the up atoms align over the boundary as indicated by the white line in Fig. 5.19. We found that for both APBs there is no change of buckling consistent with all other measured APBs. Additionally we have observed boundaries that reversed the polarity of the electronic effect after they moved a few nanometers to a new position. This could not be explained by different domains meeting at the boundary since then the polarity would have to stay the same.

To characterize the electronic effect we have performed CITS measurements as shown in Fig. 5.20 for an APB-I reconstructed boundary. The data was topography corrected and smoothed using a gliding median algorithm resulting in a resolution of 80 mV. In Fig. 5.20 a) the lateral distribution of the conductance at -1.1 V is displayed and the APB-I reconstruction is clearly visible, as in topography. To visualize the electronic effect, a cut through the CITS data is shown in Fig. 5.20 b). It displays the measured conductance averaged over the width of a single π-bonded chain on the y-axis, plotted against position on the x-axis following the indicated line in Fig. 5.20 a). The cut clearly shows the conductance and valence band peaks of the surface with the atomic corrugation. It can be seen that at the boundary, indicated by the red arrow, the bandgap is reduced whereas it is

shifted upwards to the left and downwards to the right. This shift explains the observed step like behavior of the topography and also the fact that the orientation of this step changes with the voltage polarity. It can be seen that the bands relax back towards the normal surface value when laterally going away from the boundary.

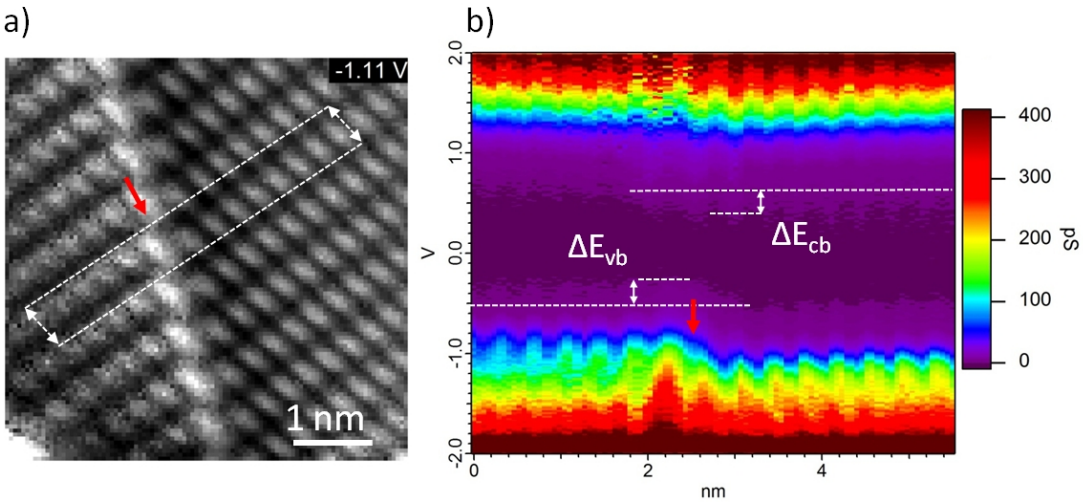

Figure 5.20: CITS data of APB-I. CITS acquired at -2 V, 300 pA setpoint. STS from -2 V to 2 V with an accuracy of 80 mV. a) Laterally resolved conductivity. b) Measured conductance on y-axis over position on x-axis following the indicated line in a).

The bandgap was found to be constant on the left and right side of the boundary with a variation of less than ± 40 mV. To the left side the surface valence band aligns with the gap of the boundary and the bands are pushed up by 60 meV compared to the clean surface. To the right side on the other hand the conduction band aligns with the gap of the boundary as the bands are pushed down by 120 meV. This results in a total shift of the bands towards each other of 180 meV. This value was found to be fairly typical as values around 200 meV were usually measured for boundaries of either polarity.

The fact that the bandgap is equal on either side of the boundary but shifted directly next to it suggests that not the properties of two different domains cause the electronic effect but the presence of the boundary itself. An effect that is commonly known to shift bands is strain. Owen et al.[126] proposed that increased constraints on atomic reconstructions lead to a brightening of dimers in the Si(100) surface whereas a darkening results from the reduction of constraints. Schofield et al.[127] later interpreted this behavior as a shifting of the bands, observing a brightening in filled states and a darkening in empty states similar to our case, as shown in Fig. 5.21 a). Theoretical calculations of strained silicon nanowires confirmed that strain shifts silicon bands in both directions depending on whether the strain is tensile or compressive[128] as shown in Fig. 5.21 b).

Based on this work we propose that the electronic contrast is caused by strain induced

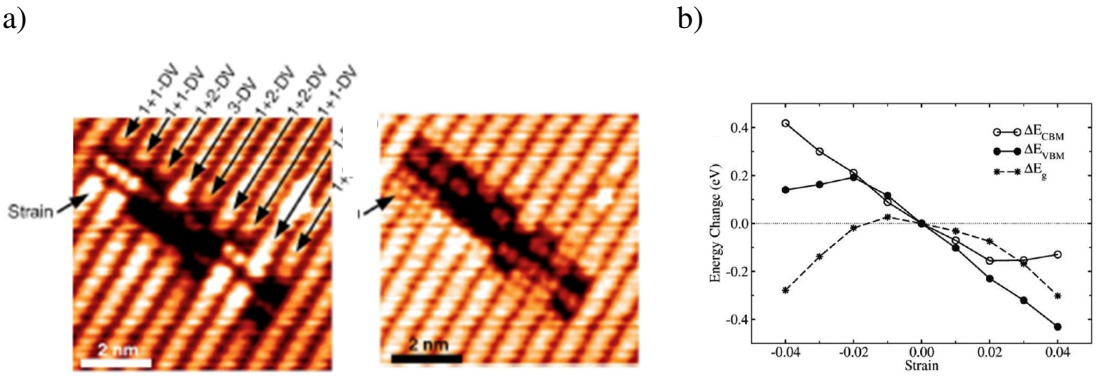

Figure 5.21: a) Observation of strain in silicon interpreted as a band shift.[127] b) Calculation of the band shift induced by strain in silicon nanowires.[128]

from the APB. The model introduced earlier to explain the movement of the APBs can be extended to also clarify the origin of the strain associated with APBs. As we have shown, APBs try to move in order to minimize their length and reduce their energy. They will relocate across the surface until one of their ends gets pinned by a step edge or an atomic scale defect. Pinned APBs are prevented from moving at one end, their path across the surface restricted to the orientations of the three different reconstructions. They are still subjected to a potential gradient, defined by the environment of their unpinned side, leading to a force acting on the boundary as previously discussed. Because the pinning prevents any movement this force results in compressive or tensile strain to either side of the APB, depending on its direction. This is in good agreement with the observed characteristics of APBs and we therefore interpret the electronic contrast as a strain induced band shift in the Si(111)-2x1 reconstruction. This model not only explains the random distribution of the orientation of the electronic effect but also the fact that it sometimes changes polarity after an APB has moved, as it may end up in a different pinning configuration.

5.6.4 Tip Induced Forces

To explain the observed relocation of a boundary, we have proposed that an interaction with the STM tip can induce forces on APBs. This is difficult to measure when looking at large scale movements where APBs completely relocate, because the movement happens very quickly and the phase boundaries end up in a more stable position from which they will not move again. To get experimental data about the tip interaction we therefore focus on APBs that move on a small scale without actually changing the points where they are pinned, as shown in Fig. 5.22. This small scale movement is often observed as a flickering around the APBs and we will show that it arises from tip induced movement of the APB which remains pinned at its ends.

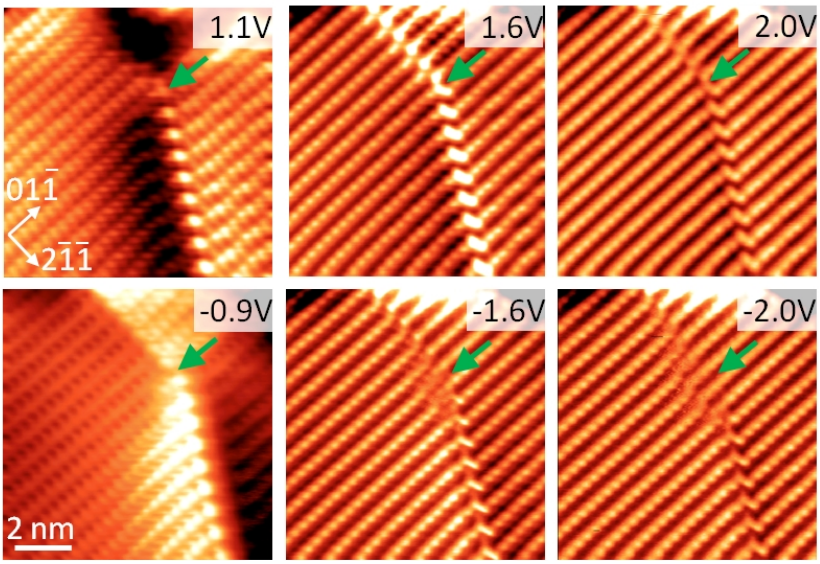

Figure 5.22: Tip induced APB movement. Images acquired at 300 pA, the green arrow is indicating the same position in all images.

In Fig. 5.22 an anti phase boundary can be seen that reconstructs as APB-I in the lower part and as APB-III in the upper part of the image. We have measured the boundary at voltages between -2 V and +2 V and found that the position of the APB changes at high negative voltages above -1.3 V. We found that the position of the boundary stays the same for all positive voltages and for negative voltages below -1.3 V, keeping the current setpoint at 300 pA. In Fig. 5.22 constant current topography images are shown and it can be seen that the boundary is pushed to the left for negative voltages above -1.3V, depending on the magnitude of the negative bias. The change in location was found to increase gradually with increasing negative voltage, demonstrating the influence of the tip. Images at +2V and -2V were acquired on the forward and backward trace of the same scan respectively, illustrating that the switching in between the two positions is very fast and completely reversible. The difference in tip height for both images was measured to be less than 2 pm and as the boundary only moves under negative voltage we can exclude tip proximity as the driving mechanism. We assume that either the electric field[129] or a vibrational excitation[130] mediate the movement; future work is required to clarify the exact mechanism.

This measurement also provides further evidence linking the measured band shift to strain, as the observed contrast is strongly correlated to the movement of APBs. In Fig. 5.22 the electronic effect is clearly evident at low bias and it can be seen that its orientation changes together with the reconstruction of the APB. In terms of surface strain this can be explained by two APBs that both try to reduce their length, pulling in opposite directions and forming a delicate balance. The APB dislocates when imaged at high negative bias and it is assumed that tip induced forces disturb the balance between the two boundaries.

This is in good agreement with the observation that the movement originates directly at the crossover of the two reconstructions where the electronic contrast changes its polarity.

5.6.5 Controlling the Location of APBs

The ability of the STM to introduce atomic scale defects combined with the mobility of APBs allows one to accurately control their position. As shown in Fig. 5.13, APBs can be released through tip induced forces and will propagate across the surface until they reach the next naturally formed energy minimum. After the observed large scale movement we scanned the APB for over one hour without measuring any change in its location, shown again in Fig. 5.23 a). As STM tips can be used to deliberately create defects in silicon[131] it is possible to control the position of APBs by introducing new pinning sites as shown in Fig. 5.23 b). It can be seen that the APB changes its location and now runs through the artificially created defect. APBs that are pinned in a small local energy minimum can therefore be released using the tip and then stopped at any desired location using a previously created artificial pinning site.

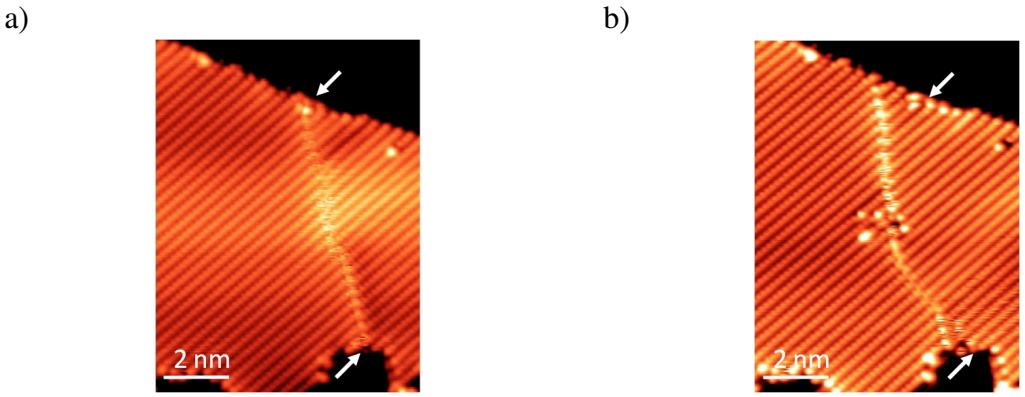

Figure 5.23: Manipulation of an APB. a) Position before manipulation. b) APB after surface manipulation.

In summary we show that APBs are a model system for studying and manipulating the influence of strain at the atomic scale. This enables the exciting possibility of using strain to influence and control the properties of individual atomic scale devices. Possible applications range from controlling the inhomogeneous broadening of dopants for optical quantum computing[8] to modifying the magnetocrystalline anisotropy of individual atoms for high density data storage.[132] The atomic model of the boundaries presented here and the detailed data about their band structure will also allow further calculations to determine the forces involved in APB movement and the magnitude of the strain resulting from their pinning.

6 Studying Implanted Dopants in STM

The ability to control the location and density of impurities in semiconductors is a key technology that enabled the realization of modern electronic devices. By controllably introducing donors and acceptors into the host crystal, the band structure of semiconductors can be engineered together with its electronic and optical properties. The increasing spatial control over the extent of these doped regions allowed the incredible trend in scaling electronic devices, witnessed over the last decades.

To fabricate devices based on charge carriers, such as pn-diodes or field effect transistors, the ideal dopant must fulfill a wide range of criteria regarding its structural and electronic compatibility. Donors and acceptors must for example have a low ionization energy, their energy levels lying just under the conduction band or just over the valence band respectively. These so called shallow donors are completely ionized at temperatures above $\sim$150 K and therefore enable the device to be operated in a wide temperature range. Furthermore, dopant impurities must be compatible with the crystal lattice of the semiconductor, enabling the controlled incorporation of dopant concentrations, ideally ranging over more than six orders of magnitude. Depending on the semiconductor, different elements were found to satisfy these criteria. For donors in silicon phosphorus (P), arsenic (As) and antimony (Sb) are commonly used whereas acceptors are mostly formed by boron (B).

Due to the continued trend in scaling down the dimensions of charge devices, they will however soon reach the point where only a few dopant atoms control their functional properties. To further increase computing power it is therefore envisaged that future devices will not rely purely on charge, but also exploit quantum properties of the carriers such as electron or nuclear spin. Architectures for these next generation electrical devices have been proposed,[7, 8] relying on the quantum states of single donor atoms in silicon. To realize quantum information processing (QIP) these device architectures intend to exploit the quantum states of a single electron bound to a donor in silicon, manipulated using electrical or optical methods. Consequently, one of the key differences regarding the selection of a suitable dopant for these novel architectures is that the donor needs to be in its non ionized state, the electron remaining bound to the donor core. Using conventional donors such as P, this creates formidable fabrication challenges as the device would have to be operated at 100 mK.[7] More recent proposals[8] are therefore suggesting the incor-

poration of different dopant species with higher ionization energy. These deep donors, such as bismuth (Bi), would be better suited for quantum information processing and might allow device operation at liquid nitrogen temperatures. More exotic dopants are also explored in other emerging fields such as silicon spintronics, where manganese (Mn) dopants in silicon are used to create magnetic semiconductors.[133, 134]

Whereas studies of shallow donors and processes to include them into single crystal silicon have been extensive during the last decades, there is comparatively little known about deep donors such as Bi. Their intended use in QIP further makes it necessary to study these dopants individually and at the atomic scale, in order to establish a basic understanding towards controlling the quantum states of a single donor atom. STM is ideally suited for such a study and has demonstrated the capability of characterizing spin states, magnetic anisotropy, wave functions and ionization energies of individual atoms.[3, 16, 88, 132] Nevertheless, none of these studies was so far conducted on deep donors in silicon and preparing a suitable sample for STM characterization remains a huge challenge. As presented in Sec. 2.3, the shallow dopants P and B have been studied in the cleaved Si(111)-2x1 surface, taking advantage of bulk doped single crystal wafers, produced using the well established processes of conventional semiconductor technology. For larger impurities such as Bi however, the low equilibrium solid solubility limit[135] of 8×10^{17} cm^{-3} at 1320 °C limits the applicability of standard crystal growth methods. It is furthermore not economically viable to develop such processes for explorative studies of different deep donors in silicon. We therefore investigate whether it is possible to develop a new sample preparation process that allows us to study Bi at the atomic scale and that could be adapted to also enable the study of a large variety of different impurities in silicon.

a) b)

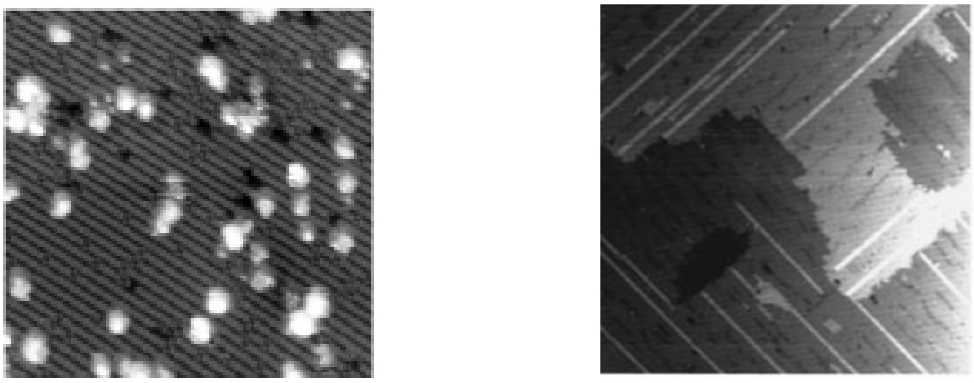

Figure 6.1: Depositing dopants on silicon using thermal evaporation. a) P deposited on silicon incorporates into a substitutional site upon annealing. Image from [90]. b) Bi deposited on a silicon surface forms nanolines upon annealing, image from [136].

Commonly used methods to introduce impurities into a silicon crystal include molecu-

lar beam epitaxy, direct thermal evaporation onto the surface, chemical vapor deposition and ion implantation. To use such samples for STM studies it is important that these methods do not contaminate the sample and that the preparation of an atomically clean surface remains possible. Furthermore it is crucial that the impurities introduced into the crystal are located in a substitutional silicon site in order to act as a dopant. This restricts the use of techniques that simply deposit dopants on the sample surface such as chemical vapor deposition or thermal evaporation in UHV. It is known that these processes do work for some dopant species, as for example phosphorus, which can be incorporated from the surface into substitutional silicon crystal sites using thermal annealing. As shown in Fig. 6.1 a) this has been demonstrated using thermal evaporation from a GaP source.[90] For Bi on the other hand, using thermal evaporation to deposit it on the surface and subsequent annealing results in the formation of long Bi nanolines[136] as shown in Fig. 6.1 b). This is not suitable to study the dopant properties of individual Bi donors in silicon and therefore techniques that deposit dopants on the surface and rely on diffusion to incorporate them into the crystal were not used in this study.

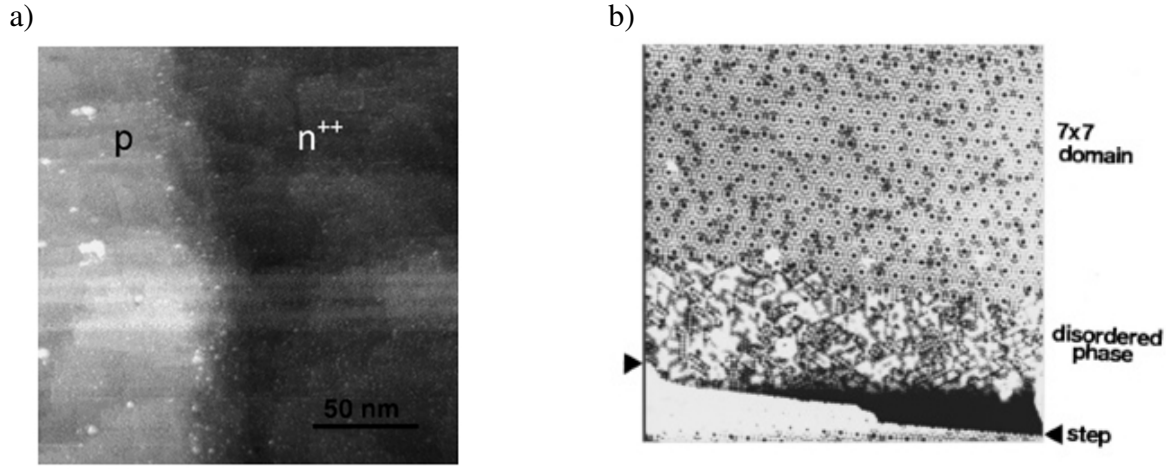

Figure 6.2: STM studies of implanted dopants. a) As implanted into Si(100) with subsequent flash annealing. Image from [137]. b) B implanted into Si(111) subsequently cleaved and annealed, image from [138].

Alternatively, techniques that allow the incorporation of dopants directly into the silicon crystal such as molecular beam epitaxy and ion implantation were considered. Molecular beam epitaxy has been successfully used to grow epitaxial layers incorporating individual dopants or even quantum dots in GaAs to study them with cross sectional STM.[3, 139] Comparable attempts to study impurities in silicon with STM[46] using MBE grown, boron doped silicon crystals however resulted in a very rough surface that did not show any contrast when measured in constant current mode. It is therefore assumed that controlling the growth of epitaxial layers with a crystal quality suitable for atomic scale STM characterization of individual dopants would be very challenging. To develop a more ver-

satile and user-friendly technique for the study of deep donors in silicon we have therefore focussed on ion implantation. The capability to implant almost every existing element into silicon to a well known depth and with precisely controlled concentration makes this the ideal technique for our purpose. Previous studies of implanted impurities[137, 138] have shown that it is possible to find and resolve the implanted area using STM, as shown in Fig. 6.2. These results are very encouraging even though they used shallow dopants and did not prepare surfaces suitable for single dopant characterization. The dopant profile in the Si(100) surface shown in Fig. 6.2 a) was created using ion implantation of As and a subsequent high temperature anneal. Figure 6.2 b) shows the transition region of a boron implanted area in a Si(111) surface which was cleaved and subsequently annealed. Both preparation methods seem promising and create a reasonably flat surface suitable for STM studies. Nevertheless, the surface quality would certainly have to be significantly improved in order to allow characterizing single dopant atoms. In collaboration with Andy Smith from the University of Surrey we have therefore developed and characterized an implantation process that allows studying Bi in silicon using XSTM, as described in this chapter. This process highlights the crucial points that have to be considered when using ion implantation for STM sample preparation and provides an easily adaptable recipe to study a wide range of different impurities in silicon.

6.1 Implanting Bi Dopants into Silicon

Bismuth is a promising deep dopant for quantum information processing applications as its high ionization energy might enable QIP even at liquid nitrogen temperatures[8] and additionally long electron spin coherence times[140] have been reported. The process of implanting Bi into silicon together with the necessary annealing step for implantation damage recovery has been characterized,[141–144] providing an excellent starting point to develop an implantation technique suitable for the very specific sample requirements of STM.

We have explored two different approaches towards preparing an atomically flat sample with Bi donors in the surface. One consists of implantation into a Si(100) wafer which is subsequently flash annealed in the STM, similar to work by Kim et al.[137] shown in Fig. 6.1 a). The other approach was to implant a Si(211) wafer and subsequently cleave it in UHV to expose a clean Si(111) cross section. In contrast to work done by Hirayama et al.,[138] shown in Fig. 6.1 b), we however abstain from an annealing step in UHV to prevent dopant diffusion and enable characterizing Bi atoms in their intrinsic crystal sites.

6.1.1 Flash Annealing Implanted Samples

In a first step we have implanted Bi into a Si(100) surface which was then prepared using the standard flash annealing procedure described in Sec. 3.3.2. Samples were implanted by A. Ferreira da Silva with a uniform density of 9.1×10^{19} cm^{-3} to a depth of 200 nm. The subsequent STM characterization is shown in Fig. 6.3 a) and a typical, atomically flat surface was found after flash annealing the sample to 1200 °C. Surprisingly, we could however not find any features resulting from the implanted Bi dopants. Besides the usual and always present surface defects, the implanted dopant concentration should lead to several Bi atoms in the surface of a 50 nm square area, but no feature with the expected density could be identified.

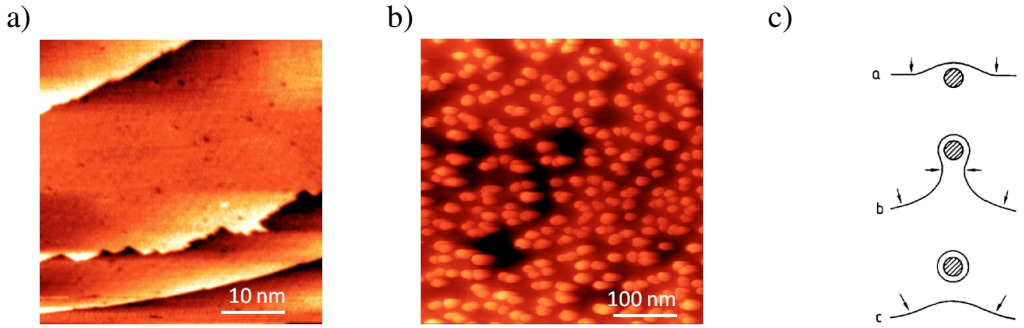

Figure 6.3: Flashing of Bi implanted samples at different temperatures. a) Implanted sample flash annealed to 1200 °C. b) Implanted sample chemically H terminated, then flash annealed to 1000 °C. c) Schematic of the hillock formation due to a point defect such as carbon. Image from [145].

It is known that annealing semiconductor samples can lead to increased dopant diffusion or even evaporation from the surface.[45] For Bi, a diffusion of dopants towards the surface has been reported[146, 147] for samples annealed with laser pulse irradiation as well as samples annealed in a furnace to temperatures of 600 °C to 700 °C. This would suggests that an increased concentration should be measured at the sample surface during STM experiments, in disagreement with our experimental results. As the flash annealing temperature used for STM surface preparation is however 1200 °C, and therefore significantly higher than the 700 °C used in previous studies, it might not only lead to surface segregation but actually evaporate Bi atoms together with the Si surface layer. It is therefore assumed that the density of dopants present at the sample surface was significantly decreased by the flash annealing and lower annealing temperatures would be preferable. Unfortunately lowering the annealing temperature is difficult as it is necessary to heat the sample to at least 1200 °C in order to clean the surface from carbon contamination. In an attempt to overcome this problem, samples were chemically cleaned and hydrogen terminated using hydrofluoric acid, a surface preparation method that prevents carbon contamination and allows lower temperature anneals.[148] Unfortunately in our case this

still did not result in a clean surface, as shown in Fig. 6.3 b). The hillocks seen in the image are a clear signature of carbon,[149] pinning the silicon step flow during the anneal and leading to the formation of a protrusion as sketched in Fig. 6.3 c).

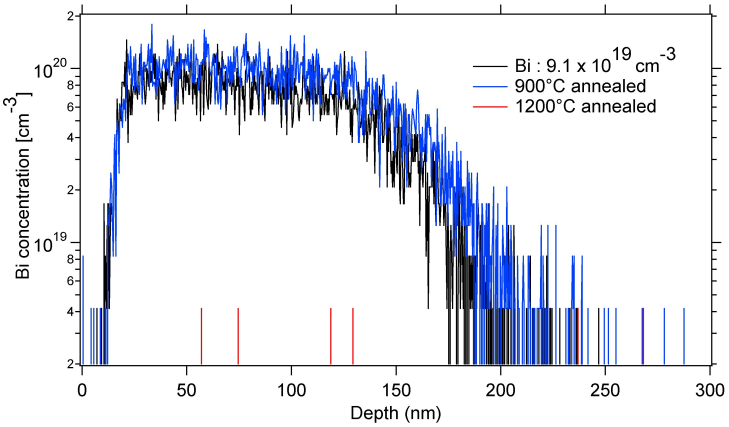

Figure 6.4: SIMS measurement of Si(100) samples implanted with Bi and subsequently flash annealed to 900 °C and 1200 °C. Whereas 900 °C does not affect the Bi concentration the anneal to 1200 °C reduces the amount of Bi below a detectable level.

To further verify whether the Bi is really influenced by the annealing process, we have used secondary ion mass spectrometry (SIMS) and determined the Bi concentration after flash annealing samples to different temperatures in UHV for 10 s. SIMS measurements were performed by Richard Morris in Warwick and the results are shown in Fig. 6.4. It can be seen that the unannealed STM samples show the expected Bi profile with a concentration of 9.1×10^{19} cm^{-3} to a depth of 200 nm. However, whereas samples annealed at 900 °C show no change in Bi concentration, samples annealed to 1200 °C show no measurable Bi concentration at all. This clearly demonstrates the loss of Bi dopants due to the high temperature surface preparation method and explains why no Bi donors were found in the flash annealed Si(100) surface. Based on these results we have decided to focus on the alternative cross sectional sample preparation method, as this allows us to measure a silicon surface in UHV without annealing it to high temperatures.

6.1.2 Implantation and Annealing for XSTM

Combining ion implantation and cross sectional STM was evaluated as a possible sample preparation method to study individual dopants at the atomic scale. To create an atomically flat surface using XSTM, the cleaving process for silicon is of crucial importance, as outlined in Sec. 3.3.3. Because it strongly depends on the atomic scale crystal structure of the sample, any crystal damage caused by the ion implantation process is likely to have an adverse effect on the measured surface quality after the cleave. It is therefore assumed necessary to reduce implantation damage to the lowest possible level. This is usu-

ally achieved with an annealing process that not only recovers implantation damage but also incorporates the dopants into substitutional Si positions, activating them electrically. Since we have already learned from the Si(100) implantation experiments that annealing samples to high temperatures removes the Bi dopants, our anneal of cleaved ion implanted Bi samples requires a tradeoff between removing damage and minimizing dopant diffusion. However, reported annealing temperatures necessary to completely recrystallize the silicon sample after implantation range from 600 °C to 900 °C and are thus significantly lower than the 1200 °C used for the flash annealing.[142] It is therefore assumed possible to find parameters that achieve an optimal balance between damage healing and dopant diffusion, enabling us to study individual Bi atoms at the atomic scale.

For STM studies a sufficiently high amount of Bi dopants has to be present in the surface of the cleaved silicon and therefore two different samples were implanted with high dopant concentrations of 1×10^{19} cm^{-3} and 1×10^{20} cm^{-3}. This corresponds to a density of 20 or 200 dopants in an measurement area of 50 nm square respectively. Such a high concentration may to some extent compensate for the fact that the electrical activation of a high dose Bi implanted sample is expected in the range of just 28% after annealing.[143] Even when taking this into account, the higher implantation dose is still suitable for measurements at cryogenic temperatures, since the concentration exceeds the metal insulator transition of Bi in silicon, reported [143] at 2×10^{19} cm^{-3}. Furthermore, the high implantation concentration may compensate the loss of dopants due to evaporation from the surface and therefore give room for increased annealing temperatures if found necessary.

Table 6.1: Used parameters for bismuth implantation.

Ion Energy (keV)	High concentration, Bi cm^{-2}	Low concentration, Bi cm^{-2}
2000	1.7x10^{15}	1.7x10^{14}
1350	1.2x10^{15}	1.2x10^{14}
850	0.9x10^{15}	0.9x10^{14}
500	0.64x10^{15}	0.64x10^{14}
250	0.41x10^{15}	0.41x10^{14}
Total Dose	4.85x10^{15}	4.85x10^{14}

Bismuth dopants were implanted into the low phosphorus doped $\{211\}$ wafer, described in Sec. 3.3.1. Because the phosphorus doping concentration is only 1×10^{15} cm^{-3}, less than one P dopant is expected in the surface of one square micrometer and since the appearance of P dopants is well known,[20] new features can be attributed to the Bi dopants that have a four orders of magnitude higher concentration. Samples were cut from the implanted wafer using a diamond dicing saw and then prepared for XSTM measurements as described in Sec. 3.3.3. As the cross section of the wafer is imaged,

a direct measurement of the depth profile of the implanted Bi is expected. To maximize the measurable implanted area in STM experiments, a uniform dopant concentration to a depth of 600 nm below the surface was created. This required five implantation cycles with different energies as shown in table 6.1. The expected dopant concentration and damage profile was simulated by A. Smith and is shown in Fig. 6.5 a) for the sample implanted to a Bi concentration of 1×10^{19} cm^{-3}. It can be seen that the five different implantation energies create a uniform dopant profile with only small variations. The end of the implanted area is characterized by the tail of the Gaussian dopant distribution of the highest energy implantation run, 600 nm away from the wafer surface.

a) b)

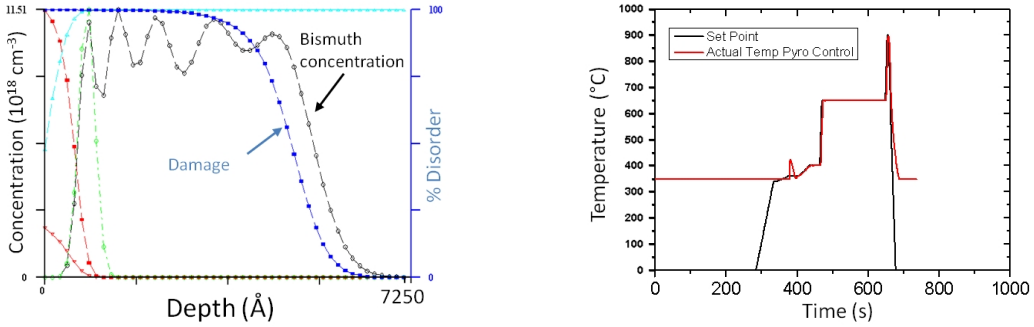

Figure 6.5: a) Simulated implantation and damage profile for an implanted Bi concentration of 1×10^{19} cm^{-3}. b) Measured temperature profile for the annealing step including 3 min at 650 °C and 1 s at 900 °C.

The annealing parameters chosen for the first implantation runs were based on work performed by Abramov et al.[143] They showed that for highly Bi implanted silicon wafers an annealing step to 600 °C was sufficient to fully recover the single crystal structure and reduce the implantation damage below the detectable limit of 1%. For lower doses, an additional step to 900 °C was reported necessary to remove the implantation damage. Anneals were performed by A. Smith at Surrey University using a rapid thermal annealer to controllably heat the sample in an inert atmosphere. In order to get a good understanding of the influence of the annealing temperatures on the damage recovery and electrical activation of the implanted dopants, we have used two different annealing schemes for both Bi concentrations. The more conservative anneal consisted of a single 3 min heating step to 650 °C. The more aggressive annealing step also heated the sample to 650 °C for 3 min but then spiked the temperature to 900 °C for one second, as seen in the pyrometry measurement shown in Fig. 6.5 b). This one second spike should remove additional residual damage without providing enough thermal budget for significant dopant diffusion.

6.1.3 Implantation Damage and Dopant Activation

Rutherford backscattering spectrometry and Hall measurements were performed by A. Smith to determine the implantation damage and electrical dopant activation respectively. Etched Hall bar structures were used to determine the Hall resistance of implanted and annealed samples. From the Hall resistance it is possible to calculate the carrier concentration and therefore the percentage of activated Bi dopants as described in Sec. 4.3.

Table 6.2: Hall measurements of the implanted samples.

Sample	Anneal	Ns (cm^{-2})	Activation
A	650°C	$7.93x10^{14}$	16.4%
A	650°C+900°C spike	$7.60x10^{14}$	15.7%
B	650°C	$4.49x10^{14}$	92.5%
B	650°C+900°C spike	$5.22x10^{14}$	107.6%

Results for the Hall measurements are shown in table 6.2, samples are labeled A and B corresponding to the nominal implanted Bi doping density of 1×10^{20} cm^{-3} or 1×10^{19} cm^{-3} respectively. It can be seen that sample A, implanted to the higher Bi density, only shows an activation of around 16%, leading to an effective substitutional dopant concentration of 1.6×10^{19} cm^{-3}. It is assumed that the other Bi atoms have precipitated from the Si crystal and occupy interstitial sites. This is in good agreement with literature,[150] as it has been shown that Bi forms a metastable state when implanted to concentrations higher than the equilibrium solid solubility of 8×10^{17} cm^{-3}. If the diffusion length of Bi during the anneal reaches the same order of magnitude as the mean distance between to Bi atoms [151] they precipitate and the activation decreases. This is again in good agreement with the fact that the Bi activation for the lower implantation dose in sample B is much higher, reaching 100%, as individual Bi dopants are further apart. Also the spike to 900 °C did not significantly influence the activation of the dopants, supporting diffusion induced precipitation. It is known that much higher Bi activation can be reached even for higher implantation concentrations using techniques that allow very short annealing cycles such as laser or electron beam annealing.[146, 150] For the purpose of creating suitable samples for STM measurements the activation is however only of secondary importance compared to the implantation damage. Both samples should still be suitable for STM analysis since activation levels are sufficiently high to create enough features at the surface and sample A is still close to the metal insulator transition, enabling spectroscopy measurements at low temperatures.

To measure the implantation damage and subsequent recovery during the different annealing steps, Rutherford backscattering spectrometry was used by A. Smith. In channeled RBS the crystal distortion is measured by observing the scattering characteristics

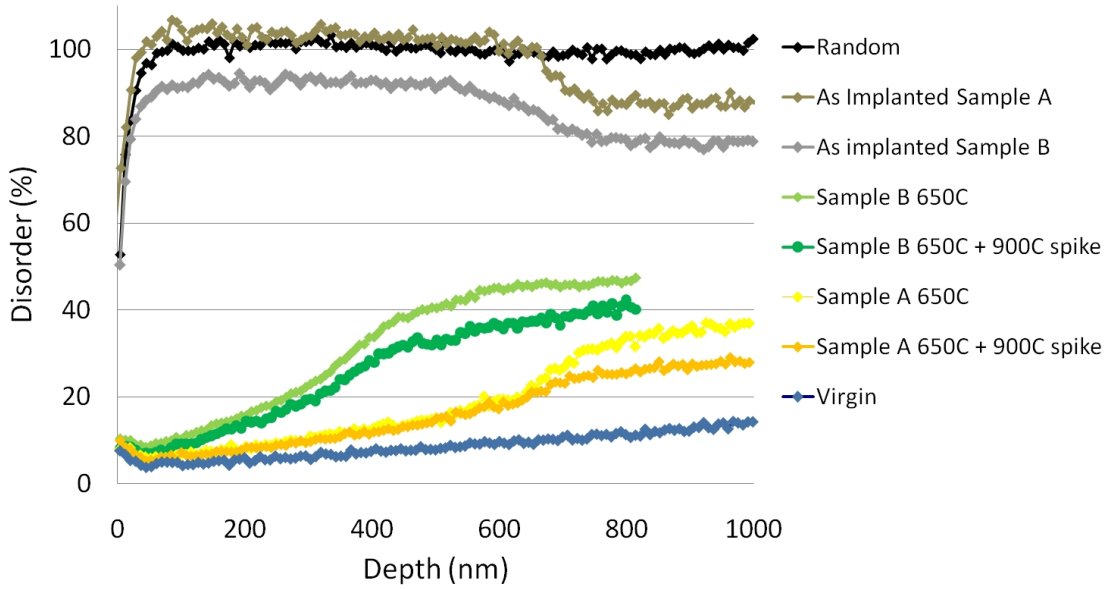

Figure 6.6: RBS measurement of the implanted samples before and after the different annealing steps.

of a ^{4}He+ ion beam. The beam is directed at the sample in one of the high symmetry axes of the silicon crystal, minimizing the scattering cross section as all Si atoms align behind each other, and providing a channel for the He+ ions to travel far into the crystal. If implantation damage distorts the crystal lattice the scattering cross section is however increased and with it the count of backscattered He+ ions. Furthermore, ions that get scattered deep within the crystal lose more energy on their path to the detector and therefore the crystal damage can be resolved as a function of depth by additionally measuring the energy of backscattered ions.

Results for the RBS measurements are shown in Fig. 6.6. Samples with each implantation dose were measured right after the implantation and after the different annealing steps. The as implanted sample can be compared to the backscattering of a He+ ion beam directed at the surface in an arbitrary direction. This prevents the channeling and is equivalent to a completely amorphised and therefore disordered crystal. It can be seen that the higher implantation dose of sample A led to a complete amorphisation of the implanted layer, the signal being equivalent to a random channel orientation. For sample B on the other hand, the damage is slightly lower and the implanted layer appears to be not completely amorphised. This is undesirable and has negative effects on the solid phase epitaxial regrowth (SPER) which is used to recover the monocrystallinity of the sample. Even though counter intuitive, a complete amorphisation is the optimal precondition to ensure best crystal quality after the annealing step. During the anneal the monocrystalline silicon substrate will seed a solid phase epitaxial regrowth and the crystal will reorder, producing a monocrystalline front moving through the amorphised layer and towards the

sample surface. If however the implanted layer still contains pockets of crystalline material, they are less likely to incorporate into the crystal growing from the substrate, and may even seed crystal growth themselves, producing different grains.

The effect of this is clearly evident in Fig. 6.6. It can be seen that sample A, with the high Bi concentration, has recovered much better after the anneal than sample B, independent of the annealing scheme that was used. The effect of the 900 °C spike anneal is also clearly visible, further reducing the damage in both samples even though mainly in the defect band at the frontier between implanted layer and silicon bulk. The increased defect density at the border of the implanted area and the bulk is well understood and attributed to the presence of dislocation loops.[152] They have a higher activation energy and therefore require increased temperatures to be annealed out, in good agreement with the measurement. Compared to the virgin, non implanted silicon, it can be seen that even the sample with the best crystal recovery, achieved by annealing sample A with the high temperature spike, has still an increased backscattering rate. The measured remaining damage, especially within the implanted area, is however very small and it is unclear whether this is due to crystal damage, increased scattering caused by interstitial Bi clusters or simply distortion of the lattice due to the incorporation of the much larger Bi atoms.

6.2 XSTM to Characterize Implantation Damage

We have shown that we can use ion implantation to produce monocrystalline silicon samples with substitutional Bi concentrations above the equilibrium solid solubility of 8×10^{17} cm^{-3}. RBS was used to characterize the implantation damage and a very high crystal quality was found for sample A, created by the complete amorphisation of the implanted layer and the following SPER during annealing. However, we have also found that the activation of dopants in sample A is only around 16% and therefore many precipitated Bi atoms are expected. For sample B a complete activation of 100% was found but also a higher crystal distortion due to incomplete surface amorphisation. It is unclear how all of these different factors will influence the surface quality resulting from cleaving this crystal. As we will cleave the sample and therefore not use an annealing step in the STM, the sample surface will reflect an actual cross section through the implantation profile and it is envisaged that precipitated Bi, crystal dislocations and interstitial Bi will be directly observable in STM images.

6.2.1 Locating the Implanted Layer

The ion implanted area of a cross sectional silicon sample is located right at the edge of the wafer, as indicated in Fig. 6.7. After thinning the sample to 100 μm, it is cleaved in UHV

and the tip is approached to the freshly exposed and clean surface as described in Sec. 3.3.3. Using the coarse motion of the STM it is then possible to walk the tip across the sample cross section towards the implanted area, indicated in Fig. 6.7. By continuously monitoring the extension of the scanner tube it is possible to detect the end of the sample, as the scanner tube will fully extend without establishing tunnelling contact once the tip has fallen over the sample edge. After the edge has been detected, the fine motion of the scanner tube can be used to accurately place the tip at any position within the 600 nm implanted area. Since RBS measurements showed an increased defect density at the interface area between bulk and implanted layer, STM images were usually acquired in the center of the implanted area, 300 nm from the surface, unless stated otherwise.

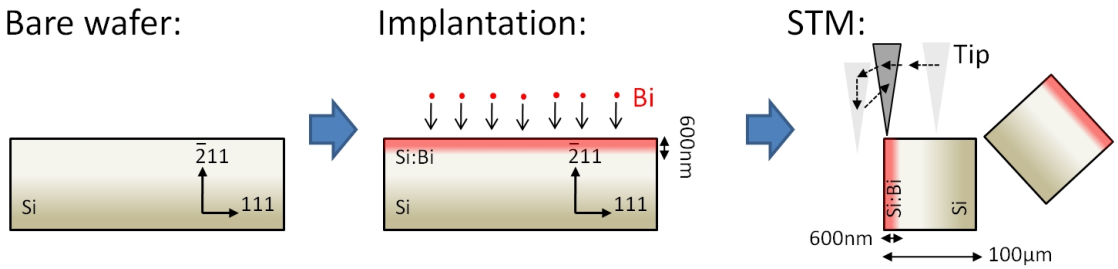

Figure 6.7: Ion implantation is used to introduce Bi dopants into the sample before cleaving them for XSTM. To image the implanted area the tip has to be moved right to the edge of the sample.

To effectively apply this method, the sample surface has to be very flat on a macroscopic scale. As the extension range of the scanner tube is only 500 nm, any step larger than this would either lead to a tip crash or be wrongly detected as the sample edge while walking the tip across the surface. It was found that our cleaving procedure resulted in an extremely flat sample surface and no steps exceeding the range of the scanner tube were detected on any of the measured samples. Another crucial factor to accurately determine the position of the implanted layer is the macroscopic sharpness of the tip. To clearly locate the sample edge, the tip needs a high aspect ratio, otherwise the sides of the tip will make contact to the sample edge and the measured drop from the sample surface will not be sharp. The used etched tungsten tips are ideally suited for this, as their small tip radius and high aspect ratio allowed us to determine the sample edge with an accuracy better than 50 nm.

In addition to the high accuracy obtained in locating the edge of the sample it is also possible to use STS in order to determine whether the tip is positioned within the implanted area or not, indicated in Fig. 6.8. As described in Sec. 5.2, the low n type doped wafer, used as a substrate to implant the Bi donors, shows asymmetric spectroscopy when measured at 78 K. Due to carrier freeze out only the electrons of the ionized background dopants are available for tunnelling and the spectroscopy therefore only shows filled states

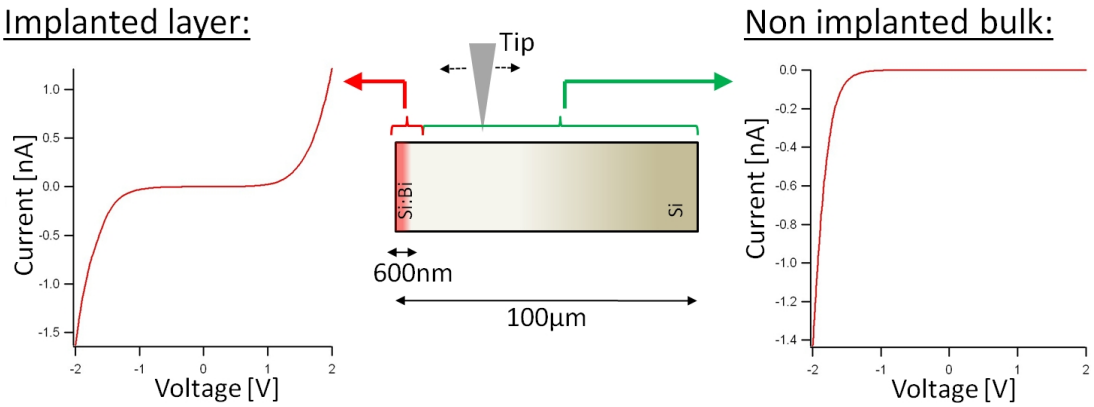

Figure 6.8: The electronic structure of the implanted layer shows conduction in both filled and empty states, characteristic of a degenerately doped semiconductor. In the bulk only filled states are measured, characteristic of a low n-type doped semiconductor at low temperatures.

conduction. The implanted area is however degenerately doped due to the high Bi concentration and the spectra, as shown in Fig. 6.8, becomes symmetric with conduction in filled and empty states. By measuring the local density of states it is therefore possible to unambiguously determine whether the tip is placed within the implanted area or within the unimplanted bulk of the wafer.

6.2.2 Cross Sectional Implantation Damage Profile

To characterize the influence of the implantation damage onto the cleaved surface quality, samples with both implantation concentrations were measured that had been annealed to 600 °C with and without a 900 °C spike. For sample B, implanted with Bi to a concentration of 1×10^{19} cm^{-3}, we found that the implanted layer was not atomically flat and could not be imaged with the STM, as shown in Fig. 6.9.

Whereas the bulk of the sample showed the usual cleavage pattern and crystal quality, the damage in the implanted area was excessive, in good agreement with the RBS data. The same results were obtained for both annealing schemes, independent of the 900 °C annealing spike. The change from monocrystalline bulk to damaged implantation layer was found to be very abrupt as shown in Fig. 6.9. The edge of the sample was located and the tip was then moved 600 nm back into the bulk, corresponding to the depth of the implanted layer. The three successive images shown in Fig. 6.9 were acquired over an area of 150 nm. The crossover from a well ordered atomic structure in the bulk to the disordered surface measured on the implanted area is clearly visible.

Sample A, implanted with Bi to a concentration of 1×10^{20} cm^{-3}, showed a much higher crystal recovery in RBS due to the successful SPER process after complete crystal amorphisation. This was confirmed by the STM images acquired in the implanted area,

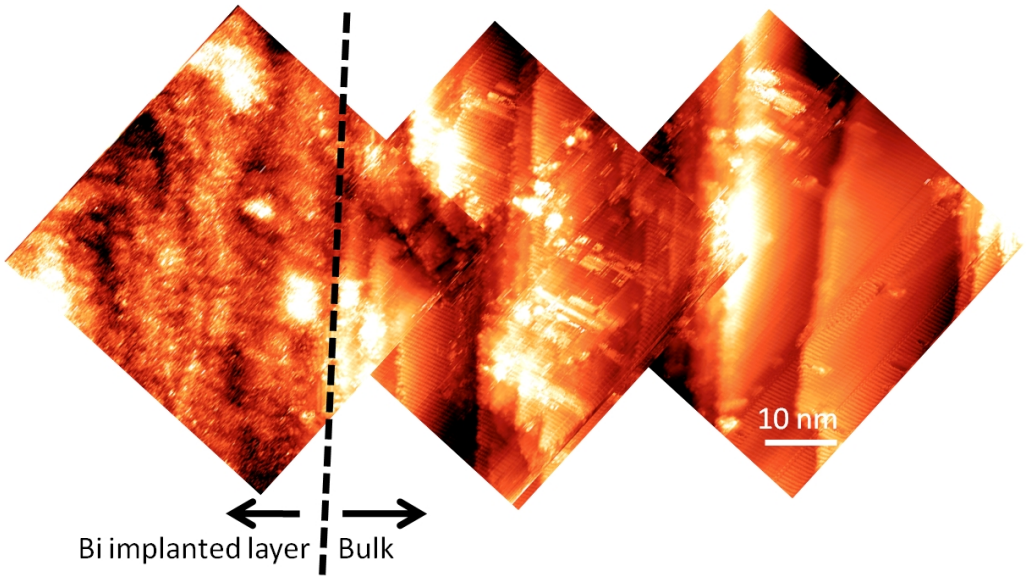

Figure 6.9: Surface characterization of sample B, implanted with Bi to a concentration of 1×10^{19} cm^{-3}. Three images are shown located 600 nm away from the detected sample edge. The change from crystalline bulk to the distorted implanted area is clearly visible.

shown in Fig. 6.10 b). Results for the two different annealing procedures were found to be very similar and the additional spike anneal was found to have no influence on the surface quality in the implanted layer. This is again in agreement with the RBS measurements, which showed that the crystal quality mainly improved at the frontier between implanted layer and silicon bulk, but not significantly in the implanted area itself.

a) b)

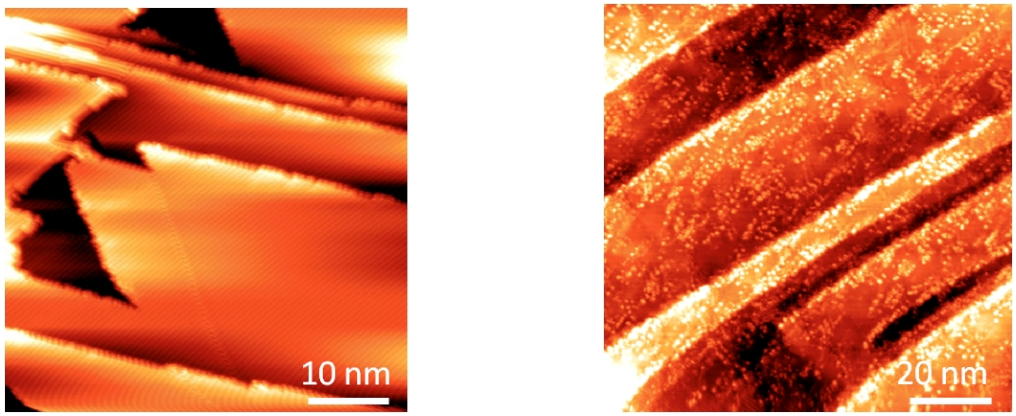

Figure 6.10: Surface characterization sample A, annealed to 650 °C plus 900 °C spike. a) Surface quality in the unimplanted bulk of the sample. b) Surface quality on the Bi implanted layer of the sample.

Figure 6.10 a) displays an image acquired in the bulk of the sample, showing the normal monocrystalline surface quality. In Fig. 6.10 b) an image in the implanted area of the same sample is shown. It can be seen that large terraces are formed similar to the

unimplanted area, representing a significant improvement compared to sample B. However, many atomic scale defects are present on the surface, disturbing the usually clean and almost defect free surface reconstruction observed in the monocrystalline bulk. To determine the nature of these defects, high resolution images of the implanted area were acquired as shown in Fig. 6.11.

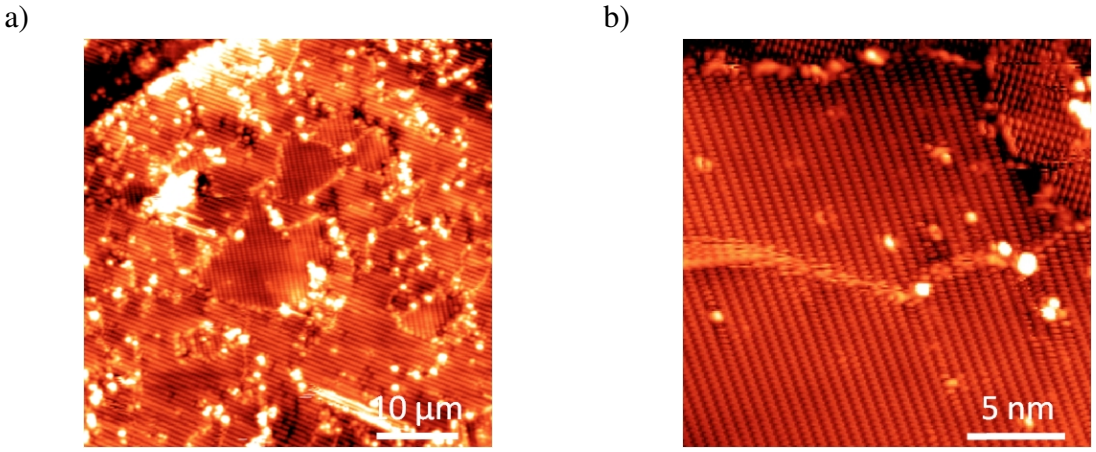

Figure 6.11: Defect characterization sample A, annealed to 650 °C plus 900 °C spike. a) Typical surface quality in the implanted area. b) Large area with lower defect concentration.

It can be seen that the surface is characterized by small but perfectly reconstructed areas, displaying the expected π-bonded chains of the Si(111)-2x1 surface. These little pockets are separated by domain and anti phase boundaries which in turn are pinned by the atomic scale defects on the surface. It is important to note that the areas displaying π-bonded chains with different orientations are not different crystal grains. As explained in Sec. 2.2.2, π-bonded chains can be oriented in all three equivalent $[01\bar{1}]$ orientations due to the symmetry of the hexagonal Si(111) surface. It is therefore assumed that, even though the crystal is largely monocrystalline, the point defects observed on the surface influence the formation of the Si(111)-2x1 reconstruction during the cleaving process and lead to the observed pattern. This is in good agreement with the proposed mechanism for the pinning of anti phase boundaries (APBs), as discussed in Sec. 5.6.5.

Even though the surface quality is still poor, inside the defect free and reconstructed Si(111)-2x1 areas a variety of features can be observed, as shown in Fig. 6.11 b). These are likely to be induced by the Bi dopants, suggesting that it is possible to study implanted Bi donors individually and at the atomic scale. However, to successfully do so the surface quality has to be further improved by reducing the number of defects which are pinning the APBs and domain boundaries.

6.3 Optimizing the Implantation and Annealing Procedure to Study Dopants in XSTM

We have demonstrated that it is possible to image the cleaved Si(111)-2x1 surface reconstruction on samples containing a high dose of implanted Bi donors. The two analyzed implantation concentrations resulted in very different crystal quality and dopant activation characteristics after annealing. We found that the surface of the sample with the higher implantation concentration was measurable in STM with atomic resolution but the sample surface was of very poor quality. To improve it, further analysis was conducted determining how the measured RBS damage profiles and Hall activation measurements correlate with the observed cleaving behavior and the sample surface contamination.

6.3.1 Interstitial Dopants vs Implantation Damage

The surface of sample A was found to be covered in adatoms and defect clusters, pinning APBs and domain boundaries and making measurements of individual Bi dopants very challenging. To determine the origin of these observed defects, two different sources were considered. RBS data has shown that the scattering rate in the implanted layer is still increased and therefore point defects in the silicon crystal may be present, causing the observed surface disturbance. On the other hand Hall measurements have shown a Bi activation of only 16% due to diffusion induced precipitation and it is therefore also plausible that the observed defects are precipitated Bi atom clusters.

Differentiating between implantation damage and precipitated Bi is possible by analyzing sample B, as it shows a higher defect density in RBS measurements but has a dopant activation of 100% and therefore contains no precipitated interstitial Bi atoms. However, sample B was found to not cleave atomically flat and acquiring STM measurements with atomic resolution was not possible. Again it is unclear whether this bad cleaving behavior is simply due to the increased defect density in the implanted layer or whether it occurs due to the increased amount of dislocation loops at the interface to the bulk. When comparing the RBS traces in Fig. 6.6 it can be seen that the defect density of sample B, 200 nm from the surface, is comparable to the defect density of sample A 800 nm from the surface. Nevertheless, sample A was measurable in STM across the whole surface, whereas sample B was not measurable anywhere in the implanted area. A possible explanation for these seemingly contradicting results can be found when considering the high concentration of dislocation loops in sample B. These large crystal defects can induce strain[153] at the interface to the bulk and might significantly disturb the macroscopic cleaving process, preventing the formation of an atomically flat surface even in the implanted area with lower defect density. To conclusively differentiate between bad macroscopic cleaving be-

havior, implantation defects and precipitated Bi, we have therefore first focussed on the influence of the dislocation loops on the macroscopic cleaving behavior of sample B.

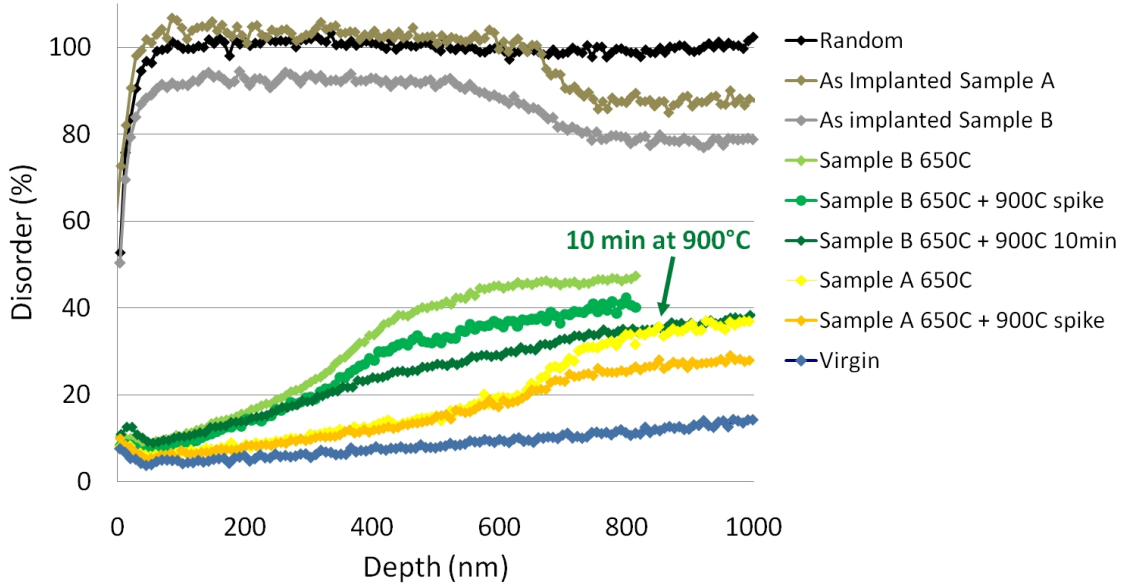

Figure 6.12: RBS measurement including the new anneal of sample B to 650 °C for 3 min and 900 °C for 10 min.

To achieve a further reduction of the dislocation loop density, the thermal budget of the annealing process for sample B was increased. Instead of annealing at 650 °C for 3 min and then spiking the temperature to 900 °C it was kept at 650 °C for 3 min and then at 900 °C for 10 min. The results of the subsequent Hall measurements showed that the electrical activation was still 100%, whereas the RBS data confirmed a significant reduction in dislocation loops, as shown in Fig. 6.12. It can be seen that the crystal damage recovery has not significantly changed up to a depth of 300 nm due to the longer anneal at 900 °C. In the dislocation loop band at the interface to the bulk, the backscattering rate was however significantly reduced and is now exactly coinciding with the RBS trace of sample A, annealed at 650 °C. From previous experiments we know that sample A annealed at 650 °C did cleave and produce an atomically flat surface, even though covered in defects. The surface properties of this newly annealed sample B can therefore not be attributed to bad macroscopic cleaving behavior and should accurately reflect the influence of increased crystal damage and reduced Bi precipitation when compared to sample A.

Results of the STM surface characterization for sample B, annealed at 900 °C for 10 min, can be seen in Fig. 6.13. The macroscopic cleaving behavior was significantly improved and the characteristic surface structure with monatomic steps was found, as shown in Fig. 6.13 a) for the interface region between implanted layer and bulk. However, the surface quality was much worse compared to sample A, as shown in Fig. 6.13 b)+c) respectively. It can be seen that the defect density on the surface of sample B is much

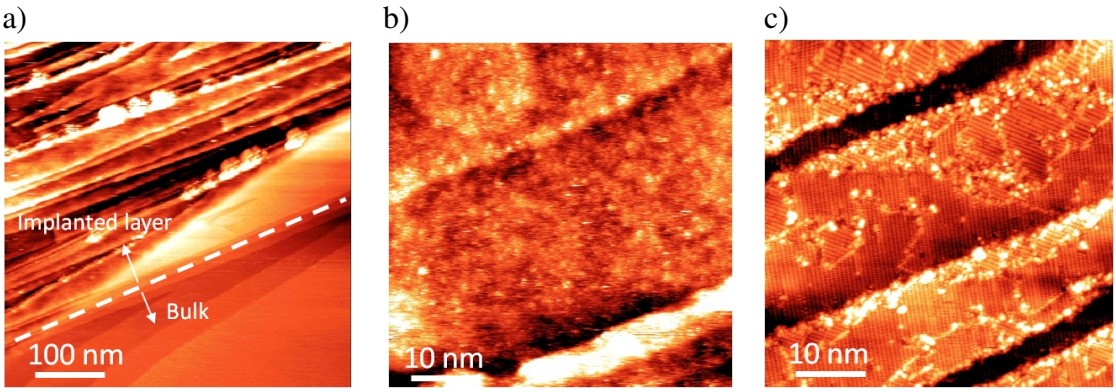

Figure 6.13: Surface characterization of the new anneal of sample B. a) Large scale image at the interface between implanted area and bulk. b) Surface quality in the implanted area sample B, annealed to 650 °C for 3 min and 900 °C for 10 min. c) Surface quality in the implanted area sample A, annealed to 650 °C for 3 min and 900 °C for 1 s.

higher than on sample A, making a measurement of the Si(111)-2x1 surface with atomic resolution impossible. As we know that dopants in sample B are 100% activated, precipitated Bi can be excluded and it is therefore concluded that the observed defects on the Si(111)-2x1 surface of implanted samples result from remaining implantation damage.

6.3.2 Crystal Recovery Beyond the Sensitivity of RBS

We have shown that the observed defects on the surface of sample A result from remaining crystal damage created by the implantation process. To test wether this damage can be further reduced, we have annealed sample A at higher temperatures and for a longer time. From the implantation run on the Si(100) surface, described in Sec. 6.1.1, we already know that annealing to 1200 °C leads to a complete removal of the Bi dopants from the Si crystal. New annealing steps at 1000 °C and 1100 °C for 3 min were therefore tested, still starting with a 650 °C annealing step for 3 min to make the results directly comparable to all other obtained data.

Table 6.3: Hall measurements of the implanted samples, including new annealing steps.

Sample	Anneal	Ns (cm^{-2})	Activation
A	650°C	$7.93x10^{14}$	16.4%
A	650°C+900°C spike	$7.60x10^{14}$	15.7%
A	650°C+1000°C 3min	$3.47x10^{14}$	7.2%
A	650°C+1100°C 3min	$3.26x10^{14}$	6.7%
B	650°C	$4.49x10^{14}$	92.5%
B	650°C+900°C spike	$5.22x10^{14}$	107.6%
B	650°C+900°C 10min	$4.94x10^{14}$	101.8%

The Hall measurements showed a further reduction in Bi activation, as displayed in table 6.3, due to the previously discussed diffusion induced precipitation. It can be seen that the percentage of electrically active donors dropped from 16% when annealed at 900 °C to 7% when annealed at 1000 °C or 1100 °C. The difference in activation between the two high temperature annealing steps is very small and they result in an activated Bi concentration of 7.2x10^{18} cm^{-3} and 6.7x10^{18} cm^{-3} respectively. This concentration is still suitable to study individual Bi atoms as it corresponds to a surface density of over 10 dopants in the area of a 100 nm square image. However, the concentration is below the metal insulator transition for Bi in silicon, which was reported[143] around 2×10^{19} cm^{-3}. Since STM measurements were conducted at 78 K, it is therefore important to verify the influence of carrier freeze out and make sure STS measurements are not distorted by tip induced band bending.

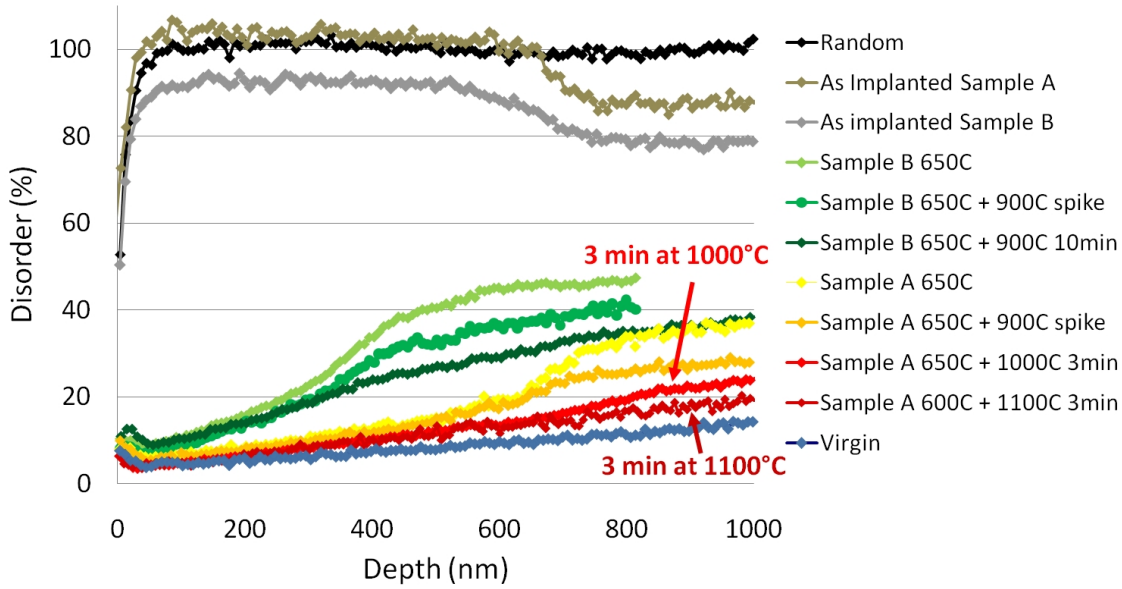

Figure 6.14: RBS damage recovery measurement. The new traces of sample A annealed at 1000 °C and 1100 °C show additional improvement in the interface area to the bulk but no measurable difference in the implanted layer itself.

The results of the RBS measurements for sample A, annealed at higher temperatures, can be seen in Fig. 6.14. The two different areas, implanted layer and dislocation loop band at the interface to the bulk, show slightly different behavior and are considered separately. The dislocation loops are clearly reduced with increased temperature. For the sample annealed at 1100 °C, they have dropped below a detectable level as the increase in scattering at the interface to the bulk is not visible anymore, indicating an excellent crystal recovery across the whole sample. When considering the implanted layer on the other hand, we can see that the change in damage recovery between 650 °C and 1100 °C is very small and there is no measurable improvement at all between 1000 °C and 1100 °C.

The measured damage profiles for the different annealing temperatures have converged and are not further improving, even though they still show a slightly increased scattering rate when compared to the non implanted crystal. This increased scattering rate could be attributed to the lattice disturbance created by the incorporation of the much larger Bi atoms and is not necessarily an indication of remaining crystal damage. At the point where STM measurements were conducted, 300 nm from the surface, RBS is therefore not able to resolve a significant difference in crystal recovery anymore as it seems the damage has already dropped below the detectable limit of 1%.[143]

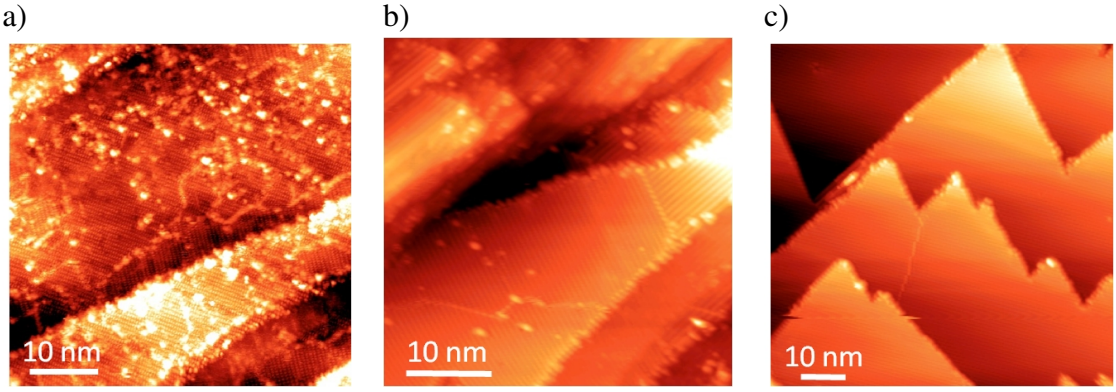

Figure 6.15: STM surface characterization of sample A annealed to different temperatures. a) Annealed to 900 °C for 1 s, high defect density. b) Annealed to 1000 °C for 3 min, defect density is reduced. c) Annealed to 1100 °C, almost no defects observed anymore.

The results of the STM surface characterization are shown in Fig. 6.15 a)-c) for annealing temperatures of 900 °C, 1000 °C and 1100 °C respectively. Even though RBS was not able to resolve a significant difference in damage recovery between these three samples, the STM surface characterization shows a very clear trend. The number of defects on the surface is significantly reduced when annealing the sample to 1000 °C and the implanted layer annealed at 1100 °C is not distinguishable from the non implanted bulk of the wafer anymore. This demonstrates the increased sensitivity of cross sectional STM to characterize crystal damage compared to RBS. Furthermore, it also confirms the fact that precipitated Bi is not the cause of the observed defects, as higher annealing temperatures correspond to lower Bi activation and therefore would lead to the opposite of the observed trend. The surface quality of both samples annealed at 1000 °C and 1100 °C is sufficiently high to enable the atomic scale characterization of single Bi atoms in the cleaved Si(111)-2x1 surface. The discussed implantation and annealing recipes might therefore provide a suitable process to prepare samples for single Bi donor characterization at the atomic scale, given that the electrical activation is sufficiently high to enable STM measurements at 78 K without significant tip induced band bending.

To determine if there is an influence of tip induced band bending when measuring sam-

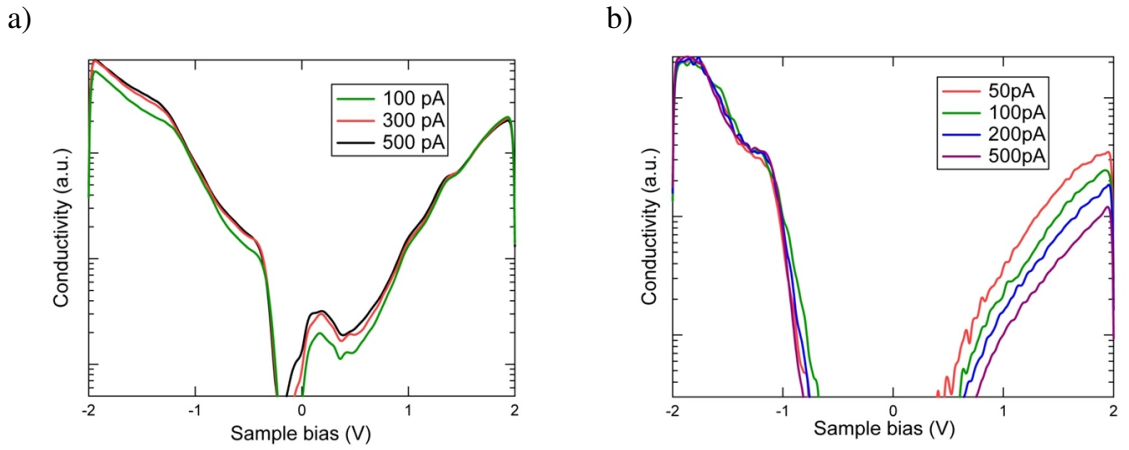

Figure 6.16: Normalized STS setpoint dependence of sample A. a) Annealed to 1000 °C, STS scales with setpoint and normalized curves therefore overlap. b) Annealed to 1100 °C, STS does not scale with setpoint, normalized curves not overlapping and onset of conduction band shifted due to tip induced band bending.

ples annealed at 1000 °C and 1100 °C, setpoint dependent scanning tunnelling spectra were recorded as shown in Fig. 6.16 a) and b) respectively. If tip induced band bending is negligible, the measured tunnelling conductance should scale linearly with the current setpoint as described in Sec. 2.1.3. If different tunnelling spectra are therefore normalized by dividing them through their current setpoint, they should be overlapping as was indeed the case for sample A annealed at 1000 °C, shown in Fig. 6.16 a). For the sample annealed to 1100 °C on the other hand, the conduction band onset and the normalized tunnelling conductance in empty states was found to be strongly dependent on the current setpoint as shown in Fig. 6.16 b). This clear signature of tip induced band bending is surprising because Hall measurements showed a very small difference in the concentration of active Bi dopants between samples annealed at 1000 °C and 1100 °C, as seen in table 6.3. Nevertheless, within the accuracy of the Hall measurements, the higher annealing temperature must have caused the concentration of activated donors to drop below a critical level. Sample A, annealed at 1100 °C, was therefore found not suitable for low temperature STM characterization of single Bi atoms due to its susceptibility to tip induced band bending. Further differences between the STS measurements recorded on the two differently annealed samples include a significant increase in the bandgap and the shift of the valence band onset towards negative voltages for the higher temperature anneal. These characteristics will be discussed in detail in Sec. 6.4.2.

Choosing suitable implantation and annealing parameters we have successfully demonstrated that it is possible to form a Si(111)-2x1 reconstructed surface with low defect density from cleaving a sample with a high concentration of electrically active Bi dopants. We found that a high Bi implantation dose is crucial in order to make the silicon crystal

completely amorphous in the implanted area and subsequently allow high quality solid phase epitaxial regrowth. However, it should be possible to also employ this process to create samples for STM measurements with low dopant densities. This can be achieved by amorphising the layer beforehand by for example implanting a high dose of Si atoms. The dopant implantation in a subsequent step can then be carried out with any desired concentration, while still achieving the necessary high quality crystal regrowth after annealing. We further found that RBS does not have sufficient sensitivity to determine whether the annealed samples are suitable for STM measurements, as samples with identical backscattering profiles resulted in very different defect densities on the surface observed in STM. Furthermore, in the case of Bi, care has to be taken when choosing the annealing temperature as a tradeoff exists between the reduction of the defect density and the deactivation of Bi donors when going to higher annealing temperatures. Nevertheless, we were able to successfully demonstrate that annealing a sample implanted with a Bi concentration of 1×10^{20} cm^{-3} to a temperature of 650 °C for 3 min followed by 1000 °C for 3 minutes results in a high quality crystal suitable for STM measurements. The concentration of electrically active Bi dopants was furthermore sufficient to allow low temperature STS measurements and is also high enough to produce a surface density of Bi atoms suitable for single dopant STM studies. This process is therefore ideally suited to enable, for the first time, the study of individual Bi dopants at the atomic scale, as we will demonstrate in the next chapter.

6.4 Resolving the LDOS along the Implantation Cross Section

When locating the edge of the wafer with the STM tip, we demonstrated that is is possible to measure the change in electronic structure induced by the dopants using STS. The clearly distinct LDOS of the highly doped implantation layer and the low phosphorus doped bulk of the wafer provided an excellent control to confirm that the tip is positioned within the implanted area, as shown in Fig. 6.8. However, besides using STS as a tool for locating the implanted layer, we can additionally harness its capabilities to analyze the evolution of the band structure within the implanted area as shown in Fig. 6.17.

The capability of STM to resolve the LDOS together with the ability to position the tip with high lateral control on any part of the implanted layer enables us to map out the LDOS of the cross sectional implantation profile. Whereas SIMS and Hall measurements are able to quantitatively determine the dopant concentration as a function of depth or the number of electrically active dopants respectively, STS can provide complementary information about the spatial distribution of the electronic properties in the implanted

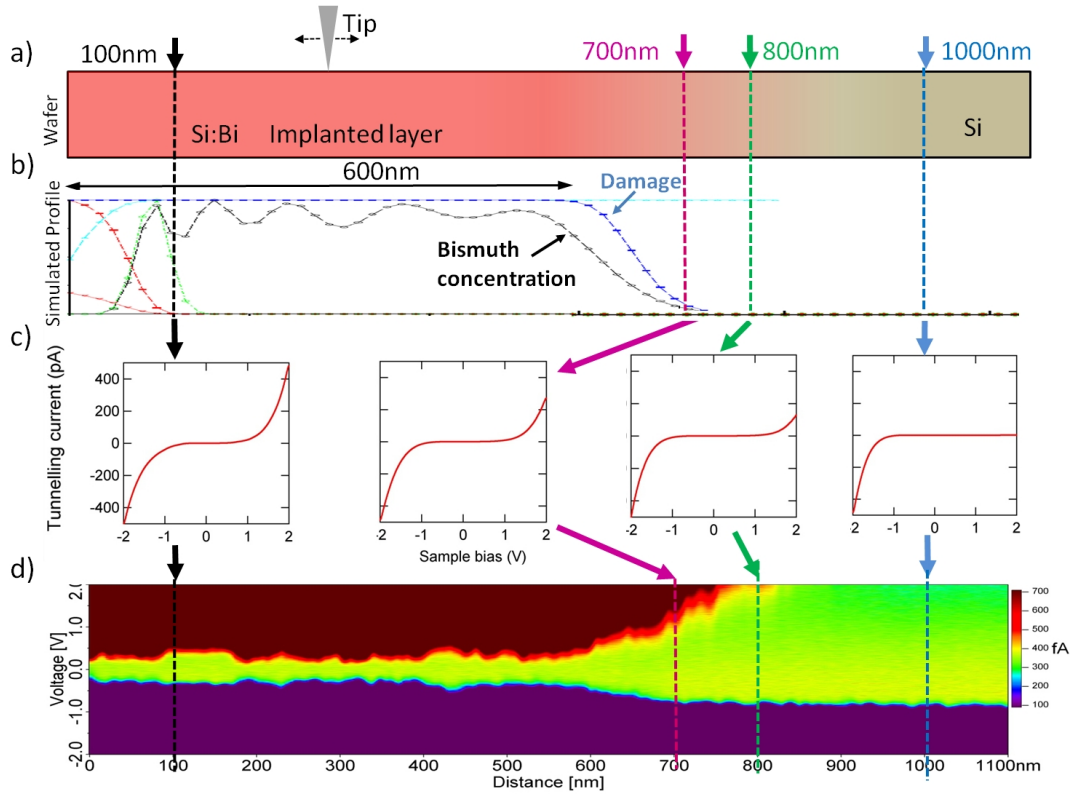

Figure 6.17: Measuring the cross sectional evolution of the LDOS. a) The tip is moved across the cross section. b) Simulated dopant implantation profile. c) STS curves acquired at positions indicated by the colored lines. d) Plotting all acquired STS curves against their position in a two dimensional image, the colour scale indicating the current magnitude.

layer. By measuring the LDOS in the implanted area we can therefore determine the depth profile of the semiconductor band structure, influenced by the electrically active dopants, and qualitatively compare it to the theoretically calculated implantation concentration as shown in Fig. 6.17.

To measure the LDOS as a function of implantation depth we positioned the tip right at the edge of the wafer, which was detectable with an accuracy of 50 nm as described in Sec. 6.2.1. The tip was then moved towards the bulk of the wafer in steps of 1 nm, covering a distance of over one micron and acquiring an STS measurement at every point along the way. As shown in the bottom part of Fig. 6.17, the acquired STS spectra were then plotted as a function of distance from the edge, the voltage on the y axis and the color indicating the measured current. The implantation layer is clearly resolved, especially when observing the measured empty states current, characterized by high currents at positive bias up to a depth of 600 nm and then tailing off towards zero. This is in excellent agreement with the theoretically calculated implantation profile shown in the top part of Fig. 6.17 and demonstrates that we are able to resolve the cross sectional LDOS of the implanted area.

6.4.1 Band Structure

Using this new technique we have analyzed the cross sectional LDOS of sample A, annealed at 650 °C and 1000 °C for 3 min, as shown in Fig. 6.18. Potential lines are overlaid to indicate constant current levels in both filled and empty states. Again the 600 nm implantation layer is clearly resolved and three different regions can be observed as indicated by the gray lines, labeled I-III respectively.

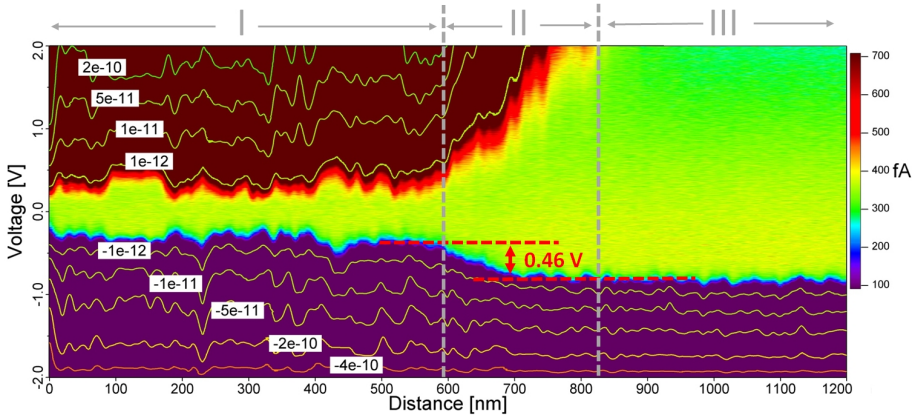

Figure 6.18: Cross sectional LDOS of sample A, annealed at 650 °C and 1000 °C for 3 min. Potential lines for the measured STS current are overlaid and three different areas marked I-III are indicated by the grey lines.

In area I, ranging from the sample edge to 600 nm, the LDOS are characteristic for a high n-type doped Si(111)-2x1 surface as described in Sec. 2.3.1. The band structure displays an almost symmetric LDOS in filled and empty states. The conductance and valence band edges are clearly resolved and the lateral extent of area I is in excellent agreement with the expected bismuth distribution resulting from the implantation process.

In area III, the acquired STS spectra are very asymmetric and no current is measured in empty states. This is again in good agreement with the expected behavior of the non implanted bulk of the wafer measured at low temperatures, as characterized in Sec. 5.2. The low phosphorus doped wafer only provides electrons as mobile charge carriers since almost all intrinsic carriers are frozen out at 78 K and the positively charged phosphorus dopant cores are too far apart to support hole conductance. As described previously, this leads to the inability of applying a positive bias between the tip and the semiconductor surface. Establishing an empty states tunnel current therefore becomes impossible, even when applying the maximum bias of ten volts.

Area II shows the intermediate range between the high Bi implanted layer and the low P doped bulk and therefore the evolution of the LDOS at 78 K when changing the n-type doping concentration from 7.2x10^{18} cm^{-3} to 1x10^{15} cm^{-3}. It can be seen that, when moving towards the bulk from 600 nm, the bandgap widens as both conduction and valence band edges are shifted to higher bias voltages. At around 700 nm, the valence

band edge reaches the level of area III and remains constant, whereas the conduction band edge keeps moving to higher energies and finally disappears from the measured range, 800 nm away from the sample edge.

To explain the observed change in the measured LDOS, occurring due to the change in dopant concentration, different possible causes were considered. One of the main effects of doping silicon is a shift in the Fermi energy and the resulting change in charge carrier concentrations. At 78 K the shift in Fermi energy, when changing the doping concentration from 7.2x10^{18} cm^{-3} to 1x10^{15} cm^{-3}, is however less than 100 meV.[113] This is significantly smaller than any of the observed changes in the conduction as well as the valence band. Furthermore, a change of the Fermi energy would result in a symmetric shift of the band structure. In the case of the decreasing n-type dopant concentration of this sample, both bands would be expected to shift upwards, clearly not in agreement with the observed widening of the bandgap. It is therefore evident that the shift in Fermi energy cannot be the main cause for the measured change in STS. This is sensible due to the fact that the Fermi level position at the surface is pinned by the surface states as described in Sec. 2.2.3. A change in the bulk Fermi level is therefore not directly observable when measuring the LDOS at the surface.

To explain the observed change in LDOS we consider empty and filled states separately. We have already discussed that a lack of hole carriers is responsible for the inability to establish a positive bias voltage between tip and sample, explaining the lacking empty states current in the bulk. The transition region imaged in area II can therefore be attributed to an increase in tip induced band bending due to the continuous decrease of hole carriers. While the doping density decreases, the positively ionized dopant cores become more separated and their ability to screen an electric field in the semiconductor is reduced. The space charge region is therefore increasing in size and tip induced band bending shifts the measured conduction band edge towards higher voltages. As the doping density is further decreased, hole conduction is suppressed because the distance between positively charged dopant cores becomes too large. Establishing a stable tunnel junction at positive bias voltages eventually becomes impossible, as shown in Sec. 5.2. The fact that tip induced band bending is responsible for the measured shift in the conduction band can be tested by acquiring STS curves in area II with varying tip sample distances, as shown in Fig. 6.19 a). STS curves were normalized by dividing them through their setpoint current as described in Sec. 6.3.2 and it can be seen that the normalized empty states current is strongly setpoint dependent, in good agreement with the proposed tip induced band bending.

Due to the symmetry of the observed shift in the conduction and valence band, a similar effect seems likely to explain the measured filled states current. In Fig. 6.18 it can be seen that the valence band edge is shifted downwards by 0.46 eV due to the changing dopant

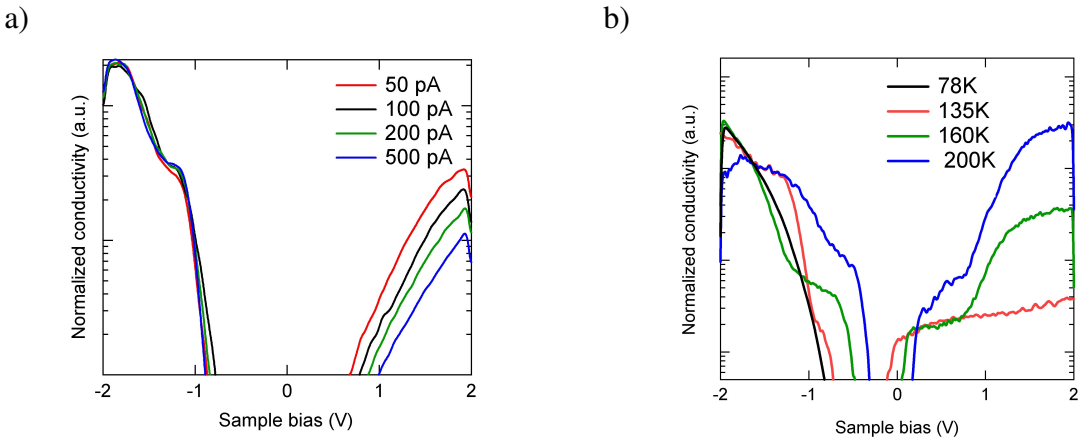

Figure 6.19: a) Setpoint dependence of normalized tunnelling conductance in area II of sample A, annealed at 1000 °C. b) Reprint of the temperature dependent tunnelling spectroscopy of the non implanted, low phosphorus doped wafer bulk.

concentration in area II. However, creating a stable tunnelling junction at negative bias is possible even in the non implanted bulk of the wafer. This demonstrates that sufficient electrons are available to shift the Fermi energy of the tip and the sample with respect to each other and establish a bias between tip and sample. Additionally, the valence band edge in Fig. 6.19 a) shows no setpoint dependence and it seems the bands can not be shifted further than the measured 0.46 eV, even when going to much higher currents. These dissimilar characteristics observed for the shifts in conduction and valence band suggest that the underlying mechanism is different.

When considering the electronic structure of the Si(111)-2x1 surface as discussed in Sec. 2.2.3, tip induced band bending at negative bias voltages seems unlikely as the Fermi level is pinned at the bottom of the surface conduction band. The band structure of the silicon surface and the tungsten (W) STM tip used in our measurements are shown as separate systems in Fig. 6.20 a). The Fermi level at the Si(111)-2x1 surface is pinned 0.4 eV above the valence band as experimentally determined by Himpsel et al.[71] Any further downward tip induced band bending is therefore unlikely as moving the Fermi level even a small amount into the surface conduction band would significantly increase the accumulation layer and effectively compensate the applied bias. Assuming a pinned Fermi level, it is therefore not possible to explain the observed shift in the valence band with tip induced band bending.

To explain the origin of the shift in the valence band we also consider a previous experiment. When analyzing the temperature dependent STS measurements of the non implanted low phosphorus doped wafer bulk in Sec. 5.3, we similarly encountered a large shift in the band structure which could not be explained by the changing Fermi energy. The STS traces are shown again in Fig. 6.19 b) and the shift of the band structure is

clearly evident and is in the same range as the measured shift in the cross sectional LDOS measurement. To explain the temperature dependent shift we suggested that the pinning position of the Fermi level at the surface might be influenced by the changing carrier concentration. This proposed effect is supported by the observations from the cross sectional LDOS measurement, since decreasing the doping concentration also results in a reduced carrier concentration and we again observe a similar shift in the electronic structure. A possible mechanism how the carrier concentration could be linked to the Fermi level pinning is shown in Fig. 6.20.

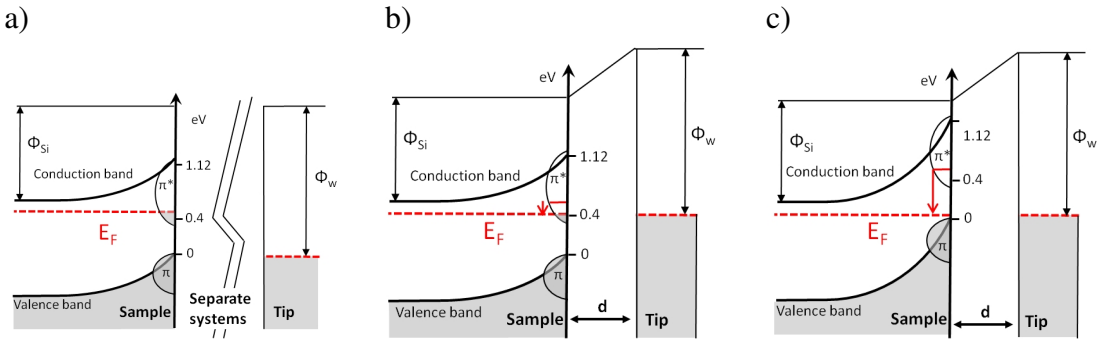

Figure 6.20: TIBB on the Si(111)-2x1 surface at different carrier concentrations. a) Band structure of the Si(111)-2x1 surface and the W tip as separate systems. b) Induced band bending by the presence of the W tip at high carrier concentration, Fermi level still pinned. c) TIBB by the presence of the W tip at low carrier concentrations, Fermi level unpinned.

In Fig. 6.20 a) the Si surface and the tip are shown as separate systems. The additionally available states in the surface conduction band pin the Fermi energy at 0.4 eV and bend the bands upwards to a depth of several nanometers. This creates a depletion region underneath the surface as electrons from the semiconductor bulk accumulate in the surface conduction band, creating the shown static band bending. The amount of electrons accumulating in the bottom of the surface conduction band is dependent on the number of carriers in the space charge region and was estimated[120] around 4×10^{13} cm^{-2} for a dopant concentration of 6×10^{18} cm^{-3}. The tungsten (W) tip is also shown and the different electron affinities of silicon and tungsten are indicated. Quoting an exact value for the expected electron affinities in the experiment is difficult especially for tungsten tips, as it is dependent on the crystal facet and values between 3.5 eV and 6.0 eV have been reported.[154] However, with a silicon electron affinity of 4.05 eV the work function of tungsten is usually assumed to be significantly higher than that of silicon,[118] as indicated in the schematic.

If the tip is approached to the semiconductor surface and brought into tunnelling range, this difference in work function results in a potential difference as shown in Fig. 6.20 b). The presence of the tip therefore induces band bending in the semiconductor even though

no bias is applied.[118, 155] In our case this band bending would occur upwards as the work function of tungsten is higher than that of silicon. However, Garleff et al.[120] calculated that the charge carrier concentration necessary to compensate the field of a tip even at 2 V bias is only 3.8×10^{12} cm^{-2}. As this charge density is only 10% of the density of electrons in the surface conduction band, the change of the Fermi level induced by the presence of the tip is negligible compared to the Fermi level pinning, as indicated in Fig. 6.20 b).

However, if the charge carrier concentration drops due to reduced temperatures or reduced doping densities, the amount of electrons trapped in the bottom of the conduction band will be significantly reduced. In the case of sample A, the doping density and with it the charge carrier concentration is reduced by almost four orders of magnitude. It is therefore assumed that, at some point, the amount of electrons pinning the Fermi level at the bottom of the conduction band reaches a comparable number to the charge carriers necessary to shield the influence of tip due to its increased work function. As this happens, the Fermi level becomes unpinned as shown in Fig. 6.20 c).

This is in excellent agreement with the measured behavior. As the Fermi level becomes unpinned, the bands will be shifted upwards due to the influence of the tip work function. This band bending is limited by the top of the surface valence band and therefore a maximum shift of 0.4 eV is expected. This new position of the Fermi level, shown in Fig. 6.20 c), has a significant influence when measuring the LDOS in STS. Upon applying a negative bias, the bands can now be bent downwards by a maximum of 0.4 eV before the Fermi level reaches the bottom of the conduction band and is pinned again. This explains why the bands can not be bent any further once the maximum band bending is reached and therefore why the filled states current in Fig. 6.19 a) was found not to be setpoint dependent. It is therefore assumed that the measured shift in both cases, the temperature dependent experiment and the area of changing dopant concentration, is caused by the unpinning of the Fermi level due to the reduced carrier concentration and the presence of the tungsten STM tip.

Of course the proposed unpinning of the Fermi level also has implications on the measured empty states current, as it would lead to a downwards shift of the conduction band. However, it is assumed that once the electron concentration is low enough to stop pinning the Fermi level, the hole concentration is already too low to effectively allow biasing the surface, dominating the influence of a shift in the Fermi energy. The fact that the measured sifts of 0.5 eV in temperature dependence and 0.46 eV for the changing dopant concentration are slightly larger than expected is sensible, as the quoted value of 0.4 eV was experimentally determined by Himpsel et al.[71] for intrinsic silicon. It can therefore be assumed that the pinning position of the Fermi energy for n-type doped semiconductors is 50 meV to 100 meV higher, as experimentally determined in this experiment.

This experiment impressively demonstrates the capability of XSTM to analyzie the

qualitative evolution of the band structure over a wider range of dopant concentrations. In order to get quantitative information from the measured LDOS profile and for example determine the Fermi level pinning position as a function of dopant concentration, SIMS measurements could be used. By correlating the measured LDOS profile with the exact dopant concentration measured from SIMS it would be possible to resolve the LDOS of the Si(111)-2x1 surface as a function of dopant or carrier concentration. However, due to the 50 nm uncertainty in determining the edge of the sample with the STM tip, slowly varying dopant profiles would have to be created. Varying the implantation concentration in discrete steps that can be resolved in the STM would then for example allow to resolve the LDOS as a function of precisely known dopant density. Nevertheless, even without knowing the exact profile of the dopant concentration, we were able to determine and explain the fundamental process taking place when performing STS measurements on the Si(111)-2x1 surface with dopant carrier concentrations varying over several orders of magnitude.

6.4.2 Evaporation of Dopants from Silicon

STS measurements performed on the implanted layer of sample A annealed to 1000 °C and 1100 °C have revealed that the concentration of electrically activated Bi dopants drops below a critical level for the higher annealing temperature. As previously shown in Fig. 6.16, the sample annealed to 1100 °C is affected by TIBB, suggesting that the Fermi level is not pinned anymore. In Sec. 6.1.1 we have suggested that the decreasing Bi concentration with increasing annealing temperatures might be a result of Bi evaporation from the surface, following its documented segregation.[146, 147] This is supported by the LDOS profile measured on sample A annealed to 1100 °C as shown in Fig. 6.21.

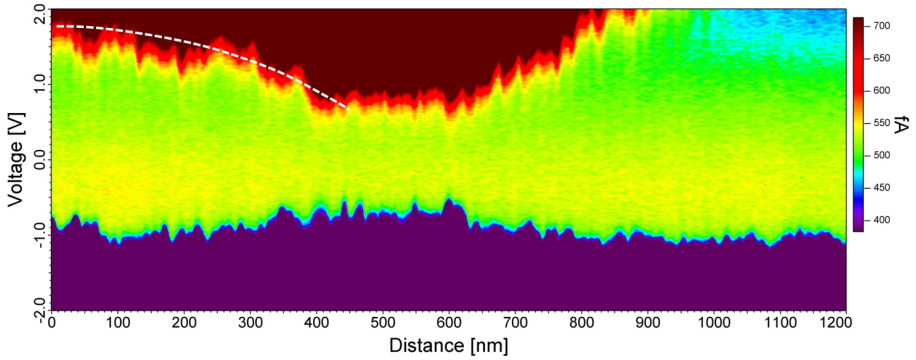

Figure 6.21: Cross sectional LDOS of sample A, annealed for 3 min at 650 °C and 1100 °C. The dopant concentration is reduced towards the surface, as indicated by the white line.

It can be seen that the LDOS profile is not constant anymore in the implanted area. Besides having a generally larger band gap and tailing off towards the non implanted bulk,

the carrier concentration also seems to reduce when moving from 400 nm towards the surface. Both the conduction and valence band are shifted towards higher voltages when approaching the surface, consistent with a reduction in the Bi concentration as discussed earlier. Even though the carrier density can not be extracted from the profile, the qualitative change in the band structure agrees well with a diffusion induced profile created from Bi evaporation at the sample surface.

7 Individual Group V Donors in Silicon

Understanding the properties of individual dopant atoms in semiconductors is of fundamental importance for next generation electronic devices and future computation concepts such as quantum information processing (QIP) or spintronics. The continued trend in scaling semiconductor devices has lead to a rapidly decreasing number of dopant atoms that govern their functionality, and it has already been shown that their random distribution can adversely influence the device characteristics.[6] As the number of dopants is further reduced, the individual characteristics of each dopant atom become statistically more important and nowadays the influence of a single donor can already be detected when operating state of the art semiconductor devices.[13]

In addition to the fact that the number of dopants in a device is reduced, the scaling of its dimensions also brings interfaces such as surfaces or contact areas of different materials closer together. The proportion of dopants located in close proximity to one of these interfaces dramatically increases and their characteristics can be severely influenced. Surfaces as well as material interfaces between semiconductor, insulating layers and metal contacts are characterized by a sudden change in the atomic reconstruction, material work function and dielectric constant. This can significantly influence the band structure, strain and screening behavior of the semiconductor host crystal and it has already been demonstrated that the binding energy and wave function of individual dopants are considerably modified when they are located in close proximity to an interface.[3, 4] For charge devices, predominantly relying on shallow dopants to modify the charge profile in the host crystal, this may result in an increased carrier freeze out or lead to random variations in threshold voltages once the number of dopants situated close to an interface becomes dominant.

The influence of interfaces is however even more important for novel device concepts such as quantum information processing or spintronics. These devices directly rely on characteristics of individual dopants such as nuclear and electron spins or Rydberg states.[7, 8, 156] Because these dopants have to be placed either in close proximity to a gate or to each other, it is of fundamental importance to understand and control how these individual donors interact with their atomic scale environment. QIP proposals furthermore intend to combine the unique characteristics of different dopant elements, including deep donors such as Bi, to exploit their unique spectral selectivity or nuclear spin states. Due to the fact that different dopants have significantly different covalent radii, the lattice distor-

tion introduced by them varies considerably,[23] and it remains an open question whether interfaces in close proximity will influence different dopant elements in different ways.

STM is ideally suited to study individual dopant characteristics and their interaction with the atomic scale environment, as it has demonstrated the capability to resolve spin states, wave functions and ionization energies of individual atomic scale impurities.[3, 16, 132] Furthermore, since dopants are measured in the surface of a semiconductor or a few atomic layers below, the influence of the abrupt change in dielectric constant and reconstruction between semiconductor and vacuum onto the dopant characteristics can be investigated. In this chapter we present STM measurements that compare different dopant elements in the Si(111)-2x1 surface and investigate the interaction of fundamental dopant characteristics, such as size and ionization energy, with their atomic scale environment.

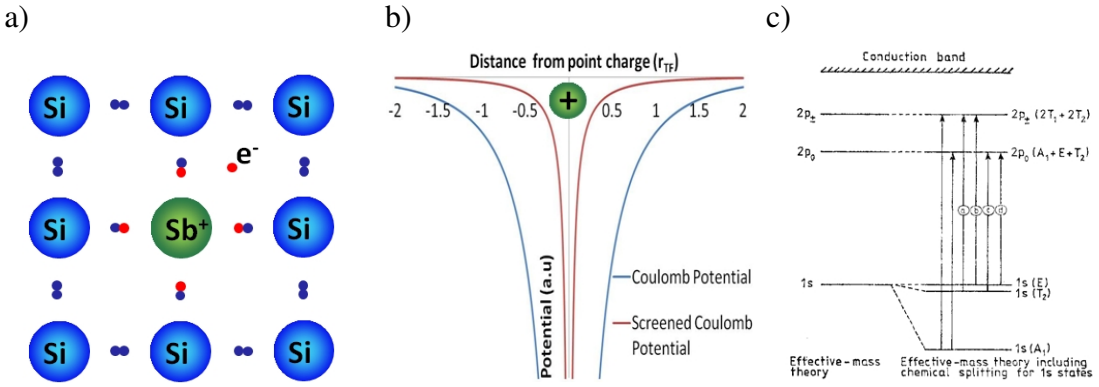

Figure 7.1: a) Single donor in silicon. b) Screened and unscreened Coulomb potential. c) Energy levels of a donor in silicon, image from [157].

To enable the interpretation of atomic scale STM measurements on individual donors, their basic properties are briefly discussed. A simplified schematic representation of a group V donor is shown in Fig. 7.1 a). It is four fold coordinated with the surrounding Si lattice and the fifth valence electron is bound within the potential well created by the Coulomb potential of the positively ionized dopant core. Because the dopant is situated within a semiconductor, the potential well is modified by reordering charge carriers and becomes a screened Coulomb potential. The size and shape of the potential well induced by an individual donor can be calculated[158] according to Eq. 7.1, whereas the screening in silicon is taken into account by using its dielectric constant ε_r=11.9.

$$V(r) = \frac{e}{4\pi\varepsilon_0\varepsilon_r r} \times e^{-r/R_s} \tag{7.1}$$

The shape of a screened and unscreened potential well are shown in Fig. 7.1 b). It can be seen that the screened potential decays much faster with increasing distance from the charged donor core, characterized by the screening length R_s. Depending on the degeneracy of the electron gas, the screening length is calculated according to Thomas-Fermi

screening in the degenerate and Debye-Hueckel screening in the non-degenerate case,[158] as shown in Eq. 7.2. In this equation, n is standing for the charge carrier concentration and for highly doped silicon surfaces, typical screening lengths around 1.2 nm have been reported.[159, 160]

$$R_{TF} = \pi^{2/3}\sqrt{\frac{\varepsilon_0\varepsilon_r\hbar^2}{e^2 m_e (3n)^{1/3}}} \quad ; \quad R_{DH} = \sqrt{\frac{kT\varepsilon_0\varepsilon_r}{e^2 n}} \tag{7.2}$$

The shape of the Coulomb potential well also defines the energy levels of the donor ground and excited states. Using the effective mass approximation, hydrogen like energy levels can be calculated, leading to an ionization energy according to Eq. 7.3. Again the influence of the silicon host crystal is included by using its effective mass m^* and the silicon dielectric constant.

$$E_A = \frac{m^* e^4}{(\varepsilon_0\varepsilon_r)^2 2\hbar^2} = \frac{m^*/m_0}{\varepsilon_{Si}^2} R_y \tag{7.3}$$

Based on this very simple model, every group V donor would have the same ionization energy of approximately 30 meV. To get a more accurate calculation of the ground state energy for the different dopants, several modifications are necessary for Eq. 7.3. Most importantly the effective mass m^* is dependent on the crystal direction due to the multi valley band structure of silicon and therefore not a simple constant. This anisotropy splits the ground state as shown in Fig. 7.1 c). Additional corrections include[161] more accurate screening theories, intervalley coupling and strain caused by lattice distortion due to the different sizes of the donor elements.[162] Another important influence is the exact shape of the potential very close to the dopant. Corrections to the potential are necessary as it is dominated by very short ranged changes in the electronic structure that can not be described with the effective mass approximation and may change the dopant ground state by several meV.[161] Experimentally determined values for the ionization energy of all group V dopants in silicon are shown in table 7.1.

Table 7.1: Size and ionization energy of all group V dopants.[8]

Dopant	Atomic number	Ionization energy	Size [$\Delta V/V_{Si}$]
Phosphorus (P)	15	44 meV	-8 %
Arsenic (As)	33	54 meV	+4 %
Antimony (Sb)	51	39 meV	+17 %
Bismuth (Bi)	83	71 meV	+30 %

When studying single donors in STM, the contrast measured in constant current topography is usually dominated by the charge state of the dopant and by the atomic scale reconstruction it forms with the host crystal. The reconstruction a dopant induces in the

semiconductor host may also be dependent on the used element, as for the case of Bi for example, a possible dopant vacancy complex has been suggested to release strain when incorporating the large dopant core into the host.[163] In table 7.1 we have therefore also given a measure of the dopant size relative to silicon, as this may have an influence on the observed STM contrast. The size is stated as a local volume change of the silicon crystal upon inserting the donor atom, deduced from spectroscopic data.[23] By comparing different dopant elements in the Si(111)-2x1 surface we are therefore able to explore how the discussed fundamental electronic and structural properties influence the donor characteristics and its environment at the atomic scale.

7.1 Identifying Individual Donors in STM

In Chap. 6 we have already discussed the importance of Bi for future QIP concepts and developed a way to prepare high quality STM samples suitable to study individual donors at the atomic scale. In table 7.1 it can be seen that Bi is the largest of all group V dopants with the highest ionization energy. Furthermore, we have discussed results of Garleff et al.[20] in Sec. 2.3.1, who have studied P in Si(111)-2x1, the smallest dopant with a low ionization energy. To understand the influence of size and ionization energy on the atomic scale environment, we have further decided to study antimony (Sb), a large donor with the lowest ionization energy as seen in table 7.1. Bulk doped Sb wafers were purchased with a doping density larger than 1×10^{18} cm^{-3}, as described in Sec. 3.3.1. Being able to compare P, Sb and Bi in the same surface and the same atomic crystal site will therefore allow us to compare the two largest dopants (Sb,Bi) with the smallest (P) and also visualize the influence of the two smallest ionization energies (P,Sb) compared to the largest (Bi).

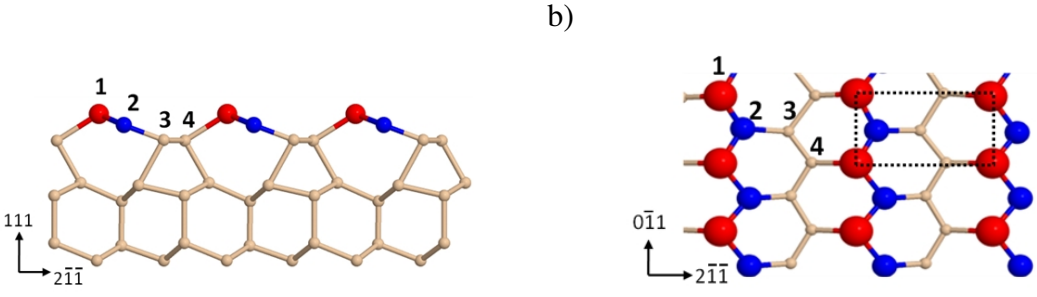

Figure 7.2: Si(111)-2x1 reconstruction showing the four distinguishable surface sites. a) Side view. b) Top view.

The Si(111)-2x1 surface reconstruction is again shown in Fig. 7.2 a)+b) in side and top view respectively. It can be seen that there are four distinguishable surface sites, labeled 1-4, two in the π-bonded chain and two in the intermediate trough region. Atoms

in the π-bonded chain are three fold coordinated and have either a filled (up buckled) or an empty (down buckled) fourth orbital, whereas atoms in the trough region are four fold coordinated, similar to the bulk. Dopants therefore are expected to show a significantly different behavior depending on their substitutional crystal site, as already shown for P.[20] To compare different dopant elements in identical atomic scale environments it is therefore important to identify all occurring contrasts in STM measurements and correlate them with the different substitutional sites in the Si(111)-2x1 surface. It furthermore should be noted that there is no annealing step in the surface preparation of XSTM and dopants thus have no additional thermal energy to diffuse into a ground state reconstruction. Different substitutional dopant sites are therefore expected to be observed, even if they have different ground state energies.

7.1.1 Identified Bi Dopants

Experiments were performed at 78 K on Bi wafer A, implanted to a dopant concentration of 1×10^{20} cm^{-3} and subsequently annealed to temperatures of 650 °C and 1000 °C for 3 min each. As described in Chap. 6, this lead to an active Bi dopant concentration of 7.2x10^{18} cm^{-3}, determined by Hall measurements. The implanted layer was scanned using constant current STM topography measurements and all identified atomic scale features in the surface layer were characterized using voltage dependent imaging, as shown in Fig. 7.3. Four different reoccurring features were found repeatedly during the measurement of several different samples. Their association with the Bi implantation process is deduced from the fact that they were only found within the implanted layer and never in the bulk of the wafer.

The four identified features, labeled Bi-1 to Bi-4 as shown in Fig. 7.3, were measured with different bias voltages in filled and empty states and show very distinct contrasts in STM topography. The number of identified and characterized features for Bi-1, Bi-2, Bi-3 and Bi-4 were 8, 4, 7 and 7 respectively. Comparing this dopant count with the expected surface density is difficult in the case of implanted samples, because the remaining damage and comparably high step density still conceal a large proportion of the surface. However, as already mentioned, the unique possibility of comparing the implanted layer with the non implanted bulk allows us to correlate the observed features with the Bi implantation process, as they were only observed in the implanted area. Other silicon impurities or standard Si(111)-2x1 surface defects can therefore be excluded as the source of the observed features. However, determining whether the features arise from Bi dopants or from remaining implantation damage is not trivial when relying purely on STM images and requires theoretical simulations, as it will be discussed in Sec. 7.2.1.

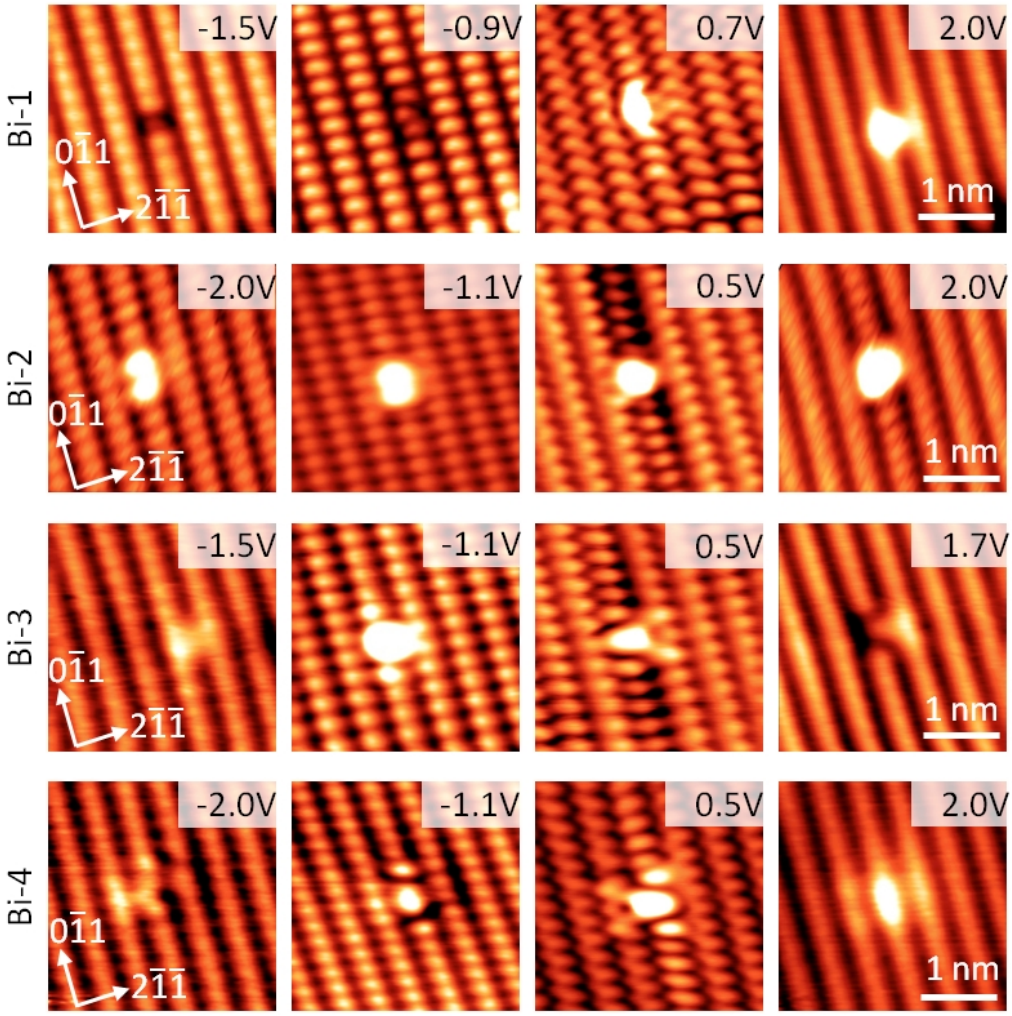

Figure 7.3: Features identified on the Bi implanted wafer. Four different features were found, shown in different filled and empty states topography measurements.

7.1.2 Identified Sb Dopants

Sb dopants were measured at 78 K by scanning a commercially available bulk Sb doped silicon wafer, as described in Sec. 3.3.1. The wafer surface was scanned using XSTM and all observed atomic scale features in the surface layer were characterized using voltage dependent imaging.

Five different features were identified, labeled Sb-1 to Sb-5, as shown in Fig. 7.4. Again the contrast of all features is very distinct when imaging at different filled and empty states voltages. Comparing the Sb features to the Bi features in Fig. 7.3, it is striking how similar Bi-1 to Bi-4 and Sb-1 to Sb-4 are respectively. They are basically not distinguishable, the small differences in shape and intensity of the observed contrasts resulting more likely from different tip characteristics. The number of identified features for Sb-1, Sb-2, Sb-3, Sb-4 and Sb-5 was 38, 18, 15, 28 and 16 respectively. In the complete measurement area of 0.2 μm square this corresponds to a bulk dopant density of 2.3×10^{18}

cm^{-3}. This is in good agreement with the nominal Sb density of the wafer which is expected larger than 1×10^{18} cm^{-3}. The five features can therefore be assumed to represent Sb dopants in the Si(111)-2x1 surface in different crystal sites or reconstructions.

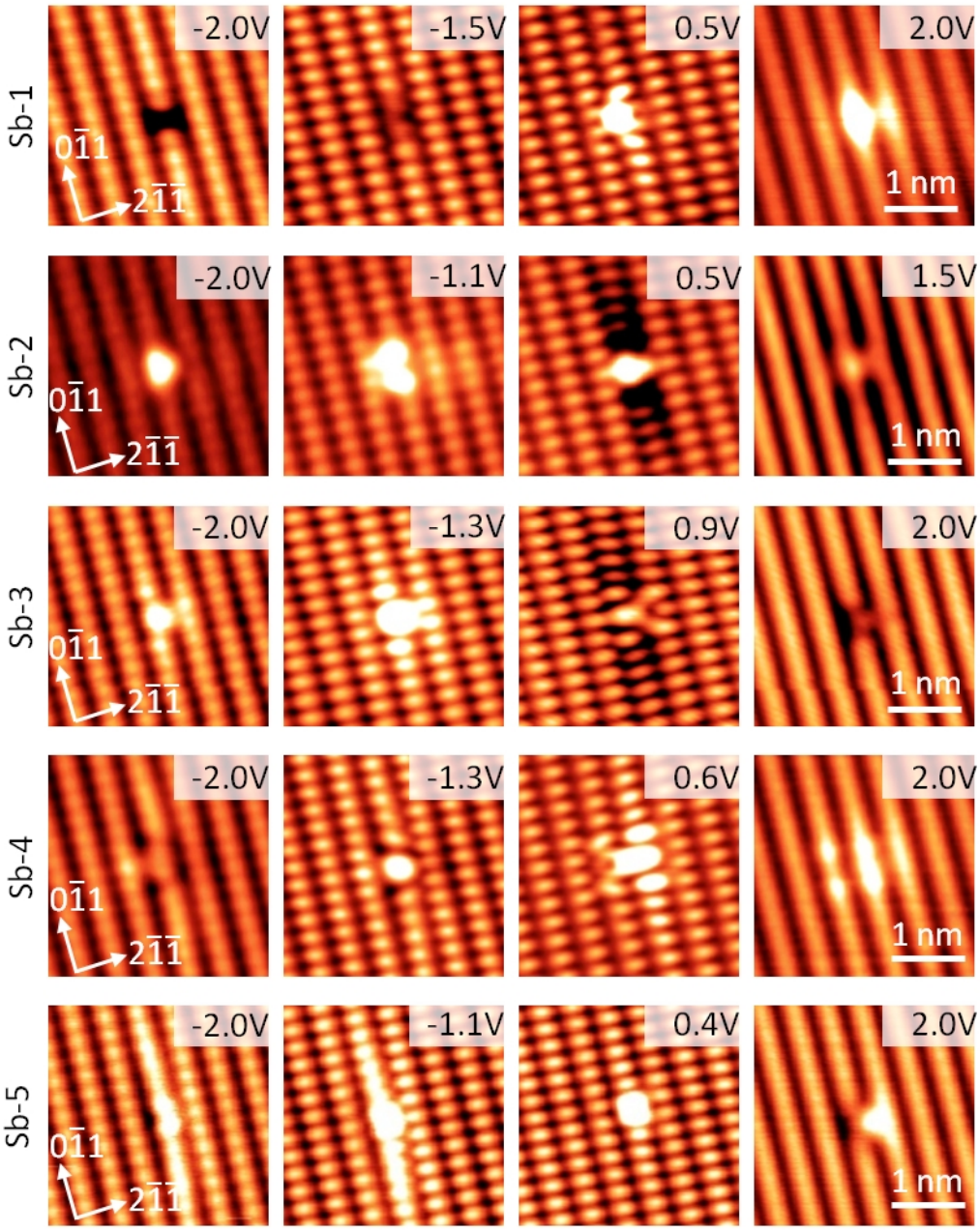

Figure 7.4: Features identified on the Sb bulk doped wafer. Five different features were found, shown in different filled and empty states topography measurements.

7.1.3 Lattice Position of Identified Features

We have shown that in the Bi (Sb) doped Si(111)-2x1 surface, four (five) different features can be repeatedly identified. It is straightforward to assume a connection between

the identified features and the four different surface sites, as was the case for P dopants.[20] However, the fact that five features were identified for the case of Sb shows that also other possibilities than the four substitutional sites must be considered. These additional features may result from interstitial dopants, dopant vacancy complexes or different surface reconstructions induced by the dopant. Such additional features are not unexpected and were already observed for P, where four features were identified but only three could be correlated to substitutional Si(111)-2x1 sites, the fourth left unassigned as discussed in Sec. 2.3.1.

To correlate the different observed contrasts with the four substitutional atomic sites in the Si(111)-2x1 surface experimentally, the ability of STM to selectively image up or down atoms in the π-bonded chain can be used. Together with the known symmetry of the Pandey reconstructed surface, this allows to determine the position of the observed feature in STM with respect to the underlying cystal lattice, as shown in Fig. 7.5.

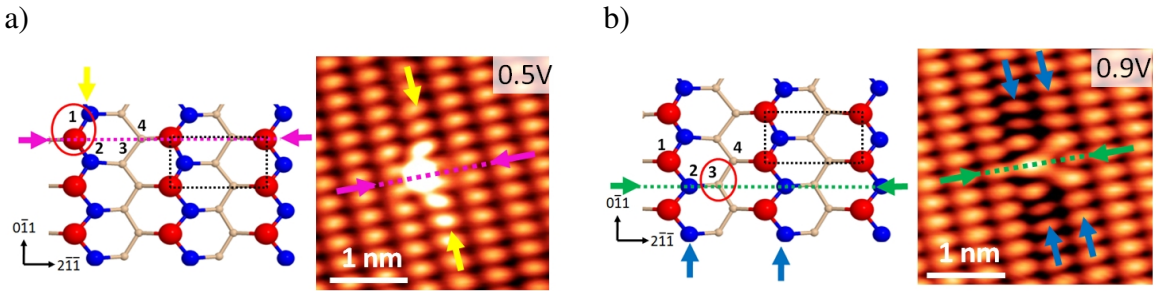

Figure 7.5: Experimental crystal site assignment. a) The contrast of Sb-1 is confined to a single π-bonded chain and in between the imaged down atoms, corresponding to site 1. a) The contrast of Sb-3 is dispersed across two π-bonded chains and in line with the imaged down atoms, corresponding to site 3.

As discussed in Sec. 5.4, the down atoms of the π-bonded chains are imaged when tunnelling into empty states at low bias values. This is shown in Fig. 7.5 a) and b) for features Sb-1 and Sb-3 respectively. In the model for the Si(111)-2x1 reconstruction it can be seen that in the $[2\overline{11}]$ direction, atomic site 4 is in line with atomic site 1, as indicated by the pink arrow in Fig. 7.5 a). Similarly, atomic site 3 is in line with atomic site 2, as indicated by the green arrow in Fig. 7.5 b). When measuring in low empty states bias and therefore imaging atomic site 2, contrasts resulting from dopants in site 2 and 3 will therefore be in line with the imaged atoms, as is the case for Sb-3 shown in Fig. 7.5 b). Contrasts from dopants in sites 1 or 4 on the other hand are expected to lie in between the imaged atoms, as is the case for Sb-1 shown in Fig. 7.5 a).

To further determine the exact crystal site it is assumed that dopants within a π-bonded chain will show a different contrast compared to dopants in the trough region. Because STM is not able to directly image atoms between the π-bonded chains, it is expected that dopants in the trough region sites 3 and 4 will induce a contrast measurable in the

two adjacent π-bonded chains. For dopants located in the π-bonded chain on site 1 or 2 however, it is assumed that the contrast will be mainly concentrated on a single chain. This is shown in Fig. 7.5 a) where Sb-1 shows a contrast on a single π-bonded chain, indicated by the yellow arrow, restricting its location to site 1 or 2. For Sb-3 on the other hand, the contrast is clearly dispersed across two adjacent chains, indicated by the two blue arrows as shown in Fig. 7.5 b), restricting its location to site 3 or 4. Applying both of the mentioned symmetry criteria simultaneously it is possible to determine the exact site of a measured feature, resulting in crystal site 1 for Sb-1 and crystal site 3 for Sb-3, as shown in Fig. 7.5.

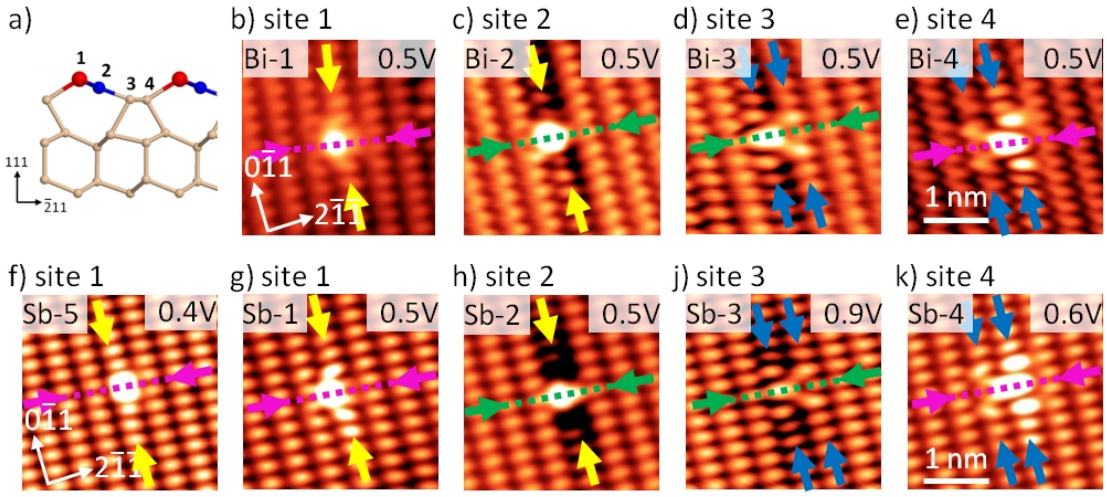

Figure 7.6: a) Crystal sites 1-4 as labeled. b)-k) Assignment for Sb and Bi. Sb-1 to Sb-4 and Bi-1 to Bi-4 are correlated to crystal sites 1-4 respectively. Sb-5 is also located on crystal site 1.

The same procedure was applied for all four Bi and all five Sb features, as shown in Fig. 7.6. It can be seen that Sb-1 to Sb-4 and Bi-1 to Bi-4 are correlated to crystal sites 1-4 respectively. Sb-5 is also found to be located on crystal site 1, similarly to Sb-1. Nevertheless, the two features are assumed of different origin due to the different contrasts measured in voltage dependent imaging, shown in Fig. 7.4.

The observation that the very similar contrasts of Bi-1-4 and Sb-1-4 correspond to the available crystal sites 1 to 4 suggests that they represent the four possible substitutional dopant sites in the Si(111)-2x1 surface. This experimental assignment is further supported by DFT calculations, performed by Veronika Brazdova, that will be discussed in Sec. 7.2.1 along with possible reconstructions for feature Sb-5.

7.2 Element Dependent Atomic Reconstruction

The identification and characterization of Bi and Sb dopants in all four crystal sites of the Si(111)-2x1 surface allows us for the first time to directly compare different dopant elements in an identical atomic environment. Together with the three previously identified P features known from literature,[20] we are in a position to compare P, Sb and Bi to study the influence of their fundamental electronic and structural properties at the atomic scale.

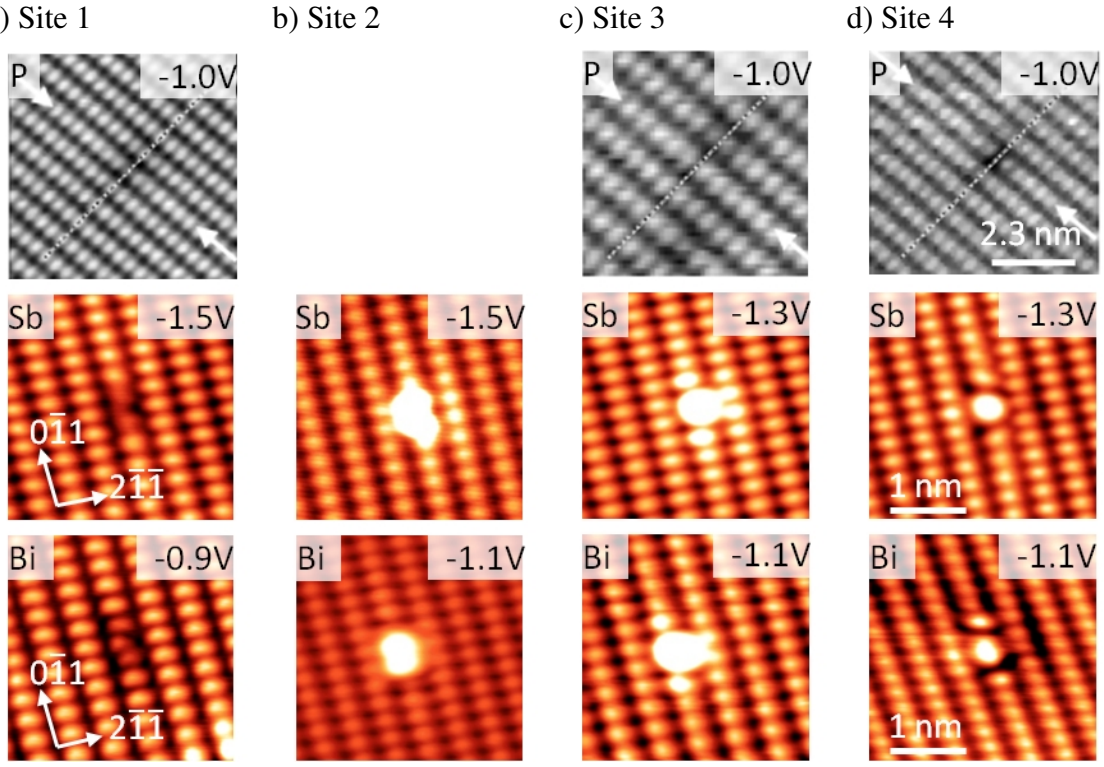

Figure 7.7: Comparison of different group V donors in identical sites of the Si(111)-2x1 surface. a)-d) Crystal sites 1-4 respectively. P images from [20].

In Fig. 7.7, filled states images of P, Sb and Bi are shown for the four different sites in the Si(111)-2x1 surface. For P dopants, no feature was identified on site 2 and therefore the relevant space is left blank. When comparing the three different elements in identical atomic positions it becomes obvious that Sb and Bi are very similar whereas P is fundamentally different. The very pronounced contrast of Bi and Sb especially for atomic sites 3 and 4 are not visible in P and only the feature on atomic site 1 looks comparable for all three dopants.

To explain the observed behavior in the dopant induced contrast, we compare it with the electronic and structural properties of the donor elements as shown in table 7.1. When considering the ionization energy, Sb and P are very similar with 39 meV and 44 meV respectively, whereas Bi has an ionization energy twice as large with 71 meV. This does not correlate well with the observed dopant contrast that was found similar for Sb and Bi

but different for P. When considering the dopant size on the other hand, we see that Sb and Bi are similar and both very large with +17% and +30%, whereas P is substantially different with a size of -8% compared to silicon. This corresponds well with the observed change in contrast that was induced by the different dopant elements. It is therefore assumed that the size of the dopant atom is crucially influencing the observed atomic scale contrast. It is however important to note that the difference in size of Bi is with +30% almost twice as large as the size of Sb with +17% when compared to silicon. Nevertheless, the observed contrast for Bi and Sb is almost identical and therefore a simple, gradual change of contrast with the dopant size seems unlikely. To further study the correlation between the dopant element and the observed STM contrast we have therefore used DFT simulations, allowing us to determine the atomic reconstruction formed by the different donors.

7.2.1 DFT Calculations of Donors in Si(111)-2x1

To determine the exact atomic reconstruction of the different dopant elements within the Si(111)-2x1 surface, DFT simulations were carried out by Veronika Brazdova. DFT calculations of the dopant structures were performed using VASP[122] with the PW91 GGA[123] functional. A 10 layer Si slab (320 atoms), with the top eight layers free to move and the bottom terminated with H (32 atoms), was used. STM images were simulated from the relaxed DFT cells using the Tersoff-Hamann method.

7.2.1.1 Charging of DFT Cells

To accurately reflect the high n-type doping of the measured samples, we found that it was necessary to adjust the charge properties of the DFT cells used in the calculations. As we have discussed in Sec. 2.2.3, the high n-type dopant concentration leads to a Fermi level which is pinned at the Si(11)2x1 surface and therefore located slightly above the onset of the surface conduction band. This leads to an accumulation of electrons, filling states at the bottom of the surface conduction band. Whereas DFT cells are usually charge neutral with E_f situated anywhere in the band gap, we found that it was necessary to shift the Fermi level slightly into the surface conduction band in order to accurately model the influence of the Fermi level pinning when simulating STM images. Different methods to achieve this were tested, including a manual shift of the Fermi level when simulating STM images, the introduction of a dopant atom into the simulated semiconductor bulk of the cell and the addition of a single electron into the cell. The effect of all three different methods was found to be very similar and we therefore chose to add a single electron to all our cells, a method well established for silicon surfaces.[18] The influence of this cell charging can be seen in Fig. 7.8 for the example of STM images simulated for Sb-1.

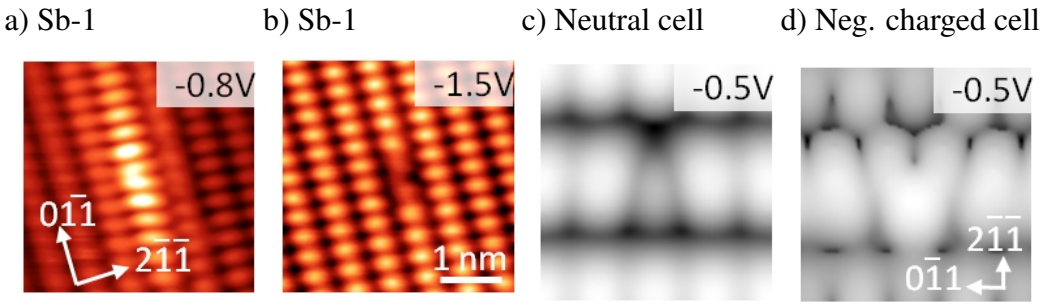

Figure 7.8: The effect of charging DFT cells. a)+b) STM measurement of Sb-1 at -0.8 V and -1.5 V respectively. c) Simulated STM image from a neutral DFT cell. d) Simulated STM image from a negatively charged DFT cell, created by adding an additional electron.

In Fig. 7.8 a) and b), STM images for Sb-1 at -0.8 V and -1.5 V are shown respectively. In Fig. 7.8 c), a simulated STM image is shown for an Sb atom in crystal site 1 of the Si(111)-2x1 surface, using a neutral DFT cell and a simulated bias of -0.5 V, E_f situated above the surface valence band. It can be seen that the image matches the Sb-1 atom measured at -1.5 V, showing the donor as a depression with two inwards orientated atoms nearby. The shift in bias between measurement and simulation is quite large, as expected due to the arbitrary positioning of E_f in DFT. However, the unexpected problem was that it was not possible to simulate the measured contrast for very low filled states bias, shown in Fig. 7.8 a), even when testing all simulated bias values between -0.5 V and 0 V. It was assumed that this discrepancy between simulation and measurement is caused by the additional filled states in the bottom of the conduction band, induced by the Fermi level pinning of the Si(111)-2x1 surface, as mentioned earlier. In STM measurements at low filled states bias, these electrons are expected to be addressed first and strongly influence the measured contrast until electrons from the valence band become dominant at higher tunnelling bias.

This is confirmed by DFT simulations when charging the cell negatively, shifting the Fermi level upwards into the surface conduction band. The simulated STM image for a sample bias of -0.5 V now compares well with the STM measurement acquired at -0.8 V, both the simulation and the experiment showing the two atoms next to the Sb atom oriented outwards and touching in the middle. Due to the charging, the simulated image previously occurring at -0.5 V is shifted to higher negative bias, now in good agreement with the measurement. The influence of the cell charging was generally found most dominant for images around the Fermi energy, where the low concentration of additional filled states in the bottom of the surface conduction band can have a significant impact. For larger bias values, a small shift was observed but images qualitatively stayed very similar. Another justification why it is crucial to charge the DFT cells is related to the observed atomic scale reconstruction and the charge state of the dopants, as will be discussed in

Sec. 7.3.2.

7.2.1.2 Donor Reconstruction in Si(111)-2x1

To determine the atomic scale reconstruction formed by the different dopant elements, DFT was used to relax cells with Sb or Bi donors substituting one of the four surface sites in Si(111)-2x1. The relaxed model for Sb in site 3 of the Pandey reconstructed surface is shown in Fig. 7.9 a), the donor indicated in green, forming a stable ground state. Results for Bi were found almost identical to Sb and are therefore not shown separately. Surprisingly it was found that if slightly different starting positions for Sb or Bi were used, the atomic scale reconstruction would converge to a completely different ground state as shown in Fig. 7.9 b). It can be seen that the dopant atom is pushed up and one bond is rearranged, now bonding to former atomic site 2 and leaving the donor only three fold coordinated. This new and significantly different structure was found to be 0.81 eV (Sb) and 1.05 eV (Bi) more stable than the dopant located in the Pandey reconstruction. It is therefore assumed that the local structure of an Sb or Bi atom in site 3 of the Si(111)-2x1 surface does not correspond to the Pandey model but forms the newly identified reconstruction shown in Fig. 7.9 b).

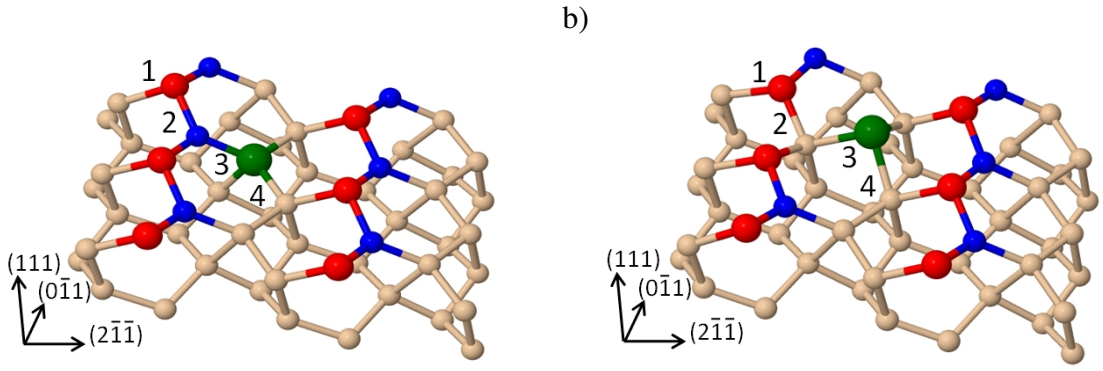

Figure 7.9: a) Relaxed DFT cell of Sb (green atom) placed in substitutional site 3 of the Pandey reconstruction. b) Lowest energy ground state reconstruction, found by varying the initial Sb position in the calculations.

A very similar behavior was found for atomic site 4, as shown in Fig. 7.10 for the example of Sb, whereas results for Bi are essentially identical. Even though the original Pandey reconstruction converged to a stable energy minimum, as shown in Fig. 7.10 a), the ground state energy could be further reduced by 0.44 eV (Sb) or 0.75 eV (Bi) when pushing the dopant atom up, forming a reconstruction as shown in Fig. 7.10 b). The new reconstruction is again characterized by the rearrangement of one bond, changing from the donor to the up atom in the adjacent π-bonded chain and leaving the dopant three fold coordinated.

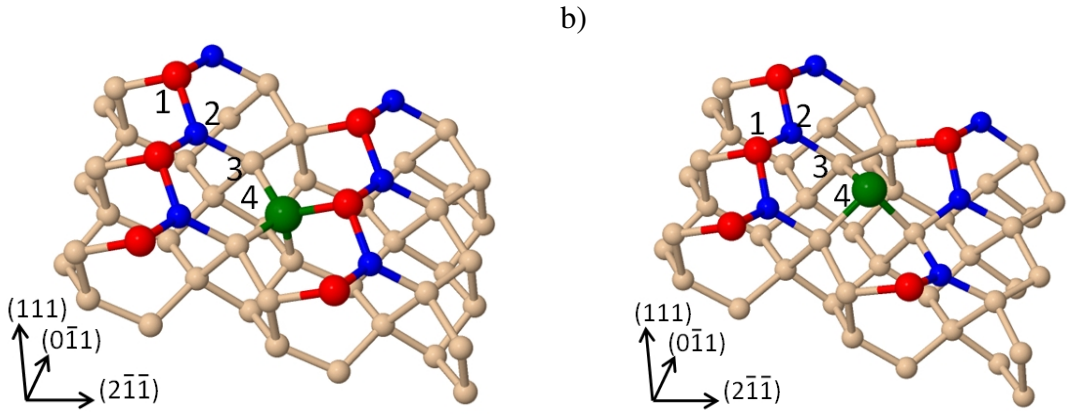

Figure 7.10: a) Relaxed DFT cell of Sb (green atom) placed in substitutional site 4 of the Pandey reconstruction. b) Lowest energy ground state reconstruction, found by varying the initial Sb position in the calculations.

For a dopant substitutional in site 1, no alternative reconstruction could be identified, as the up atom in the π-bonded chain is already sticking furthest out of the surface and pushing it down into the surface was found to be unstable. For donors in site 2, the dopant located in the substitutional site of the Pandey reconstruction also resulted in a stable local energy minimum, as shown in Fig. 7.11 a). A configuration where the donor buckles upwards was however again found more stable by 0.27 eV (Sb) or 0.44 eV (Bi), as shown in Fig. 7.11 b). In this new reconstruction only the buckling of the dopant atom is changed and no bonds were rearranged, leaving adjacent atoms almost completely unaffected.

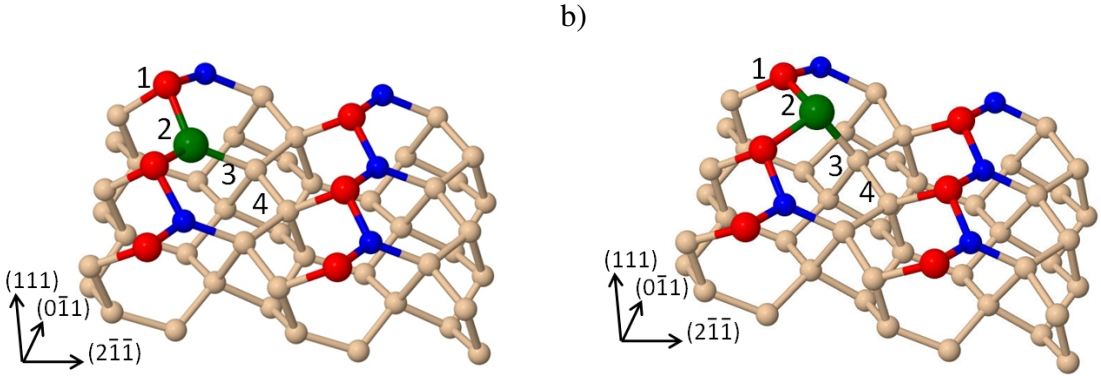

Figure 7.11: a) Relaxed DFT cell of Sb (green atom) placed in substitutional site 2 of the Pandey reconstruction. b) Lowest energy ground state reconstruction, found by varying the initial Sb position in the calculations.

Using DFT we have identified three new ground state reconstructions for Sb and Bi in crystal sites 2,3 and 4 of the Si(111)-2x1 surface. This is surprising as no similar changes in reconstruction were found for P dopants,[20] and might therefore explain the different appearance of the measured donor elements.

7.2.1.3 Simulated STM Images of Donors in Si(111)-2x1

Simulated STM images of donors in the original Pandey model and the newly identified reconstructions were calculated by Veronika Brazdova to allow the comparison of the ground state calculations with the experimental data. The simulated STM images and all relaxed structures for antimony are shown in Fig. 7.12.

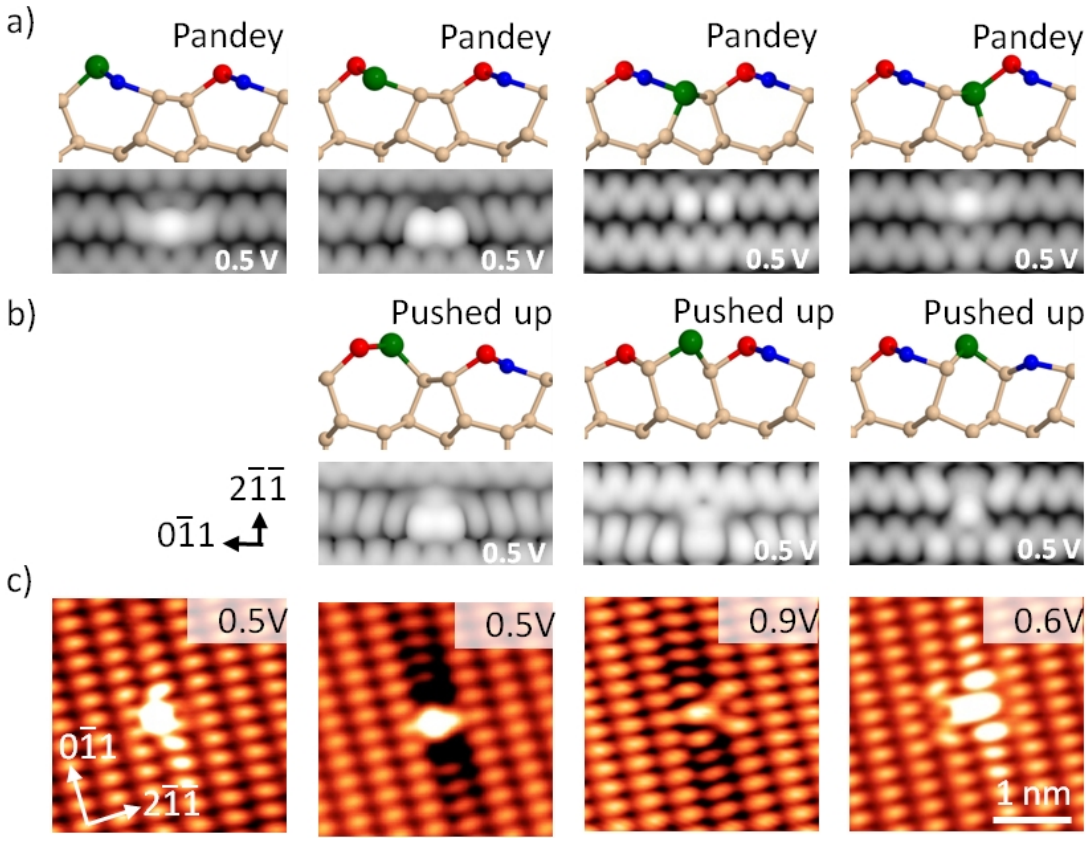

Figure 7.12: Simulated STM images for Sb dopants in the Si(111)-2x1 surface. a)+b) Simulated STM images and structure of dopants placed in different sites of the Pandey reconstruction and the newly identified ground state reconstruction respectively. c) STM measurements for comparison with the simulation.

As mentioned before, cells were negatively charged and STM images were simulated for dopants in the original Pandey Si(111)-2x1 reconstruction sites as well as the ”pushed up” reconstruction that was found to be the energetic ground state. The simulated STM images for a bias of 0.5 V, showing Sb dopants in the original Si(111)-2x1 reconstruction, are displayed in Fig. 7.12 a). When comparing the images with the data, shown in Fig. 7.12 c), it can be seen that site 1 matches very nicely, reproducing the central bright feature with the two arms around it. However, site 2,3 and 4 all considerably differ from the experimental data and it is therefore unlikely that the measured features originate from Sb dopants in the original Pandey reconstruction. In Fig. 7.12 b), the newly discovered ground state reconstructions for sites 2,3 and 4 are shown together with the corresponding

simulated STM images.

For site 2, the Sb atom is simply buckled upwards, producing an extra bright peak in the simulated image when comparing it to the dopant in the original Pandey reconstruction. This corresponds reasonably well with the experimental data, where the two adjacent up atoms and the Sb donor are all shown as a single, bright protrusion. It should at this point be mentioned that the increased (site 1 and 4) or reduced (site 2 and 3) contrast along the π-bonded chain in the experimental data is thought to be related to charge screening, as will be discussed in Sec. 7.4.1.2. Because this feature is extending over a large distance, it is assumed that it cannot be perfectly reproduced in DFT due to the limited cell size.

For site 3 and 4 a substantially new Sb reconstruction is formed as discussed earlier, leaving the dopant sticking out of the surface and being only threefold coordinated. The simulated STM images created from these atomic structure models are in excellent agreement with the observed STM contrasts, producing the bright central features with the arms and legs in the correct orientation. The good correlation between theory and measurement therefore confirms the experimental assignment of the observed STM contrast to the four substitutional dopant sites. Furthermore, it also supports the fact that Sb forms a new and substantially different reconstruction when incorporated into crystal sites 2, 3 and 4, as predicted by DFT ground state calculations.

Simulated STM images for Bi are shown in Fig. 7.13 together with relaxed structure models and the measured STM topography images. The behavior of Bi is found to be very similar to Sb. Again, simulated STM images for dopants in the original Pandey reconstruction do not match the STM data, apart from site 1, as shown in Fig. 7.13 a). When on the other hand considering the newly identified ground state reconstructions, DFT simulations for Bi in site 2, 3 and 4 again are in excellent agreement with the measurement, as shown in Fig. 7.13 b) and c).

For Sb we have shown that a fifth feature exists, situated on crystal site 1, as discussed in Sec. 7.1.3. This feature did not match any simulations for Sb dopants, neither in the original Pandey reconstruction nor in the new ground state relaxation. A large variety of different reconstructions were explored, including locally changed buckling, missing atoms, interstitial dopants, H-adsorbates and Sb adatoms. None of the mentioned structures compared well with the observed contrast of Sb-5 and its origin is therefore left unclear. Future work is needed to determine whether feature Sb-5 is resulting from Sb dopants or whether it might be a general impurity present in highly doped Cz-grown wafers.

Using DFT and STM, we were able to determine the reconstructions formed by Sb and Bi in the different substitutional crystal sites of the Si(111)-2x1 surface. The fact that Sb and Bi form new, previously unidentified reconstructions in site 2, 3 and 4 explains why the STM contrast for these features is fundamentally different from the P contrast,

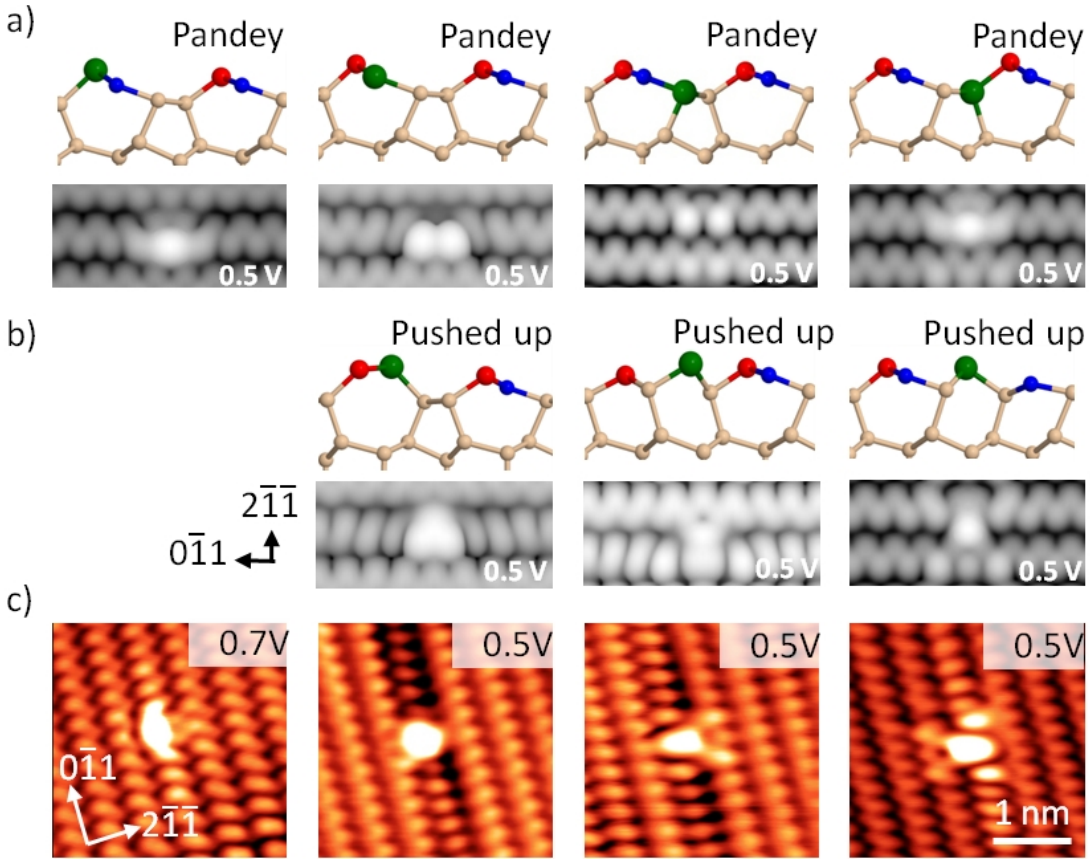

Figure 7.13: Simulated STM images for Bi dopants in the Si(111)-2x1 surface. a) Simulated STM images and structure of dopants placed in different sites of the Pandey reconstruction. b) Simulated STM images and structure of dopants placed in the newly identified ground state reconstruction. c) STM measurements for comparison with the simulation

previously observed by Garleff et al.[20] It furthermore illustrates why Sb and Bi produce very similar STM contrasts even though their size is considerably different. It is assumed that the new reconstructions are favored by dopants that exceed a certain threshold size, leading to the vastly different characteristics when measured in STM.

7.2.2 Theoretical Prediction for all Group V dopants

We have shown that Sb and Bi dopants in substitutional sites 2, 3 and 4 of the Si(111)-2x1 surface form a substantially different reconstruction compared to P. To test whether this change in reconstruction is indeed correlated to the size of the donor atom, the energy differences between Pandey and "pushed up" reconstructions were calculated for all group V donors as shown in table 7.2.

It can be seen that the energy gained by forming the "pushed up" reconstruction, is generally increasing with increasing donor size. This clear correlation confirms that the new reconstructions are indeed influenced by the larger size of Bi and Sb when compared

Table 7.2: Energy gained by the ”pushed up” reconstruction for different dopant elements.

Element	Size [$\Delta V/V_{Si}$]	S2-S2P	S3-S3P	S4-S4P
Phosphorus (P)	-8 %	0.04 eV	0.64 eV	0.33 eV
Arsenic (As)	+4 %	0.13 eV	0.76 eV	0.45 eV
Antimony (Sb)	+17 %	0.27 eV	0.81 eV	0.44 eV
Bismuth (Bi)	+30 %	0.44 eV	1.05 eV	0.75 eV

to P. However, it is interesting to note that even for P dopants the energy gain for the ”pushed up” reconstruction is positive, indicating that P dopants would be expected to show the same reconstruction as Sb and Bi. This seems to be in clear disagreement with literature,[20] where P dopants were observed in the original Pandey reconstructed surface, also confirmed by simulated STM images using DFT.

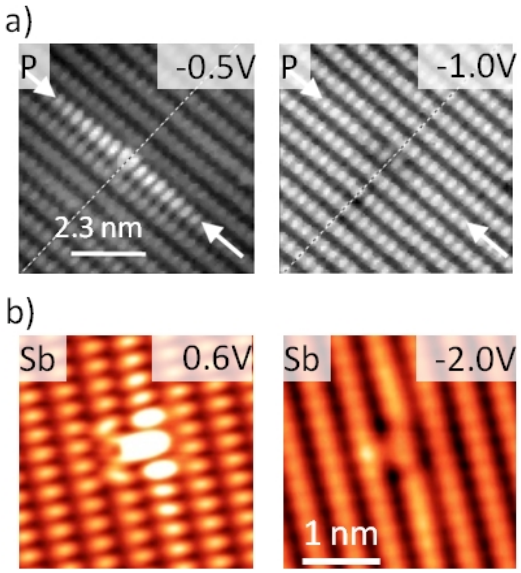

Figure 7.14: a) Unidentified P feature, image from [20]. b) Feature Sb-4.

However, as discussed in Sec. 2.3.1, one P feature that could not be correlated to any of the simulated STM images was identified and is shown again in Fig. 7.14 a). A possible explanation for this feature might be that it actually shows P in crystal site 4, but in the new ”pushed up” reconstruction. This is supported by the similarity in the induced contrasts when comparing the feature to Sb-4, as shown in Fig. 7.14 b). More experimental work on the P doped Si(111)-2x1 surface would be required to determine if dopants really coexist in the ”pushed up” and the Pandey reconstruction.

The clear correlation between the dopant size and the energy gain upon forming the ”pushed up” reconstruction confirms the very intuitive assumption that larger dopants form a different reconstruction and therefore induce a substantially different contrast when measured in STM. However, the fact that the ground state energy for P in the

”pushed up” reconstruction is lower than in the original Pandey reconstructed surface indicates that other influences than the dopant size also play a role in determining the way in which dopants are incorporated within the Si(111)-2x1 surface. As we will discuss in Sec. 7.3.2, the new reconstruction also influences the charge state that can be measured on the surface and therefore the different electronic properties of the dopants also have to be considered. It is suggested that, for the smaller dopants like P, donors in Pandey reconstructed and ”pushed up” configurations might coexists as the energy difference is small. For large dopant elements such as Bi and Sb, the energy gain due to the new ”pushed up” reconstruction is however significantly larger and dopants in the original Pandey reconstruction become less probable, in excellent agreement with the measurement.

7.3 Charge State of Dopants in Si(111)-2x1

The charge state of dopants is of fundamental importance for conventional semiconductor devices as well as proposed QIP or spintronics concepts. It is known that the binding energy of donors can be significantly modified[4] if they are situated close to an interface, as for example a semiconductor surface. We have already shown that large donors in the Si(111)-2x1 surface form new, previously unidentified atomic reconstructions, and a possible influence on the dopant charge state is therefore investigated.

Charged atomic scale impurities and defects can easily be identified in STM measurements due to the effects of their associated, screened Coulomb potential. The locally induced band bending of this potential well is imaged as a protrusion or a depression superimposed onto the atomic corrugation of the surface. This is shown in Fig. 7.15 for the example of subsurface As and B dopants measured on the hydrogen terminated Si(100) surface together with schematic band diagrams. The screened Coulomb potential of the charged dopants locally bends the bands and therefore changes the available states for tunnelling in STM measurements. The correlation between the measured current in STM topography and the induced band bending of the dopant potential is however not trivial, and it is therefore difficult to obtain quantitative information about the charge. Nevertheless, determining the polarity of the charge is possible when following a few simple guidelines as proposed by Ebert et al.[158]

The screened Coulomb potential well is expected to locally shift the bands downwards or upwards for positively and negatively charged defects respectively. Such a shift affects both the conduction and the valence band of the semiconductor, and can therefore influence filled and empty states measurements in different ways. For an n-type doped sample with the Fermi level in the conduction band, as is the case for our experiment, a downwards shift would increase the filled states current measured for very low bias values by pushing the bands surrounding the charged defect below the Fermi level. This increase

is then compensated or even reversed when increasing the bias to higher negative values, as the valence band is also bent down, pushing the states to higher energy values. This complicates a possible determination of the charge state when measuring n-type doped samples in filled states tunnelling. If on the other hand measuring in empty states bias, only the conduction band will contribute to the measured current, independently of the used tunnelling bias. A positive charge will therefore increase the measured current and a negative charge will decrease it, making the determination of the charge polarity straight forward. This behavior is obviously reversed for p-type doping and to unambiguously determine the charge state of defects, Ebert et al.[158] therefore proposed to always measure by injecting majority carriers into the sample.

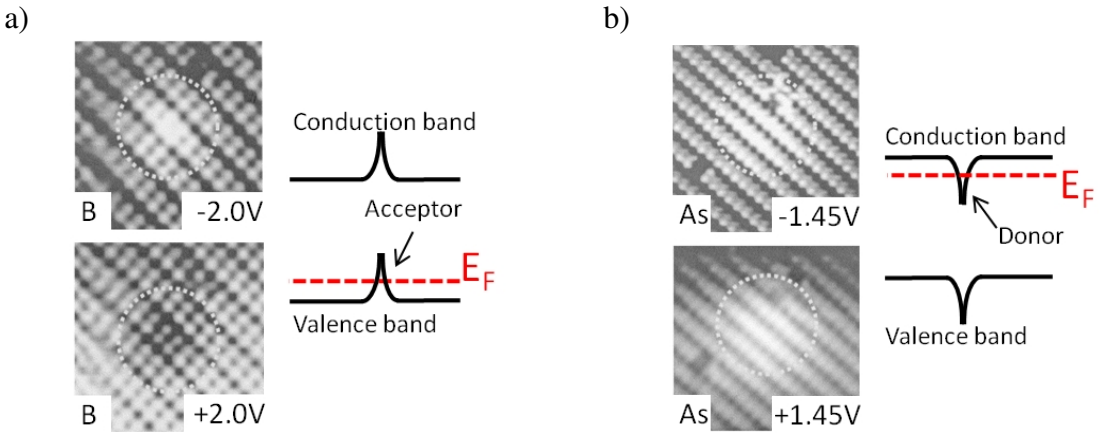

Figure 7.15: a) Subsurface boron (B) dopant imaged in Si(100) together with schematic band diagram. b) Subsurface arsenic (As) dopant imaged in Si(100) together with schematic band diagram. Images from [160].

Following this rule, p-type doped samples should be measured in filled states where positively and negatively charged defects will be imaged with a surrounding depression and elevation respectively. This can be seen in Fig. 7.15 a), where B displays as a protrusion in negative bias, in good agreement with the expected ionized negative charge state at room temperature. For n-type doped samples on the other hand, empty states measurements should be used to determine charge states. Positively and negatively charged defects will then be imaged with a surrounding elevation and depression respectively. This is shown in Fig. 7.15 b), where an As dopant is measured as a protrusion using positive tunnelling bias, in good agreement with its ionized, positively charged dopant core.

7.3.1 Measured Charge State of Individual Donors

Sb and Bi dopants in degenerately doped silicon samples are expected to be ionized, even at the low measurement temperature of 78 K. The positively charged dopant cores are therefore assumed to show up as protrusions in empty states topography images, based

on the previously discussed effect of the screened Coulomb potential on the silicon band structure. However, the influence of surfaces is still poorly understood and for example P was measured ionized at RT[79] but neutral at 8 K,[120] even though the sample was degenerately doped.

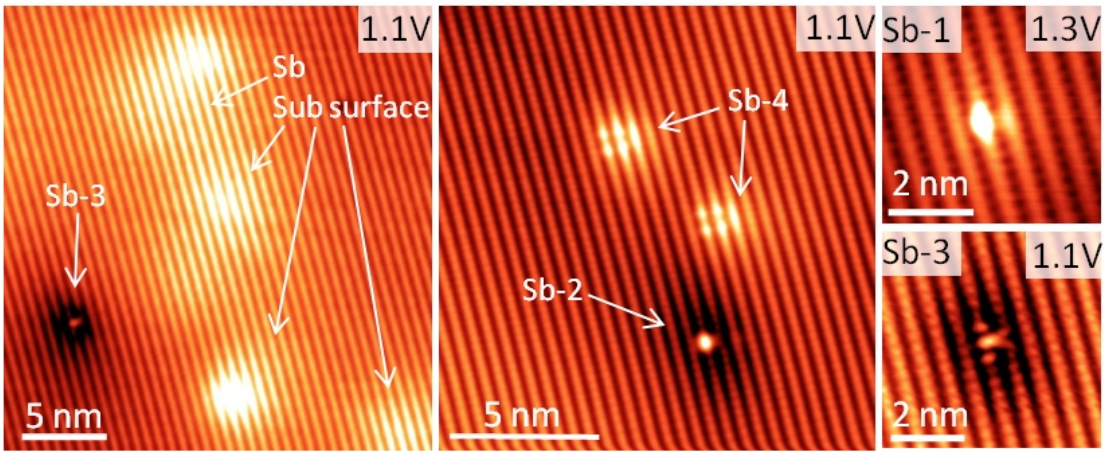

Figure 7.16: Charge state of Sb donors in Si(111)-2x1. Subsurface Sb and donors in sites 1 and 4 were found positively charged whereas donors in site 2 and 3 were found negatively charged. Identical results were obtained for Bi.

To determine the charge of dopants in the Si(111)-2x1 surface, empty states images were evaluated for both the Bi and Sb samples, as they are highly n-type doped. In Fig. 7.16, different large scale images are shown for the example of Sb, whereas identical contrasts were found for all Bi features. So far we have only focussed on dopants in the surface layer, ignoring features induced by subsurface donors. They were however frequently observed and are clearly distinguishable from surface dopants as they do not disturb the atomic scale reconstruction of the surface, but only produce the characteristic elevation due to their screened Coulomb potential. In the measured area we have identified almost twice as many subsurface dopants compared to surface features and it is therefore assumed that we can see Bi and Sb dopants buried up to two atomic layers deep.

All subsurface dopants were found to produce a bright protrusion superimposed over the Si(111)-2x1 surface reconstruction when measured in empty states, as indicated in Fig. 7.16. This is in excellent agreement with the expected band shift of the ionized, positively charged Bi and Sb dopant cores. A very similar bright elevation was found to surround Sb and Bi dopants in substitutional positions 1 and 4, as indicated in Fig. 7.16, also indicating a positive charge. Sb and Bi dopants in site 2 and 3 however were found to induce a depression around them when measured in empty states, indicating a negative charge. This is highly surprising as group V donors are expected to be either positively charged when ionized or electrically neutral when not ionized. In the conventional dopant model, as shown in Fig. 7.1, a negative charge can therefore not be explained as it is

unlikely that Sb or Bi bind a second electron.

However, we have already shown that the new surface reconstructions for Bi and Sb lead to dopants that are only three fold coordinated within the Si(111)-2x1 surface. The conventional model where a donor is considered four fold coordinated and either ionized or not can therefore not be directly applied and the interaction of the Si(111)-2x1 surface with the introduced group V donor was analyzed to find a possible explanation for the observed charging effects.

7.3.2 Reconstruction-dependent Surface Charge

STM topography measurements have demonstrated the surprising fact that Bi and Sb dopants appear positively charged in site 1 and 4 whereas they appear negatively charged in sites 2 and 3. Negatively charged donors seem highly unlikely in the conventional dopant model as it would correspond to a four fold coordinated donor core binding two additional electrons. However, we will show that all observed charge states can be explained for dopants embedded within the Si(111)-2x1 surface reconstruction, when taking the charge distribution within the π-bonded chains into account.

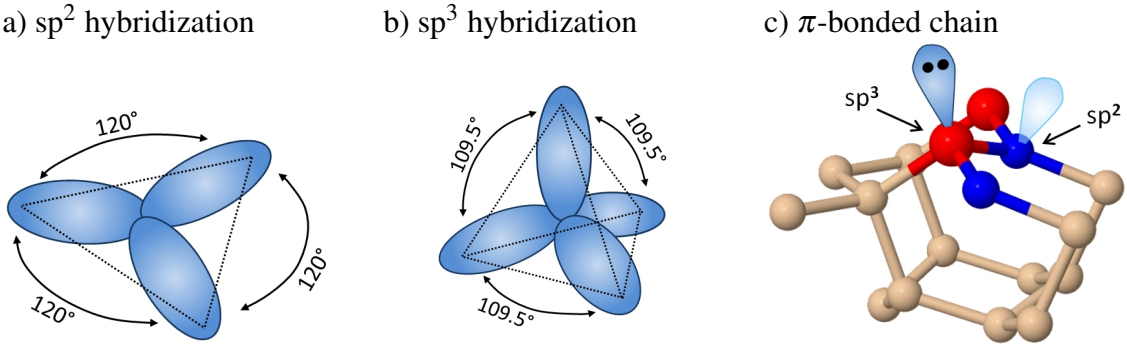

Figure 7.17: Charge distribution of the Si(111)-2x1 surface. a) sp^2 hybridization. b) sp^3 hybridization. c) Pandey reconstructed surface, showing the up atom with the filled lone pair in sp^3 and the down atom with the empty lone pair in sp^2 configuration.

The π-bonded chains in the Si(111)-2x1 reconstructed surface, as described by the Pandey model, are characterized by a strong buckling and an associated charge transfer from the down to the up atom, as described in Sec. 2.2.2. The buckling allows the clean surface to reduce its energy by redistributing charge from high energy p-like orbitals into lower energy s-like orbitals,[164] whereby the up atom forms an sp^3 hybridization and the down atom hybridizes in sp^2 configuration. This is illustrated in Fig. 7.17. Atoms hybridized in sp^2 are characterized by three hybridized orbitals in a planar configuration with an angle of 120° in between them, as shown in Fig. 7.17 a). This corresponds well with the down atom configuration extracted from relaxed DFT cells as shown in Fig.

7.17 c), where a planar bond configuration with an average angle of 119.8° was found. The fourth, unhybridized p orbital corresponds to the empty orbital of the down atom, forming the surface conduction band. Atoms hybridized in sp^3 are on the other hand characterized by four hybridized orbitals in a tetrahedral configuration with an angle of 109.5° in between them, as shown in Fig. 7.17 b). This corresponds well to the up atom of the π-bonded chain, shown in Fig. 7.17 c), where an average bond angle of 108.2° was calculated. The fourth, filled orbital is then forming the surface valence band.

In the π-bonded chains the up and down atoms therefore have a filled and an empty lone pair respectively, forming a balanced charge distribution responsible for the observed Si(111)-2x1 band structure. Rohlfing et al.[57] calculated that the charge transfer between up and down atoms is proportional to the buckling angle and that there is a strong interplay between geometry and electronic structure within the π-bonded chains. It can therefore be assumed that any disturbance of the Si(111)-2x1 reconstruction also has a significant influence on the charge distribution of the surface. We have already demonstrated that the insertion of significantly larger dopant atoms into the Si(111)-2x1 reconstruction creates new, previously unidentified reconstruction that, in the case of site 3 and 4, even rearrange bonds within the π-bonded chains. To accurately describe the measured charge of donor atoms we must therefore not only consider their ionization state but also have to evaluate the influence of their reconstruction onto the charge distribution within their atomic scale environment. This evaluation was done using the relaxed DFT models as shown in Fig. 7.18-7.21. Whereas DFT can be used to directly determine the number of electrons bound to any of the atoms within the cell we will, for illustrative purposes, use sp^2 and sp^3 bonding as an indicator for filled and empty lone pairs respectively. Both methods were found to produce identical results and allow us to determine the charge of the dopant in combination with its atomic scale environment.

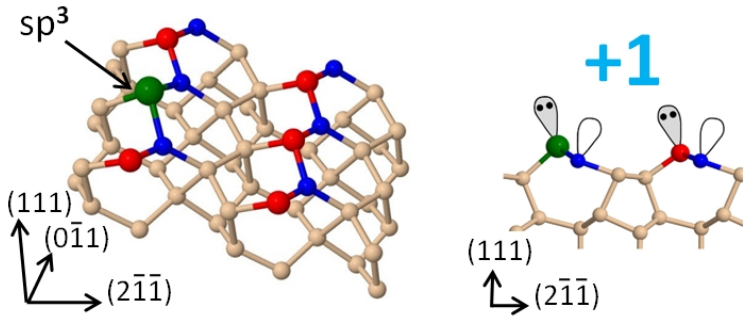

Figure 7.18: Charge state of dopant-surface complex for site 1.

For Sb and Bi in surface site 1, the dopant was found in an sp^3 configuration as shown in Fig. 7.18, indicating a filled lone pair. All other surface atoms were found undisturbed and therefore the only change is that a Si atom with a filled lone pair was replaced by a group V donor with a filled lone pair. Three fold coordinated Sb and Bi dopants

with a filled lone pair are electrically neutral, in disagreement with the measured positive charge. However, if a neutral donor substitutes a Si atom of the Si(111)-2x1 surface, the charge reordering on the surface will be disturbed due to the different electronic properties of the dopant core. It could be expected that the adjacent atoms neutralize this charge by adapting their buckling and retaining the overall, neutral charge state of the surface. However, any structural adaption to compensate this charge would represent a reconstruction different from the ground state of the Si(111)-2x1 Pandey model, increasing its energy. A competition between retaining the lowest energy reconstruction and creating a charge neutral state therefore exists. In contrast to Si(100) it is important to keep in mind that this competition is not limited to isolated dimers but takes place within the π-bonded chains, where every up atom has two neighboring down atoms and vice versa. When changing the electronic properties of one of the atoms in the π-bonded chains, for example by replacing it with a group V dopant, it is therefore not trivial to determine the reaction of the neighboring two atoms, now themselves bonded to a dopant on one side and the normal π-bonded chain to the other side.

When considering the balanced charge distribution of the surface-donor complex we have to take into account that the neutral dopant replaced a Si atom which had a filled lone pair, and was therefore negatively charged. As DFT simulations revealed that all other atoms in the surface are not influenced, this results in an apparent positive charge, in excellent agreement with the measurement. A different, more simplified way to look at the same concept is shown in the right side of Fig. 7.18, where a cross section through the atomic model is depicted. All the charges can be summed up, where a Si atom with a filled or empty lone pair is treated as negatively or positively charged respectively. Donor atoms with a filled lone pair are on the other hand counted as electrically neutral. Again this results in a positive surface charge, in excellent agreement with the measurement.

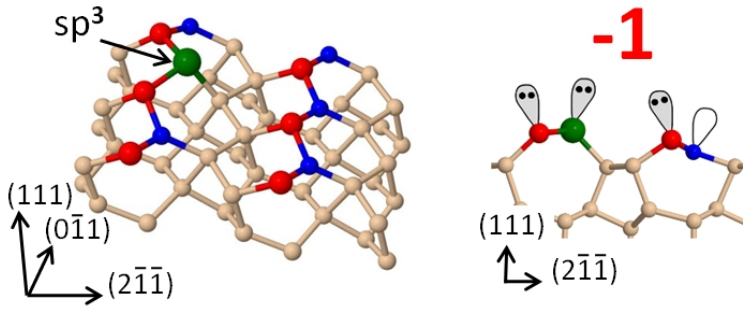

Figure 7.19: Charge state of dopant-surface complex for site 2.

The same analysis was performed for site 2, as shown in Fig. 7.19. It can be seen that the dopant is in an sp^3 configuration whereas all other atoms are left essentially undisturbed. Because this time the dopant is however replacing a Si atom that had an empty

lone pair (pos charged), the resulting apparent surface charge is negative. Again this can be easily confirmed by counting all the charges in the cross sectional view of the atomic scale reconstruction. It has to be stressed that Sb and Bi atoms in site 2 are not negatively charged but electrically neutral when following this model. Only in conjunction with the charge balance of the Si(111)-2x1 surface, an apparent negative charge is created due to the replacement of a positively charged Si atom with a neutral group V element.

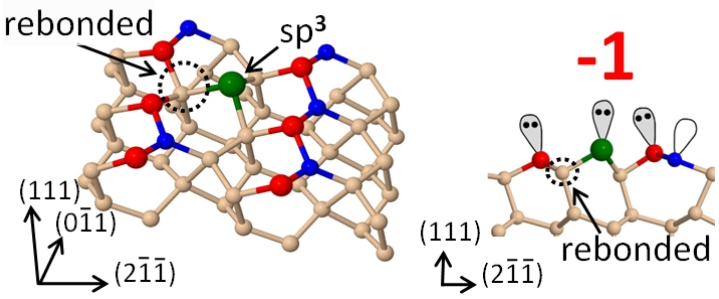

Figure 7.20: Charge state of dopant-surface complex for site 3.

For a dopant in site 3, the experiment predicts a negative charge. The donor is in this case substituting a four fold coordinated Si atom from the trough region, as shown in Fig. 7.20, which is electrically neutral. In the surface reconstruction, the dopant is found again in an sp^3 configuration, also making it electrically neutral. However, in the new reconstruction we can see that the down atom in a neighboring π-bonded chain is pushed down and now four fold coordinated, removing its empty lone pair. All other atoms were found to be undisturbed, leaving them in the same charge state as in the original Pandey reconstruction. When adding the charges present in the vicinity of the dopant atom we can therefore see that the dopant-surface complex is negatively charged due to the elimination of the positively charged down atom.

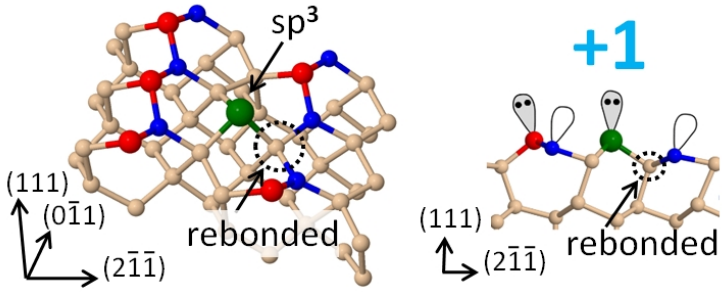

Figure 7.21: Charge state of dopant-surface complex for site 4.

The situation for site 4 is similar, as shown in Fig. 7.21. Again the dopant is found in an sp^3 configuration, replacing a neutral, four fold coordinated Si atom. This time the reconstruction however pushes down an up atom in a neighboring π-bonded chain, making it four fold coordinated and removing the filled lone pair. Adding all the charges

therefore results in an apparent positive charge due to the elimination of the negatively charged up atom, in excellent agreement with the measurement.

Again it is pointed out that the Bi and Sb dopants are assumed neutral in all four surface sites due to their filled lone pair. However, the introduction of this neutral donor into the Si(111)-2x1 surface reconstruction disturbs the delicate charge balance of the surface and leads to the observed apparent charging effect in STM measurements. Whereas a positive charge is created by the donation of an electron to the bulk, identical to subsurface donors, negative charge has to be explained by acquiring an extra electron from the bulk, similar to p-type doping. In the experiment this is considered feasible since the pinning of the Fermi level within the surface conduction band creates an accumulation layer, supplying a sufficiently high electron concentration. In the DFT simulation this however represented an interesting problem, since the limited cell size and the absence of dopants makes it impossible for the surface to just grab an additional electron. This is the other reason why we introduced an additional electron into all DFT cells, as mentioned earlier. The effect of this cell charging onto the calculated reconstructions can be seen in Fig. 7.22 for the example of site 2.

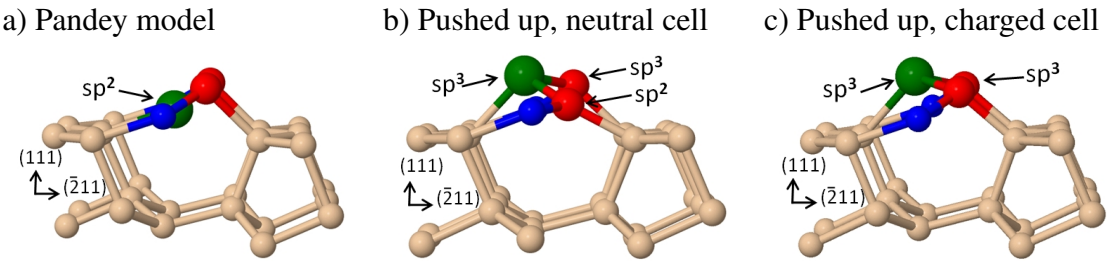

Figure 7.22: Influence on the dopant reconstruction when charging DFT cells. a) Dopant in the Pandey reconstructed Si(111)-2x1 surface. b) Ground state relaxation for a neutral cell. c) Ground state relaxation for a negatively charged cell.

In Fig. 7.22 a), a dopant in the Pandey model is shown, forming a local energy minimum. The dopant is in an sp^2 configuration which would lead to a positive surface charge, in disagreement with the measurement. If the dopant is pushed up within a neutral cell, we found a ground state reconstruction as shown in Fig. 7.22 b). It can be seen that the dopant is now in an sp^3 configuration, but also one of the two neighboring up atoms has suddenly buckled down, changing from sp^3 into an sp^2 hybridization. This structure relaxation was found to be 0.14 eV more stable than the Pandey reconstruction but would result in a positive charge, in disagreement with the measurements. Furthermore, simulated STM images were found strongly asymmetric, also in clear disagreement with the measured contrast in STM. It is assumed that the asymmetric structure was formed due to the lack of an additional electron that would allow the down buckled up atom to remain in an sp^3 configuration, keeping its filled lone pair. This was confirmed by the relaxation of

a negatively charged DFT cell, as shown in Fig. 7.22 c). This reconstruction was found 0.27 eV more stable than a dopant in the Pandey reconstructed site of a negatively charged cell, and is therefore the lowest energy reconstruction we were able to identify. It can be seen that the structure is now symmetric and due to the sp^3 configuration of the dopant and both of its neighboring up atoms, the resulting charge state is negative, in excellent agreement with the measurement.

7.4 STS Measurements of Donor LDOS in Silicon

Based on STM topography measurements we were able to determine the polarity of the charge state associated with dopants in different positions of the Si(111)-2x1 surface and subsurface layers. Using scanning tunnelling spectroscopy we are furthermore able to directly measure the local density of states and therefore resolve the influence of the dopants on the band structure of their atomic scale environment.

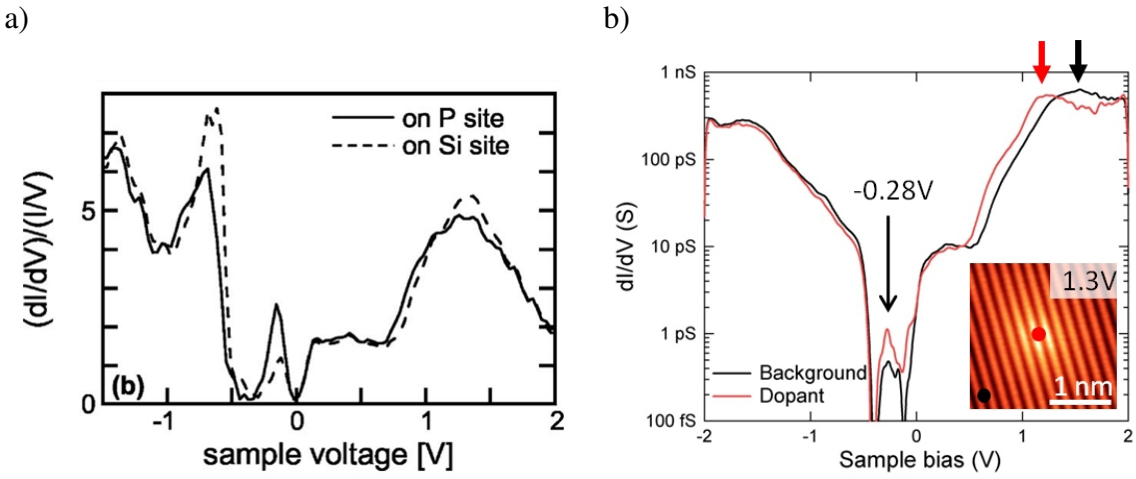

Figure 7.23: a) STS measurement P dopant at 8 K. Image from [82]. b) STS measurement of an Sb dopant at 78 K. The inset shows a topography image of the dopant, the colored circles indicating the positions where the spectra were acquired.

STS measurements of P in the Si(111)-2x1 surface layer were previously reported by Garleff et al.[82] and are shown in Fig. 7.23 a). The STS trace was recorded at 8 K and is shown normalized as (dI/dV)/(I/V). It can be seen that the surface valence band peak at -0.5 V is decreased, whereas the peak at -0.25 V is increased when measuring on top of the P donor. The filled states peak at -0.25 V was described to be a part of the surface conduction band that is pushed below the Fermi energy, based on the fact that images taken at -0.25 V sample bias revealed the same corrugation as images taken in low empty states bias. The increase in this peak measured on the P dopant was therefore assumed to be caused by defect induced broadening of the surface conduction band whereas the

gap in the STS curve around the Fermi level is attributed to a Coulomb blockade formed by the one dimensional π-bonded chains.[82] Garleff et al. found that STS measurements for different surface sites were identical and no peak shifts were measured, leading to the assumption that P dopants are not ionized at 8 K.

STS measurements recorded at 78 K for a subsurface Sb donor are shown in Fig. 7.23 b). We found that the LDOS for Sb and Bi were basically identical, whereas the tip quality when measuring on the Bi wafers was usually inferior due to the need to walk the tip to the implanted layer and due to the imaging of additional defects caused by the implantation damage. The STS curve shown Fig. 7.23 b) was normalized as Log(dI/dV) in order to avoid the introduction of band edge artifacts, as previously discussed in Sec. 2.1.3. Nevertheless, it is possible to directly compare the P and Sb spectra qualitatively as the energy of peaks and their relative height compared to the clean surface are not affected by the normalization.

The STS measurement for subsurface Sb looks very similar to that of P, also showing an increased intensity of the peak in the surface band gap at -0.28 V. However, as we have already discussed, we found that subsurface Sb and Bi are ionized and therefore positively charged. The effect of this can be clearly seen in the STS measurements where the surface conduction band is shifted to lower energies around the donor when compared to the clean surface, as indicated by the arrows. This is in excellent agreement with the expected potential well of a positively ionized dopant core.

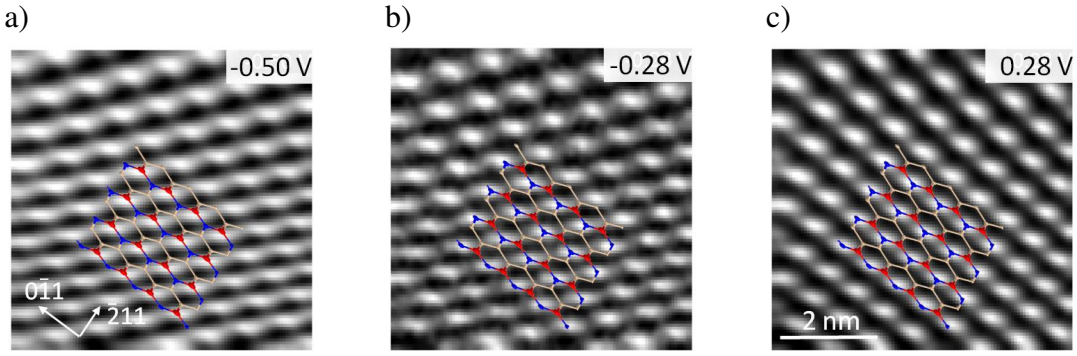

Figure 7.24: Laterally resolved differential conductance of Si(111)-2x1 shown for different energies. a) Low filled states. b) Peak at -0,28 eV. c) Low empty states.

To explain the increase of the peak at -0.28 V, the LDOS on the surface were measured using CITS. The laterally resolved differential conductance of the bare surface for low filled states and low empty states bias is shown for in Fig. 7.24 a)+c) respectively. As expected, the LDOS are localized on the up atom in filled states and the down atoms in empty states, indicated by the overlayed Si(111)-2x1 structure. The LDOS at the peak energy of -0.28 eV is shown in Fig. 7.24 b), and it can be seen that the measured contrast is also centered on the down atom, very similar to the measured empty states in the conduc-

tion band. This is in excellent agreement with the results of Garleff et al.[20] and confirms that this peak represents filled states at the bottom of the surface conduction band. These states are likely to be caused by the Fermi level pinning, as discussed in Sec. 2.2.2. A defect induced broadening of the surface conduction band was suggested to be the cause for an increase of this peak, measured near the neutral P dopants. It is assumed that the charged Sb and Bi donors may additionally increase this peak due to the induced potential well, further pushing the Fermi level upwards and therefore increasing the number of filled states in the bottom of the surface conduction band. No peak could be directly assigned to the subsurface dopant state of either Bi or Sb. Theoretically this state should be situated just below the bulk valence band and therefore at around +0.6 V in the STS spectra, assuming the Fermi level to be pinned 0.4 eV above the surface valence band. It is assumed that the large LDOS in the surface conduction band at this energy masks the influence of the additional subsurface dopant state.

In contrast to P, we found that the measured LDOS for Bi and Sb dopants in the different sites of the Si(111)-2x1 surface varied considerably. This is not surprising when considering the fact that we identified three completely new reconstructions, formed due to the incorporation of the larger group V dopants as discussed previously. STS measurements for Sb and Bi in all four surface sites are shown in Fig. 7.25. The inset also shows a topography image with colored circles, indicating the position where STS measurements were acquired. It can be seen that traces for Sb and Bi in identical crystal sites are very similar, even though the quality of the Bi STS is not as good as for the Sb measurements due to the more difficult measurement conditions.

When comparing the different crystal sites, it can be seen that the positively charged sites 1 and 4 are similar, characterized by a high LDOS throughout the bandgap, an increased surface conduction band peak and a decreased filled states current. The negatively charged sites 2 and 3 are also alike, showing two characteristic peaks in the valence band as well as an increase in the surface conduction band. It is assumed that the main influences onto the measured LDOS are created by the dopant charge state and the disturbance of the surface charge balance within the π-bonded chains. We could not resolve any features that allow distinguishing between Sb and Bi dopants and therefore assume that the newly identified reconstructions in the different surface sites are the main cause for the measured change in LDOS. Further theoretical analysis would be required to correlate the identified structural changes with the measured LDOS of dopants in the surface layer. This would allow to determine the exact origin of the different observed peaks and evaluate the influence of the discussed charge states and reconstruction changes.

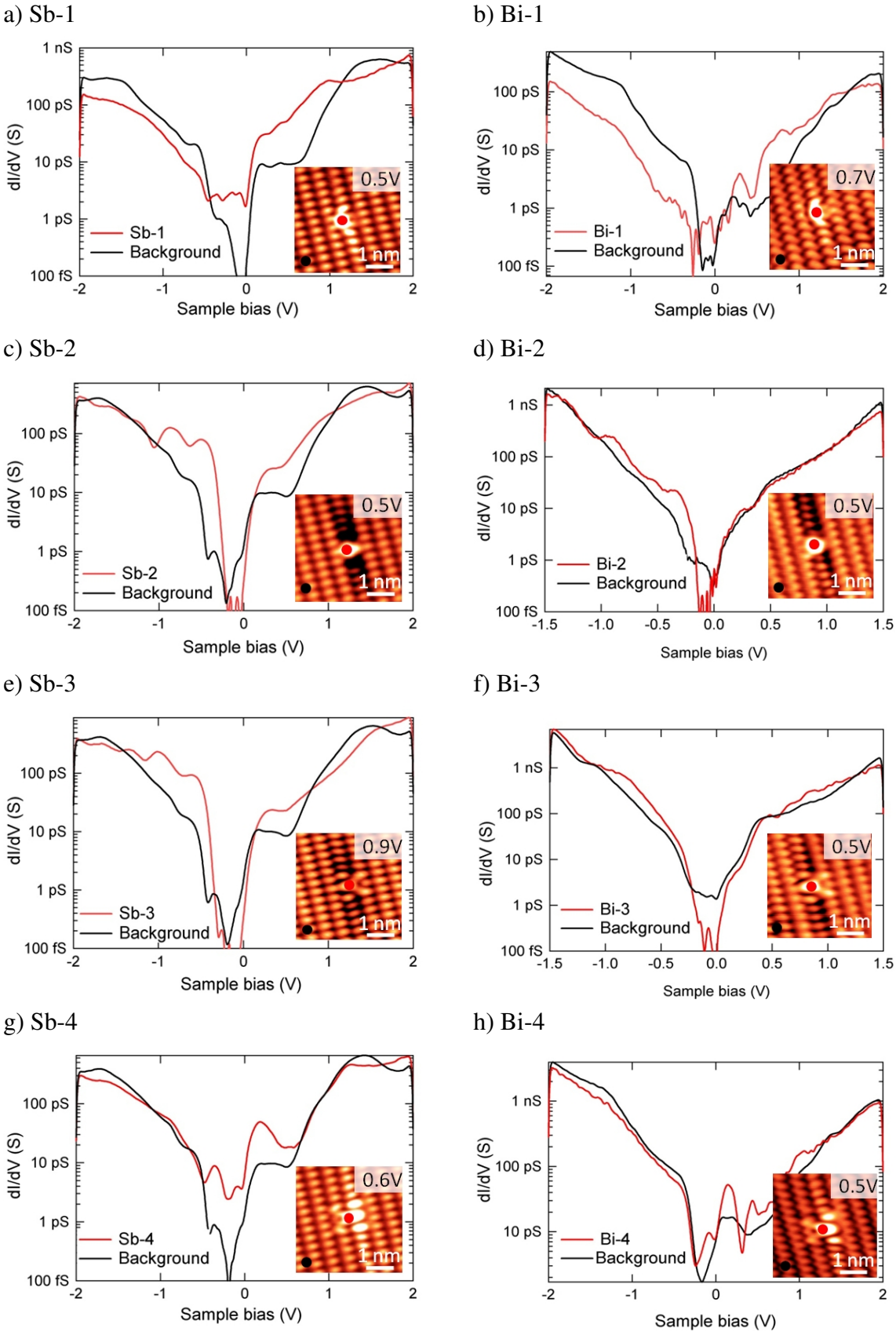

Figure 7.25: STS of Bi and Sb in different surface sites. The inset shows a topography image with colored circles, indicating the position where STS measurements were acquired.

7.4.1 Measuring the Screened Potential Well

The extent and size of the screened potential well of group V donors is an important characteristic for the design of future devices, as it determines the energy levels of individual dopants and governs the interaction of donors with each other. We have shown that it is possible to measure the influence of the screened Coulomb potential in STM topography images, observing the characteristic protrusion in empty states. The measured height and shape of this protrusion is directly related to the band bending of the induced Coulomb potential, but due to the complex relation between band bending and tip height it is difficult to accurately determine the shape of the potential well from STM topography images. Even though it is possible to estimate the screening radius by fitting a simple exponential curve to the measured z-height,[158, 159] the depth and shape of the potential well can not be extracted from topography measurements.

Teichmann et al.[16] found a way to measure the potential well of a single silicon dopant atom in GaAs, taking advantage of the unique surface properties of this semiconductor. Because there are no surface states in GaAs, tip induced band bending has a much more severe effect than in silicon and can be used to controllably ionize the dopant, pulling its state above the Fermi level. By measuring the band shift, induced by the deliberate ionization of the dopant, at different positions on the surface, they were able to map out the shape and strength of the Coulomb potential induced by a single donor. On the Si(111)-2x1 surface this method can not be applied due to the pinned Fermi energy, preventing the controlled charge switching of individual dopants. Hasegawa et al.[165] however developed a method to measure the surface potential on Si(111)$\sqrt{3}x\sqrt{3}$Ag, which we find to be transferrable to Si(111)-2x1. They used CITS to measure the spatially resolved LDOS near a step edge and found that the peaks of the individual STS traces were periodically shifted due to a Friedel oscillation, occurring in the two dimensional electron gas of this specific system. By plotting the peak energy as a function of surface position they were able to directly visualize the surface potential, a method that we find to be applicable to measure the screened potential well of a single dopant in silicon.

7.4.1.1 Screening of Subsurface Dopants

To precisely measure the potential well induced by a single dopant in the Si(111)-2x1 surface, we mapped out the surface potential of its atomic scale environment as shown in Fig. 7.26. As previously discussed, STS curves show a characteristic shift in the surface conduction band when measured in the vicinity of an ionized subsurface dopant. This is shown in Fig. 7.26 a), where three STS curves are displayed that were acquired with increasing distance from an Sb donor, as indicated in inserted topography image. When observing the peak around 1.45V, it can be seen that there is a gradual shift to lower

energies when measuring closer to the dopant, as expected for a positively ionized dopant core. Using CITS, we have measured the peak voltage as a function of position, plotted in the image shown in Fig. 7.26 b). The x and y coordinates of this image represent the lateral tip position, as in regular topographic STM images, but instead of plotting the tip height, the color scale indicates the observed relative peak shift. The potential well is clearly visible at the location of the subsurface dopant and a maximum relative peak shift of -0.3 eV is measured immediately on top of the dopant. Using this technique we are observing the band bending induced by the dopant and are therefore directly measuring the screened Coulomb potential well. To plot the shape of the measured potential, the relative peak shifts were radially averaged as indicated in the image, resulting in the red line profile shown in Fig. 7.26 c).

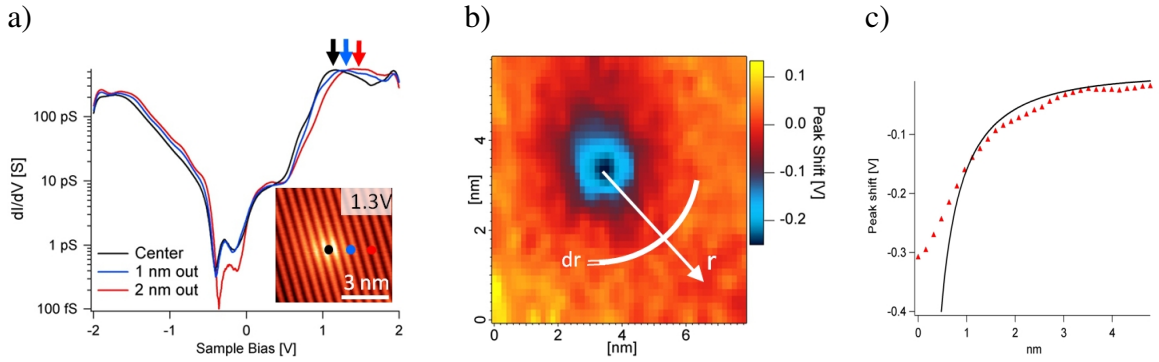

Figure 7.26: Surface potential imaging. a) STS traces acquired with different distances from the subsurface dopant as indicated by the colored circles in the insert. b) Surface potential image measured by plotting the laterally resolved relative peak shift around 1.45 V. c) Surface potential averaged radially from the dopant outwards (red) and calculated coulomb potential (black).

When comparing the shape of the measured potential well, shown in red in Fig. 7.26 c), with the theoretically calculated screened potential, indicated in black and previously shown in Fig. 7.1 b), it becomes obvious that they are qualitatively very different. Most striking is the singularity at 0 nm in the calculated potential well that is not reproduced in the measurement data. This is to be expected, as the dopant is subsurface and we are therefore not measuring the Coulomb potential directly through its origin, as indicated in Fig. 7.27 a). It can be seen how the measured potential profile is offset by a distance d from the dopant core, creating a potential profile much more closely resembling the measured potential well. In the equation for the screened Coulomb potential, the distance r therefore has to be modified to $r = \sqrt{d^2 + x^2}$, as shown in Eq. 7.4. In this equation x is indicating the distance from the measured center of the dopant in STM and d the depth of the donor below the surface.

$$V(r) = \frac{e}{4\pi\varepsilon_0\varepsilon_r\sqrt{d^2+x^2}} \times e^{-\frac{\sqrt{d^2+x^2}}{R_s}} \tag{7.4}$$

When considering the cross section of the Si(111)-2x1 surface, as shown in Fig. 7.27 b), it can be seen that dopants in the first and second subsurface layer are buried approximately 4.5 $\AA$ and 7.5 $\AA$ deep, giving us close approximations for the expected d value. Another factor that has to be considered is the dielectric constant influencing the screening of a dopant close to the surface. In the bulk crystal we used the dielectric characteristics of silicon, ε_{Si}=11.9, to calculate the screened Coulomb potential. A dopant close to the surface layer is however influenced by the interface between silicon and vacuum, both materials having significantly different dielectric properties. For a dopant placed directly at an interface the dielectric constant is, according to the image potential result,[166] assumed to be the average of the two interfacing materials $\varepsilon_r = \frac{\varepsilon_{Si}+\varepsilon_{Vac}}{2} = 6.45$, vacuum and silicon in our case. However, because we are looking at subsurface dopants placed at a distance d from the interface, it is likely that they are more strongly influenced by the dielectric properties of silicon than that of the vacuum. This leads to an expected range for ε_r between 6.45 and 11.9.

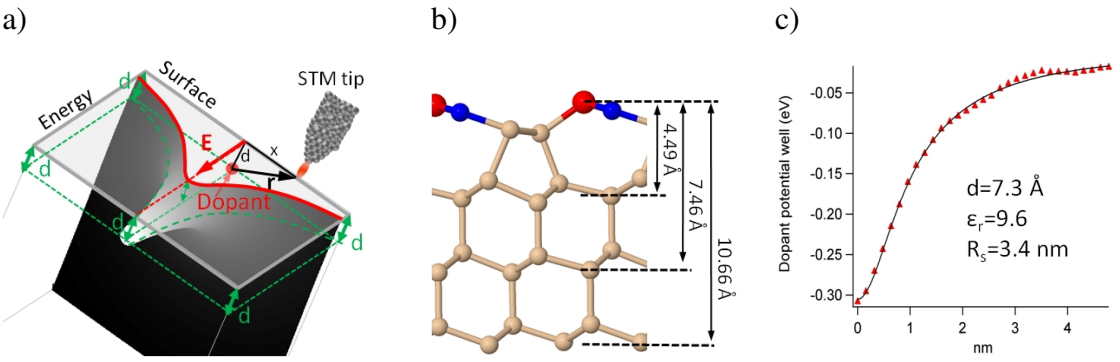

Figure 7.27: Fitting the screened Coulomb potential well. a) Three dimensional representation of the buried Coulomb potential and the observed shape at the surface. b) Layer depths of Si(111)-2x1. c) Fitted screened subsurface Coulomb potential.

Eq. 7.4 was fitted to the measured shape of the screened Coulomb potential, leaving d, ε_r and R_s as adjustable parameters. The results are shown in Fig. 7.27 c) and it can be seen that the fitted line shape closely matches the measurement. Furthermore, the parameters resulting from the fitting process, as stated in the insert of the image, are all lying within the expected range. We find a dopant distance of 7.3 $\AA$ below the surface, in excellent agreement with a dopant in the second atomic layer, 7.5 $\AA$ below the up buckled atom in the π-bonded chains. The dielectric constant ε_r of the measured potential well is calculated to be 9.6, again in excellent agreement with the expected range between 6.45 and 11.9. The resulting screening radius is 3.4 nm and therefore slightly larger

than reported screening radii of around 1.2 nm,[159, 160] extracted from topography images for dopants in silicon. However, this slightly larger screening radius is expected when considering the specific charge carrier distribution of the Si(111)-2x1 surface. As shown in Eq. 7.2, the screening radius is strongly dependent on the carrier concentration and in the silicon bulk, screening lengths larger than 5 nm occur[167] for low doped samples. Garleff et al.[82] have shown that the pinning of the Fermi level in the Si(111)-2x1 surface state creates a depletion region underneath the surface layer, strongly reducing the carrier concentration. This suggests that a subsurface dopant would be subjected to a much lower carrier density compared to a bulk dopant, in good agreement with the measured, large screening radius. It is difficult to predict how exactly a dopant situated within the depletion layer, but also very close to the high carrier concentration in the surface states, would be screened. The measured screening length of 3.4 nm seems in good agreement with the discussed effects and provides a valuable experimental measurement for future theoretical work, describing the screening of dopants close to a semiconductor surface.

7.4.1.2 Screening of Dopants in the Surface Layer

The complex screening characteristics of dopants within a reconstructed semiconductor surface are still subject to discussions,[54, 168, 169] the highly confined and anisotropic surface states making it difficult to accurately formulate a theoretical model. The band structure of the Pandey π-bonded chain reconstruction is of fundamental importance for the screening properties of this surface. As discussed in Sec. 2.2.3, π-bonded chains show a high dispersion, giving carriers a low effective mass and making them delocalized. Perpendicular to the chains on the other hand, the dispersion is significantly lower and carriers are expected to be highly localized due to their high effective mass. These properties were confirmed with surface differential reflectivity measurements by Chiaradia et al.,[40] who reported highly anisotropic dielectric properties for the Si(111)-2x1 surface, in good agreement with the Pandey chain model.

Reining et al.[168, 169] developed a model to describe the influence of the Si(111)-2x1 surface states onto the screening of charges, based on the assumption that electrons are completely confined to a single π-bonded chain. They concluded that surface states enhance the screening by a factor of two in close proximity to the charge, which was lower than expected as the dielectric constant had been found to be six times higher than in the silicon bulk. This weak screening enhancement was attributed to the reduced dimensionality of the π-bonded chains and they even found that, at distances of two or more unit cells along the same chain, the screening contribution of the surface states is negative. Rohlfing et al.[54] on the other hand used first principles calculations to investigate the properties of the Si(111)-2x1 surface, and found that a complete confinement of electrons to a single π-bonded chain is not realistic. To visualize the degree of confinement, Rohlf-

ing et al. plotted the electron-hole wave function of the lowest-energy spin-singlet surface exciton in real space,[54] fixing the hole at an up atom as shown in Fig. 7.28. It can be seen that the wave function is anisotropic and strongly extended along the π-bonded chains, but nevertheless it significantly affects the two adjacent π-bonded chains, questioning the results of the previously described model.

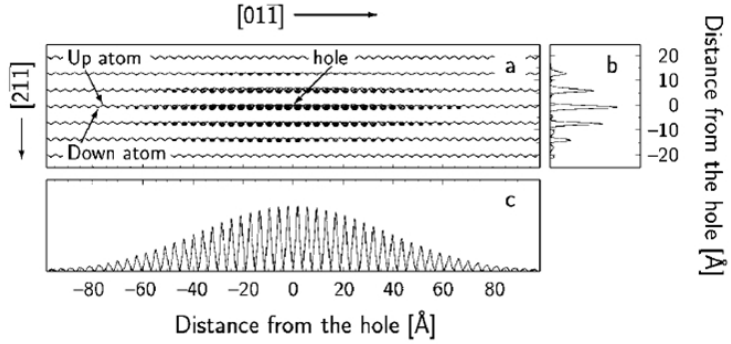

Figure 7.28: The electron-hole wave function of the lowest-energy spin-singlet surface exciton plotted in real space. The plot shows the distribution of the electron relative to the hole position in a (111) plotting plane slightly above the surface. Figure from [54].

Using STM topography and STS measurements, we are able to address the surface and bulk states separately and can investigate the influence of a charged defect onto the band structure of the Si(111)-2x1 surface. As mentioned previously, we have found that Sb and Bi in site 3 and 4 create a negative and positive charge state respectively. We are therefore able to investigate screening effects in both charge polarities as shown for the example of an Sb dopant in Fig. 7.29 and Fig. 7.30 for surface sites 4 and 3 respectively.

In Fig. 7.29 a) and b), STM topography images at 0.6 V and 1.3 V are shown respectively for an Sb donor in surface site 4. Bi was found to create identical contrasts, shown in the inserts, as did measurements for the positively charged surface site 1. As discussed in Sec. 5.4, the tunnel current at 0.6 V is dominated by empty states of the surface conduction band whereas bulk states are dominating the image measured at higher bias voltages. Topography images at these voltages are therefore mainly showing the influence of the charged Sb reconstruction onto the surface conduction band and bulk states on the surface respectively. It can be seen that at 1.3 V, the effect of the positively charged Sb-4 reconstruction produces the characteristic circular protrusion of a screened Coulomb potential in the bulk states, similar to what was observed for subsurface dopants. When on the other hand considering the surface states, imaged in Fig. 7.29 a), it can be seen that the protrusion is confined to the direction of the π-bonded chains, in good agreement with the expected localization of the charge. From the atomic model of Sb-4, shown in Fig. 7.21, we can furthermore see that the brightened π-bonded chain to the right of the Sb dopant is where the up buckled atom was eliminated, creating the positive charge state

of the SB-4 reconstruction. A connection between the charge state and the single elevated π-bonded chain therefore seems likely.

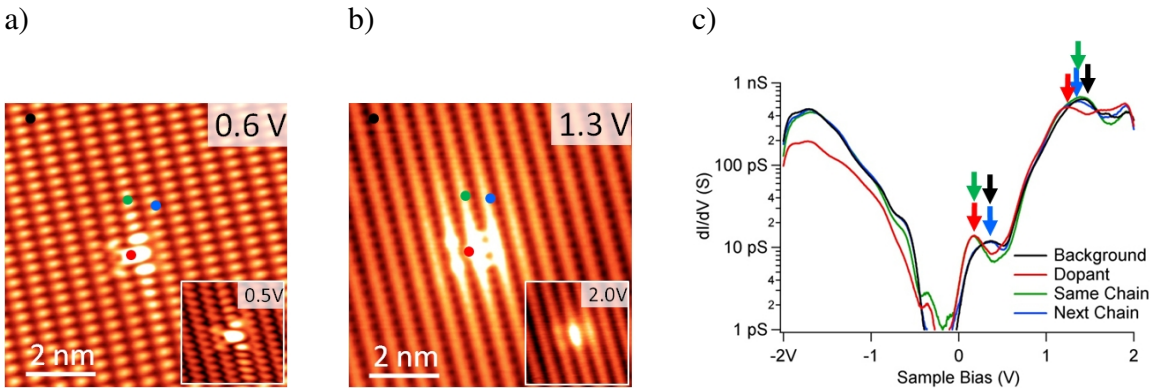

Figure 7.29: Surface potential of Sb-4, Bi-4 shown in inset. a) Topography image of the empty surface state band. b) Topography image dominated by bulk empty states. c) STS analysis of band shift in surface and bulk peaks.

We have shown that the potential well of a subsurface dopant can be visualized in STS by directly measuring the induced band shift in the peak around 1.45 V. A similar analysis was performed to characterize the highly anisotropic charge distribution found in the surface states. STS curves were acquired at different locations around the dopant, as shown in Fig. 7.29 c), their location on the surface indicated in the topography images by the colored circles. It can be seen that the STS spectra on the Sb dopant shows the surface conduction band peak around 0.4 V and the bulk peak around 1.45 V shifted to lower energies when compared to the background, in good agreement with a positive charge. Two more STS spectra are shown, taken with identical distance from the Sb dopant, but one within the brightened and one in an adjacent π-bonded chain. When considering the bulk state peak at 1.45 V of these spectra, it can be seen that both peaks are half way in between the dopant and background peak, in good agreement with a radially decaying potential well. When on the other hand considering the surface states, it can be seen that the STS curve within the same π-bonded chain has its peak strongly shifted, whereas the STS curve acquired in the adjacent π-bonded chain shows no measurable peak shift at all. The fact that we see a shift in the STS measurement of the surface conduction band that is strongly confined to a single π-bonded chain supports the assumption that the measured brightening of the chain is indeed caused by a highly anisotropic potential well.

The same measurement was repeated for a negatively charged Sb dopant reconstruction in site 3, as shown in Fig. 7.30. Again Bi was found to produce identical contrasts, shown in the insert, as did measurements for the also negatively charged surface site 2. The topography measurements in Fig. 7.30 a) and b) show identical characteristics as described for Sb-4 but with reversed polarity. In the bulk state image at 1.1 V we can see the characteristic circular contrast induced by a screened Coulomb potential well of

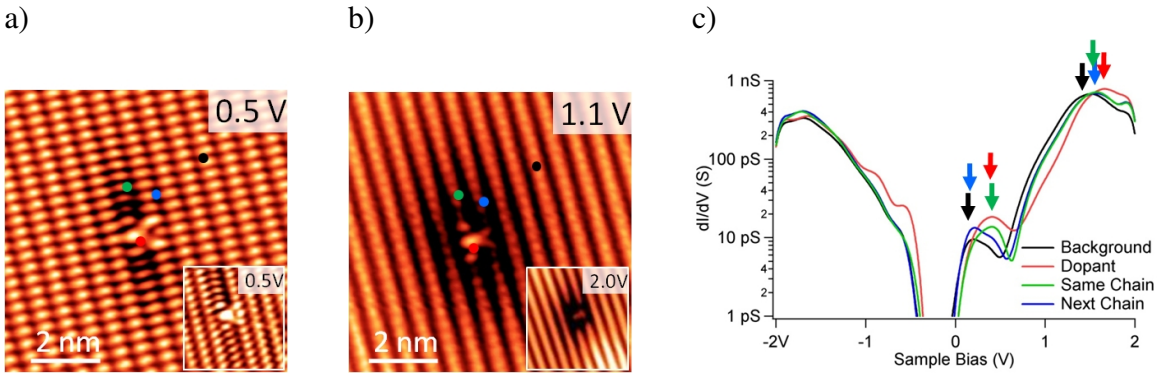

Figure 7.30: Surface potential of Sb-3, Bi-3 shown in inset. a) Topography image of the empty surface state band. b) Topography image dominated by bulk empty states. c) STS analysis of band shift in surface and bulk peaks.

a negative charge. When measuring the surface states at 0.5 V on the other hand, the depression is again confined to a single π-bonded chain, this time to the left of the dopant where the down atom was eliminated, as shown in the atomic model in Fig. 7.20. The STS measurements shown in Fig. 7.30 c) also display the exact same characteristics as Sb-4 but with reversed sign. On the dopant, the surface state peak and the bulk peak are shifted to higher energies, in agreement with a negatively charged defect. The STS traces acquired with identical distance from the dopant but in different π-bonded chains show again that the potential is radially decaying in the bulk states but highly confined to a single π-bonded chain in the surface states.

To characterize the observed potential wells in the surface and bulk states in more detail, we determined their screening radii. Visualizing the potential shift using CITS measurements, as we have done it for subsurface dopants, was unfortunately found to be not possible as the induced dopant reconstruction obscures the relevant peaks in the immediate vicinity of the donor. To determine the different screening radii, the exponential part of Eq. 7.1 was therefore fitted to the measured protrusions and depressions in STM topography outside of the main dopant reconstruction. This analysis, as proposed by Hamers et al.,[159] is shown in Fig 7.31.

We found that the screening radius of the Sb-4 protrusion and Sb-3 depression measured at high filled states bias was 1.8 nm and 2.2 nm respectively, as shown in Fig.7.31 b) and d). When on the other hand fitting an exponential curve to the decay measured within the brightened and darkened π-bonded chain of site 4 and 3, we found a much shorter screening length of 1.4 nm and 1.2 nm respectively, as shown in Fig.7.31 a) and c). This matches well with the expected increased screening in the surface state as proposed by Reining et al.[168] The observed brightening/darkening of the individual π-bonded chain was found to be visible for around 4 nm in either direction of the dopant and its length scale therefore corresponds reasonably well with the theoretically calculated wave func-

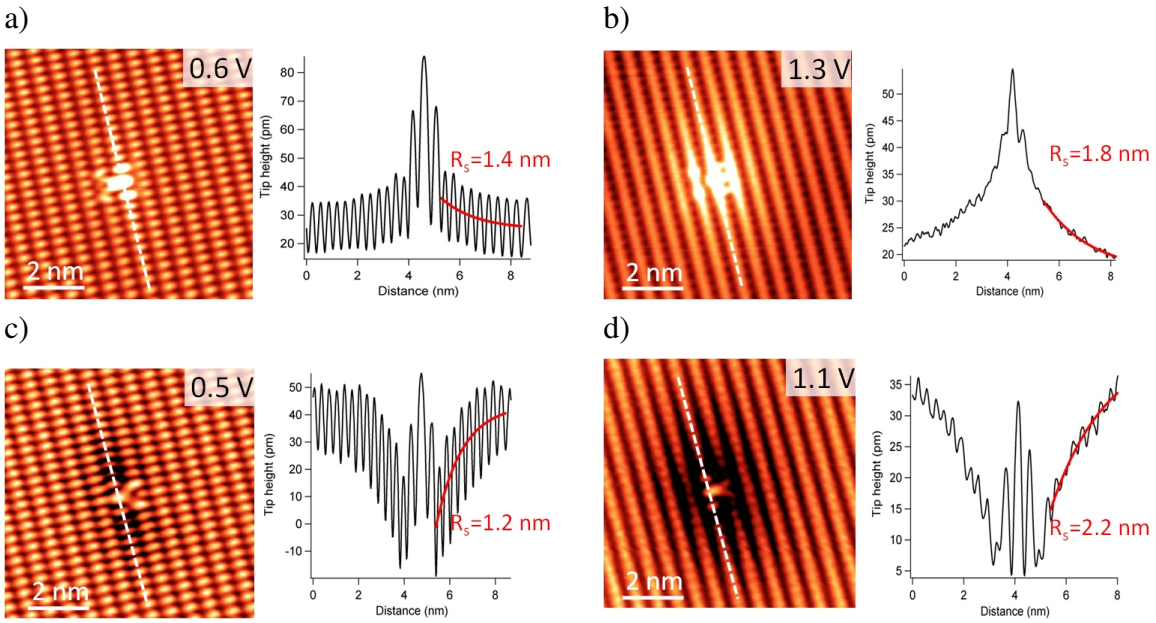

Figure 7.31: a) Screening in surface states of positively charged Sb-4. b) Screening in bulk states of positively charged Sb-4. c) Screening in surface states of negatively charged Sb-3. d) Screening in bulk states of negatively charged Sb-3.

tion by Rohlfing et al., as shown in Fig. 7.28. However, the observed localization perpendicular to the π-bonded chains appears to be stronger than anticipated by the calculations, as no effect was measured on neighboring chains. Since the localization of a hole on an up atom is however not simulating the same situation occurring in our measurement- where a large dopant core creates a new, charged surface reconstruction in its atomic scale environment- the results are not directly comparable, which might explain the observed difference in localization. Furthermore, it could be that STS measurements acquired at 78 K do not have the required energy resolution to detect a shift of the surface state in adjacent chains and measurements at lower temperatures could be necessary to detect the calculated wave function distribution.

Using STM topography and STS measurements we were able to visualize the influence of a charged defect onto the band structure of its atomic scale environment. Due to the high energy resolution of STS we were furthermore able to characterize the induced potential well for surface and bulk states of the Si(111)-2x1 surface separately by determining the laterally resolved peak shifts of the different states. We found that the induced potential well in the surface states is highly anisotropic, confined to the orientation of the π-bonded chains, whereas the potential well in the bulk is radially decaying, as previously observed for subsurface dopants. The atomic scale characterization of the energy resolved potential distributions and the determined screening radii provide experimental data that might help to verify future theoretical studies, describing the complex surface screening of Si(111)-2x1.

8 Summary and Discussion

In this thesis we presented a comprehensive study of individual group V donors in the Si(111)-2x1 surface. Their properties were characterized at the atomic scale using scanning tunnelling microscopy and their usability for single dopant devices was investigated. We started by developing necessary sample preparation methods to study Bi in silicon, a deep donor with interesting characteristics for QIP,[8, 140] but not commonly used in semiconductor industry. The cleaved Si(111)-2x1 surface was characterized and in particular we focused on anti phase boundaries, demonstrating that they can be used as a model system for controlling strain at the atomic scale. Utilizing a newly developed sample preparation process based on ion implantation and cross sectional STM, we were furthermore able to characterize individual Bi and Sb atoms at the atomic scale. We demonstrated how the fundamental properties of different dopant elements interact with their atomic scale environment and how the Si(111)-2x1 surface reconstruction influences the electronic properties of single donors. In this chapter, the most important findings are summarized and their relevance for the implementation of future single dopant devices is discussed.

8.1 Cross Sectional Scanning Tunnelling Microscopy

To enable the characterization of different group V dopants in substitutional silicon crystal sites, a sample preparation method that enables STM measurements on atomically clean surfaces without employing any heat treatments was developed. This is necessary to avoid unintended dopant behavior such as donor atoms segregating and diffusing towards surfaces,[146, 147] forming pairs,[43] interacting with defects[44] or evaporating from the crystal.[45] Cross sectional STM is ideally suited for such measurements on semiconductors,[170] as surfaces can be prepared with large, defect free and atomically clean terraces without the need of in situ annealing. Specialized sample holders were designed and custom built, as shown in Sec. 3.3.3, and the cleaving behavior of silicon was characterized together with the observed Si(111)-2x1 surface reconstruction, as described in Chap. 5.

We found that the implemented cleaving process results in atomically flat terraces with sizes on the order of 100 nm, in good agreement with values reported in literature, ranging

from 10 nm to 150 nm.[74, 112] Si(211) wafers were cleaved along a $\{111\}$ cross section, creating the well known Pandey reconstructed Si(111)-2x1 surface.[53] We used low P doped wafers with a donor concentration around 1×10^{15} cm^{-3}, ensuring that STM measurements were not influenced by the background dopant atoms, as less than one donor is expected in the surface of one square micrometer. These substrates were used to characterize the bare surface, creating a good understanding of all occurring surface defects and distinguishing them from implanted Bi dopants, investigated in a subsequent step.

8.2 Anti Phase Boundaries in Si(111)-2x1

Experiments were conducted at cryogenic temperatures in order to allow high quality STS measurements. We found that the measured scanning tunnelling spectra at 78 K were highly asymmetric, in good agreement with the expected freeze out of intrinsic charge carriers in non degenerately n-type doped silicon. This was confirmed by temperature dependent STS measurements between 78 K an 200 K, showing that the concentration of mobile charge carriers measured in empty states recovers with increasing temperatures. Measurements of surface defects on the bare Si(111)-2x1 surface were therefore conducted at 200 K, where the local density of states was found to be in excellent agreement with reported measurements in literature.[56]

The most frequently observed defect in the Si(111)-2x1 surface reconstruction is the anti phase boundary (APB), formed when two domains meet that have their π-bonded chains shifted by half a unit cell. These boundaries were previously observed and are thought to act as nucleation sites for silicon adatoms, crucially influencing the thermal conversion of the 2x1 into the 5x5 or 7x7 reconstruction,[73] as well as epitaxial growth on silicon. Trappmann et al.[74] further observed that APBs are able to move and induce a characteristic local contrast in their vicinity. However, the exact nature of both of these effects were unclear.

High resolution STM topography images were used in conjunction with DFT calculations, performed by Greg Lever, to identify the atomic reconstruction of anti phase boundaries in Si(111)-2x1. These atomic models allowed us to determine a possible pathway for APB movement by rearranging two bonds per π-bonded chain. It was found that the atomic bonds that had to be rearranged in order to move an APB were identical to the ones in a process describing the original formation of the Si(111)-2x1 surface after cleaving.[62] Based on this process, the energy barrier for APB movement could be estimated to be below 100 meV, explaining the frequently observed relocation of APBs on the surface.

To explain the driving force of the observed APB movement, a model for macroscopic APBs from the literature was adapted. The free energy stored in a boundary is usually

thought to act as a driving force,[124] moving boundaries into a direction where they become shorter. In the case of APBs in Si(111)-2x1, all boundaries were found to start and end in step edges, crossing the whole length of the atomic terrace they were situated on. Whether a movement increases or reduces the length of an APB is therefore determined by the shape of the terrace and a new model was developed, explaining the observed movement of an APB based on the atomic scale environment of its end points. This new model was also found to be in excellent agreement with the pinned locations in which APBs were usually observed during STM measurements.[74]

Laterally resolved scanning tunnelling spectroscopy measurements were used to characterize the previously observed contrast around APBs. In STM topography measurements this contrast was found to increase the brightness to one side of an APB and decrease it to its other side. It was found that the sides of increased and decreased brightness reversed with the voltage polarity, demonstrating the electronic nature of this effect. STS measurements further revealed that the contrast, measured in STM topography, is induced by a small shift of states close to the Fermi level. Such an effect is commonly associated with strain,[126, 127] which is know to shift bands to both higher or lower energies, depending on whether it is tensile or compressive.[128] Based on the previously mentioned model for the APB movement, we are furthermore able to explain the formation of this strain based on the driving forces acting on pinned APBs.

Using the capability of STM to induce atomic scale defects in silicon,[131] we demonstrate that it is possible to controllably manipulate the location of APBs. By introducing artificially created pinning sites we are therefore able to control the location of the strain, associated to the boundaries, at the atomic scale. This enables the exciting possibility of using strain to influence and control the properties of individual donors. An application of strain, controllable at the atomic scale, was proposed by Stoneham et al.,[8] suggesting to use it in order to engineer the inhomogeneous broadening of dopants in silicon for optical quantum computing devices. Future experiments on highly doped wafers would therefore be of interest, investigating dopant atoms in close proximity to APBs and therefore characterizing the influence of strain on their electronic and optical properties. Applications can also be imagined in the area of high density data storage, where strain could be used to modify the magnetocrystalline anisotropy of individual atoms.[132]

8.3 Using Ion Implantation for STM Sample Preparation

Bismuth is a promising deep donor that has been suggested for optical quantum computing applications.[8] Its high ionization energy might enable QIP even at liquid nitrogen temperatures and long electron spin coherence times[140] have been reported. However, compared to phosphorus, little is known about Bi dopants in silicon especially at the

atomic scale. Bismuth is the largest of all group V donors, has the highest ionization energy and is, due to its low equilibrium solid solubility, not normally used in conventional semiconductor devices. Monocrystalline wafers with a high Bi concentration are therefore not commercially available and a sample preparation method had to be developed that allows to study Bi at the atomic scale in STM.

An approach that consisted of flash annealing samples with a high implanted Bi concentration proved unsuccessful, the required flashing temperature of 1200 °C completely removing the implanted Bi from the substrate. As described in Chap. 6, we therefore focussed on developing a process that allowed measuring implanted Bi using cross sectional STM. A similar approach was previously demonstrated by Hirayama et al.,[138] who implanted As, cleaved the sample and subsequently annealed it in situ. To avoid dopant diffusion, we however aimed to develop a process where defects are removed with an ex situ anneal before samples are cleaved. By employing temperatures lower than 1200 °C it was ascertained that this anneal did not completely remove the Bi concentration, enabling us to subsequently study a high density of Bi dopants in the original sites of the cleaved Si(111)-2x1 surface.

To implant Bi dopants into silicon, we used standard process parameters as described in the literature.[141–144] The implantation was performed by Andy Smith from the University of Surrey, as were RBS and Hall measurements to determine the crystal quality and electrical activation of the implanted samples. Besides the standard RBS measurements to determine the crystal quality, cross sectional STM is also tested as a tool to characterize implantation processes. We demonstrate that it is possible to resolve implantation damage with atomic resolution by directly comparing the implanted layer to the non implanted bulk. We found that STM was considerably more sensitive to implantation damage than RBS, as samples with identical RBS spectra showed a significantly different surface quality in STM topography measurements. To create a sample for single dopant characterization, the annealing temperature was found to be of crucial importance. Whereas increased temperatures are favorable regarding the damage annealing, they also led to increased Bi precipitation, reducing the amount of substitutional dopants. Through several iterations of implantation and STM characterization we identified the optimal implantation and annealing parameters and were able to create an almost defect free sample with an active Bi dopant concentration of $7.2\text{x}10^{18}$ cm^{-3}.

Using ion implantation in conjunction with cross sectional STM further allowed us to directly visualize the depth profile of the implanted layer. Laterally resolved STS measurements across the implanted area were recorded and we resolve the influence of the high concentration of implanted dopants onto the band structure of the silicon sample. The measured gradual change in the local density of states when reducing the dopant concentration over several orders of magnitude revealed that the Fermi level pinning at the

Si(111)-2x1 surface is strongly dependent on the charge carrier concentration. We found that the Fermi level is originally pinned at 0.5 eV above the surface valence band for a high n-type doped sample with a donor concentration of $7.2\text{x}10^{18}$ cm^{-3}. If the doping concentration is reduced by three orders of magnitude, the Fermi level becomes gradually unpinned, shifting to the top of the surface valence band due to the influence of the STM tip work function. This is in good agreement with the reported Fermi level pinning 0.4 eV above the valence band for intrinsic silicon at room temperature, experimentally determined by Himpsel et al.[71]

The process developed to create samples suitable for cross sectional STM using ion implantation enables us to study Bi at the atomic scale. The presented characterization should furthermore facilitate an adaption of this process for alternative implantation species, enabling STM studies of other, more exotic elements. This might for example be of interest in the emerging fields of silicon spintronics, where manganese (Mn) dopants in silicon are used to create magnetic semiconductors.[133, 134]

8.4 Individual Group V Donors in Si(111)-2x1

Implanted Bi and bulk doped antimony (Sb) dopants were studied with atomic resolution using cross sectional STM. Together with the phosphorus dopants known from literature,[20] measurements of these three dopant elements enabled us to characterize the influence of fundamental dopant properties, such as size or ionization energy, on their atomic scale environment. Using voltage dependent topography images we characterized the surface and catalogued all occurring features on the Bi and Sb doped wafers, identifying four Bi and five Sb contrasts that were found repeatedly when using different tips and samples. The features that were identified on the implanted wafer were associated with Bi dopants as they were not present outside of the implanted layer. Features found on the Sb wafer on the other hand were associated with dopants due to their measured density on the surface, matching the nominal dopant concentration of the wafer.

The identified contrasts were, based on the measured crystal symmetry, assigned to the four distinguishable atomic sites of the Si(111)-2x1 surface. DFT calculations, performed by Veronika Brazdova, further confirmed this assignment and conclusively determined the four features representing Sb and Bi dopants in the substitutional surface sites of Si(111)-2x1. The fifth feature measured on the Sb doped wafer could not be assigned and it is unclear whether it is correlated to the Sb donors.

The influence of different dopant elements located in identical atomic scale environments was analyzed by comparing the measured Bi and Sb dopants with the reported contrasts of P.[20] STM topography measurements of Bi and Sb were found to be very similar to one another but distinctively different from P. This behavior could not be explained by

considering the ionization energy of these dopants, as P and Sb are shallow dopants and therefore expected to be similar but different from the deep Bi donor. However, the size of the different dopant elements was found to correlate well with the measurements since Bi and Sb are both significantly larger than Si whereas P is smaller.[23] DFT simulations revealed that the larger dopants formed a significantly different atomic reconstruction within the Si(111)-2x1 surface, rebonding atoms in the neighboring π-bonded chains and leading to the different appearance in STM topography measurements. The energy gain due to this new reconstruction was found to be strongly dependent on the size of the dopants, matching the observed differences between P, Sb and Bi in the measurement.

The charge state of Bi and Sb donors was determined by characterizing the influence of their screened Coulomb potential in STM topography, as proposed by Ebert et al.[158] Surprisingly, it was found that Sb and Bi are positively charged in two of the four surface sites and negatively charged in the other two. A crystal site dependent charge state is not expected based on the theoretical description of shallow dopants in silicon, and especially a negatively charged group V donor seems unlikely, as it would have to correspond to a dopant that binds two electrons. However, we found that it is possible to explain the observed apparent charge states when considering the balanced charge distribution of the clean Pandey reconstructed Si(111)-2x1 surface. The buckling of the π-bonded chains leads to an electron transfer[57] from the down to the up buckled atoms, creating the filled and empty surface states in the band gap. In contrast to Si(100) however, this does not happen on isolated dimers but within the π-bonded chains, where every up atom has two neighboring down atoms and vice versa. If the charge state of one of the atoms in the π-bonded chain is altered, for example by replacing it with a group V dopant, it is therefore not trivial to determine how the neighboring two atoms are influenced, now themselves bonded to a dopant on one side and the normal π-bonded chain to the other side.

Based on DFT simulations we demonstrate that Sb and Bi dopants themselves always retain a filled lone pair, corresponding to a neutral charge state, independent of their substitutional surface site. This seems to contradict the measurement, where positive and negative charge states were found. However, if a neutral donor substitutes a Si atom of the Si(111)-2x1 surface, the charge reordering on the surface is disturbed due to the different electronic properties of the dopant atom and its additional electron. It could be expected that the surrounding atoms neutralize this charge by changing their buckling and retaining the overall, neutral charge state of the surface. However, this change in buckling would represent a reconstruction different from the ground state of the Si(111)-2x1 Pandey model, increasing its energy. A competition between retaining the structural ground state of the Si(111)-2x1 surface in atoms surrounding the dopant on the one hand and creating a charge neutral state on the other therefore exists. Based on the DFT simulations we demonstrate that the charge distribution found on silicon atoms in the immediate

vicinity of dopants is not changed and remains identical to the clean surface. Therefore, depending on whether the neutral donors replace an up buckled Si atom with a filled lone pair or a down buckled Si atom with an empty lone pair, this results in an apparent positive or negative charge state respectively. This very intuitive model was found to excellently match the measured charge states of the four distinguishable surface sites in Si(111)-2x1.

The measured charge, induced by dopants in the surface layer of silicon, has a significant impact especially for thin film technologies, as for example used to cap atomic scale devices.[12] The Coulomb potential affects the sticking of charged deposits in MBE or CVD processes and can therefore influence the resulting roughness of grown layers.[158] The fact that P dopants were found charge neutral in all surface sites[20] highlights that different dopant elements will react in fundamentally different ways when employed in future atomic scale device fabrication processes. It is assumed that similar effects occur on other semiconductor surfaces which display charge reordering as part of their surface reconstruction. The competition between structural relaxations and charge neutrality would however have to be re-evaluated for every surface independently.

Besides characterizing dopants in the surface layer of Si(111)-2x1, we were also able to identify subsurface Sb and Bi, down to two layers underneath the surface. They showed the characteristic protrusion of a positively charged donor when measured in empty states, indicating an ionized state. This is expected due to the Fermi level pinning of the Si(111)-2x1 surface, which raises the conduction band far above the Fermi energy as shown by Himpsel et al et al.[71] Using surface potential imaging, as suggested by Hasegawa et al.,[165] we demonstrate that it is possible to map out the screened Coulomb potential well of a single Sb dopant at the atomic scale. Laterally resolved STS measurements were used to determine the band shift induced by the individual Sb donor atom, enabling us to resolve the exact shape and depth of the screened Coulomb potential. Fitting the measured potential well to the theoretical model allowed us to extract the depth of the dopant below the surface, the dielectric constant it is exposed to and its screening radius. All parameters were found in excellent agreement with expected values. The dopant depth of 7.3 $\AA$ compared well with a dopant in the second layer of the Si(111)-2x1 surface, expected around 7.5 $\AA$ below the surface. The screening radius was found to be 3.4 nm and therefore higher than values reported in literature, usually around 1.2 nm.[159, 160] This is however to be expected as it is know that the Fermi level pinning in Si(111)-2x1 creates a depletion region underneath the surface, decreasing the carrier concentration around the dopant and increasing the screening radius. The dielectric constant of a dopant in the surface is expected to be $\varepsilon_r = 6.45$, the average between the half sphere of vacuum $\varepsilon_r = 1$ and the other half sphere of silicon $\varepsilon_r = 11.9$. However, since the measured dopant is 7.3 $\AA$ below the surface, a larger influence of silicon is expected, in excellent agreement with the measured dielectric constant of $\varepsilon_r = 9.6$.

Being able to determine the screened Coulomb potential of individual dopants in close proximity to an interface is of fundamental importance for highly scaled devices and future QIP architectures. With the reduction of device dimensions, an increasing fraction of dopants will be located in close proximity to surfaces or material contact areas between semiconductor, leads and oxides. All of these interfaces are characterized by a sudden change in dielectric constant, material work function and atomic reconstruction. It is therefore crucial to understand how interfaces alter the local electrostatic potential around dopants, providing a basis to calculate their influence on macroscopic electronic properties and, even more importantly, enabling their controlled employment in future single dopant devices. Future experiments measuring a large number of dopants at various depths would enable one to study the correlation between their position, their screening radius and the dielectric constant, providing further insights into the behavior of individual donors close to interfaces.

Using STS we have furthermore investigated the shape of the dopant potential well in the Si(111)-2x1 surface layer. The screening of charges in a reconstructed surface, especially in the presence of surface states, is a complex subject and still discussed in literature.[54, 168, 169] Based on the high energy resolution of STS we are able to determine the influence of the charge screening for surface and bulk states individually, showing a strongly asymmetric potential well along the π-bonded chains in the surface states. The screening radius measured for charge carriers in the surface state was found to be smaller than for bulk state carriers, in good agreement with predictions by Reining et al.[168] The lateral dimensions of the asymmetric potential well also compare reasonably well with calculations from Rohlfing et al.,[54] even though we found a stronger localization to the π-bonded chains than was predicted in the simulations. The atomic scale characterization of the energy resolved potential well and the identified screening radii provide experimental measurements for future theoretical studies, contributing to the understanding of the complex screening behavior in semiconductor surfaces.

In summary this thesis presents a comprehensive study of how the fundamental characteristics of group V dopants influence their atomic scale environment. We present an extensive characterization of the Si(111)-2x1 surface and show how the incorporation of different dopant elements into substitutional crystal sites is influences by their size. Furthermore, we present a model explaining how these new reconstructions create different charge states within the surface and discuss the screening properties of individual donors in or close to the Si(111)-2x1 surface. To enable atomically controlled device fabrication, we implemented and characterized necessary cleanroom fabrication and STM processes that allow the placement of individual dopants with atomic scale precision. This will enable the exploitation of the findings presented in this thesis for the fabrication of future single dopant devices.

List of Publications

Journal publications and patents

1. Philipp Studer, Steven R. Schofield, Greg Lever et al., ”Model system for controlling strain in silicon at the atomic scale,” Physical Review B 84 (4), 041306. (2011)
2. P. Studer et al., ”A Method of Local Surface Modification” Patent Application Number GB1100248.2 (2010)
3. P. Studer et al., ”Individual group V donors in silicon” (in preparation)
4. P. Studer et al., ”Implanting dopants for XSTM characterization” (in preparation)
5. S.R. Schofield, P. Studer et al., ”Quantum defect engineering in Si” (in preparation)

Conference presentations

1. Poster presentation: COMPASS workshop, Utrecht 2011
2. Talk given at: Condensed Matter and Material Physics (CMMP10), UK 2010
3. Talk given at: IOP Nanoscale Physics and Technology AGM Nottingham 2010
4. Poster presentation: UKSPM, London 2010
5. Poster presentation: Single dopant control workshop, Leiden (2009)
6. Poster presentation: Atomscale-Silicon Hybrid Nanotechnologies, South Hampstead (2009)
7. Poster presentation: Interdisciplinary Surface Science Conference (ISSC17), Reading (2009)

List of Figures

List of Tables

Bibliography

[1] F. J. Ruess, L. Oberbeck, M. Y. Simmons, K. E. J. Goh, A. R. Hamilton, T. Hallam, S. R. Schofield, N. J. Curson, and R. G. Clark. Toward atomic-scale device fabrication in silicon using scanning probe microscopy. *Nano Letters*, 4(10):5, 2004.

[2] S. R. Schofield, N. J. Curson, M. Y. Simmons, F. J. Ruess, T. Hallam, L. Oberbeck, and R. G. Clark. Atomically precise placement of single dopants in Si. *Phys. Rev. Lett.*, 91(13):4, 2003.

[3] A. M. Yakunin, A. Y. Silov, P. M. Koenraad, J.-M. Tang, M. E. Flatté, J.-L. Primus, W. Van Roy, J. De Boeck, A. M. Monakhov, K. S. Romanov, I. E. Panaiotti, and N. S. Averkiev. Warping a single Mn acceptor wavefunction by straining the GaAs host. *Nature Materials*, 6:4, 2007.

[4] A. P. Wijnheijmer, J. K. Garleff, K. Teichmann, M. Wenderoth, S. Loth, R. G. Ulbrich, P. A. Maksym, M. Roy, and P. M. Koenraad. Enhanced donor binding energy close to a semiconductor surface. *Phys. Rev. Lett.*, 102(16):166101, 2009.

[5] ITRS. International technology roadmap for semiconductors. *http://www.itrs.net/Links/2010ITRS/Home2010.htm*, 2009.

[6] T. Shinada, S. Okamoto, T. Kobayashi, and I. Ohdomari. Enhancing semiconductor device performance using ordered dopant arrays. *Nature*, 437(7062):1128–1131, 2005.

[7] B. E. Kane. A silicon-based nuclear spin quantum computer. *Nature*, 393:5, 1998.

[8] A. M. Stoneham, A. J. Fisher, and P. T. Greenland. Optically driven silicon-based quantum gates with potential for high-temperature operation. *J. Phys.: Condens. Matter*, 15(27):L447–L451, 2003.

[9] T. Schenkel. Single ion implantation and deterministic doping. *Lawrence Berkeley National Laboratory*, pages 1–10, 2010.

[10] W. J. MoberlyChan, D. P. Adams, M. J. Aziz, G. Hobler, and T. Schenkel. Fundamentals of focused ion beam nanostructural processing: Below, at, and above the surface. *MRS BULLETIN*, 32, 2007.

[11] C. D. Weis, A. Schuh, A. Batra, A. Persaud, I. W. Rangelow, J. Bokor, C. C. Lo, S. Cabrini, D. Olynick, S. Duhey, and T. Schenkel. Mapping of ion beam induced current changes in FinFETs. *Nuclear Instruments and Methods in Physics Research B*, 267:1222, 2009.

[12] M. Fuechsle, S. Mahapatra, F. A. Zwanenburg, M. Friesen, M. A. Eriksson, and M. Y. Simmons. Spectroscopy of few-electron single-crystal silicon quantum dots. *Nature Nanotechnol.*, 5(7):502–505, 2010.

[13] H. Sellier, G. P. Lansbergen, J. Caro, S. Rogge, N. Collaert, I. Ferain, M. Jurczak, and S. Biesemans. Transport spectroscopy of a single dopant in a gated silicon nanowire. *Phys. Rev. Lett.*, 97(20):206805–4, 2006.

[14] G. P. Lansbergen, R. Rahman, C. J. Wellard, I. Woo, J. Caro, N. Collaert, S. Biesemans, G. Klimeck, L. C. L. Hollenberg, and S. Rogge. Gate-induced quantum-confinement transition of a single dopant atom in a silicon FinFET. *Nat Phys*, 4(8):656–661, 2008.

[15] A. Morello, J. J. Pla, F. A. Zwanenburg, K. W. Chan, K. Y. Tan, H. Huebl, M. Mottonen, C. D. Nugroho, C. Yang, J. A. van Donkelaar, A. D. C. Alves, D. N. Jamieson, C. C. Escott, L. C. L. Hollenberg, R. G. Clark, and A. S. Dzurak. Single-shot readout of an electron spin in silicon. *Nature*, 467(7316):687–691, 2010.

[16] K. Teichmann, M. Wenderoth, S. Loth, R. G. Ulbrich, J. K. Garleff, A. P. Wijnheijmer, and P. M. Koenraad. Controlled charge switching on a single donor with a scanning tunneling microscope. *Phys. Rev. Lett.*, 101(7):076103, 2008.

[17] D. Kitchen, A. Richardella, P. Roushan, J.-M. Tang, M. E. Flatté, and A. Yazdani. *Hole-mediated interactions of Mn acceptors on GaAs (110) (invited)*, volume 101. AIP, 2007. 9 Journal of Applied Physics.

[18] M. W. Radny, P. V. Smith, T. C. G. Reusch, O. Warschkow, N. A. Marks, H. Q. Shi, D. R. McKenzie, S. R. Schofield, N. J. Curson, and M. Y. Simmons. Single P and As dopants in the Si(001) surface. *The Journal of Chemical Physics*, 127(18):184706–9, 2007.

[19] G. W. Brown, H. Grube, and M. E. Hawley. Observation of buried phosphorus dopants near clean Si (100) - (2x1) surfaces with scanning tunneling microscopy. *Physical Review B*, 70(12):121301, 2004.

[20] J. K. Garleff, M. Wenderoth, R. G. Ulbrich, C. Surgers, H. v. Lohneysen, and M. Rohlfing. Identification of P dopants at nonequivalent lattice sites of the

Si(111)-(2x1) surface. *Physical Review B (Condensed Matter and Materials Physics)*, 76(12):125322–5, 2007.

[21] D. H. Lee and J. A. Gupta. Tunable field-control over the binding energy of single dopants by a charged vacancy in GaAs. *Science*, 330(6012):1807–1810, 2010.

[22] M. C. M. M. van der Wielen, A. J. A. van Roij, and H. van Kempen. Direct observation of friedel oscillations around incorporated SiGa dopants in GaAs by low-temperature scanning tunneling microscopy. *Phys. Rev. Lett.*, 76(7):1075, 1996.

[23] B. Pajot and A. M. Stoneham. A spectroscopic investigation of the lattice distortion at substitutional sites for groups V and VI donors in silicon. *Journal of Physics C: Solid State Physics*, 20(32):5241, 1987.

[24] G. Binnig, H. Rohrer, C. Gerber, and E. Weibel. Tunneling through a controllable vacuum gap. *Applied Physics Letters*, 40(2):178–180, 1982.

[25] G. Binnig, H. Rohrer, C. Gerber, and E. Weibel. Surface studies by scanning tunneling microscopy. *Phys. Rev. Lett.*, 49(1):57, 1982.

[26] G. Binnig, H. Rohrer, C. Gerber, and E. Weibel. 7 x 7 reconstruction on Si(111) resolved in real space. *Phys. Rev. Lett.*, 50(2):120, 1983.

[27] D. M. Eigler and E. K. Schweizer. Positioning single atoms with a scanning tunneling microscope. *Nature*, 344:3, 1990.

[28] G. Binnig, C. F. Quate, and C. Gerber. Atomic force microscope. *Phys. Rev. Lett.*, 56(9):930, 1986.

[29] D. W. Pohl, W. Denk, and M. Lanz. Optical stethoscopy: Image recording with resolution lambda/20. *Applied Physics Letters*, 44(7):651–653, 1984.

[30] C. J. Chen. *Introduction to Scanning Tunneling Microscopy Second Edition*. 2008.

[31] J. G. Simmons. Electric tunnel effect between dissimilar electrodes separated by a thin insulating film. *Journal of Applied Physics*, 34(9):2581–2590, 1963.

[32] R. M. Feenstra and J. A. Stroscio. Reconstruction of steps on the Si(111)-2x1 surface. *Phys. Rev. Lett.*, 59(19):2173, 1987.

[33] K. Nagaoka, M. J. Comstock, A. Hammack, and M. F. Crommie. Observation of spatially inhomogeneous electronic structure of Si(100) using scanning tunneling spectroscopy. *Physical Review B*, 71(12):121304, 2005.

[34] R. M. Feenstra and J. A. Stroscio. Tunneling spectroscopy of the GaAs(110) surface. *Journal of Vacuum Science and Technology B: Microelectronics and Nanometer Structures*, 5(4):923–929, 1987.

[35] S. Loth, M. Wenderoth, R. G. Ulbrich, S. Malzer, and G. H. Doehler. Connection of anisotropic conductivity to tip-induced space-charge layers in scanning tunneling spectroscopy of p -doped GaAs. *Physical Review B*, 76(23):235318, 2007.

[36] M. McEllistrem, G. Haase, D. Chen, and R. J. Hamers. Electrostatic sample-tip interactions in the scanning tunneling microscope. *Phys. Rev. Lett.*, 70(16):2471, 1993.

[37] J. J. Lander, G. W. Gobeli, and J. Morrison. Structural properties of cleaved silicon and germanium surfaces. *Journal of Applied Physics*, 34(8):2298–2306, 1963.

[38] F. J. Himpsel, P. M. Marcus, R. Tromp, I. P. Batra, M. R. Cook, F. Jona, and H. Liu. Structure analysis of Si(111)-2x1 with low-energy electron diffraction. *Physical Review B*, 30(4):2257, 1984.

[39] R. M. Tromp, L. Smit, and J. F. van der Veen. Si(111)-(2 x1) surface: Buckling, chains, or molecules? *Phys. Rev. Lett.*, 51(18):1672, 1983.

[40] P. Chiaradia, A. Cricenti, S. Selci, and G. Chiarotti. Differential reflectivity of Si(111)-2x1 surface with polarized light: A test for surface structure. *Phys. Rev. Lett.*, 52(13):1145, 1984.

[41] A. Feenstra. http://www.andrew.cmu.edu/user/feenstra/, —2011—.

[42] G.-X. Qian and D. J. Chadi. Si(111)-7 x 7 surface: Energy-minimization calculation for the dimer-adatom-stacking-fault model. *Physical Review B*, 35(3):1288, 1987.

[43] T. Komeda and Y. Nishioka. Atomic structure of segregated boron on Si(001) surface; scanning tunneling microscopy and cluster model calculation study. *Surface Science*, 405(1):38–45, 1998.

[44] P. M. Fahey, P. B. Griffin, and J. D. Plummer. Point defects and dopant diffusion in silicon. *Reviews of Modern Physics*, 61(2):289, 1989.

[45] S. Whelan, V. Privitera, G. Mannino, M. Italia, C. Bongiorno, E. Napolitani, E. J. H. Collart, and J. A. van den Berg. Dopant behaviour and damage annealing in silicon implanted with 1 keV arsenic. *Nuclear Instruments and Methods in Physics Research Section B: Beam Interactions with Materials and Atoms*, 186(1-4):271–275, 2002.

[46] R. Nuffer, H. J. Muessig, and J. Dabrowski. Cross-sectional STM/STS - a useful tool for identification of dopants in silicon. *Solid-State Electronics*, 44(5):875–880, 2000.

[47] J. K. Garleff. *Vergleichende Rastersonden- und lichtmikroskopische Untersuchungen der Morphologie von (110) und (111)-Spaltflaechen an Silizium*. Master thesis, 2001.

[48] M. A. Lutz, R. M. Feenstra, and J. O. Chu. Scanning tunneling microscopy of in situ cleaved and hydrogen passivated Si(110) cross-sectional surfaces. *Surface Science*, 328(3):215–226, 1995.

[49] R. Pérez and P. Gumbsch. An ab initio study of the cleavage anisotropy in silicon. *Acta Materialia*, 48(18-19):4517–4530, 2000.

[50] T. Hoshi, Y. Iguchi, and T. Fujiwara. Nanoscale structures formed in silicon cleavage studied with large-scale electronic structure calculations: Surface reconstruction, steps, and bending. *Physical Review B*, 72(7), 2005.

[51] D. Sen, C. Thaulow, S. V. Schieffer, A. Cohen, and M. J. Buehler. Atomistic study of crack-tip cleavage to dislocation emission transition in silicon single crystals. *Phys. Rev. Lett.*, 104(23):235502, 2010.

[52] R. Pérez and P. Gumbsch. Directional anisotropy in the cleavage fracture of silicon. *Phys. Rev. Lett.*, 84(23):5347, 2000.

[53] K. C. Pandey. New pi-bonded chain model for Si(111)-(2x1) surface. *Phys. Rev. Lett.*, 47(26):1913, 1981.

[54] M. Rohlfing and S. G. Louie. Excitons and optical spectrum of the Si(111)-2x1 surface. *Phys. Rev. Lett.*, 83(4):856, 1999.

[55] R. M. Feenstra, W. A. Thompson, and A. P. Fein. Real-space observation of pi -bonded chains and surface disorder on Si(111)-2x1. *Phys. Rev. Lett.*, 56(6):608–611, 1986.

[56] J. K. Garleff, M. Wenderoth, K. Sauthoff, R. G. Ulbrich, and M. Rohlfing. 2x1 reconstructed Si(111) surface: STM experiments versus ab initio calculations. *Phys. Rev. B*, 70(24):245424, 2004.

[57] M. Rohlfing and J. Pollmann. Localization of optically excited states by self-trapping. *Phys. Rev. Lett.*, 88(17):176801, 2002.

[58] D. Haneman. Surface structures and properties of diamond-structure semiconductors. *Physical Review*, 121(4):1093, 1961.

[59] D. Haneman. Surfaces of silicon. *Reports on Progress in Physics*, 50(8):1045, 1987.

[60] D. Haneman. Structure of cleavage steps on Si(111). *Physical Review B*, 42(14):8982–8985, 1990.

[61] S.-H. Lee and M.-H. Kang. Model-dependent electronic structure of the Si(111)-2x1 surface. *Physical Review B*, 54(3):1482, 1996.

[62] J. E. Northrup and M. L. Cohen. Reconstruction mechanism and surface-state dispersion for Si(111)-(2x1). *Phys. Rev. Lett.*, 49(18):1349, 1982.

[63] H. Sakama, A. Kawazu, and K. Ueda. Structural studies of Si (111) 2x1 surfaces using low-energy electron diffraction. *Physical Review B*, 34(2):1367, 1986.

[64] R. M. Tromp, L. Smit, and J. F. van der Veen. Structure determination of the Si(111)-(2x1) surface with channeling and blocking. *Physical Review B*, 30(10):6235, 1984.

[65] R. I. G. Uhrberg, G. V. Hansson, J. M. Nicholls, and S. A. Flodstroem. Experimental evidence for one highly dispersive dangling-bond band on Si(111)-2x1. *Phys. Rev. Lett.*, 48(15):1032, 1982.

[66] P. Perfetti, J. M. Nicholls, and B. Reihl. Unoccupied surface-state band on Si(111)-2x1. *Physical Review B*, 36(11):6160–6163, 1987.

[67] B. I. Craig and P. V. Smith. Slab-mindo calculations on the Si(111)-2x1 surface. *Surface Science*, 225(3):225–232, 1990.

[68] S. Nie, R. M. Feenstra, J. Y. Lee, and M.-H. Kang. Buckling of Si and Ge(111)-2x1 surfaces. *Journal of Vacuum Science and Technology A: Vacuum, Surfaces, and Films*, 22(4):1671–1674, 2004.

[69] G. Bussetti, B. Bonanni, S. Cirilli, A. Violante, M. Russo, C. Goletti, P. Chiaradia, O. Pulci, M. Palummo, R. Del Sole, P. Gargiani, M. G. Betti, C. Mariani, R. M. Feenstra, G. Meyer, and K. H. Rieder. Coexistence of negatively and positively buckled isomers on n+-doped Si(111)-2x1. *Phys. Rev. Lett.*, 106(6):067601, 2011.

[70] P. Martensson, A. Cricenti, and G. V. Hansson. Photoemission study of the antibonding surface-state band on Si(111)-2x1. *Physical Review B*, 32(10):6959, 1985.

[71] F. J. Himpsel, G. Hollinger, and R. A. Pollak. Determination of the Fermi-level pinning position at Si(111) surfaces. *Phys. Rev. B*, 28(12):7014, 1983.

[72] J. A. Stroscio, R. M. Feenstra, and A. P. Fein. Electronic structure of the Si(111)-2x1 surface by scanning-tunneling microscopy. *Phys. Rev. Lett.*, 57(20):2579–2582, 1986.

[73] R. M. Feenstra. Band gap of the Ge(111)-2x1 and Si(111)-2x1 surfaces by scanning tunneling spectroscopy. *Phys Rev B Condens Matter*, 44(24):13791–13794, 1991.

[74] T. Trappmann, C. Sürgers, and H. v. Löhneysen. Investigation of the (111) surface of P-doped Si by scanning tunneling microscopy. *Appl. Phys. A*, 68(2):167–172, 1998.

[75] Y. Einaga, H. Hirayama, and K. Takayanagi. Role of 2x1 domain boundaries on the transition from 2x1 to c(2x8) at Ge(111) surfaces. *Phys. Rev. B*, 57(24):15567, 1998.

[76] H. Hirayama, N. Sugihara, and K. Takayanagi. Chain-left isomer of the pi-bonded chain reconstruction at the Ge(111)-2x1 surface. *Phys. Rev. B*, 62(11):6900, 2000.

[77] D. A. Muzychenko, S. V. Savinov, V. N. Mantsevich, N. S. Maslova, V. I. Panov, K. Schouteden, and C. Van Haesendonck. Low-temperature scanning tunneling microscopy and spectroscopy of spatial oscillations in the density of states near domain boundaries at the Ge (111) 2 x1 surface. *Physical Review B*, 81(3):035313, 2009.

[78] P. I. Arseyev, N. S. Maslova, V. I. Panov, S. V. Savinov, and C. Van Haesendonck. Bias voltage dependent shift of the atomic-scale structure of a Ge(111)-(2x1) reconstructed surface measured by low temperature scanning tunneling microscopy. *JETP Letters*, 85(6):277–282, 2007.

[79] T. Trappmann, C. Suergers, and v. H. Loehneysen. Observation of P donors on the Si(111) surface by scanning tunneling microscopy. *EPL (Europhysics Letters)*, 38(3):177, 1997.

[80] M. Schock, C. Surgers, and H. Von Lohneysen. Investigation of single boron accepters at the cleaved Si : B(111) surface. *Physical Review B*, 61(11):7622–7627, 2000.

[81] C. Suergers, M. Schoeck, T. Trappmann, and H. v. Loehneysen. STM and STS on single dopants and Au-induced chains at the Si(111) surface. *Applied Surface Science*, 212-213:105–109, 2003.

[82] J. K. Garleff, M. Wenderoth, R. G. Ulbrich, C. Suergers, and H. v. Loehneysen. Evidence for one-dimensional electron propagation on Si (111)-(2x1) from Coulomb blockade. *Physical Review B*, 72(7):073406, 2005.

[83] K. Hata, T. Kimura, S. Ozawa, and H. Shigekawa. How to fabricate a defect free Si(001) surface. 18:1933–1936, 2000.

[84] I. Langmuir. The electron emission from thoriated tungsten filaments. *Physical Review*, 22(4):357, 1923.

[85] I. Ekvall, E. Wahlstrom, D. Claesson, H. Olin, and E. Olsson. Preparation and characterization of electrochemically etched W tips for STM. *Measurement Science and Technology*, 10(1):11–18, 1999.

[86] R. H. Fowler and L. Nordheim. Electron emission in intense electric fields. *Proceedings of the Royal Society of London. Series A, Containing Papers of a Mathematical and Physical Character*, 119(781):173–181, 1928.

[87] R. Gomer. *Field Emission and Field Ionization*. Harvard University Press, 1961.

[88] C. F. Hirjibehedin, C. P. Lutz, and A. J. Heinrich. Spin coupling in engineered atomic structures. *Science*, 312:5, 2006.

[89] J. W. Lyding, K. Hess, G. C. Abeln, D. S. Thompson, J. S. Moore, M. C. Hersam, E. T. Foley, J. Lee, Z. Chen, S. T. Hwang, H. Choi, P. Avouris, and I. C. Kizilyalli. Ultrahigh vacuum-scanning tunneling microscopy nanofabrication and hydrogen/deuterium desorption from silicon surfaces: implications for complementary metal oxide semiconductor technology. *Applied Surface Science*, 130-132:221–230, 1998.

[90] K. E. J. Goh, L. Oberbeck, M. J. Butcher, N. J. Curson, F. J. Ruess, and M. Y. Simmons. Comparison of GaP and PH3 as dopant sources for STM-based device fabrication. *Nanotechnology*, 18(6):065301, 2007.

[91] J. L. O'Brien, S. R. Schofield, M. Y. Simmons, R. G. Clark, A. S. Dzurak, N. J. Curson, B. E. Kane, N. S. McAlpine, M. E. Hawley, and G. W. Brown. Towards the fabrication of phosphorus qubits for a silicon quantum computer. *Physical Review B*, 64(16):161401, 2001.

[92] M. Y. Simmons, S. R. Schofield, J. L. O'Brien, N. J. Curson, L. Oberbeck, T. Hallam, and R. G. Clark. Towards the atomic-scale fabrication of a silicon-based solid state quantum computer. *Surface Science*, 2003.

[93] F. J. Ruess, L. Oberbeck, K. E. J. Goh, M. J. Butcher, E. Gauja, A. R. Hamilton, and M. Y. Simmons. The use of etched registration markers to make four-terminal electrical contacts to STM-patterned nanostructures. *Nanotechnology*, 16(10):2446–2449, 2005.

[94] T. Hallam, M. J. Butcher, K. E. J. Goh, F. J. Ruess, and M. Y. Simmons. Use of a scanning electron microscope to pattern large areas of a hydrogen resist for electrical contacts. *Journal of Applied Physics*, 102(3):034308–5, 2007.

[95] F. J. Ruess, W. Pok, T. C. G. Reusch, M. J. Butcher, K. E. J. Goh, L. Oberbeck, G. Scappucci, A. R. Hamilton, and M. Y. Simmons. Realization of atomically controlled dopant devices in silicon. *Small*, 3(4):563–567, 2007.

[96] F. J. Ruess, K. E. J. Goh, M. J. Butcher, T. C. G. Reusch, L. Oberbeck, B. Weber, A. R. Hamilton, and M. Y. Simmons. Narrow, highly P-doped, planar wires in silicon created by scanning probe microscopy. *Nanotechnology*, 18(4):044023, 2007.

[97] F. J. Ruess, K. E. J. Goh, B. Weber, A. R. Hamilton, and M. Y. Simmons. Electrical properties of atomically controlled Si:P nanowires created by scanning probe microscopy. *AIP Conference Proceedings*, 893(1):687–688, 2007.

[98] F. J. Ruess, W. Pok, K. E. J. Goh, A. R. Hamilton, and M. Y. Simmons. Electronic properties of atomically abrupt tunnel junctions in silicon. *Physical Review B (Condensed Matter and Materials Physics)*, 75(12):121303–4, 2007.

[99] A. Fuhrer, M. Fuechsle, T. C. G. Reusch, B. Weber, and M. Y. Simmons. Atomic-scale, all epitaxial in-plane gated donor quantum dot in silicon. *Nano Letters*, 9(2):707–710, 2009.

[100] T. C. G. Reusch, A. Fuhrer, M. Fuechsle, B. Weber, and M. Y. Simmons. Aharonov-Bohm oscillations in a nanoscale dopant ring in silicon. *Applied Physics Letters*, 95(3):032110–3, 2009.

[101] K. Kato, T. Ide, S. Miura, A. Tamura, and T. Ichinokawa. Si(100)2xn structures induced by Ni contamination. *Surface Science*, 194(1-2):L87–L94, 1988.

[102] K.-C. Chang and J. M. Blakely. Arrays of widely spaced atomic steps on Si(111) mesas due to sublimation. *Surface Science*, 591(1-3):133–141, 2005.

[103] S. Tanaka, C. C. Umbach, J. M. Blakely, R. M. Tromp, and M. Mankos. Fabrication of arrays of large step-free regions on Si(001). *Applied Physics Letters*, 69(9):1235–1237, 1996.

[104] Y. Homma, N. Aizawa, and T. Ogino. Ultra-large-scale step-free terraces formed at the bottom of craters on vicinal Si(111) surfaces. *Jpn. J. Appl. Phys.*, 35:3, 1996.

[105] T. Ogino, H. Hibino, and Y. Homma. Step arrangement design and nanostructure self-organization on Si surfaces. *Appl. Surf. Sci.*, 117-118:642–651, 1997.

[106] J. F. Nielsen, J. P. Pelz, H. Hibino, C. W. Hu, and I. S. T. Tsong. Enhanced terrace stability for preparation of step-free Si(001)-(2x1) surfaces. *Phys. Rev. Lett.*, 87(13):136103, 2001.

[107] W. K. Burton, N. Cabrera, and F. C. Frank. The growth of crystals and the equilibrium structure of their surfaces. *Philosophical Transactions of the Royal Society of London. Series A, Mathematical and Physical Sciences (1934-1990)*, 243(866):59, 1951.

[108] M. Fuechsle, F. J. Ruess, T. C. G. Reusch, M. Mitic, and M. Y. Simmons. Surface gate and contact alignment for buried, atomically precise scanning tunneling microscopy-patterned devices. *J. Vac. Sci. Technol.*, 25:6, 2007.

[109] T.-C. Shen, C. Wang, G. C. Abeln, J. R. Tucker, J. W. Lyding, P. Avouris, and R. E. Walkup. Atomic-scale desorption through electronic and vibrational excitation mechanisms. *Science*, 268(5217):1590–1592, 1995.

[110] L. J. van der Pauw. A method of measuring the resistivity and hall coefficient on lamellae of arbitrary shape. *Phil. Tech. Rev.*, 20:5, 1958.

[111] K. Sauthoff, M. Wenderoth, A. J. Heinrich, M. A. Rosentreter, K. J. Engel, T. C. G. Reusch, and R. G. Ulbrich. Nonlinear dynamic instability in brittle fracture of GaAs. *Physical Review B*, 60(7):4789, 1999.

[112] H. Tokumoto, S. Wakiyama, K. Miki, H. Murakami, S. Okayama, and K. Kajimura. Scanning tunneling microscopy of microstructures on cleaved Si(111) surface. In *5th International Conf on Scanning Tunneling Microscopy/Spectroscopy*, pages 695–698, Baltimore.

[113] S. M. Sze and K. N. Kwok. Physics of semiconductor devices. 2007.

[114] Y. Hasegawa, I.-W. Lyo, and P. Avouris. Measurement of surface state conductance using STM point contacts. *Surface Science*, 357-358:32–37, 1996.

[115] S. Ciraci and E. Tekman. Theory of transition from the tunneling regime to point contact in scanning tunneling microscopy. *Physical Review B*, 40(17):11969, 1989.

[116] J. K. Gimzewski and R. Mueller. Transition from the tunneling regime to point contact studied using scanning tunneling microscopy. *Physical Review B*, 36(2):1284, 1987.

[117] P. Avouris, I. W. Lyo, and Y. Hasegawa. Scanning tunneling microscope tip-sample interactions: Atomic modification of Si and nanometer Si Schottky diodes. In *39th National Symposium of the American Vacuum Society*, volume 11, pages 1725–1732, Chicago, Illinois (USA), —1993—. AVS.

[118] M. Weimer, J. Kramar, and J. D. Baldeschwieler. Band bending and the apparent barrier height in scanning tunneling microscopy. *Physical Review B*, 39(8):5572, 1989.

[119] P. Jelinek, M. Scaronvec, P. Pou, R. Perez, and V. Chab. Tip-induced reduction of the resonant tunneling current on semiconductor surfaces. *Phys. Rev. Lett.*, 101(17):176101, 2008.

[120] J. K. Garleff. *Quasi-eindimensionale elektronische Zustaende auf der Si(111) 2x1 Oberflaeche*. Dissertation, 2005.

[121] G. Lever. *Electronic Structure Calculation of Si(111) (2x1)*. Master thesis, 2010.

[122] G. Kresse and J. Furthmüller. Efficiency of ab-initio total energy calculations for metals and semiconductors using a plane-wave basis set. *Comp. Mat. Sci.*, 6(1):15–50, 1996.

[123] J. P. Perdew and Y. Wang. Accurate and simple analytic representation of the electron-gas correlation energy. *Phys. Rev. B*, 45(23):13244, 1992.

[124] S. M. Allen and J. W. Cahn. A microscopic theory for antiphase boundary motion and its application to antiphase domain coarsening. *Acta Metall.*, 27(6):1085–1095, 1979.

[125] M. Rohlfing, M. Palummo, G. Onida, and R. Del Sole. Structural and optical properties of the Ge(111)-(2x1) surface. *Phys. Rev. Lett.*, 85(25):5440, 2000.

[126] J. H. G. Owen, D. R. Bowler, C. M. Goringe, K. Miki, and G. A. D. Briggs. Identification of the Si(001) missing dimer defect structure by low bias voltage STM and LDA modelling. *Surf. Sci.*, 341(3):L1042–L1047, 1995.

[127] S. R. Schofield, N. J. Curson, J. L. O'Brien, M. Y. Simmons, R. G. Clark, N. A. Marks, H. F. Wilson, G. W. Brown, and M. E. Hawley. Split-off dimer defects on the Si(001)2x 1 surface. *Phys. Rev. B*, 69(8):085312, 2004.

[128] Z. Wu, J. B. Neaton, and J. C. Grossman. Charge separation via strain in silicon nanowires. *Nano Lett.*, 9(6):2418–2422, 2009.

[129] W. G. Schmidt and K. Seino. Si(001) c(4x2)-p(2x2) surface phase transitions induced by electric fields and doping. *Current Applied Physics*, 6(3):331–333, 2006.

[130] K. Stokbro, C. Thirstrup, M. Sakurai, U. Quaade, B.-K. Hu, F. Perez-Murano, and F. Grey. STM-induced hydrogen desorption via a hole resonance. *Phys. Rev. Lett.*, 80(12):2618, 1998.

[131] I.-W. Lyo and P. Avouris. Field-induced nanometer- to atomic-scale manipulation of silicon surfaces with the STM. *Science*, 253(5016):173–176, 1991.

[132] A. A. Khajetoorians, B. Chilian, J. Wiebe, S. Schuwalow, F. Lechermann, and R. Wiesendanger. Detecting excitation and magnetization of individual dopants in a semiconductor. *Nature (London)*, 467(7319):1084–1087, 2010.

[133] T. Dietl, H. Ohno, F. Matsukura, J. Cibert, and D. Ferrand. Zener model description of ferromagnetism in zinc-blende magnetic semiconductors. *Science*, 287(5455):1019–1022, 2000.

[134] P. R. Bandaru, J. Park, J. S. Lee, Y. J. Tang, L. H. Chen, S. Jin, S. A. Song, and J. R. O'Brien. Enhanced room temperature ferromagnetism in Co- and Mn-ion-implanted silicon. *Applied Physics Letters*, 89(11), 2006.

[135] F. A. Trumbore. Solid solubilities of impurity elements in germanium and silicon. *Bell Syst. Tech.*, 39(205), 1960.

[136] K. Miki, D. R. Bowler, J. H. G. Owen, G. A. D. Briggs, and K. Sakamoto. Atomically perfect bismuth lines on Si(001). *Physical Review B*, 59(23):14868, 1999.

[137] J. C. Kim, J. S. Kline, and J. R. Tucker. Fabrication of contact electrodes in Si for nanoelectronic devices using ion implantation. *Applied Surface Science*, 239(3-4):335–341, 2005.

[138] H. Hirayama, M. Koike, Y. Einaga, A. Shibata, and K. Takayanagi. Cross-sectional scanning tunneling microscope study of a boron-implanted Si wafer. *Physical Review B*, 56(4):1948, 1997.

[139] A. M. Yakunin, A. Y. Silov, P. M. Koenraad, J. H. Wolter, W. Van Roy, J. De Boeck, J.-M. Tang, and M. E. Flatté. Spatial structure of an individual Mn acceptor in GaAs. *Phys. Rev. Lett.*, 92(21):4, 2004.

[140] G. W. Morley, M. Warner, A. M. Stoneham, P. T. Greenland, J. van Tol, C. W. M. Kay, and G. Aeppli. The initialization and manipulation of quantum information stored in silicon by bismuth dopants. *Nat Mater*, 9(9):725–729, 2010.

[141] J. P. de Souza and P. F. P. Fichtner. Electrical activation of bismuth implanted into silicon by rapid thermal annealing and kinetics of defects. *Journal of Applied Physics*, 74(1):119–122, 1993.

[142] A. F. da Silva, B. E. Sernelius, J. P. de Souza, and H. Boudinov. Electrical resistivity of bismuth implanted into silicon. *Journal of Applied Physics*, 79(7):3453–3455, 1996.

[143] E. Abramof, A. Ferreira da Silva, B. E. Sernelius, J. P. de Souza, and H. Boudinov. Metal-nonmetal transition and resistivity of silicon implanted with bismuth. *Journal of materials research*, 12(3):5, 1997.

[144] E. Abramof, A. Ferreira da Silva, B. E. Sernelius, J. P. de Souza, and H. Boudinov. Transport properties of silicon implanted with bismuth. *Physical Review B*, 55(15):9584, 1997.

[145] M. Mundschau, E. Bauer, W. Telieps, and W. Swieh. Atomic steps on Si100 and step dynamics during sublimation studied by low-energy electron microscopy. *Surface Science*, 223(3):413–423, 1989.

[146] S. U. Campisano, P. Baeri, E. Rimini, A. M. Malvezzi, and G. Russo. Impurity redistribution in Bi-implanted Si after nanosecond and picosecond Nd laser pulse irradiation. *Applied Physics Letters*, 41(5):456–458, 1982.

[147] A. G. Wagh, P. K. Bhattacharya, and M. J. Kansara. Furnace and laser annealing of bismuth implanted silicon. *Nuclear Instruments and Methods in Physics Research*, 191(1-3):96–100, 1981.

[148] J. A. Mol, S. P. C. Beentjes, and S. Rogge. A low temperature surface preparation method for STM nano-lithography on Si(100). *Applied Surface Science*, 256(16):5042–5045, 2010.

[149] B. S. Swartzentruber, Y. Mo, M. B. Webb, and M. G. Lagally. Scanning tunneling microscopy studies of structural disorder and steps on Si surfaces. *Journal of Vacuum Science and Technology A: Vacuum, Surfaces, and Films*, 7(4):2901–2905, 1989.

[150] A. Bontemps, H. J. Smith, and R. Danielou. Scanning electron-beam annealing of arsenic- and bismuth-implanted silicon. *Journal of Applied Physics*, 53(7):5258–5264, 1982.

[151] S. U. Campisano, E. Rimini, P. Baeri, and G. Foti. Supersaturated solid solutions after solid phase epitaxial growth in Bi-implanted silicon. *Applied Physics Letters*, 37(2):170–172, 1980.

[152] M. Tamura. Damage formation and annealing of ion implantation in Si. *Materials Science Reports*, 6(4-5):141–214, 1991.

[153] P. Sutter and M. G. Lagally. Quantitative determination of dislocation-induced strain at the surface of (001) silicon-on-insulator. *Phys. Rev. Lett.*, 82(7):1490, 1999.

[154] A. P. Wijnheijmer, J. K. Garleff, M. A. v. d. Heijden, and P. M. Koenraad. Influence of the tip work function on scanning tunneling microscopy and spectroscopy on zinc doped GaAs. *Journal of Vacuum Science and Technology B: Microelectronics and Nanometer Structures*, 28(6):1086–1092, 2010.

[155] G. J. de Raad, D. M. Bruls, P. M. Koenraad, and J. H. Wolter. Interplay between tip-induced band bending and voltage-dependent surface corrugation on GaAs(110) surfaces. *Physical Review B*, 66(19):195306, 2002.

[156] P. T. Greenland, S. A. Lynch, A. F. G. van der Meer, B. N. Murdin, C. R. Pidgeon, B. Redlich, N. Q. Vinh, and G. Aeppli. Coherent control of rydberg states in silicon. *Nature*, 465(7301):1057–1061, 2010.

[157] A. K. Ramdas and S. Rodriguez. Spectroscopy of the solid-state analogues of the hydrogen atom: donors and acceptors in semiconductors. *Reports on Progress in Physics*, 44(12):1297–1387, 1981.

[158] P. Ebert. Nano-scale properties of defects in compound semiconductor surfaces. *Surface Science Reports*, 33(4-8):121–303, 1999.

[159] R. J. Hamers. Characterization of localized atomic surface defects by tunneling microscopy and spectroscopy. *Journal of Vacuum Science and Technology B: Microelectronics and Nanometer Structures*, 6(4):1462–1467, 1988.

[160] L. Lequn, Y. Jixin, and J. W. Lyding. Subsurface dopant-induced features on the Si(100)2x1:H surface: fundamental study and applications. *Nanotechnology, IEEE Transactions on*, 1(4):176–183, 2002.

[161] A. M. Stoneham. *Theory of defects in Silicon*. 2001.

[162] A. Rockett, D. D. Johnson, S. V. Khare, and B. R. Tuttle. Prediction of dopant ionization energies in silicon: The importance of strain. *Physical Review B*, 68(23):233208, 2003.

[163] S. T. Picraux, W. L. Brown, and W. M. Gibson. Lattice location by channeling angular distributions: Bi implanted in Si. *Physical Review B*, 6(4):1382, 1972.

[164] P. Badziag and W. S. Verwoerd. Cluster study of the Si(111)-2x1 reconstruction. *Surface Science*, 201(1-2):87–96, 1988.

[165] Y. Hasegawa, M. Ono, Y. Nishigata, T. Nishio, and T. Eguchi. Real-space observation of screened potential and friedel oscillation by scanning tunneling spectroscopy. *Journal of Physics: Conference Series*, 61(1):399, 2007.

[166] T. Ando, A. B. Fowler, and F. Stern. Electronic properties of two-dimensional systems. *Reviews of Modern Physics*, 54(2):437, 1982.

[167] H. Van Cong and S. Brunet. Doping effects on the band structure in n-type silicon at 300 K. *Solid-State Electronics*, 28(6):587–595, 1985.

[168] L. Reining and R. Del Sole. Screened Coulomb interaction at Si(111)-2x1. *Physical Review B*, 44(23):12918, 1991.

[169] L. Reining and R. Del Sole. Quasi one dimensional excitons and the optical properties of Si(111)-2x1. *Phys. Rev. Lett.*, 67(27):3816, 1991.

[170] J. K. Garleff, A. P. Wijnheijmer, and P. M. Koenraad. Challenges in cross-sectional scanning tunneling microscopy on semiconductors. *Semiconductor Science and Technology*, 26(6):064001, 2011.